Simulations of Earth's Local Particulate Environment

A Thesis submitted for the degree of Doctor of Philosophy

By
Neil G. Mackay

Unit For Space Science
Department of Physics
University of Kent at Canterbury
1994

Abstract

Since the dawn of the space age the near earth environment has been becoming increasingly more cluttered with man made products. In recent years there has been a growing fear that the size of this population is approaching a critical threshold. If the population should pass this threshold there would follow a catastrophic series of collision related breakups resulting in a space environment too 'dirty ' to make further satellite launches feasible. The situation is further aggravated by the existence of natural cosmic dust passing through near Earth space.

The broad aim of the project was to help achieve a better understanding of the near Earth cosmic dust and space debris environment. Specifically the aim was to test existing theories about the dust and debris populations by the use of modelling, experiments and of actual data taken from space exposed materials, from the Long Duration Exposure Facility (LDEF).

Two independent computer models were created. The first model simulates impacts on LDEF from cosmic dust particles. The second model simulates impacts on LDEF from space debris.

The models allow the researcher to vary certain parameters about debris and dust populations. The models will then predict, from the researcher's defined parameters, the quantity and distribution of impacts expected on LDEF. These predictions can then be compared with the data gathered from microscopic examination of LDEF materials.

A number of possible scenarios were investigated in this manner and their strengths and weaknesses assessed in terms of how well they satisfied the LDEF data.

In addition an experimental program using a light gas gun and an electrostatic accelerator to produce hypervelocity impact craters was initiated. Ways of attaining more information about individual impact events by study of the impact crater morphology were investigated.

Acknowledgements

Over the past three years I have received help and advice from more than a few people. I would like to start be expressing my thanks to all my friends and colleagues who have made this PhD so much fun. You dudes know who you are!

Specific thanks must go to a number of collaborators without whose help this PhD would have been impossible. Piers Newman for first noticing the elliptical craters and for all his subsequent hours spent scanning the LDEF clamps and taking images of the craters. Mike Cole and Wayne Brooke-Thomas for all their work involved with getting the Light Gas Gun to work. I knew we would get there in the end guys. Ron Bernhard and the Light Gas Gun crew at JSC who supplied the sabots that worked. Tony McDonnell who had the idea for the ski-slope target. Thanks are also due to anyone anywhere who performed any kind of scanning of LDEF and helped define the fluxes so well. Also everyone in the Lab. who have ever answered a question for me (Neil McBride, Ralphy D., Sunil Deshpande, Andrew Taylor , Steve Mullen to name but a few).

Very special thanks are due to a few other people.

Mark English who's put up with the worst and most basic of my questions and patiently explained the fundamental workings of the universe, on the back of an envelope, in words of not more than two syllables, at ungodly hours of the morning, without making me feel stupid.

Simon Green for all his original work on the debris modelling. Also his supervision throughout the past three years, during which time he's always

made him self available to answer questions and give helpful suggestions when they were needed. Thanks especially for all the red pen which has, I hope, eventually taught me how to write.

Finally very special thanks to my parents. They got me here in the first place and supported their spaced out son in this crazy PhD thing.

CONTENTS

Chapter 1

Introduction

1.1 Space Debris

In recent years, there has been a huge increase in the amount of launches of spacecraft into Low Earth Orbit (see Figure 1.1). The nature of these varies from manned missions to simple communication satellites but regardless of there mission there is great concern as to the danger of impacts from uncontrolled particles. These impacts can do varying quantities of damage depending on the velocity and size of the impactor and on the point of impact. In extreme cases this could lead to oxygen leakage on a manned spacecraft, or, in the case of an impact onto a fuel tank, an explosion.

The nature and quantity of these particles are at present ill-defined. Factors such as the velocity, size, mass and spatial density have only so far been estimated. It is also becoming apparent that there is a much higher proportion of man-made particles than was previously thought.

The man-made particles can be almost any part of a satellite or anything connected with a satellite. Known pieces of space debris range from small paint flecks off the surface of a spacecraft to an astronauts glove known to be orbiting the planet. The great fear is that the increasing quantity of debris in the Near Earth Environment could lead to a series of catastrophic break-ups of satellites, causing a still greater quantity of debris culminating in a vicious circle which could effectively render further launches impossible for a great number of years to come. So far there have already been a number of spacecraft break-ups for a variety of reason, some of which are known (e.g.. the intentional explosion of satellites at the end of there missions) but the cause of other break-ups are not certain and may have been caused by impacting debris. In opposition to the continued build up of man-made particles is the de-orbiting of particles due to atmospheric drag. The

effectiveness of this varies greatly with the expansion and contraction of the Earth's atmosphere through solar activity.

In 1988 the space debris question became of such concern to the space industry in general that ESA commissioned the Space Debris Report.[1]

1.2 Interplanetary Dust

Natural particles can come from a variety of sources . Firstly is the "sporadic" count which consists of particles from the asteroid belt being decelerated due to Poynting-Robertson drag and falling in towards the sun, there is also a scattered cometary component from very disperse streams and meteoroids whose orbits have been affected by collisions or close encounters with large bodies, and it has been more recently postulated that there may also be a component of interstellar particles.

A smaller source than the sporadics, are the identifiable streams. These are associated with the orbits of known cometary bodies and roughly follow identifiable orbits which are at times intercepted by the Earth's orbit. This is however, on average, a considerably smaller component than the sporadics and since there are a number of these streams intercepting the Earth at different angles, it is expected to result in only a small asymmetry in the overall encounter geometry with the Earth.

1.3 Dust and Debris Experiments

Telescopes and radar can detect the larger size ranges of particles (see Figure 1.2) and have yielded estimates of the quantity, size and velocity of larger particles. However to estimate the quantity of smaller particles, which

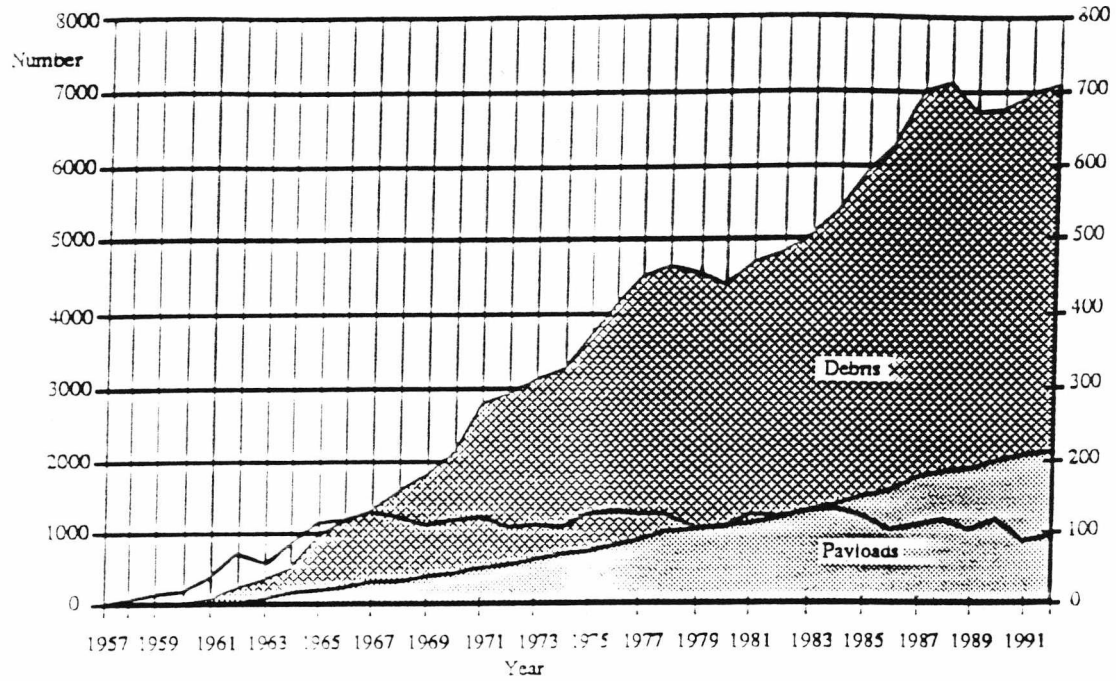

Figure 1.1 Time evolution of debris and payloads in orbit since spaceflight began until 1st January 1993. The left hand axis represents the number of debris and payloads in orbitand the right hand axis the number of launches per year.

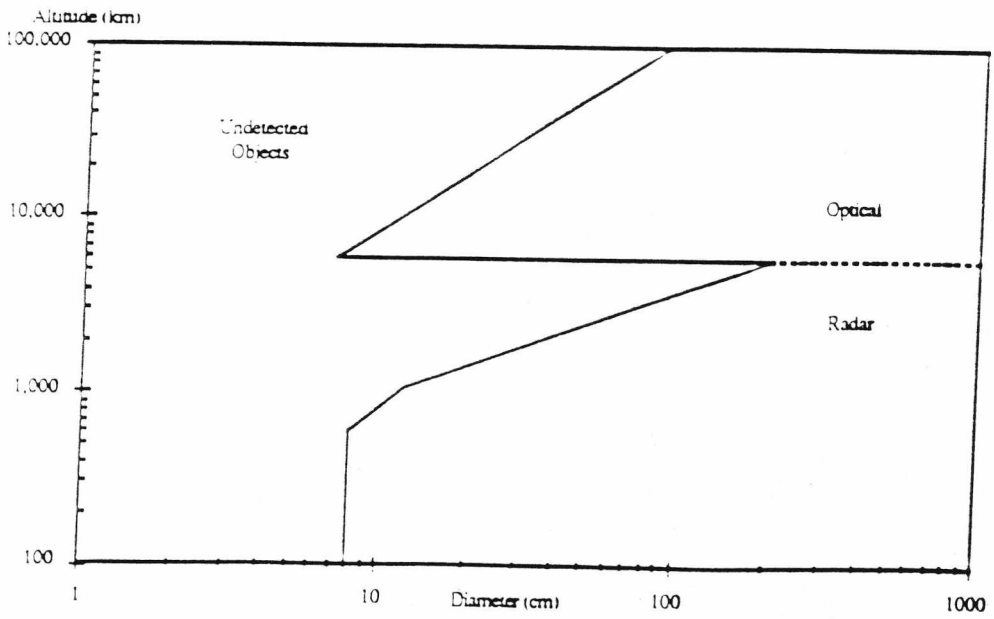

Figure 1.2 Detection limits and operational capabilities of ground based tracking facilities. The optically detected objects take into account all forms of optical detection from the naked eye to powerful ground based telescopes and allowing for orbital velocities and telescope skewing times.

can still be very dangerous because of there high velocities (typical velocities for debris in LEO would be 8 km s^{-1} and for natural particles upwards of 11 km s^{-1}), in situ experiments are required. In the past experiments have been flown on spacecraft such as Pegasus and some of the Pioneer class missions. However to date the satellite with by far the longest area x exposure time, is the Long Duration Exposure Facility (LDEF) .

1.4 Modelling

When the data from these experiments is returned to Earth, it must then be interpreted. A simple count of the impacts can yield only a limited amount of information. In order to test our theories of debris and natural dust populations we need to compare the fluxes of both, with data from satellites. However fluxes on satellites can only be calculated as a function of a cratering property (often the ballistic limit, F_{max}). These F_{max} versus flux plots cannot be converted back to compare with mass distributions because the conversions would require complex penetration equations which include velocity factors, which will vary enormously over the range of natural dust and debris. So we must convert the natural dust and debris mass distributions to flux versus F_{max} curves.

This is where models are useful tools. Using a model, which starts with assumptions about the distribution of natural and man-made particles, we can extrapolate and see what the resultant distribution of particles on a spacecraft would be. We can then compare this with the actual impacts found on a spacecraft to see if they agree. If they don't, we can then change our initial assumptions and repeat the process until we have better defined the environment.

As we will see later, the result of this kind of analysis produces strong evedince that existing quantitative models are inadequate.

At the start of this research program the standard tool which most people used was the Kessler model[2]. The advantage of the Kessler model is that it is a single analytical equation for estimating debris fluxes on a spacecraft in a given circular orbit. However the Kessler model is only 2-dimensional, assuming that all debris are in circular orbits . Also predictions from the Kessler model are of the "random tumbling plate " type, meaning there is no directionality in the results purely average flux levels on the spacecraft.

The Kessler model is used as the basis for the debris flux predictions in ESABASE[3]. ESABASE gives a limited amount of directionality in it's predictions of space debris impacts but still assumes that all the debris is in 2D- orbits. The result of this would be that for a spacecraft like the Long Duration Exposure Facility ESABASE predicts no impacts on a number of it's faces, when in reality there are reasonably high numbers of impacts from debris in elliptical orbits.

More recently the Population Model of Small Size Space Debris[4] was created which performs debris modelling at a more sophisticated level than ESABASE. The drawback with this package is that external researchers are not given access to the code and time periods between requesting an execution of the code and receiving the results are resultantly lengthy.

Section 2.1 of this thesis is an overview of some of the properties of space debris, and a summary of some of the work done previously in the field by Dr S. F. Green. The rest of the chapter then goes on to discuss the Long Duration Exposure Facility and the interpretation of debris and interplanetary

dust fluxes with respect to the LDEF satellite. Included in this is a discussion of the impact physics and equations necessary for this purpose.

Chapter 3 starts with an in depth outline of the interplanetary dust model. This simulation only models the background sporadic meteors (no streams) and assumes directional randomness of the sporadic meteorites with respect to the any Earth orbiting satellite.

Although the source directions of the sporadics is not truly random it is expected that the movement of the Earth round the sun with respect to these particles and the orbit of any satellite around the Earth will tend to average out any directionality quite quickly over short periods of time (and the LDEF satellite, which is being modelled, spent 5.75 years orbiting the planet).

Chapter 3 then goes on to use the interplanetary dust model to analyse the variation of the distribution of impacts on LDEF for a variety of particle velocities. There is then a short review of work performed by previous researchers to define the size and speed distribution of micrometeoroids. Finally a size and velocity distribution are chosen and these are transformed to LDEF's altitude for estimating the LDEF's true environment during its 5.75 years in space.

Chapter 4 starts with an in depth outline of the space debris model. It then goes on to perform an analysis of relative flux levels on different faces of LDEF for a range of individual space debris orbits. Finally the distribution of impact angles on each face for these orbits is analysed in order to look for typical signatures from orbit classes.

The advantage of the space debris model used for the purpose of this thesis is that, unlike ESABASE, it is a 3-dimensional model (ie. debris in eccentric orbits are included).

Chapter 5 begins with a summary of LDEF data sources then goes on to define an LDEF dataset on which to base comparisons with the space debris and interplanetary dust models. Both the models are then used in conjunction with data acquired by analysis of space exposed materials, taken from LDEF, to assess what the actual relative debris/dust levels are in the near Earth environment and the accuracy of the model inputs.

The chapter then goes on to perform a similar analysis for an alternative debris population estimate. This population estimate is based on chemical data taken from LDEF. An attempt is made to explain discrepancies between the LDEF data and predictions from the modelling. Finally suggestions are made for further analysis of the interplanetary dust populations.

Chapter 6 takes a more detailed look at specific craters found on the LDEF materials. A number of elliptical craters are observed which are explained as likely to have been caused by oblique angle impacts.

Modelling is then used for comparison of the LDEF elliptical craters and the expected directionality of the impacts on LDEF's individual faces. As a result of this an experimental investigation of hypervelocity impacts is proposed.

1.5 The Experimental Program

Investigation of hypervelocity impacts is not an easy process. In order to achieve velocities above 1 km s^{-1} very specialised equipment is necessary.

Velocities in the region at which interplanetary dust particles collide with spacecraft are even harder to achieve. Figure 1.3 shows the approximate velocities which can be achieved by different pieces of equipment. Facilities available to the researcher were the Unit for Space Sciences Van de Graaff accelerator and Light Gas Gun. The Light Gas Gun was chosen as the main tool for the experimental program since although it was not capable of such high velocities it was known that the very high velocity impacts from the Van de Graaff accelerator would produce impact craters so small that even the available Scanning Electron Microscope (SEM) would produce images of too poor a quality to make confident measurements from.

When the experimental program was proposed the Light Gas Gun had never yet been successfully used as an experimental tool. Development work which had been performed on it since its inception had been spectacularly ineffective and even the simplest shot was usually a failure. There followed a very extensive period of time consuming tests and modifications on the gun before it could be used for experiments. The length of time spent on this section of the research can not unfortunately be adequately reflected in this thesis.

Chapter 7 begins by outlining the long process of developing the Light Gas Gun into a useful experimental tool. It then goes on to define the experiments performed on both the Light Gas Gun and the Van de Graaff accelerator. Finally the results of the experimental program are presented and conclusions are drawn from them.

Chapter 8 is a summary of the main conclusions arrived at in this Thesis and some recommendations for further research.

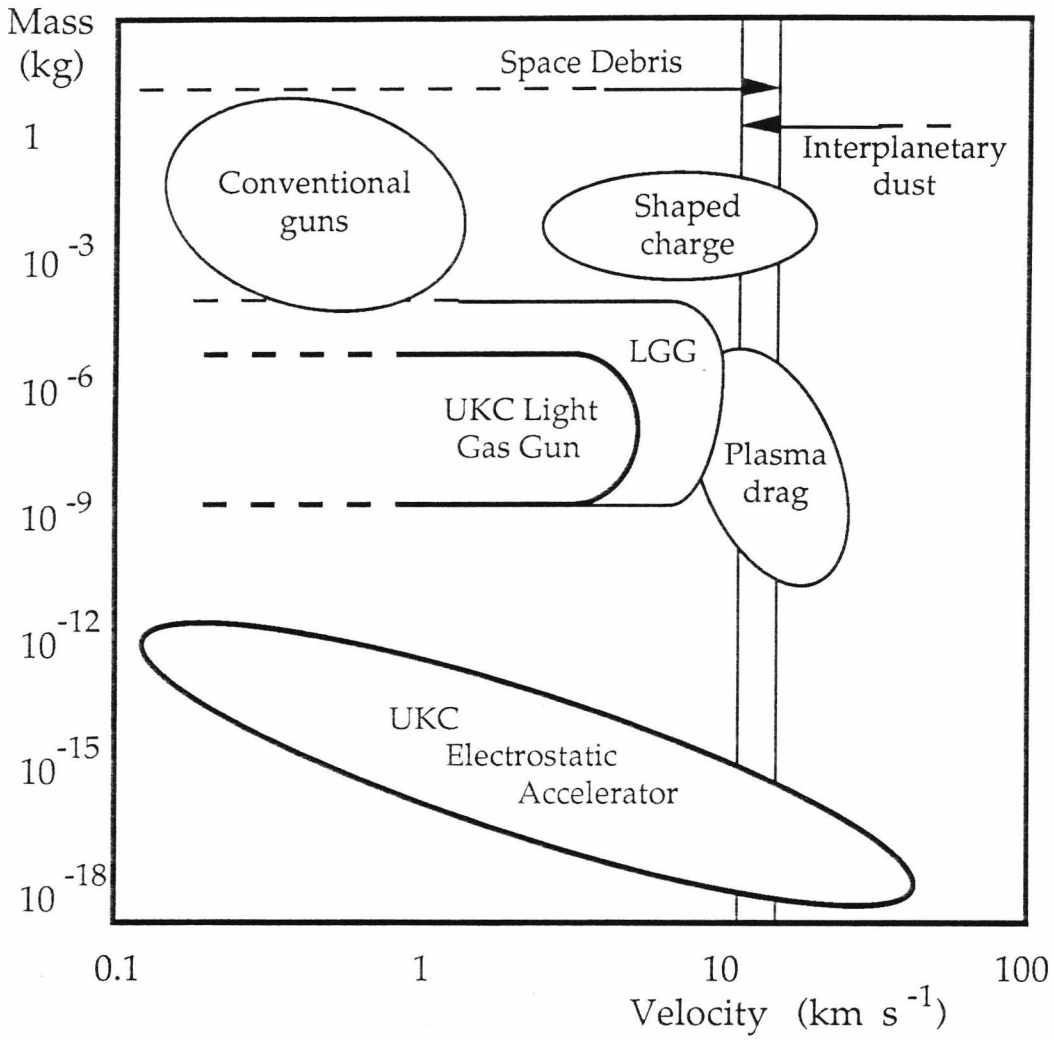

Figure 1.3. An outline of the capabilities of particle accelerators with respect to interplanetary dust and space debris.

Chapter 2

Space Debris and LDEF

2.1 Space Debris

A great deal of work has been done in the past on the subject of defining the nature of space debris and its orbital characteristics[5]. There are at present over 22,000 objects being tracked by USSPACECOM, including objects a few centimetres and above in LEO and upwards of around 1 metre in GEO. This population increases exponentially into the smaller size regimes, which includes in addition to the paint flakes and aluminium oxide spherules (from upper stage motor burns) fragmentation products from collisions of larger objects.

Within ESA, in order to further investigate this threat, the Space Debris Working Group was established. In 1988 they produced a report called "Space Debris"[1]. The recommendations made included the building and operation of a dedicated electro-optical facility for continuous monitoring, the possible use of existing medium-sized optical telescopes which are not fully exploited for astronomical observations and the use of space borne infrared telescopes.

In order to fully implement this an estimate of the properties of the space debris being targeted was required. To this end, Workpackage 2100[1] was commissioned. It's aims were

> to define the physical and dynamical statistical characteristics of space debris, including size, velocities, and spatial distribution functions, and the mean and standard deviations of albedo and emissivity and
> Establish standard radiative descriptions for representative types of space debris in the visible and infrared spectral bands, taking into account physical, orbital and radiative environment considerations

In this workpackage Green uses data from the DISCOS database to define a distribution of debris orbits in perigee, inclination and eccentricity bins. Using this data he builds a simple model describing the spatial and velocity distributions of debris in altitude-latitude bins around the Earth. He also identifies a technique for defining a size distribution of debris particles in these bins.

Further to this in workpackages 3100,3200,4100 and 4200 ground and space based telescopes for monitoring orbital debris are designed and observation scenarios defined. Workpackage 4300[6] then goes on to asses the prospective performance of the ground and space based concepts in terms of

Detection frequency and limitations on debris orbits, types and sizes covered
Uncertainties in debris characterisation
Selection effects on observed objects.

In order to do this Green creates a model of debris dynamics, capable of determining which orbital regimes pass through the field of view of a telescope. The debris distributions from Workpackage 2100 are incorporated in this with orbits representing each of the perigee-inclination-eccentricity bins being considered, with the appropriate weighting attached. He later went on to convert this to produce a distribution of impact vectors on a spacecraft in circular orbit.

This model assumes that individual orbits suffer rapid regression of nodes and advance of the lines of apsides. due to non-sphericity of the Earth's gravitational field (caused by the Earth's oblateness). This is true except for orbits with an inclination of 63.4°, which is the inclination on the boundary between orbits with prograde and retrograde perturbatons and as a

result suffers no perturbations itself. So randomness of nodes and lines of apsides is assumed for each of the orbits.

2.2 LDEF

The Long Duration Exposure Facility (LDEF) was designed to take advantage of the recovery capabilities of the Space Shuttle. LDEF was a container for a large number of scientific experiments which would require minimal quantities of power and data processing while in Space but which could benefit from in depth analysis when returned to Earth.

LDEF was essentially a polygonal frame with 12 peripheral sides and two ends (see Figure 2.1). The frame was about 30 feet long and 14 feet in diameter and capable of holding 86 experimental trays. Typical experimental trays were 34 inches wide, 50 inches long and 3, 6 or 12 inches deep.

The LDEF experiments were aimed at studying effects of the space environment (i.e. ionising radiation, meteoroids, cosmic dust, and high altitude atomic oxygen) on materials and mechanical, electronic, optical, and living systems. They were grouped into four categories

1) Materials, Coatings and Thermal Systems
2) Power and Propulsion
3) Science
4) Electronics and Optics

There were a number of science experiments which were aimed at the study of cosmic dust and/or space debris. These were

Multiple-Foil Microabrasion Package
Study of Meteoroid Impact Craters on Various Materials

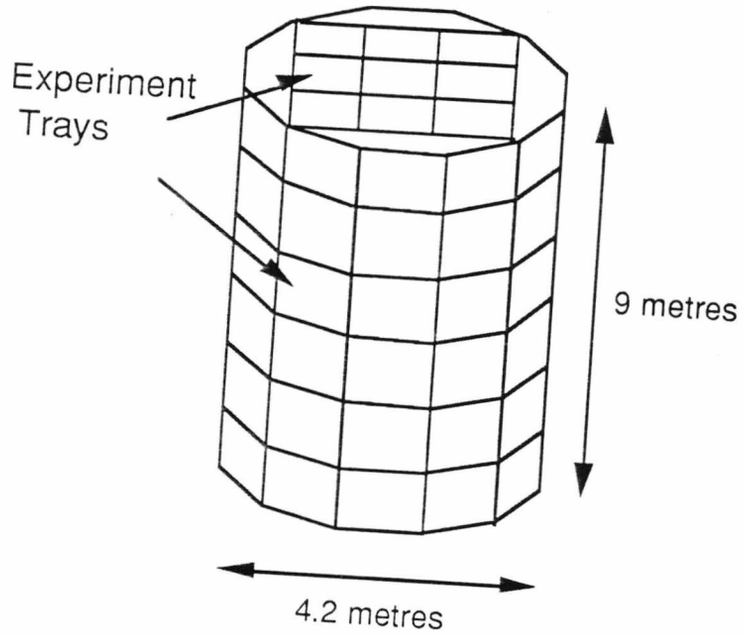

Figure 2.1 The Long Duration Exposure Facility.

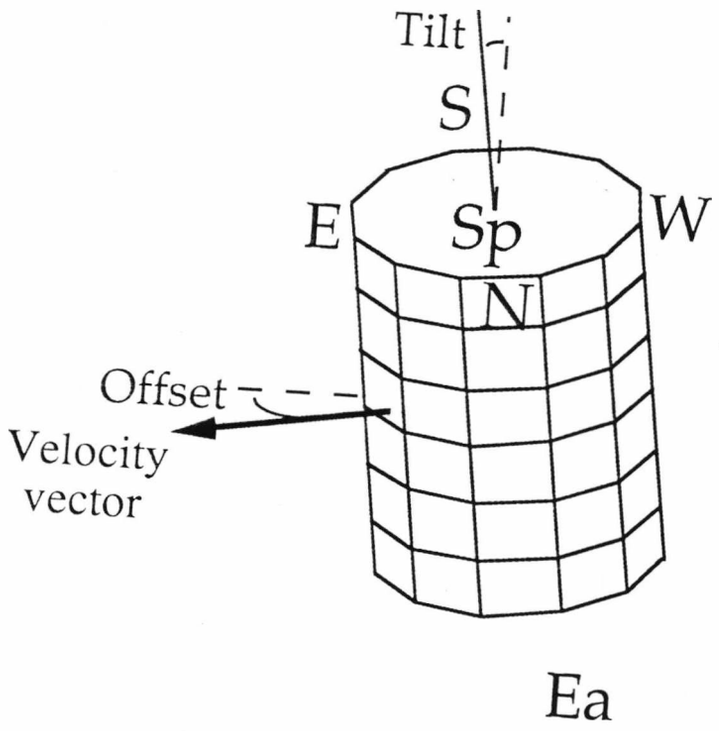

Figure 2.2 LDEF's offset and tilt.

Attempt at Dust Debris Collection with Stacked Detectors

The Chemistry of Micrometeoroids

Chemical and Isotopic Measurements of Micrometeoroids by Secondary Ion Mass Spectrometry

Interplanetary Dust Experiment

Space Debris Impact Experiment

Meteoroid damage to Spacecraft

In addition to these planned experiments, useful data could also be gleaned from incidentally exposed surfaces,. For example LDEF's frame and cosmic ray covers from a number of experiments were analysed on LDEF's return and produced quantities of valuable data.

LDEF was deployed into a 28.5° inclination, circular, Low Earth Orbit (LEO) in April 1984 by the Space Shuttle Challenger. It's planned retrieval date was 12 months later but due to the Challenger disaster it was not retrieved until 57 months later than this. As a result of it's extended stay of 69 months in space LDEF provides us with the largest time x area exposure for the study of dust and debris impacts yet achieved.

LDEF was gravity gradient stabilised which meant that one face would always face in the direction of the velocity vector, another would point away etc. while one end would point permanently towards the Earth and the other towards Space. The two ends were called the Earth and Space ends respectively while the peripheral faces were numbered from 1 to 12. In addition 4 of the peripheral faces were given names corresponding to there nominal pointing directions. These were

Face 3 = West face, nominally facing West, in the opposite direction from the velocity vector (or anti-RAM direction)

Face 6 = North face, nominally towards the North pole

Face 9 = East face, nominally facing East, in the direction of the velocity vector (or RAM direction)

Face 12 = South face, nominally pointing towards the South pole

In reality LDEF had an 8° offset, twisting the North face towards the direction of the velocity vector and a 1.1° tilt, tilting the Space end towards the velocity vector (see Figure 2.2).

LDEF's deployment altitude was 476 km but this deteriorated throughout the 69 months in space (rapidly towards the end) to 332 km when it was retrieved shortly before it would of burnt up re-entering the Earth's atmosphere. The average altitude over the 69 months was estimated to be 468 km.

2.3 Model Overview

Both the interplanetary dust and space debris models produce the same format of output.

The interplanetary dust model begins with an isotropic distribution of dust vectors and a velocity distribution. It then transforms these vectors to take account of the spacecraft's motion and produces the effective distribution of impact vectors and corresponding fractions, which represent the proportion of the total flux which is coming from that direction (see Chapter 3 for more details of these calculations). This distribution of impact vectors can then be applied at any point on the spacecraft's surface. Then the size distribution is incorporated and the appropriate fluxes can be calculated and summed, and a total flux rate at that point can thus be estimated.

The space debris model begins with a distribution of debris orbits (with inherent velocities). It similarly calculates from this a distribution of impact vectors on a spacecraft taking into account the spacecraft's velocity. A weighting factor of (probability of debris in this orbit intersecting spacecraft)/(total no. of debris orbits) is assigned to each of the orbits thus dealt with (see Chapter 4 for more details of these calculations) . The impact vector is once more applied to any point on the spacecraft and when the debris size distribution is incorporated a total flux rate at that point is calculated.

For both the IP and the debris models, once the distribution of impact vectors and the associated fractions are calculated the same routine is used to interpret these impacts in terms of the spacecraft's geometry. The procedure for doing this is outlined below.

2.4 LDEF Geometry

Having calculated a distribution of impact vectors and associated flux levels, for a satellite at a given altitude, from either the interplanetary dust (chapter 3) model or the debris (chapter 4) model, this must then be applied to the individual geometry of the spacecraft in question.

For each impact vector and associated flux, the impact vector (V_{rd}) and flux (Ωf) are then used to calculate the impacts on the real satellite (i.e. LDEF, although the models are designed to make the calculations for any polyhedral satellite in any circular orbit).

Each face of the satellite is taken in turn and tested to see if this V_{rel} is coming from in front or behind the face. To do this we must first calculate the normal vectors to all the surfaces of the satellite.

2.4.1 Calculations Of Normal Vectors

Taking axis as shown in Figure 2.3, with the X1 axis pointing in the direction of motion , the Z1 axis pointing away from the Earth , and the Y1 axis perpendicular to both of these.

If we rotate LDEF through its offset angle and create a new set of axis as below in Figure 2.4.

The new co-ordinate system has the X2 axis perpendicular to the East face , the Y2 axis perpendicular to the South face and the Z2 axis pointing away from the Earth (coinciding with the Z1 axis).

2.4.1.1 The Peripheral Faces

Using this new "2" Co-ordinate system the normals to the peripheral faces are

$$N(\theta)= (\cos\theta,\sin\theta,0)_2$$

where θ is the angle between the normal to the East face and the normal to the face in question (e.g. for South $\theta=90°$).

We then perform the tilt rotation , keeping the "2" Co-ordinate system (see Figure 2.5).

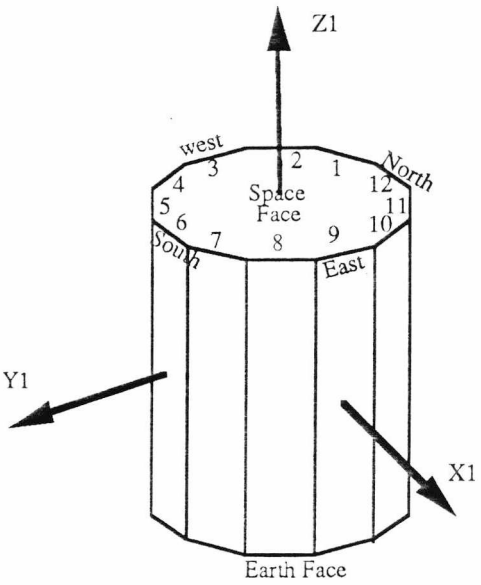

Figure 2.3 LDEF and co-ordinate axis.

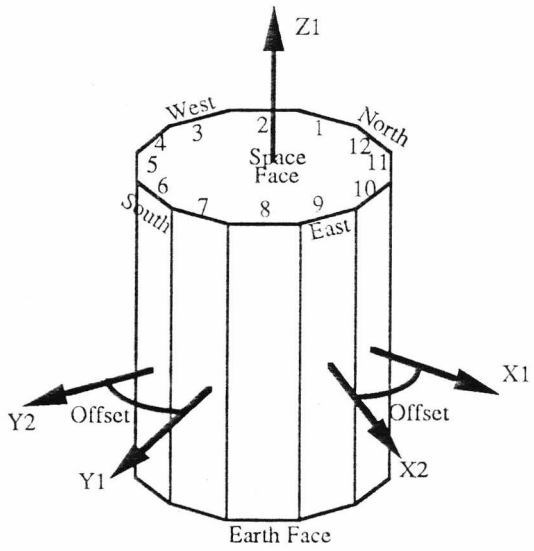

Figure 2.4 LDEF after it's 8° offset is included, with a new co-ordinate system.

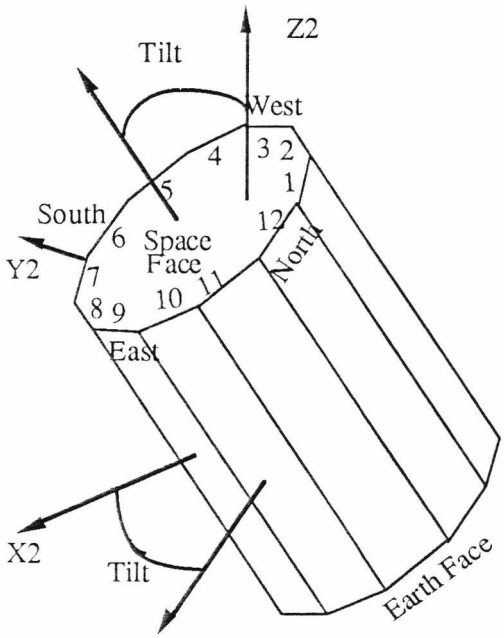

Figure 2.5 LDEF after offset and tilt.

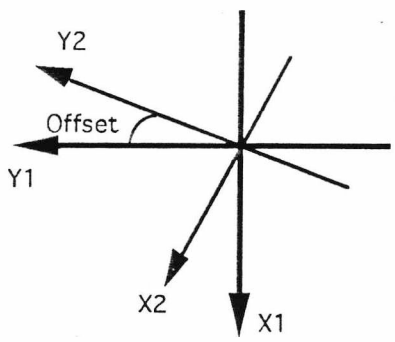

Figure 2.6 The two co-ordinate systems.

The Y2 component of the normal, $N(\theta)$, to the peripheral faces is unaffected by the tilt rotation since the Y2 axis is also the axis of rotation. The X2 and the Z2 components on the other hand are directly in the direction of the tilt.

So still in the "2" Co_ordinate system , assuming that before the tilt we had

$$N(\theta)=(\cos\theta,\sin\theta,0)_2$$

Then after the tilt we get

$$N(\theta)=(\cos(tilt)\cos\theta,\sin\theta,-\sin(tilt)\cos\theta)_2 \qquad \text{Equation 2.1}$$

We must now convert this back to the "1" Co-ordinate system. In order to derive the transformation required we start with an arbitrary vector in the "2" system.

$$N(\theta) = (a,b,c)_2$$

$$=(a,0,0)_2+(0,b,0)_2+(0,0,c)_2$$

and we have

$$(a,0,0)_2=(a\cos(offset),a\sin(offset),0)_1$$

$$(0,b,0)_2=(-b\sin(offset),b\cos(offset),0)_1$$

$$(0,0,c)_2=(o,o,c)_1$$

So we have in the "1" Co_ordinate system

$$N(\theta)=(a\cos(offset)-b\sin(offset), a\sin(offset)+b\cos(offset), c) \qquad \text{Equation 2.2}$$

Then using a, b and c as calculated earlier for $N(\theta)$ we get

$$X1(N(\theta))=\cos\theta\cos(tilt)\cos(offset)-\sin\theta\sin(offset)$$

$$Y1(N(\theta))=\cos\theta\cos(tilt)\sin(offset)+\sin\theta\sin(offset)$$

$$Z1(N(\theta))=-\cos\theta\sin(tilt)$$

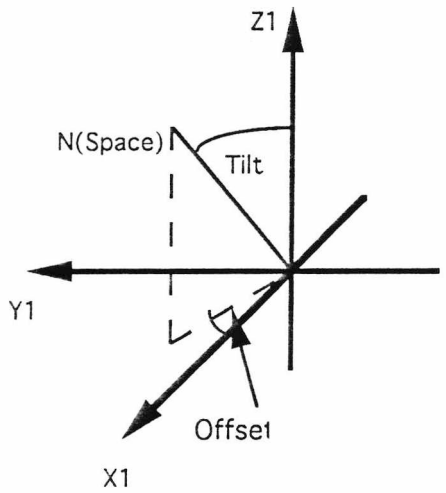

Figure 2.7 The normal vector to the Space Face.

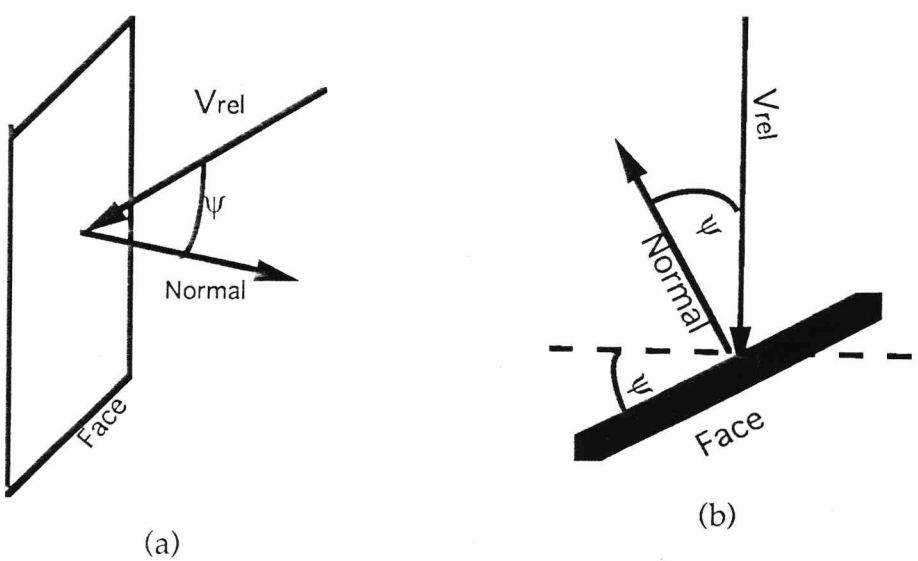

Figure 2.8 Dust impacting one of LDEF's Faces.

2.4.1.2 Space and Earth faces

The normal to the Space face is unaffected by the offset but is tilted in the direction of the East face.

So we have

N(Space)=(Cos(offset)Sin(tilt), Sin(offset)Sin(tilt), Cos(tilt)) Equation 2.3

The normal to the Earth Face is the negative of the Space Face normal.

2.4.2 Calculation Of Flux On Faces

To find out if V_{rel} is coming from in front or behind a face we use the dot product.

If V_{rel} . normal < 0 Then $\psi>90°$ so the particle is coming from behind the face (Figure 2.8 (a)).

Similarly

If V_{rel} . normal > 0 Then $\psi<90°$ so the particle is coming from the front of the face.

If V_{rel} is coming from the front of the face then the component of the flux from this direction which impacts on the plate is (Figure 2.8 (b))

$P=\Omega f \cos\psi$ Equation 2.4

In this case the angle between the normal and $V_{rel}(\psi)$.the normal component of the velocity ($V_{rel}\cos\psi$) and the impacting component of the flux (P) are stored.

This process is repeated for all the peripheral faces and for the Space and Earth faces.

In this way all the fluxes "P" are added to give estimates of total fluxes on each face and velocity and angular distribution of the fluxes etc. on each face.

2.5 Impact Physics

In order to make useful comparisons between the models and the LDEF data, we require directly comparable figures. Fluxes at a particle size or mass are of no use for this . What is required is fluxes as a function of some crater or perforation characteristic. The characteristic chosen was the F_{max}.

F_{max} is a value associated with each impact. The F_{max} value is the maximum possible thickness of foil which can be perforated by a projectile at it's impact velocity.

There are many equations which can be used to estimate Fmax. None of these equations are known to be more accurate or reliable for the general case (most are derived from specific materials in specific size and velocity regimes). The one selected was created by Hill[7] (Equation 2.5 and 2.6). This is a reasonably simple equation which requires only target material properties, projectile density and normal impact velocity. Since a target material for study is chosen and the projectile densities are assumed elsewhere (see chapters 3 and 4), there are no new assumptions than are already inherent in the models.

$$f=0.6d\left(\frac{\rho_P}{\rho_T}\right)^{0.26}\left(\frac{\sigma_T}{\sigma_o}\right)^{-0.08}V^{\beta} \qquad \text{Equation 2.5}$$

Where

$$\beta=0.69\left(\frac{\rho_p}{\rho_T}\right)^{0.09} \qquad \text{Equation 2.6}$$

and

f = projectile F_{max}

d= projectile diameter

ρ_p = projectile density

ρ_T= target density

σ_T= target tensile strength

σ_o= a scaling factor of 80 MPa

V= normal component of impact velocity (=V_{rel} Cosψ in the earlier notation) and is measured in km s^{-1}

For example, we find that for an aluminium target and a 1mm diameter natural particle of density 1000 kg m^{-3} travelling at 20 kms^{-1} we have.

d = 1mm, ρ_p = 1000 kg m^{-3}, ρ_T = 2710 kg m^{-3}, σ_T = 80 Mpa,

V = 20 km s^{-1}

Which gives β = 0.631 and thus f = 3.07 mm.

Thus for any given target material and assuming projectile densities as stated in chapters 3 and 4 we can make an estimate of the F_{max} for each impacting particle in the models. From this we can estimate fluxes as a function of F_{max} for comparison with LDEF data.

Chapter 3

The Interplanetary Dust Model

3.1 Assumptions

The interplanetary dust particles are assumed to have an isotropic geocentric spatial distribution. An effective atmospheric height of 150 km is used in calculating the Earth shielding cone.

3.2 The Algorithm

3.2.1 The Isotropic Flux

A regular array of vectors was chosen to represent the isotropic dust distribution. This array of vectors was defined by splitting the sphere of possible directions into sections, as shown below. It was first split into θ–sectors from $0 \rightarrow 2\pi$ as shown (Figure 3.1), with the θ_plane parallel to the Earth's surface . These sectors were of equal size (1° steps were used , although this could be easily altered if required).

It was then split similarly into φ-sectors from $-\pi/2 \rightarrow \pi/2$, these sectors being in a plane from the Earth pointing direction to the space pointing direction. Again these were of a regular size and 1° steps were used.

The two above steps effectively split the sphere into angular bins with a θ and a φ co-ordinate. It is worth noting here, that although the bins are of regular dimensions (i.e.. 1° x 1°) the angular bins are not of a constant size.

From Figure 3.3 it can be easily seen that the bins nearer the $\varphi=0$ level of the sphere are larger than the bins at the extreme ends ($\varphi=\pm \pi/2$). So an associated fraction of the total incoming flux is calculated for each bin.

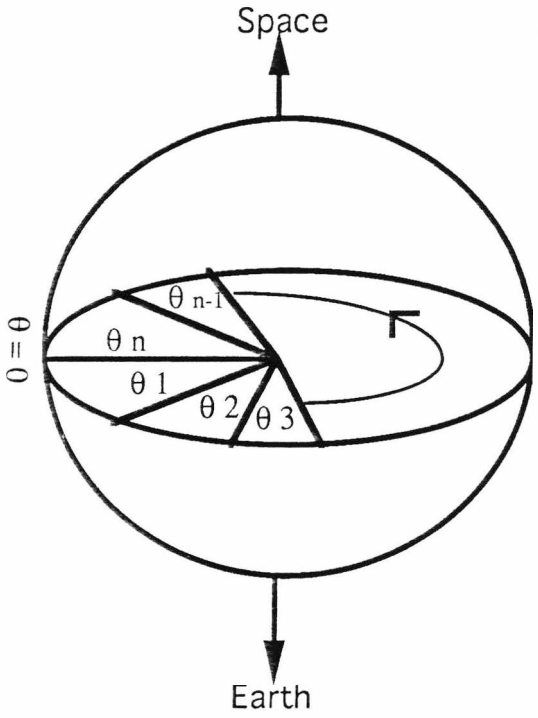

Figure 3.1 An arbitrary sphere in Space is split into segments in a plane parallel to the Earth's surface.

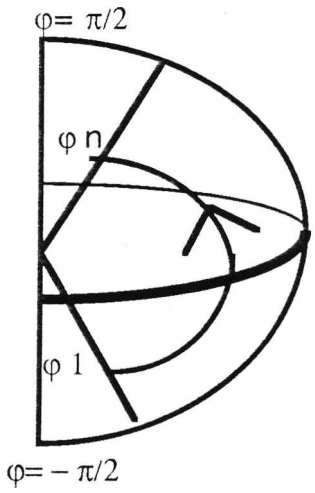

Figure 3.2 The sphere is then split into sectors in a plane perpendicular to the first.

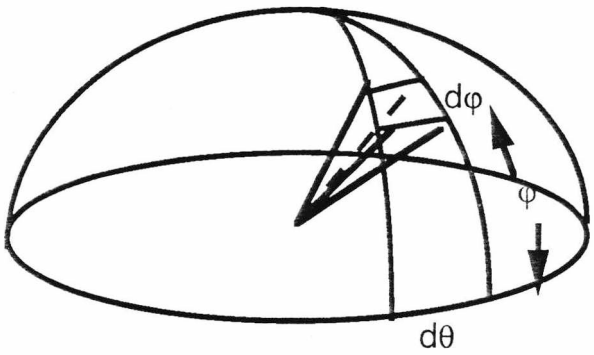

Figure 3.3 The sphere is effectively split into angular bins.

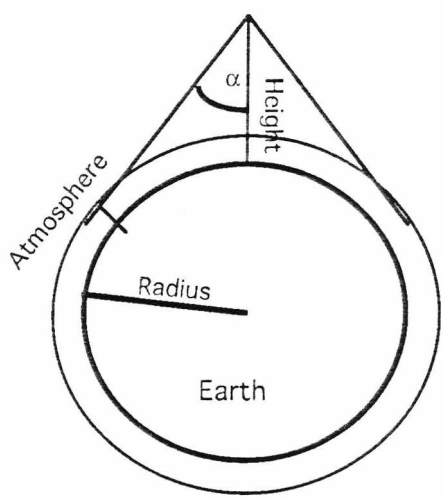

Figure 3.4 Earth Shielding

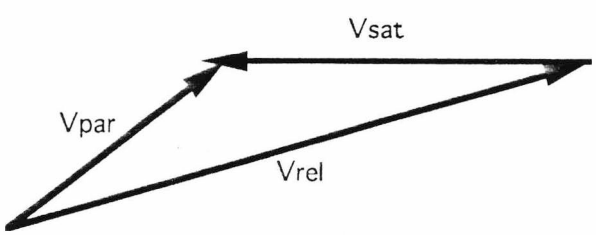

Figure 3.5 The velocity of a particle relative to the spacecraft.

This is

$$d\Omega = d\varphi \mathrm{Cos}\varphi d\theta$$

The flux from each of these quadrants of space is then represented by a single vector (V_{par}), which contains information about the dust's velocity and direction of motion, and an associated flux (Flux x $d\Omega$).

3.2.2 Earth Shielding

Each of these vectors, V_{par}, is tested to see if it is contained within the Earth shielding cone.

The shielding angle (α) is calculated as follows.

$$\alpha = \sin^{-1}((R_e + h_A)/(R_e + h_S)) \qquad \text{Equation 3.1}$$

Where Rad = Earth's radius,

h_A= The effective atmospheric height

and

h_S = The height of the satellite above the Earth's surface.

If the φ-value of the vector is less than $-\pi/2+\alpha$ it lies within the Earth's shielding cone and can be discounted as a potential source of impacts onto a satellite at this altitude..

3.2.3 The Flux on A Moving Spacecraft

The vectors (V_{par}) are each then corrected for the satellite's orbital velocity (V_{sat}) and an array of new vectors (V_{rel}) are calculated. The new array

represents the impact vectors of the dust relative to a satellite orbiting at the given altitude.

As a result of the dusts velocity relative to the satellite, the associated flux for each of these vectors is altered (the spatial density remains constant, but the flux depends on the relative velocities between the satellite and the dust). The new flux to be associated with the V_{rel} array of vectors is calculated as below.

$$\Omega f = f\, d\Omega\, (V_{rel}/V_{par}) \qquad \text{Equation 3.2}$$

Where Ωf is the new flux, f the old flux and $d\Omega$ is as defined in 3.2.1.

The array of vectors, V_{rel}, can then be passed on to a routine that takes into account the satellite's geometry and can calculate flux levels for specific spacecraft in the defined orbit (see chapter 2).

3.3 Analysis Of Variation Of Parameters

Firstly the distribution of impact vectors was studied for various possible dust velocities. The dust velocities chosen ranged from 10 km s^{-1} to 30 km s-1. This range was chosen because the vast majority (over 90 %) of dust is expected to lie in this range for encounters with LEO.

From geometric considerations all the impact velocities must lie in the range $V_{par} \pm 7.64$ km s^{-1} . The velocity distribution of the impact vectors, is shown in Figure 3.6, while Figure 3.7 and Figure 3.8 show the angular distribution of the impact vectors. Figure 3.7 gives the distribution in the

"vertical" (or φ plane as defined in Figure 3.2), -90° being Earth pointing, 0° including vectors pointing in the plane parallel to the Earth's surface and 90° being the Space pointing direction. Figure 3.8 is the distribution of vectors in the plane parallel to the Earth's surface (or the θ plane as defined in Figure 3.1).

For all dust velocities the relative flux levels increase towards the maximum possible impact velocity (V_{par} +7.64 km s^{-1}) . The slightly smaller value before the cut-off is a binning effect (the data is binned in 1 km s^{-1} steps but the final bin will only contain impacts in a 0.64 km s^{-1} broad region). As the dust velocities increase, the distributions begin to level off and would approach a straight line from V_{par}-7.64 to V_{par}+7.46 as the dust velocity approaches infinity.

For low particle velocities the sweeping up effect dominates the graph in Figure 3.7 (Ωflux = flux $d\Omega$ (V_{rel}/V_{par})) causing a much larger flux on the front of the satellite where the impact velocities are also higher. However as the dust velocity increases, the right hand side of the curve will tend towards a section of a cosine wave (the 0 to $\pi/2$ section). This is purely a result of the varying bin size as φ increases ($d\Omega=d\varphi Cos\varphi d\theta$) . The left hand side of the curve is affected by Earth shielding, hence the very sharp cut-off.

When the spacecraft's motion is incorporated to calculate the effective impact vector of a particle, the impact vectors of low velocity particles will undergo a larger angular displacement than similar high velocity particles. This means that low velocity particles from the near anti-ram direction will have effective impact vectors at quite large angles from the anti-ram direction. The result is that for low velocities we can have particles impacting at , for example Φ= -45°, where at higher particle velocities there's nothing coming in with Φ< -25°.

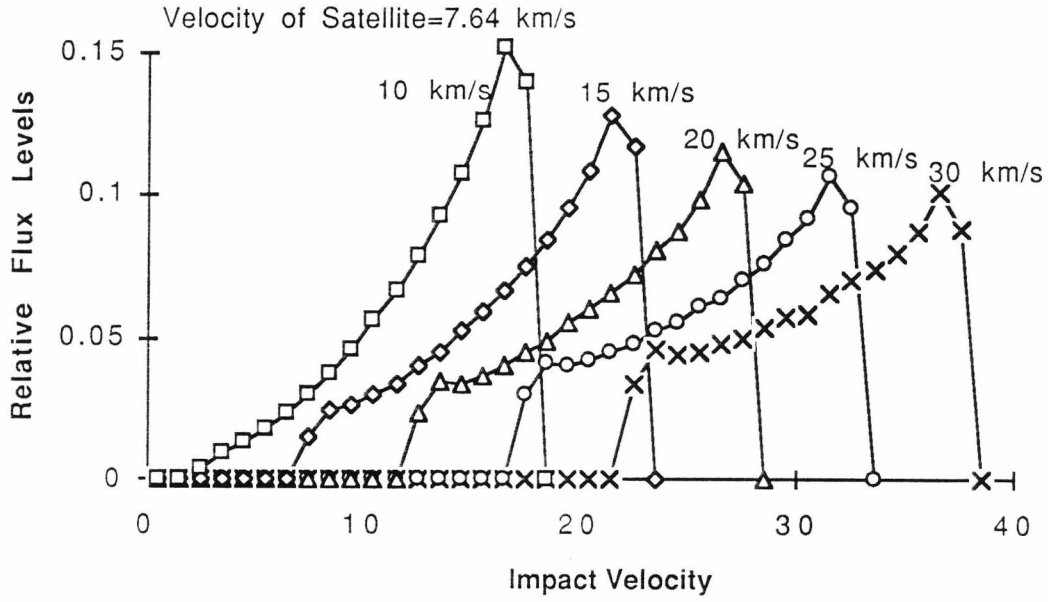

Figure 3.6 Distribution of velocities of impact vectors on a satellite orbiting at an altitude of 468 km for various IP dust velocities.

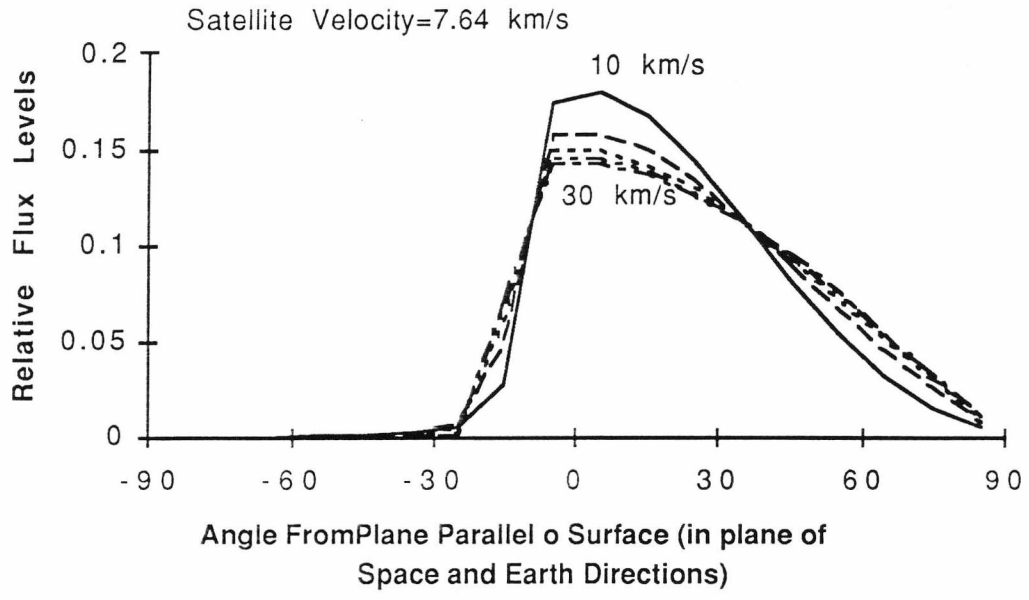

Figure 3.7 Angular distribution in a plane perpendicular to the Earth's surface of the impact vectors on a satellite orbiting at an altitude of 468 km for various IP dust velocities.

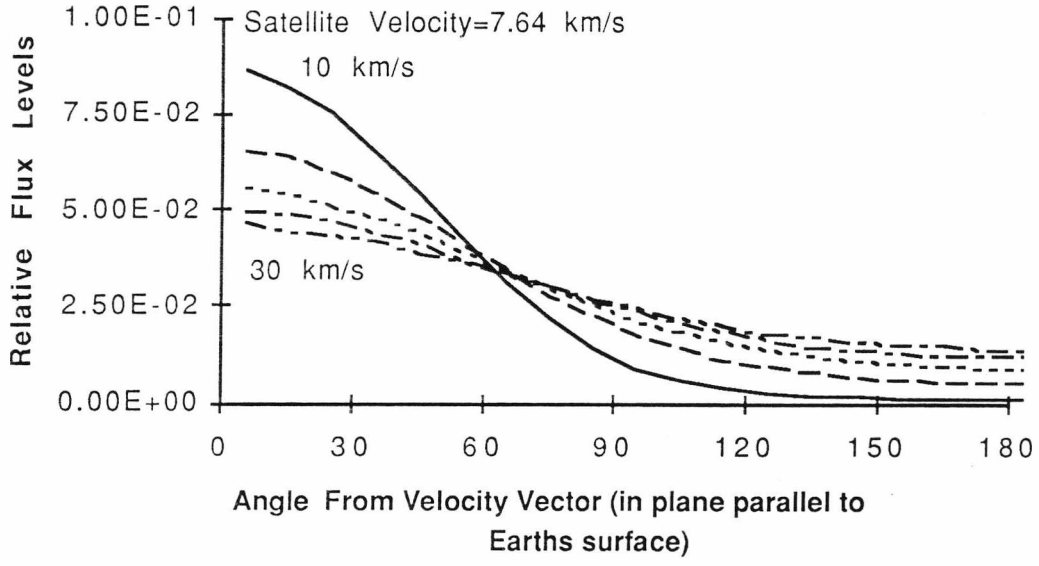

Figure 3.7 Angular distribution in a plane parallel to the Earth's surface of the impact vectors on a satellite orbiting at an altitude of 468 km for various IP dust velocities.

Again in Fig 3.8, as particle velocities increase the sweeping up effect becomes less significant (since $V_{rel}/V_{par} \rightarrow 1$ as $V_{par} \rightarrow \infty$) so we see the graph flattening out towards a constant flux around the satellite . This time however, as the dust velocity approaches infinity, the graph will flatten out and become a straight line (since the bins in the θ direction are of constant size) but at very low velocities the difference in relative flux levels between the vectors from the direction of motion and from the opposite direction can be orders of magnitude.

The next step was to study how the dust velocity affected the actual distribution of impacts on the individual faces of LDEF. Fig 3.9 shows the relative flux levels on LDEF's individual faces.

Figure 3.9 shows that for low dust velocities the difference between fluxes on leading and trailing edges of LDEF can be as much as a factor of 30, but as dust velocities increase this disparity begins to level out. North and South have similar fluxes but the North faces slightly higher as it faces slightly towards the front due to the 8° offset. The Space face shows a slightly higher flux than North and South but this is due purely to the Earth shielding effect on North and South which does not affect the Space face. In contrast, the very low fluxes on the Earth face (lower, for most dust velocities, than the West face) is due entirely to the Earth shielding effect.

Figures 3.11-3.16 show the angular distributions of impacts on the 6 cardinal faces of LDEF.

In Figures 3.11-3.16 the relative levels plotted refer to all impacts coming in from within an annulus at an angle ψ from the normal to the surface. (As shown in Figure 3.10).

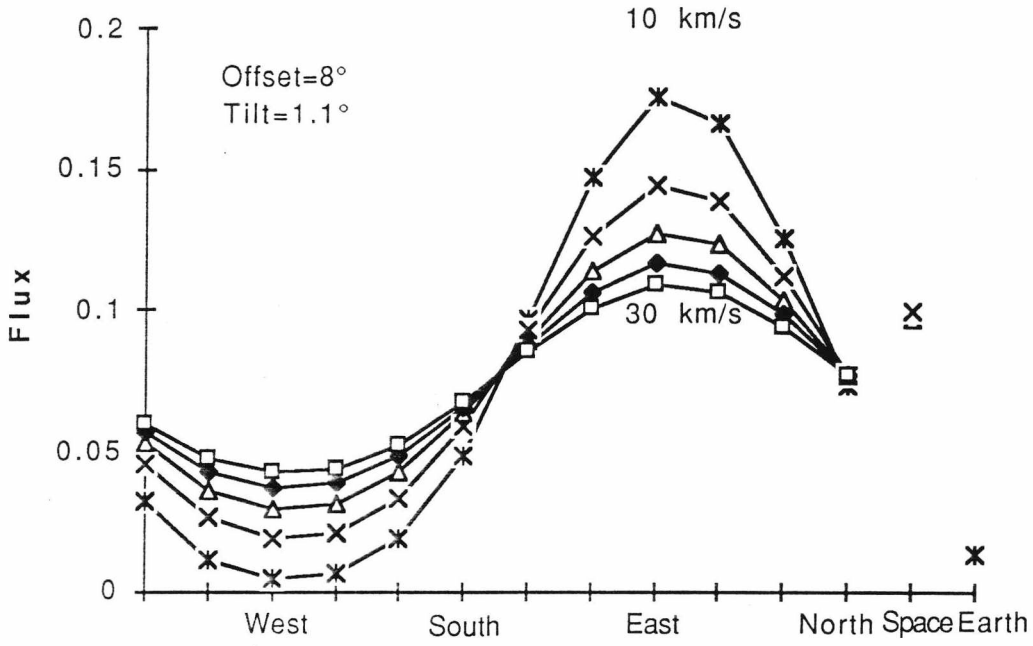

Figure 3.9 Relative flux levels on LDEF's faces for various particle velocities.

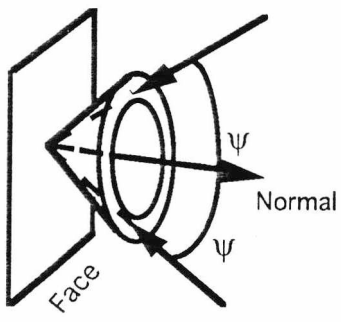

Figure 3.10 Definition of flux plotted in Figures 3.11 to 3.16

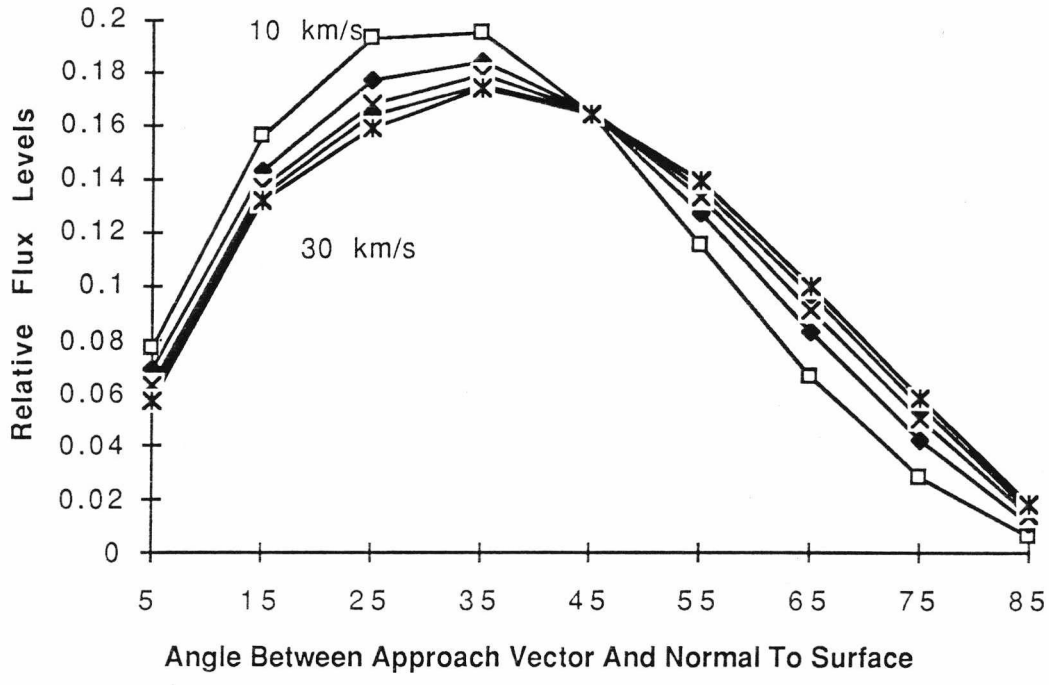

Fig 3.11. Angular distribution of impacts on LDEF's East face for various particle velocities.

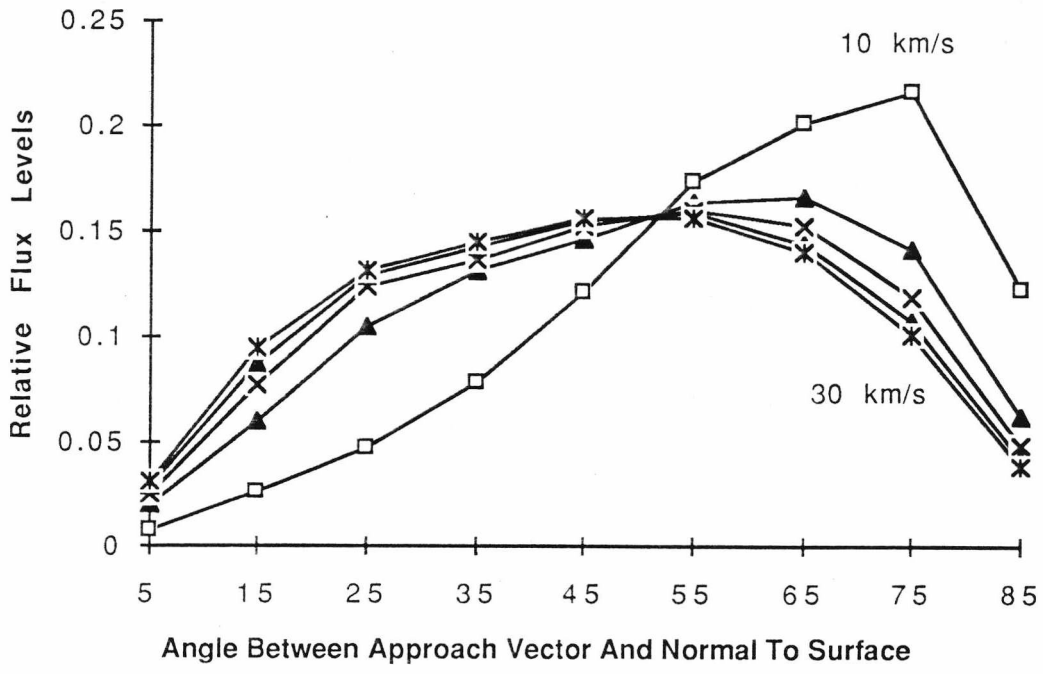

Fig 3.12. Angular distribution of impacts on LDEF's West face for various particle velocities.

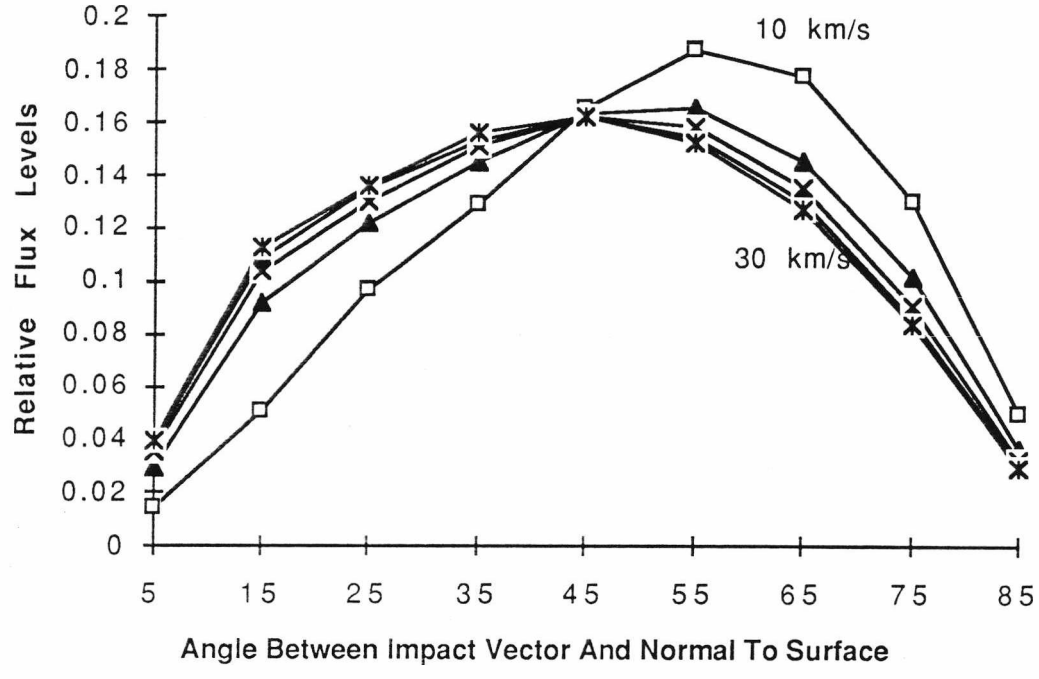

Fig 3.13. Angular distribution of impacts on LDEF's South face for various particle velocities.

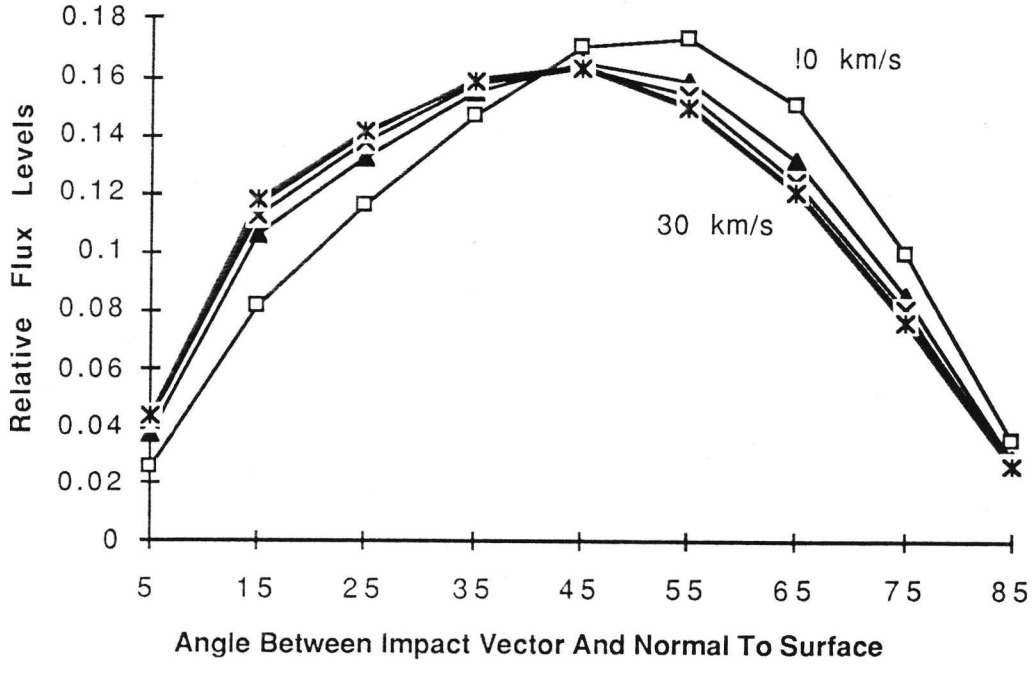

Fig 3.14. Angular distribution of impacts on LDEF's North face for various particle velocities.

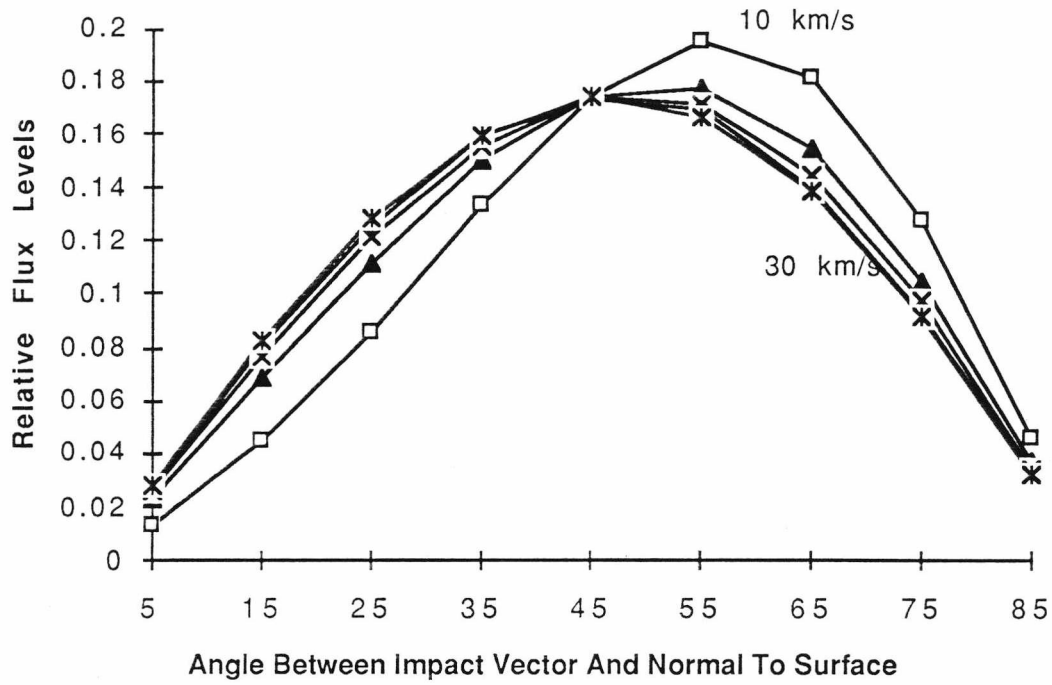

Fig 3.15. Angular distribution of impacts on LDEF's Space face for various particle velocities.

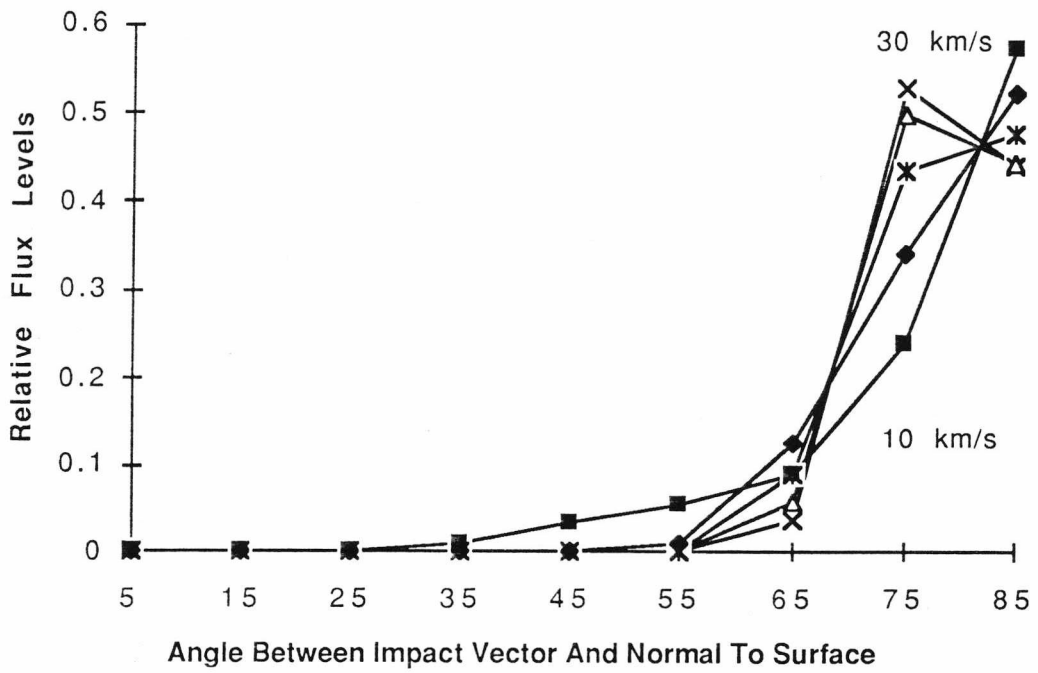

Fig 3.16. Angular distribution of impacts on LDEF's Earth face for various particle velocities.

The basic shape of all these curves, if LDEF were stationary and there was no Earth shielding to be considered, would be a part of a Cosine x Sine wave (the part from 0 to $\pi/2$). This is purely as a result of the geometric considerations. The area of each angular bin varies as a Sine wave (Area=$2\pi\text{Sin}\psi$), and the exposed area varies as a cosine of the angle to the normal.

The graph for the East face (Figure 3.11) shows that the impacts are asymmetrically skewed in favour of those close to the normal vector. This is partly a result of the satellite's motion and partly Earth shielding. However higher dust velocities tend to begin to smooth out the effect of the satellite's motion.

On the West face (Figure 3.12) again the Earth shielding is biasing the distribution in favour of impacts close to the normal, however this time the spacecraft's motion is acting to bias the impacts towards grazing impacts and this influence is stronger. So as a result the graph is skewed towards grazing impacts but except in the case of very low dust velocities the skewing is visibly less pronounced.

On the North and South faces (Figures 3.13, 3.14) the interactions are somewhat more complex. The spacecraft's motion again causes an enhanced flux towards the Ram direction. This will , in addition to transforming the near normal incidence impacts into grazing impacts from the Ram direction, cause the anti-ram direction grazing impacts to become near normal impacts (although the total effect is in favour of grazing impacts). Earth shielding is once more cutting out some of the grazing earth direction impacts. However the net effect of all this is that both these faces have only a very slight skewing

towards the grazing impacts. The difference between the curves for the North and South faces is due purely to the 8° offset of the spacecraft. As the North face is pointing slightly more towards the Ram direction it is far more affected by the Earth shielding since the 'effective ' shielding cone is swept forward by the spacecraft's motion. As a result of this there is more skewing on the South face than the North.

The Space face (Figure 3.15) is similar to the North and South faces since it is also almost perpendicular to the direction of motion (apart from the 1.1° tilt of the satellite). This time however there is no contribution at all from Earth shielding so the skewing is completely caused by the satellites motion and is therefore larger.

The opposite is true of the Earth face (Figure 3.16). In this instance the distribution is enormously dominated by the Earth shielding effect, and as a result it is only for very slow dust velocities that there are any near normal impacts.

The velocity distributions in Figures 3.17 - Figure 3.22 show the relative flux levels for the normal components of impact velocities. This quantity was chosen as opposed to the actual impact velocities since the normal component of the velocities is more significant in determining the ballistic limit for a given impact.

On the East face (Figure 3.17) the velocities are considerably greater than on the other faces. This is helped by the Earth shielding which will cut out some of the low velocity impacts on the East face (Low normal velocity equates to grazing impacts on the East face). It is true also on the West face (Figure 3.18) that the grazing impacts will have slowest normal velocities. However, since all impacts on this face are catching up with the spacecraft

and therefore have a considerably slower impact velocity, the West face impacts are still by far the slowest of the peripheral faces (but this disparity will become less pronounced as the dust velocities increase).

The North and South faces (Figures 3.19,3.20) again show very similar distributions which once more are a compromise between the extreme cases of the East and West faces.

The Space face (Figure 3.21) distribution is similar in shape to the North, South, East and West face distributions but again covers a different range of velocities. However the Earth face (Figure 3.22) distribution is once more visibly affected by Earth shielding. It only covers a very narrow velocity band and the shape of the distribution does not resemble the shape of the other distributions.

The lower flux of slower more oblique angle impacts on the rear of the spacecraft will cause far fewer (for some dust velocities, orders of magnitude fewer) foil perforations on the rear (and Earth faces) of LDEF than on the Leading faces. This result is not due to any inhomogeneity in the dust distribution, but purely due to the spacecraft's motion and the Earth shielding effect.

The purpose of the modelling was to be able to compare it with LDEF data in order to better identify the micrometeoroid and space debris populations. In order to do this the models were given what was considered to be the most appropriate input data.

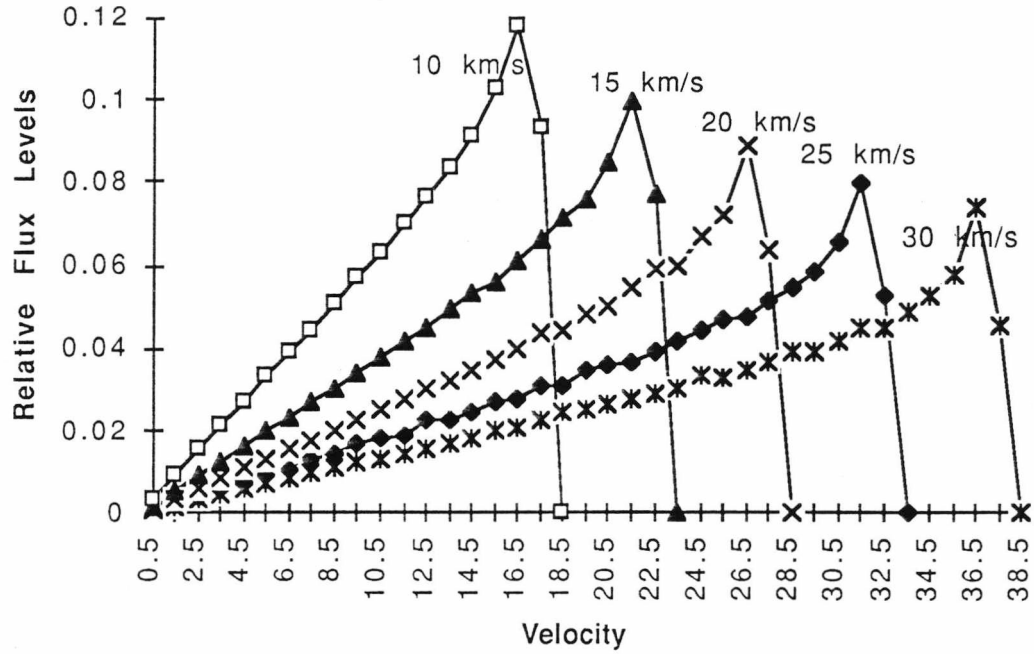

Fig 3.17. Distribution of normal components of impact velocities on LDEF's East face for various particle velocities.

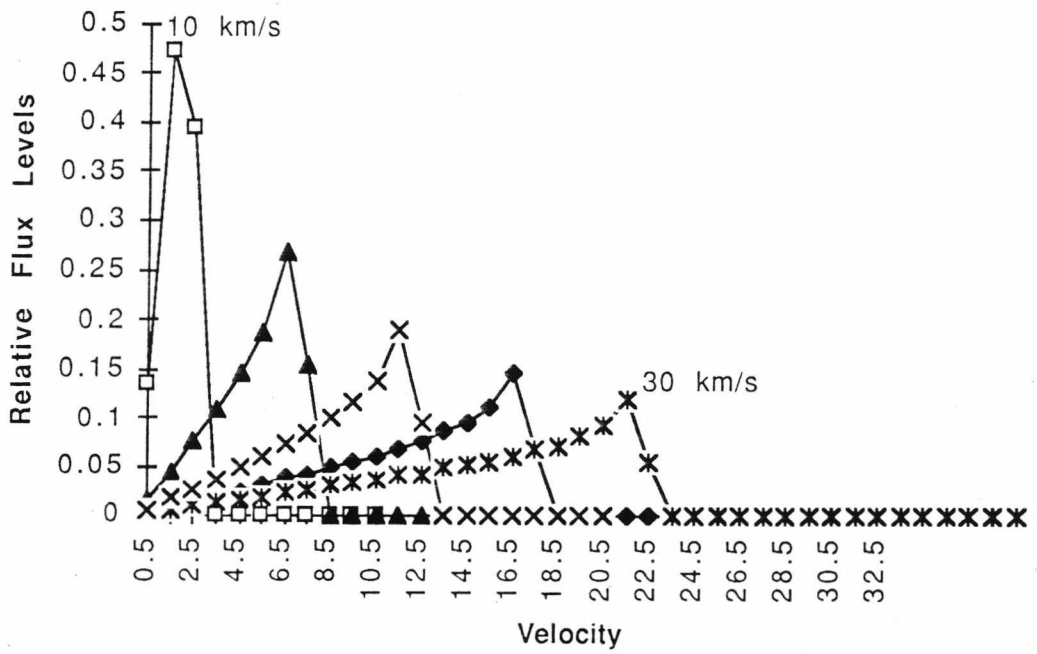

Fig 3.18. Distribution of normal components of impact velocities on LDEF's West face for various particle velocities.

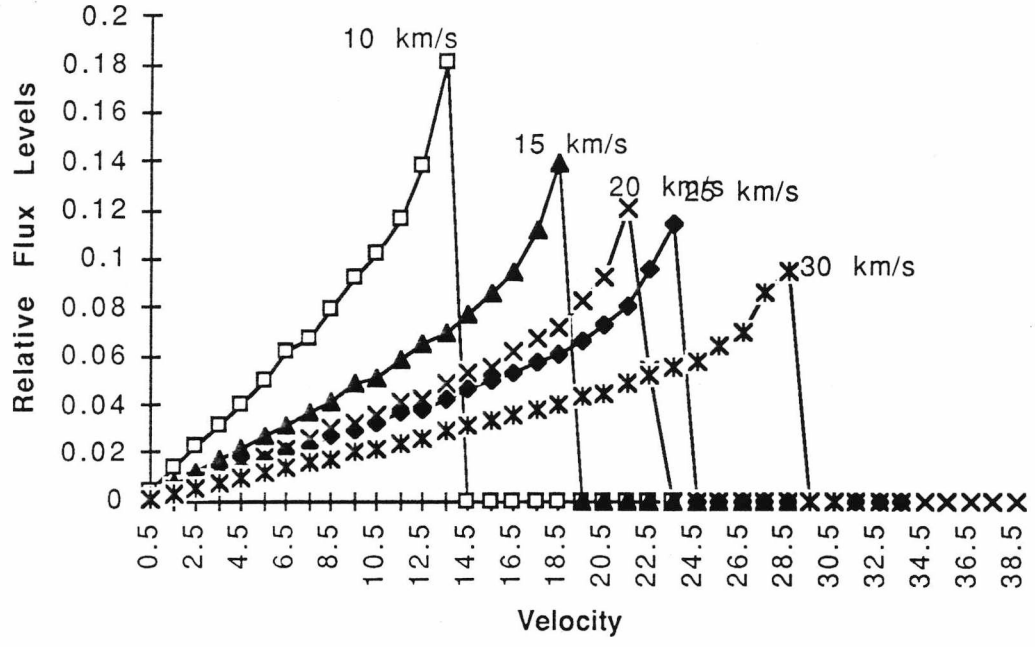

Fig 3.19. Distribution of normal components of impact velocities on LDEF's South face for various particle velocities.

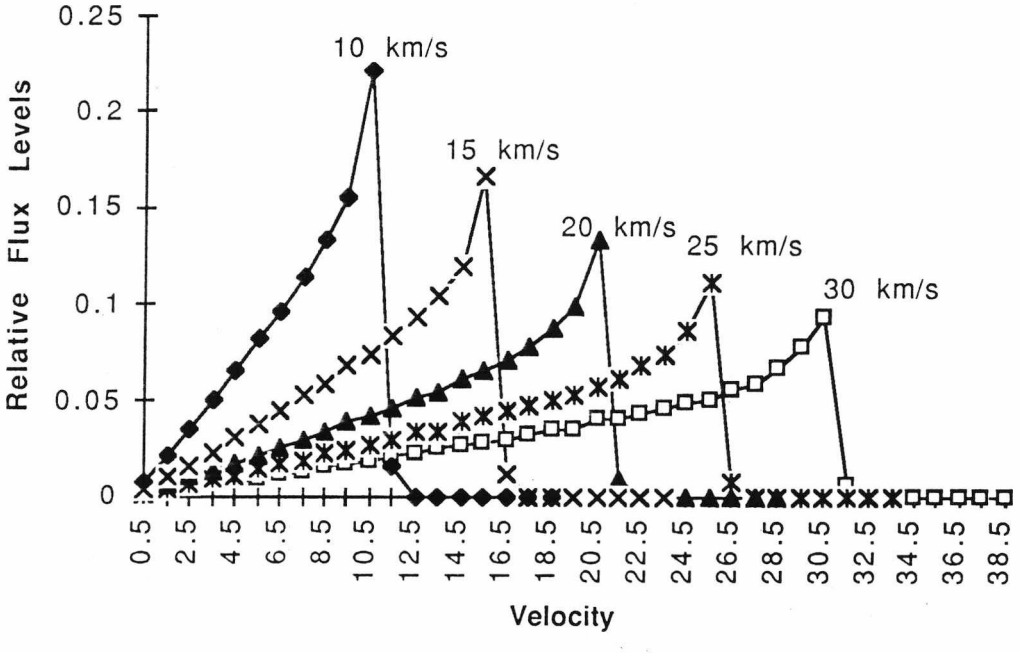

Fig 3.20. Distribution of normal components of impact velocities on LDEF's North face for various particle velocities.

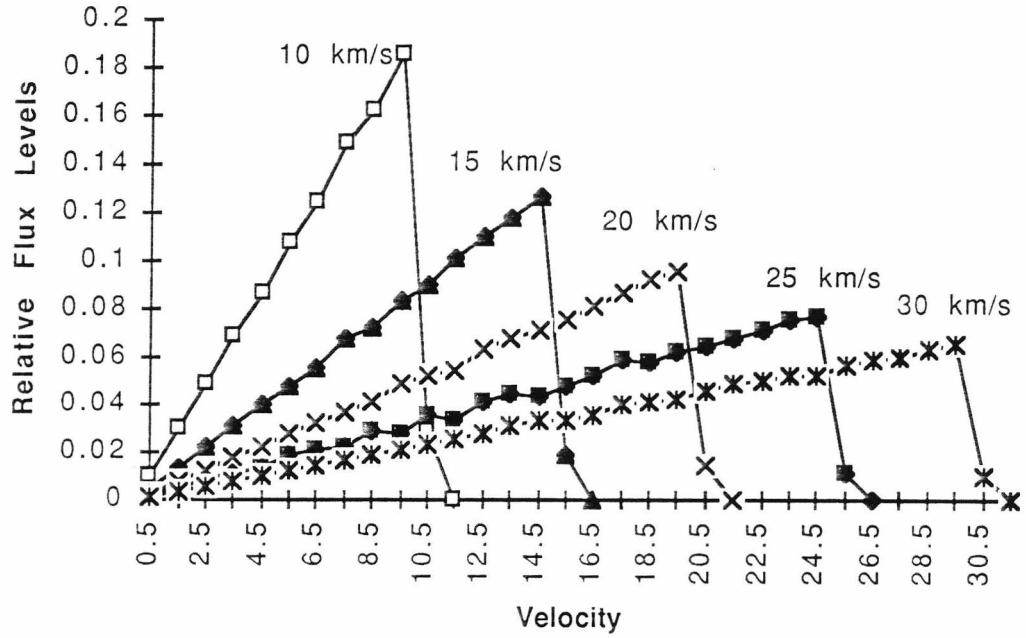

Fig 3.21. Distribution of normal components of impact velocities on LDEF's Space face for various particle velocities.

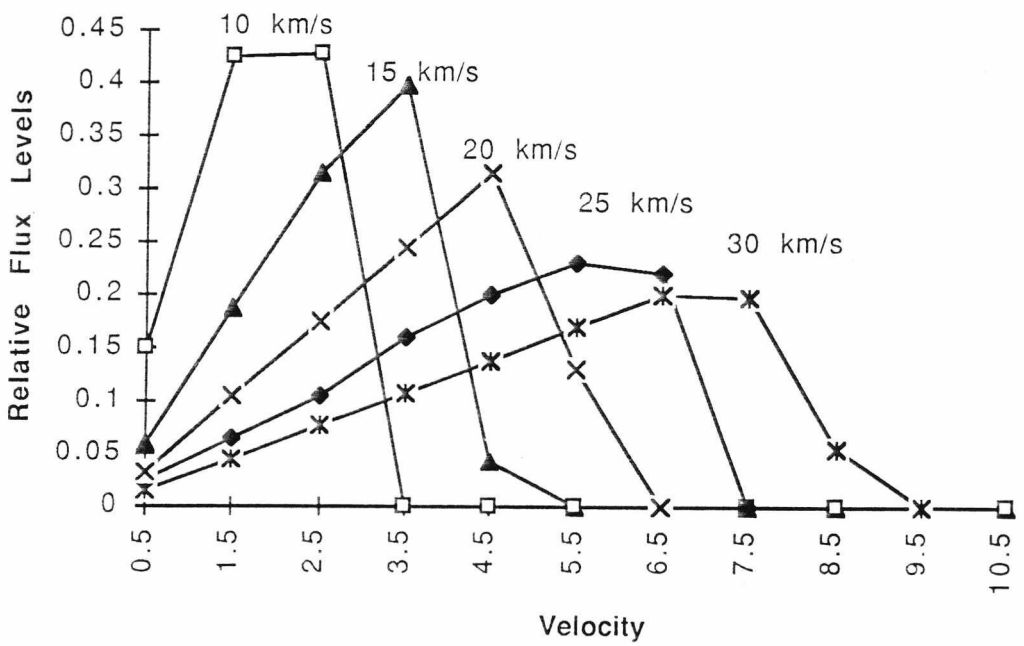

Fig 3.22. Distribution of normal components of impact velocities on LDEF's Earth face for various particle velocities.

3.4 Interplanetary Dust Model Input

3.4.1 The Velocity Distribution

First a velocity distribution was required to be selected to represent that of the cosmic dust population.

A number of such velocity distributions were studied.

Southworth and Sekanina [8]	(derived from data from the Harvard Radio Meteor Program)
Dohnanyi[9]	(a model of photographic meteors)
Erickson[10]	(derived from photographic meteor data)
Kessler[11]	(derived from photographic meteor data)

The general shape of the four velocity distributions seem to agree fairly well with each other above 20 km s^{-1} but below this they vary quite a bit (see Figure 3.23). The Southworth and Sekanina distribution is that which is most biased towards the low velocities and seems to have a near asymptotic behaviour as it approaches the orbital velocity. The Dohnanyi distribution on the other hand behaves in the opposite manner and rapidly falls off from about 17 km s^{-1}, this is the other extreme case of the four distributions analysed so was discounted.

The Kessler and Erickson distributions agree very well with each other, following an almost indistinguishable path. These two also lie right in the middle of the first two so it was decided that either of these would be an appropriate velocity distribution to use. On studying the Kessler and Erickson distributions further it was found that the Erickson distribution was available in a more appropriate and easily manageable form so this one was selected for use.

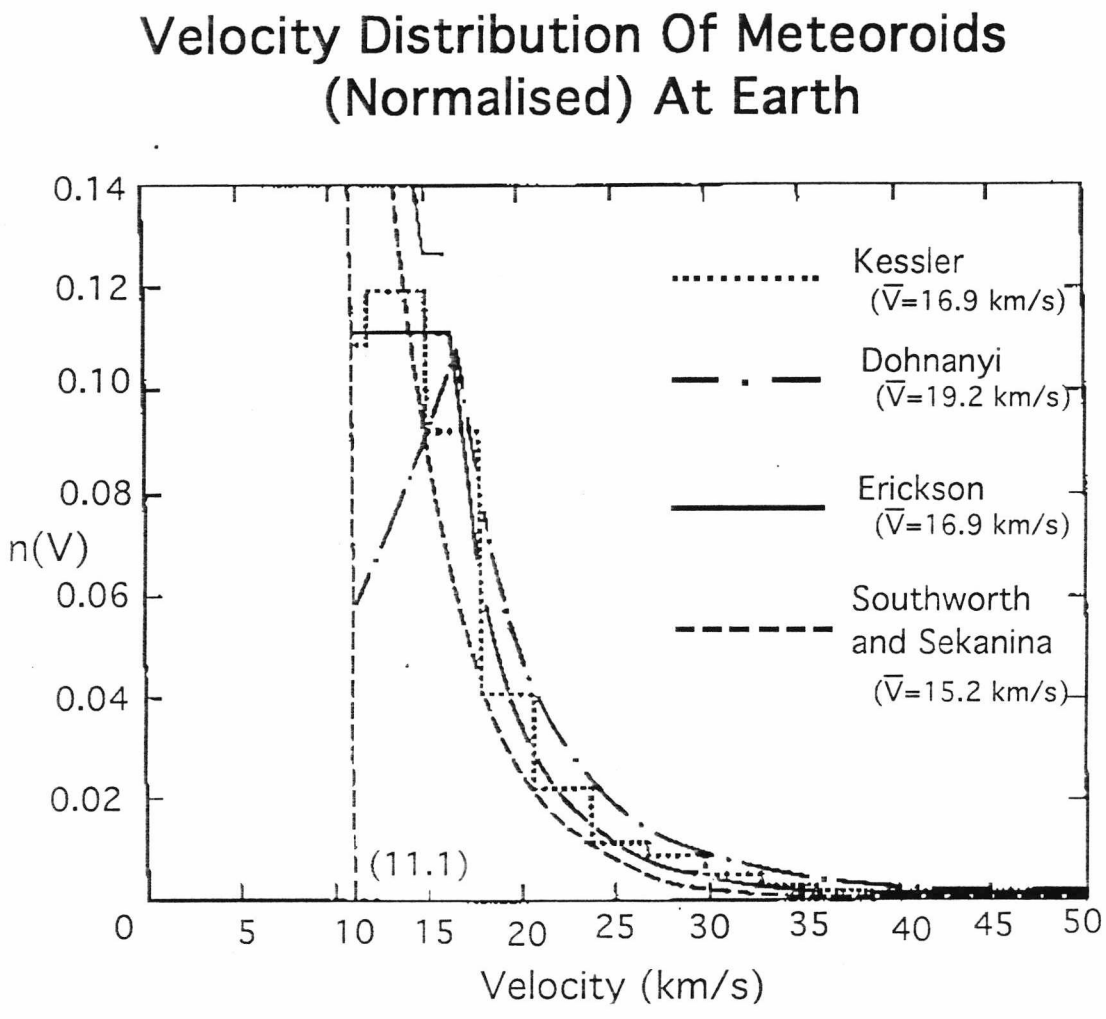

Figure 3.23 A comparison of velocity distributions . (Taken from Zook 1975[12])

Table 3.1 The Erickson velocity distribution.

Velocity Range (km/s)	Median Of Bin	Flux (normalised)
11.00 - 13.25	12.125	0.243
13.25 - 15.90	14.575	0.341
15.90 - 19.15	17.525	0.263
19.15 - 23.00	21.025	7.61×10^{-2}
23.00 -27.65	25.325	4.64×10^{-2}
27.65 - 33.25	30.45	2.37×10^{-2}
33.25 - 40.00	36.625	5.94×10^{-3}
40.00 - 48.00	44.00	3.45×10^{-3}
48.00 - 57.80	52.90	1.45×10^{-3}
57.80 - 65.80	61.80	1.39×10^{-3}
65.80 - 72.10	68.45	8.32×10^{-4}

The data given for the Erickson distribution was quoted at an altitude of approximately 100 km however LDEF's altitude was around 460 km so a scaling for the velocities had to be introduced . By the use of the law of conservation of Energy we can convert this to LDEF's altitude of 460 km .

P.E. + K.E. = constant Equation 3.3

At 100 km

$$E = \frac{m M_E G}{R + 100000} + \frac{1}{2} m V_{100000}^2 \qquad \text{Equation 3.4}$$

Where

M_E = the mass of the Earth

R = the Radius of the Earth

m = mass of meteorite

G = gravitational constant

V_{100000} = velocity of particle at an altitude of 100000 metres

V_{460000} = velocity of particle at an altitude of 460000 metres

Similarly at 460 km

$$E = \frac{m M_E G}{R + 460000} + \frac{1}{2} m V_{460000}^2 \qquad \text{Equation 3.5}$$

Therefore we have

$$V_{460000}^2 = \frac{2 M_E G}{R + 100000} - \frac{2 M_E G}{R + 460000} + V_{100000}^2 \qquad \text{Equation 3.6}$$

Applying this to the median velocity values of the Erickson velocity distribution we get the velocity distribution shown in Table 3.2 .

Deceleration due to atmospheric drag had already been accounted for in Erickson's calculation so the above velocity distribution was used to represent IP dust velocity distribution at LDEF's altitude.

3.4.2 The Mass Distribution

The next step was to find an appropriate mass distribution to represent the IP. dust.

After some research the conclusion was reached that the Grun mass distribution[13] was the most comprehensive. This mass distribution includes data from Zook et al[14] Fechtig et al[15] McDonnell[16] Le Sergeant and Lamy[17]. The data is processed and combined to provide an interplanetary flux model (number/m^2 sec) at 1 AU. of the form

$$F(m,r_0) = (c_4 m^{\gamma 4} + c_5)^{\gamma 5} + c_6(m + c_7 m^{\gamma 6} + c_8 m^{\gamma 7})^{\gamma 8} + c_9(m + c_{10} m^{\gamma 9})^{\gamma 10} \quad \text{Equation 3.7}$$

(r_0 = 1 AU.)

with constants

$c_4 = 2.2\times10^3$, $c_5 = 15$, $c_6 = 1.3\times10^{-9}$, $c_7 = 10^{11}$, $c_8 = 10^{27}$, $c_9 = 1.3\times10^{-16}$, $c_{10} = 10^6$

and the exponents

$\gamma 4 = 0.306$, $\gamma 5 = -4.38$, $\gamma 6 = 2$, $\gamma 7 = 4$, $\gamma 8 = -0.36$, $\gamma 9 = 2$, $\gamma 10 = -0.85$

Since the object of the modelling was to compare it's results with LDEF data, the mass range over which the Grun mass distribution was to be used was decided after considering the actual LDEF data (see later).

The range of particle *diameters* selected was from 10^{-6} m (1 micron) to approximately 5×10^{-3} m (5 mm) using intervals of 0.2 on a log scale.. Assuming an average particle density of 1g cm^{-3}, and that impactors are spherical this can be easily converted to mass using

$$m = \frac{4}{3}\pi r^3 \rho \qquad \text{Equation 3.8}$$

where ρ is the particle density

A particle density of 1g cm^{-3} was assumed. (The average density of micrometeoroids is an ill-defined quantity, with estimates ranging from below 1 g cm^{-3} to over 2 g cm^{-3}. However although the materials composing these particles may be more dense than here estimated it should be noted that the micrometeoroid particles are likely to be conglomerates and therefore could contain large voids. As a result of this it was felt that 1 g cm^{-3} was an appropriate value to choose.)

A weighted average for the flux within each of the bins (of width 0.2 on the log scale) would then be calculated as below.

$$N_{weighted} = \frac{\sum_{i=0}^{4} \left\{ 10^{(\log D_1 - ((i+1)\times 0.04))} - 10^{(\log D_1 - (i\times 0.04))} \right\} \times N_i}{D_1 - D_2} \qquad \text{Equation 3.9}$$

Where D_1 and D_2 are the lower and upper bounds of the diameter bin respectively, and N_i is the flux given by the Grun distribution at the mass which corresponds to the diameter.

Table 3.2 Erickson's velocity distribution scaled to LDEF's altitude.

Velocity at 460 km (Km/s)	Flux (normalised)
11.849	0.243
14.346	0.341
17.335	0.263
20.917	7.61×10^{-2}
25.194	4.64×10^{-2}
30.34	2.37×10^{-2}
36.534	5.94×10^{-3}
43.925	3.45×10^{-3}
52.837	1.45×10^{-3}
61.746	1.39×10^{-3}
68.902	8.32×10^{-4}

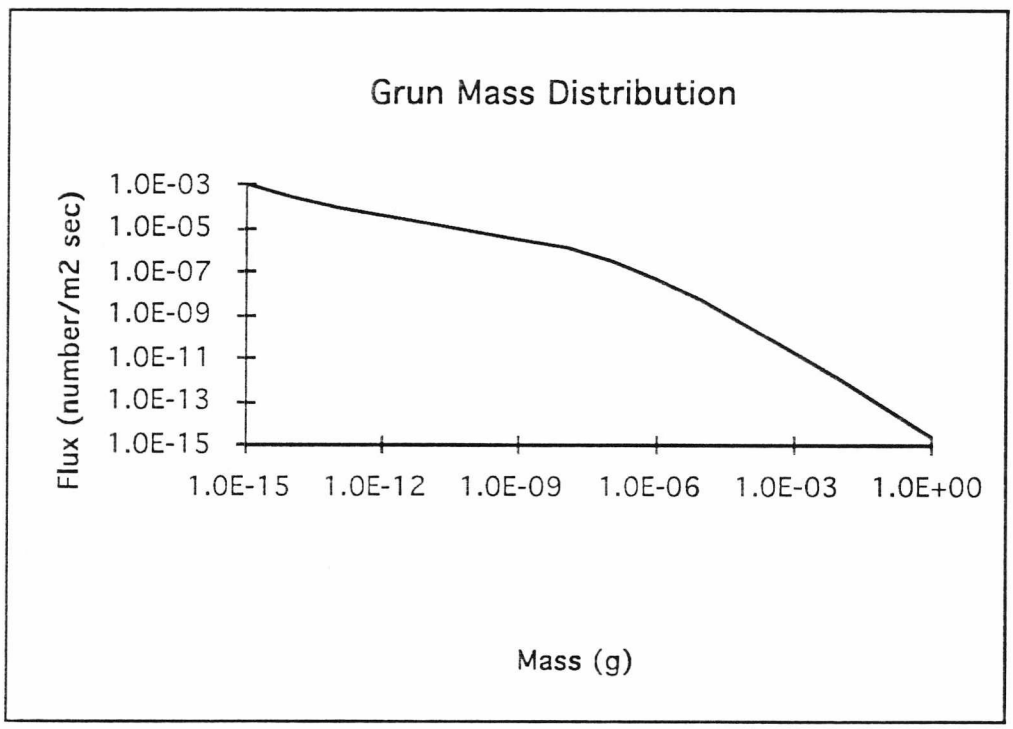

Figure 3.24. The Grun mass distribution.

$$D_i = 10^{(\log D_1 - ((i+0.5)\times 0.04))}$$ Equation 3.10

This, however, gives the flux for a randomly tumbling plate at 1 AU. and what we require is the flux for a viewing angle of 4π steradians after gravitational enhancement at the Earth.

The flux impacting on a flat plate, assuming an isotropic dust distribution and an intensity of I is given by

$$F = I\int_0^{2\Pi}\int_0^{\frac{\Pi}{2}} \sin\phi\times\cos\phi\, d\phi\, d\theta$$ Equation 3.11

$$=2\Pi\times I\int_0^{\frac{\Pi}{2}} \sin\phi\times\cos\phi\, d\phi$$

$$=2\Pi\times I\int_0^{\frac{\Pi}{2}} \frac{1}{2}\sin 2\phi\, d\phi$$

$$=\Pi\times I\left[-\frac{1}{2}\cos 2\phi\right]_0^{\frac{\Pi}{2}}$$

$$=\Pi\times I$$

Therefore we must multiply the fluxes calculated from the Grun mass distribution by 4 to take account of this geometric factor.

The multiplying factor to account for gravitational enhancement as the dust accelerates in towards the Earth is given in[18] to be

$$G = 1 + 0.76\left(\frac{r_e}{r}\right)$$ Equation 3.12

Where r_e is the Earth's radius and r is the radius of the satellites orbit from the centre of the Earth.

In the case of LDEF this works out as 1.71 and when multiplied into the flux's from Grun gives the final size distribution shown overleaf (Table 3.3).

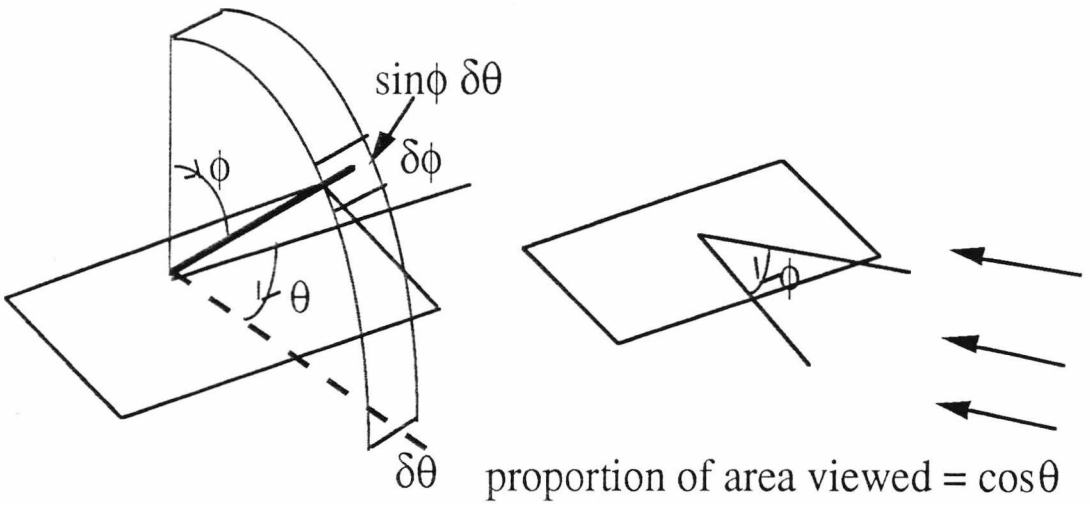

(a) (b)

Figure 3.25. Proportion of total flux which impacts on a flat plate from any given direction . (a) Proportion of total flux which comes from any angular bin (b) Proportion of flux from each bin which impacts plate.

Table 3.3. The size distribution used by the interplanetary dust model.

Particle Diameter	Flux
4.92948E-03	1.16756E-12
3.11070E-03	7.10072E-12
1.96310E-03	4.21774E-11
1.23900E-03	2.41918E-10
7.82091E-04	1.31844E-09
4.93769E-04	6.67865E-09
3.11812E-04	3.05614E-08
1.96964E-04	1.22111E-07
1.24456E-04	4.11024E-07
7.86660E-05	1.13111E-06
4.97494E-05	2.52047E-06
3.14592E-05	4.63922E-06
1.98828E-05	7.00763E-06
1.26211E-05	9.65195E-06
8.02099E-06	1.43668E-05
5.07562E-06	2.49849E-05
3.18696E-06	4.46934E-05
2.00586E-06	7.20158E-05
1.27028E-06	1.16302E-04
8.03544E-07	2.09853E-04
5.07099E-07	4.27408E-04
3.19462E-07	9.81691E-04
2.00967E-07	2.52317E-03
1.26348E-07	7.09364E-03
7.94697E-08	2.11950E-02

Chapter 4

The Space Debris Model

4.1 Introduction and Assumptions

The space debris model as outlined in chapter 2 was already in existence at the inception of this research program. The main modification which was made was in the debris orbits tested. The original model used a series of orbital perigee-inclination-eccentricity bins with an orbit representing each bin (and an appropriate weighting factor). The model was modified to use the actual debris orbits listed by DISCOS (or any other list of orbits chosen).

The output from the new model was then interpreted in terms of LDEF's geometry (see chapter 2).

The theory behind the final model is outlined in section 2.5 of workpackage 2100[5] and section 3.2 of workpackage 4300[6]. What follows is an outline of the final version, which was created after modifications of Green's work for the two workpackages.

Assumptions made in the Space debris model are

1) The nodes of debris orbits are random.
2) The lines of apsides of debris orbits are random.
3) The distribution of debris orbits found in the DISCOS database is representative of debris in smaller size regimes.
4) The spacecraft is in a circular orbit.

4.2 The Algorithm

The Spacecraft altitude and inclination is defined by the user (from this the Period of orbit and orbital velocity is calculated). An altitude bin is also defined. Any debris within this bin is considered to have a finite probability of impacting LDEF. In order to take account of the deterioration of LDEF's orbit and the spread of small particles around the absolute orbital parameters of any larger piece of debris, 200 km was chosen as the bin size for LDEF (this is a bin spanning LDEF's Altitude ± 100 km).

One hemisphere of the sky is additionally split into latitude (b) bins of a size defined by the user. For LDEF, 1° bins were chosen. Smaller bins will allow a more precise calculation but would be more time consuming. In view of the assumptions and other inherent errors, 1° steps was deemed as sufficiently small. The upper and lower limits of these latitude bins are then defined. In the case of LDEF the bin boundaries are defined as below in table 4.1.

The other hemisphere of the sky will be identical by symmetry, and from the assumptions made above.

The model then steps through each of the latitude bins in turn, performing calculations as follows.

The volume of each of the h-b bins (W_{hb}) is calculated as follows.

$$W_{hb}=\frac{2\pi}{3}(r_2^3-r_1^3)(\sin\beta_2-\sin\beta_1) \qquad \text{Equation 4.1}$$

Where $r_1 = r_e + h_1$, $r_2 = r_e + h_2$ and r_e is Earth's mean radius and h_1, h_2 are the lower and upper boundaries, respectively, of the altitude bin .

So the debris density (D(d)) of particles of diameter d in this h-b bin is given by

$$D(d) = N(d)/W_{hb}$$

Where N(d) is the total number of particles of diameter d.

The size distribution, N(d), is in the form of total debris numbers in LEO. The size distribution from the model by Kessler et al[19] is for impact fluxes and so cannot be deconvolved to space densities without a knowledge of the impact velocity distribution. Therefore the shape of this size distribution (which does not differ significantly with inclination or altitude above 200 km) has been used with a normalisation to the total numbers of catalogued objects in LEO, from the DISCOS database, at the largest sizes (see Figure 4.1).

The size distribution thus calculated is shown in Table 4.2.

The time, after passing the ascending node, at which the spacecraft reaches the centre of the bin is calculated as a fraction of the orbital period. Equation 4.1 gives us the latitude (β) of an object in an orbit of inclination i at time t_n after passing the ascending node.

$$\sin \beta = \sin \left(\frac{2\pi t_n}{P}\right) \sin i \qquad \text{Equation 4.1}$$

Where P is the period of orbit.

This gives us

Table 4.1 Latitude Bins. Note that the bins on the boundaries are only half as big as the rest. and there centres are on the boundaries. This is as a result of symmetry considerations of the model.

Latitude Bin	Bin Boundaries	Centre of Bin
1	0.0 0.5	0.0
2	0.5 1.5	1.0
3	1.5 2.5	2.0
4	2.5 3.5	3.0
.	.	.
.	.	.
89	87.5 88.5	88.0
90	88.5 89.5	89.0
91	89.5 90.0	90.0

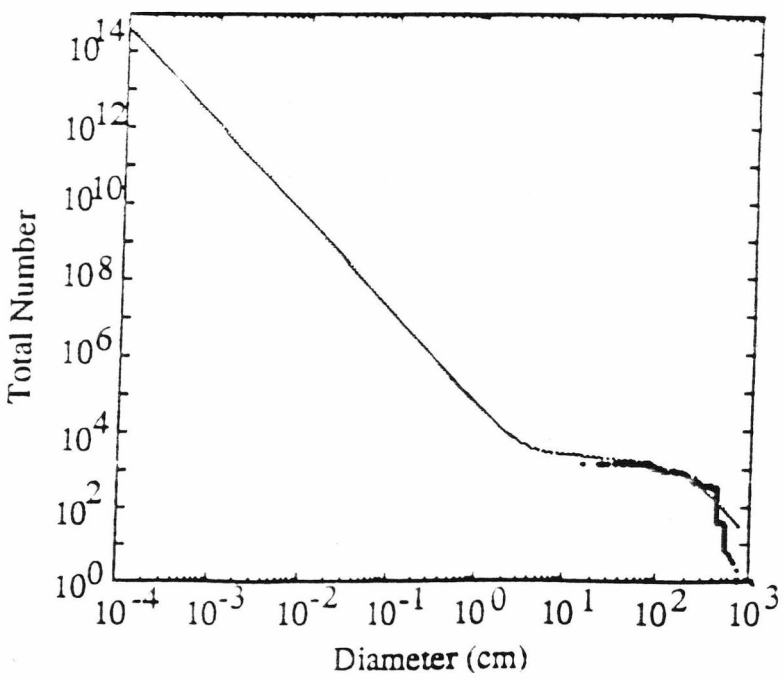

Figure 4.1. Space debris model size distribution. The shape is from Kessler et al, the absolute numbers obtained from fitting to the size distribution of catalogued objects at sizes above 60 cm.

Table 4.2 The debris size distribution. The mean diameter of each bin is calculated taking into account the slope of the distribution over this region.

Diameter Range (m)	Mean Diameter (m)	Number in Bin
1.00e-7 - 1.58e-7	1.25e-7	1.45e+17
1.58e-7 - 2.51e-7	1.99e-7	4.58e+16
2.51e-7 - 3.98e-7	3.15e-7	1.45e+16
3.98e-7 - 6.31e-7	4.99e-7	4.58e+15
6.31e-7 - 1.00e-6	7.91e-7	1.45e+15
1.00e-6 - 1.58e-6	1.25e-6	4.58e+14
1.58e-6 - 2.51e-6	1.99e-6	1.45e+14
2.51e-6 - 3.98e-6	3.15e-6	4.58e+13
3.98e-6 - 6.31e-6	4.99e-6	1.45e+13
6.31e-6 - 1.00e-5	7.91e-6	4.58e+12
1.00e-5 - 1.58e-5	1.25e-5	1.45e+12
1.58e-5 - 2.51e-5	1.99e-5	4.58e+11
2.51e-5 - 3.98e-5	3.15e-5	1.45e+11
3.98e-5 - 6.31e-5	4.99e-5	4.58e+10
6.31e-5 - 1.00e-5	7.91e-5	1.45e+10
1.00e-4 - 1.58e-4	1.25e-4	4.58e+9
1.58e-4 - 2.51e-4	1.99e-4	1.45e+9
2.51e-4 - 3.98e-4	3.15e-4	4.58e+8
3.98e-4 - 6.31e-4	4.99e-4	1.45e+8
6.31e-4 - 1.00e-3	7.91e-4	4.58e+7
1.00e-3 - 1.58e-3	1.25e-3	1.45e+7
1.58e-3 - 2.51e-3	1.99e-3	4.58e+6
2.51e-3 - 3.98e-3	3.15e-3	1.45e+6
3.98e-3 - 6.31e-3	4.99e-3	4.60e+5
6.31e-3 - 1.00e-2	7.91e-3	1.47e+5
1.00e-2 - 1.58e-2	1.25e-2	4.83e+4

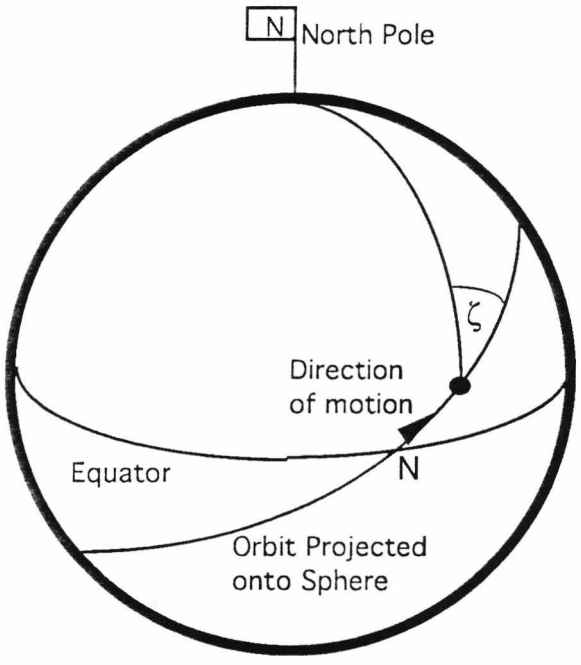

Figure 4.2. The angle ζ_s relative to the spacecraft.

$$\frac{t_n}{P} = \frac{\sin^{-1}\left(\frac{\sin\beta}{\sin i}\right)}{2\pi}$$ Equation 4.2

From this, the angle between the spacecraft's velocity vector and the north pole (Figure 4.2) is calculated for the spacecraft when it is at the centre of each latitude bin. Equation 4.3 defines this angle (ζ_{sc}) as

$$\cos\zeta = \cos\left(\frac{2\pi t_n}{P}\right)\frac{\sin i}{\sin\beta}$$ Equation 4.3

The time of spacecraft entry and exit to this latitude bin is then calculated. This once more employs Equation 4.1, but this time using the bin limits as the latitudes for which the time is required. This gives us two values, t_1/P and t_2/P.

From this we calculate the fraction of time which the spacecraft spends in this latitude bin (F_{bsc}).

$$F_{bsc} = 2\left(\frac{t1}{P} - \frac{t2}{P}\right)$$ Equation 4.4

Note, the factor of two is because the spacecraft will spend the same length of time in this latitude bin while descending as while ascending.

Each of the 6600 debris orbits in the DISCOS database are then considered in turn.

First the model checks that the debris in this orbit will pass through the spacecraft's altitude bin at some point (if not then this orbit is ignored). Then

the model checks the debris will enter the latitude bin being considered at this time (again the orbit will be ignored if it does not fulfil this criteria).

If the orbit passes through the altitude latitude bin being considered then the semi-major axis (a) of the debris orbit is calculated, using equation 4.5 .

$$a = q/(1-e) \qquad \text{Equation 4.5}$$

Where q is the perigee , and e the eccentricity of the debris orbit.

The eccentric anomaly (E) is also calculated for the upper (E_2) and lower (E_1) boundaries of the altitude bin, using equation 4.6 shown below.

$$r = a(1-e\cos E) \qquad \text{Equation 4.6}$$

Which gives

$$E = \cos^{-1}\left(\frac{\left(1 - \frac{r}{a}\right)}{e}\right) \qquad \text{Equation 4.7}$$

Where r is the radius of the upper (r_2) and lower (r_1) boundaries of the altitude bin, for E2 and E1 respectively.

From this, using equation, 4.8, we can derive the entry time to (t_{h1}) and exit time from (t_{h2}) the altitude bin, after passing the ascending node, as a fraction of the orbital period.

$$E - e\sin E = \frac{2\pi t_h}{P} \qquad \text{Equation 4.8}$$

Which gives

$$\frac{t_h}{P} = \frac{E - e \sin E}{2\pi}$$ Equation 4.9

From this we calculate the total fraction of time (F_h), which the debris will spend in the altitude bin (as below).

$$F_h = 2\left(\frac{t_{h2}}{P} - \frac{t_{h1}}{P}\right)$$ Equation 4.10

Again the factor of two is because the debris will spend the same length of time in the altitude bin while descending as while ascending.

The fraction of time which the debris spends in the latitude bin (F_b) is then calculated, as with the spacecraft (see earlier), using Equations 4.2 and 4.4.

From this we can calculate the total fraction of time (F) in which the debris and spacecraft are capable of interacting.

$$F = F_{bsc}\, F_b\, F_h$$ Equation 4.11

The velocity of the debris (v) at the midpoint of the altitude latitude bin is then calculated using equation 4.12

$$v = \left[\mu\left(\frac{2}{r} - \frac{1}{a}\right)\right]^{0.5}$$ Equation 4.12

Where μ is the gravitational constant times the Earth's mass.

Equation 4.13, then gives us the angle from this velocity vector to the tangent plane (γ).

$$\cos\gamma = \left[\frac{a^2(1-e^2)}{r(2a-r)}\right]^{0.5} \qquad \text{Equation 4.13}$$

From this we calculate the radial (v_r) and spherical (v_c) components of the debris velocity.

$$v_r = v \sin(\gamma) \qquad \text{Equation 4.14}$$

$$v_c = v \cos(\gamma) \qquad \text{Equation 4.15}$$

We then calculate the angle from the spherical component of the velocity vector to the north pole direction, ζ (as with the spacecraft), see Figure 4.3. For this we again use equations 4.2 and 4.3.

For the debris we must, however consider two cases. ζ_1 when the orbit is ascending and ζ_2 when the orbit is descending. From Figure 4.3 we can see that

$$\alpha = \zeta_1$$

and therefore

$$\zeta_2 = \pi - \zeta_1.$$

The two interactions, above, will be the same geometries for the spacecraft ascending or descending (see Figure 4.4).

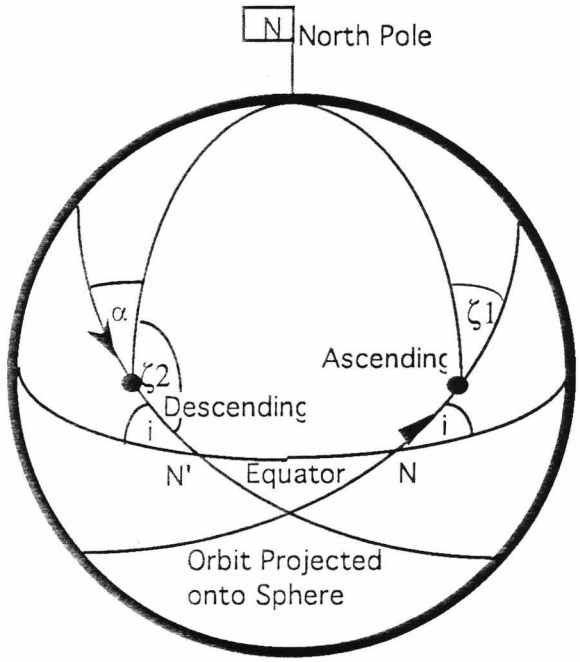

Figure 4.3 . The relationship between the ζ values for debris when it is leaving the ascending node and approaching the descending node.

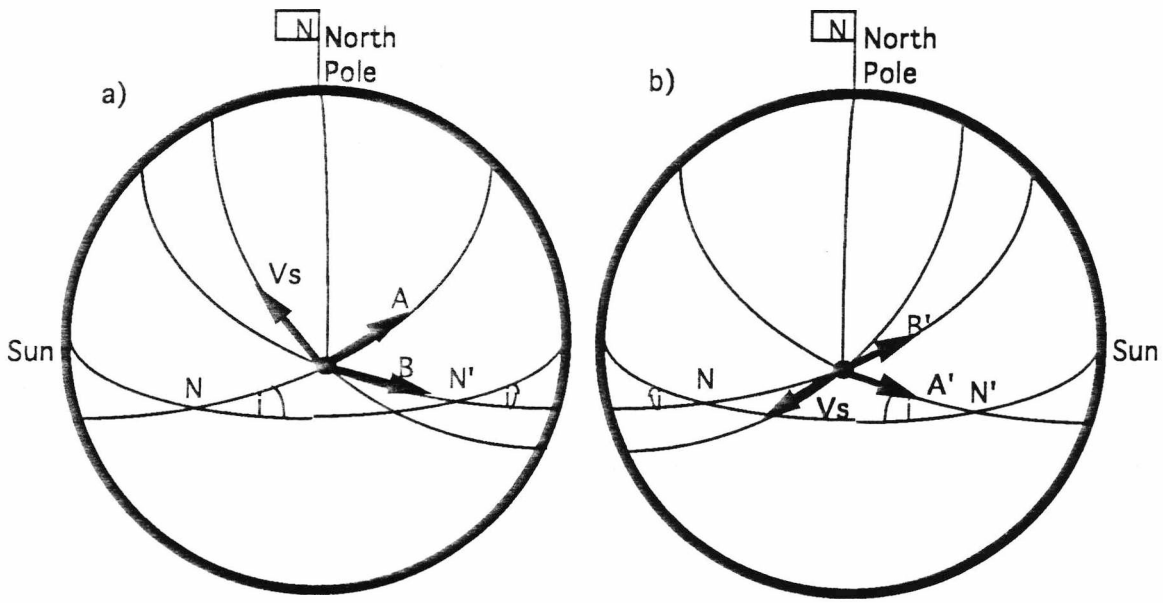

Figure 4.4. Relative velocities of spacecraft Vs (located in northern hemisphere) and debris in an orbit inclination i. In a) the debris has a velocity A as it intercepts the spacecraft after passing the ascending node of its orbit and velocity B if it intercepts the spacecraft before reaching the descending node. If the spacecraft is at the same latitude but approaching it's descending node, the geometry in b) pertains. The cases A' and B' are identical to A and B with respect to the relative velocities.

For both ζ_1 and ζ_2 we then proceed to calculate the impact velocity of the debris on the spacecraft.

Firstly we calculate the spherical component of the impact velocity.

From Figure 4.5 a) we can see that the impact angle (β) between the debris and the spacecraft is given by ζ_s-ζ, and Figure 4.5 b) shows us we can calculate the spherical component of the impact velocity (xv_c) by the cosine rule which gives us.

$$xv_c = (v_c^2 + v_s^2 - 2\, v_c\, v_s \cos(\zeta_s - \zeta))^{0.5} \qquad \text{Equation 4.16}$$

We then calculate the impact angle relative to the spacecraft velocity vector in the plane of the spherical velocity components (θ). This is again given to us from Figure 4.4 b) and the cosine rule.

$$\cos\theta = (xv_c^2 + v_s^2 - v_c^2) / 2\, xv_c\, v_s \qquad \text{Equation 4.17}$$

The radial component of the impact velocity is simply v_r (the radial component of the debris velocity) since the spacecraft is in a circular orbit and thus has no radial velocity component.

From this we can simply calculate the total relative impact velocity (xv) to be

$$xv = (xv_c^2 + v_r^2)^{0.5} \qquad \text{Equation 4.18}$$

We can then calculate the angle between the impact vector and the plane of the spherical velocity components $x\gamma$ by

$\cos x\gamma = xv_c/xv$

We then calculate the Cartesian co-ordinates of the impact vector in the same axis system used in chapter 3. The positive x-direction is in the direction of the spacecraft's velocity vector, the positive z-direction pointing away from the Earth's surface (the space direction) and the y-axis perpendicular to the x and z axis. This gives us

$$x = xv_c \cos\theta$$
$$y = xv_c \sin\theta \qquad \text{Equation 4.19}$$
$$z = v_r$$

This is only, however one of the possible impact scenarios for debris in this orbit. It assumes that the debris is either rising (positive v_r) or falling (negative v_r) and that the debris and spacecraft are in the northern hemisphere. (The cases of the debris leaving the ascending node or approaching the descending nodes has been accounted for earlier by the two possible ζ)

In the southern hemisphere case we find that all the interactions are the same except the θ is exchanged for a value of $-\theta$.

We therefore have a total of 8 sets of Cartesian co-ordinates as shown below.

case 1	nominal		
case 2	$\zeta = \zeta_2$		
case 3		$v_r = -v_r$	
case 4			$\theta = -\theta$
case 5	$\zeta = \zeta_2$	$v_r = -v_r$	
case 6	$\zeta = \zeta_2$		$\theta = -\theta$
case 7		$v_r = -v_r$	$\theta = -\theta$
case 8	$\zeta = \zeta_2$	$v_r = -v_r$	$\theta = -\theta$

We then calculate what proportion of the total debris density is in each of these orbits.

$$F_o = \frac{1}{6600} \frac{1}{8}$$

So the flux of debris impacting the spacecraft from this orbit, in this latitude bin is given by.

$$Fl_o = D(d)\ F\ F_o\ xv$$

Having performed all these calculations the results are then applied to LDEF as shown in chapter 2.

4.3 Analysis of Individual Orbits

In order to have a better understanding of the interaction of different types of debris orbits with LDEF, a series of sample runs of the debris model were performed. Each of the runs was for a different possible debris orbit and fluxes estimated are flux levels assuming that the sample orbit is simply one of the 6600 DISCOS defined orbits.

The selected orbits were of inclinations 0°, 30°, 60°, 90°, 120°, 150° and eccentricities and apogees outlined in Table 4.3.

Predictions for relative flux levels on each of LDEF's faces, for each of the sample orbits, are shown in Figures 4.5 to 4.9.

4.3.1 Circular Orbits

Figure 4.5 is a graph of the flux on LDEF's faces, at F_{max} of 1 μm for circular orbits, of varying inclinations, at LDEF's altitude.

Orbits with low inclinations result in generally higher fluxes on the anti-RAM end than orbits with high inclinations. However the inclination of 30° (almost identical to LDEF's inclination) is the only orbit with any impacts on the West or Earth faces.

Low inclination orbits have lower fluxes on the RAM end and Space face of the spacecraft than high inclination orbits. Note also that for the low inclination orbits there is a significantly lower flux on the East face than on the adjoining faces. This is as a result of the different distribution (see the 8

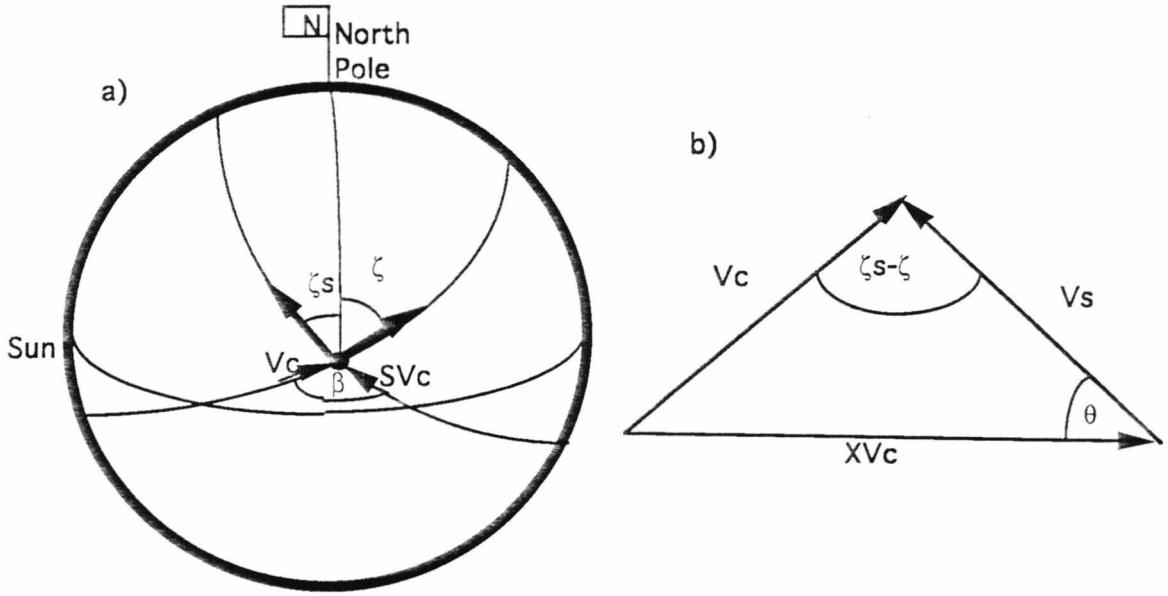

Figure 4.5. The spherical component of the impact velocity.

Table 4.3. Eccentricities and apogees of sample orbits. The eccentricity of 0.73 was chosen as this represents a GTO orbit.

Eccentricity	Apogee (km from centre of Earth)
0.0	6848
0.2	10005
0.4	15470
0.6	26400
0.73	42250

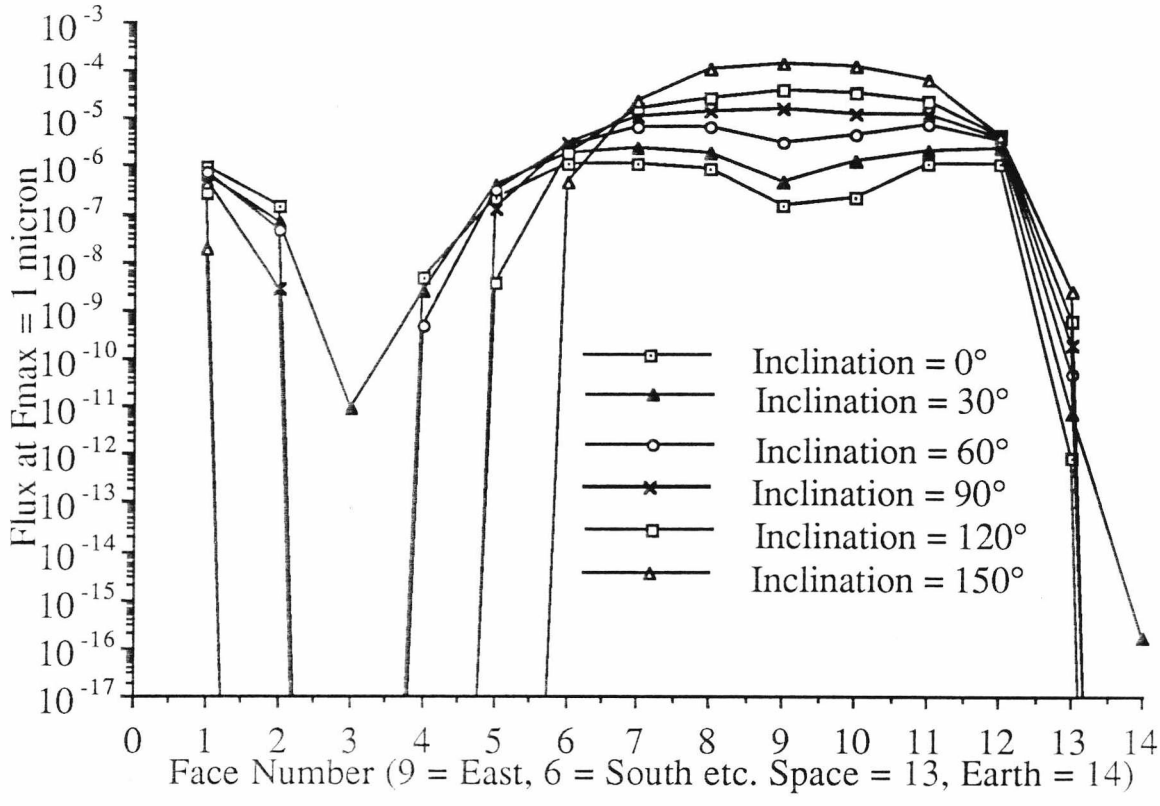

Figure 4.5. Flux on LDEF's faces, at F_{max} of 1 μm for circular orbits, of varying inclinations at LDEF's altitude. Where no point is plotted for a face, at a given inclination, the flux is zero. Orbits with low inclinations result in generally higher fluxes on the anti-RAM end than orbits with high inclinations. However the inclination of 30° (almost identical to LDEF's inclination) is the only orbit with any impacts on the West or Earth faces. Low inclination orbits have lower fluxes on the RAM end and Space face of the spacecraft than high inclination orbits and we can see that there is a dip in flux levels on the East face for these low inclination orbits. For these circular orbits the RAM flux is considerably higher than the anti-RAM flux. The RAM to anti -RAM ratio is lower for low inclination orbits.

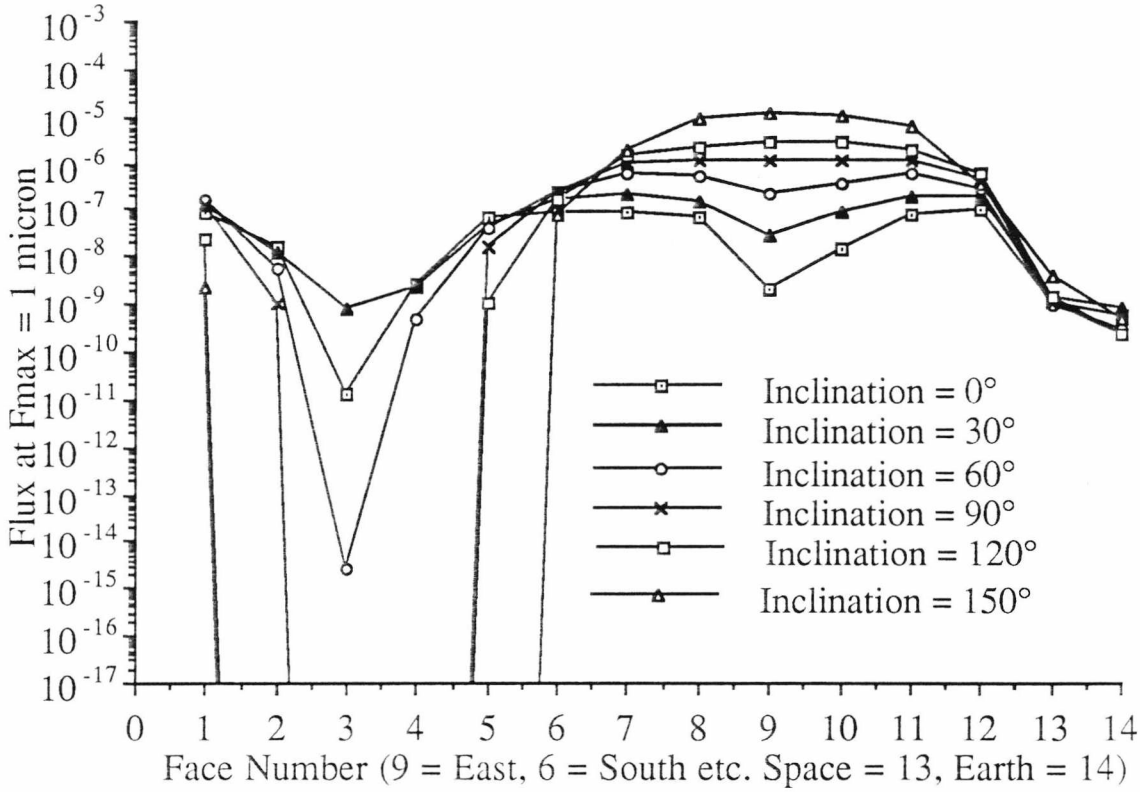

Figure 4.6. Flux on LDEF's faces, at F_{max} of 1 μm for orbits of eccentricity 0.2 and apogee at 10005 km, of varying inclinations. Where no point is plotted for a face, at a given inclination, the flux is zero. Orbits with low inclinations result in generally higher fluxes on the anti-RAM end than orbits with high inclinations. The inclination of 30° (almost identical to LDEF's inclination) is the orbit with the highest flux on the West and Earth faces. Note that these slightly eccentric orbits will result in impacts on the West and Earth faces for a much wider range of inclinations. Low inclination orbits have lower fluxes on the RAM end and Space face of the spacecraft than high inclination orbits. This time the dip in the East face fluxes for the low inclination orbits is far more pronounced. For these slightly eccentric orbits the RAM to anti-RAM ratio is much reduced for the low inclination orbits. However this ratio is still very high, if we look at the East to West ratio for the 30° inclination specifically the ratio is still a factor of about 30. If we take the face 6 (South) flux level as representative of the overall flux levels we can see that they have been decreased by an order of magnitude by introducing this eccentricity.

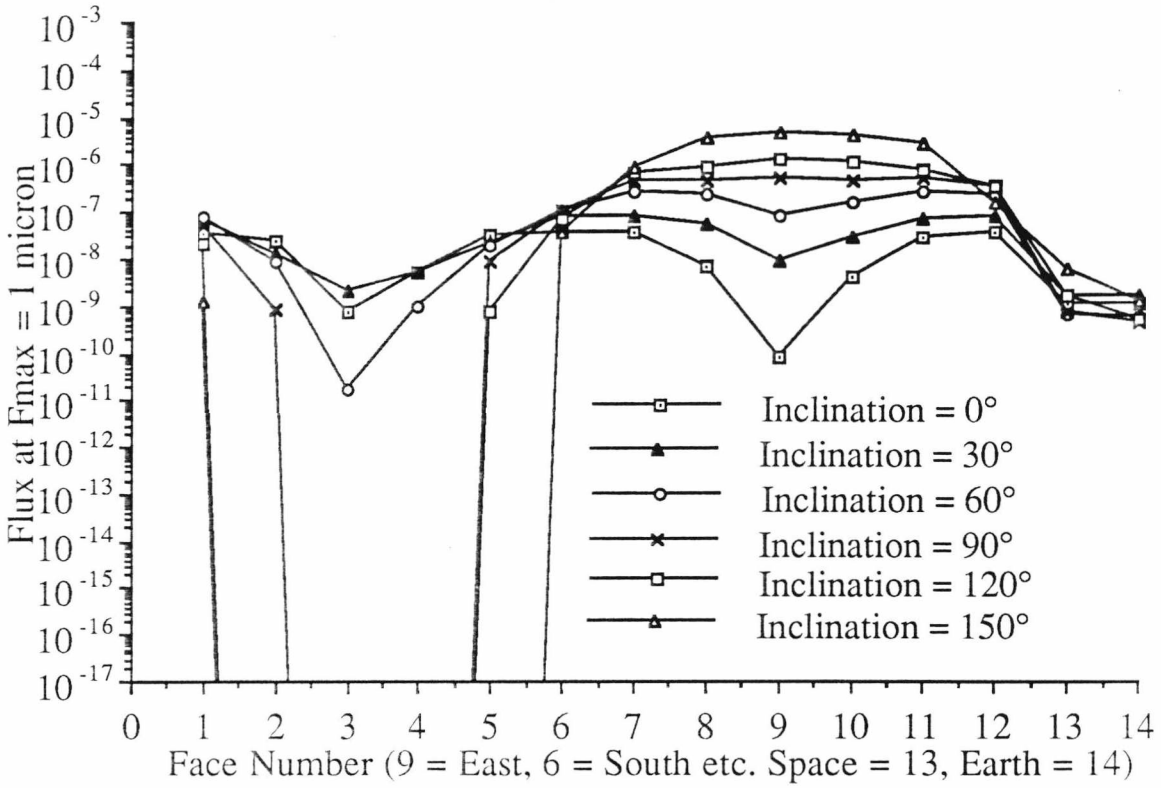

Figure 4.7. Flux on LDEF's faces, at F_{max} of 1 μm for orbits of eccentricity 0.4 and apogee at 15470 km, of varying inclinations. Where no point is plotted for a face, at a given inclination, the flux is zero. Orbits with low inclinations result in generally higher fluxes on the anti-RAM end than orbits with high inclinations. The inclination of 30° (almost identical to LDEF's inclination) is the orbit with the highest flux on the West and Earth faces. These more eccentric orbits will result in impacts on the West and Earth faces for the same range of inclinations as the case of eccentricity = 0.2. Low inclination orbits have lower fluxes on the RAM end and Space face of the spacecraft than high inclination orbits. For the very low inclination orbits we see that the East face dip in flux levels is becoming much more significant. Now we find that for inclination 0° the anti-RAM end has a slightly higher flux than the RAM end and for inclination 30° the RAM to anti-RAM ratio is much reduced again. If we look at East to West ratio's specifically we find that for e=30° we have a ratio of about 4 and for e=0° we have a ratio of 0.1 (ten times higher flux on West than East).If we take the face 6 (South) flux level as representative of the overall flux levels we can see again that they have been decreased but this time not by as great an amount (about 1/2 an order of magnitude), as we increase the eccentricity.

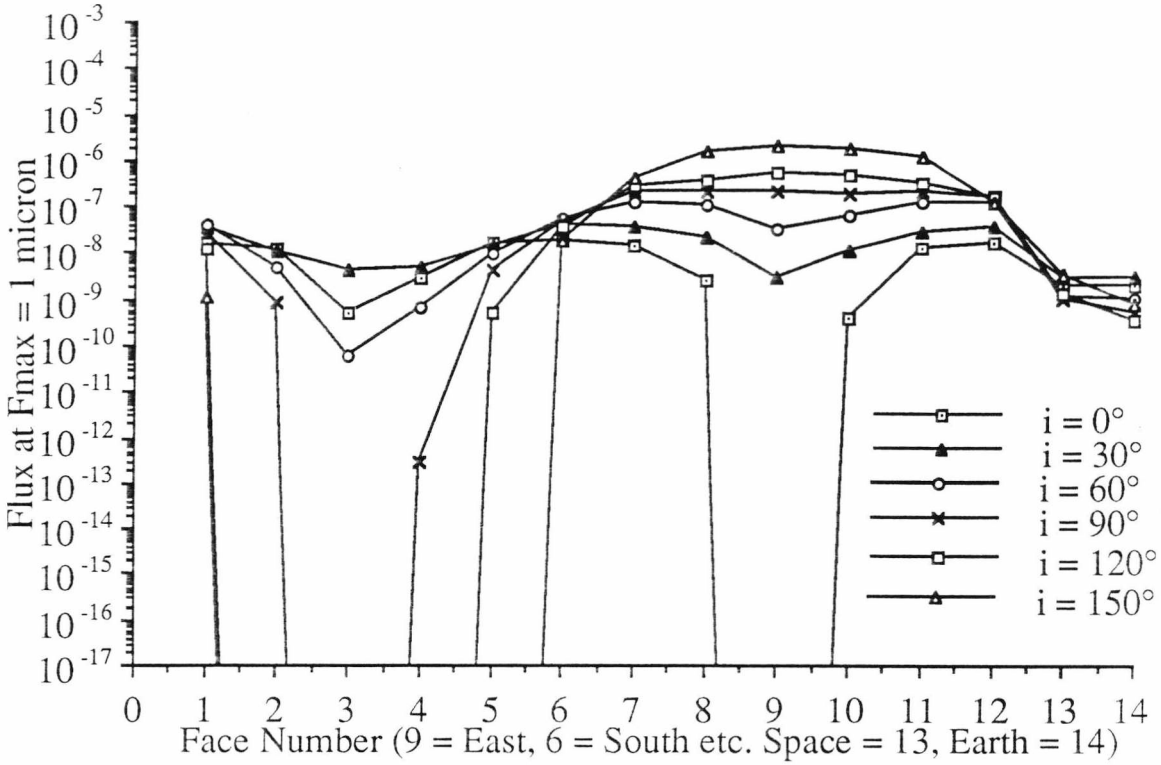

Figure 4.8. Flux on LDEF's faces, at F_{max} of 1 μm for orbits of eccentricity 0.6 and apogee at 26400 km, of varying inclinations. Where no point is plotted for a face, at a given inclination, the flux is zero. Orbits with low inclinations result in generally higher fluxes on the anti-RAM end than orbits with high inclinations. The inclination of 30° (almost identical to LDEF's inclination) is the orbit with the highest flux on the West and Earth faces. These orbits will result in impacts on the West and Earth faces for the same range of inclinations as the case of eccentricities = 0.2 or 0.4. Low inclination orbits have lower fluxes on the RAM end and Space face of the spacecraft than high inclination orbits. For the inclination = 0° orbits we see that there are no East face impacts. We find that for inclination 30° the anti-RAM end has a higher flux than the RAM end. If we look at East to West ratio's specifically we find that for e=30° we have a ratio of just less than 1.0 (for e=0° the East to West ratio is 0). If we take the face 6 (South) flux level as representative of the overall flux levels we can see again that they have been decreased but this time only by a factor of about 2.

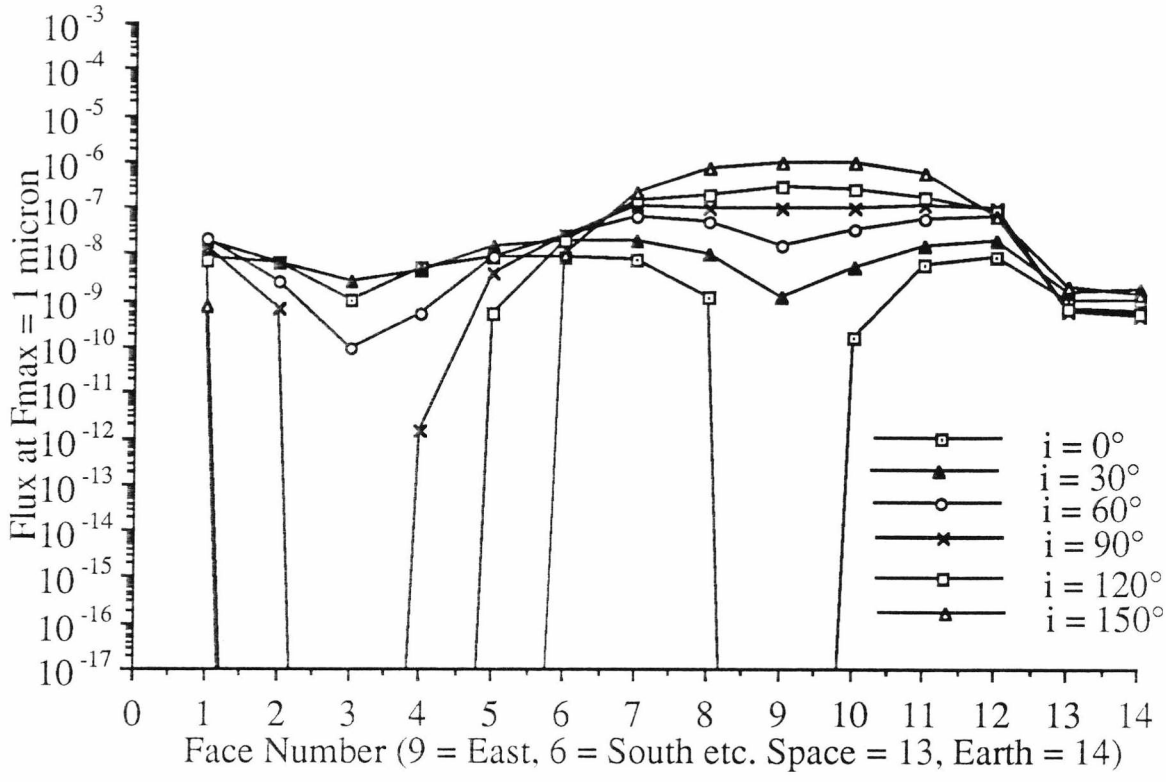

Figure 4.9. Flux on LDEF's faces, at F_{max} of 1 μm for orbits of eccentricity 0.73 and apogee at 42250 km, of varying inclinations. Where no point is plotted for a face, at a given inclination, the flux is zero. Orbits with low inclinations result in generally higher fluxes on the anti-RAM end than orbits with high inclinations. The inclination of 30° (almost identical to LDEF's inclination) is the orbit with the highest flux on the West and Earth faces. These orbits will result in impacts on the West and Earth faces for the same range of inclinations as the case of eccentricities = 0.2, 0.4 or 0.6. Low inclination orbits have lower fluxes on the RAM end and Space face of the spacecraft than high inclination orbits. For the inclination = 0° orbits we see that there are no East face impacts. Again we find that for inclination 30° the anti-RAM end has a higher flux than the RAM end. If we look at East to West ratio's specifically we find that for e=30° we have a ratio of about 0.5 (for e=0° the East to West ratio is 0). If we take the face 6 (South) flux level as representative of the overall flux levels we can see again that they have been decreased but the decrease is very small this time and we can see that the flux is beginning to level off.

possible interaction geometries earlier) of impact angles with which the flat plate faces and the debris interact.

For these circular orbits the RAM flux is considerably higher than the anti-RAM flux. The RAM to anti -RAM ratio is lower for low inclination orbits.

4.3.2 Orbits With Eccentricity = 0.2

Figure 4.6 is a graph of the flux on LDEF's faces, at F_{max} of 1 μm for orbits of eccentricity 0.2 and apogee at 10005 km, of varying inclinations.

Orbits with low inclinations result in generally higher fluxes on the anti-RAM end than orbits with high inclinations. The inclination of 30° (almost identical to LDEF's inclination) is the orbit with the highest flux on the West and Earth faces.

This time inclinations of 0°, 30° and 60° also produce impacts on the West face of the spacecraft. Low inclination orbits have lower fluxes on the RAM end and Space face of the spacecraft than high inclination orbits.

The dip in the East face flux for the low inclination orbits is far more pronounced this time than it was for the circular orbits.

The RAM to anti-RAM ratio is much reduced for the low inclination orbits compared to the circular orbits, however the actual value of this ratio is still very high. If we look at the East to West ratio for the 30° inclination specifically, we find it to be about 30.

If we take the face 6 (South) flux level as representative of the overall flux levels we can see that they have been decreased by an order of magnitude by introducing this eccentricity. This decrease is not uniform throughout the data, the RAM end tending to have a larger decrease and the anti-RAM end a smaller decrease, however it does give us a pointer to the general trend of the flux levels as we increase the eccentricity of the sampled orbits.

4.3.3 Orbits With Eccentricity = 0.4

Figure 4.7 is a graph of flux on LDEF's faces, at F_{max} of 1 μm for orbits of eccentricity 0.4 and apogee at 15470 km, of varying inclinations.

Orbits with low inclinations result in generally higher fluxes on the anti-RAM end than orbits with high inclinations. The inclination of 30° (almost identical to LDEF's inclination) is the orbit with the highest flux on the West and Earth faces.

Again the inclinations of 0°, 30° and 60° will result in impacts on all of LDEF's faces and the low inclination orbits have lower fluxes on the RAM end and Space face of the spacecraft than high inclination orbits.

For the very low inclination orbits we see that the East face dip in flux levels is becoming much more significant. Now we find that for inclination 0° the anti-RAM end has a slightly higher flux than the RAM end and for inclination 30° the RAM to anti-RAM ratio is much reduced again. If we look at East to West ratio's specifically we find that for e=30° we have a ratio of about 4 and for e=0° we have a ratio of 0.1 (ten times higher flux on West than East).

If we once more look at the flux on face 6 (South) we can see again that they have been decreased but this time not by as great an amount (about 1/2 an order of magnitude), as we increase the eccentricity of the orbits.

4.3.4 Orbits With Eccentricity = 0.6

Figure 4.8 is a graph of flux on LDEF's faces, at F_{max} of 1 μm for orbits of eccentricity 0.6 and apogee at 26400 km, of varying inclinations.

Orbits with low inclinations result in generally higher fluxes on the anti-RAM end than orbits with high inclinations. The inclination of 30° (almost identical to LDEF's inclination) is the orbit with the highest flux on the West and Earth faces.

This eccentricity of orbits will result in impacts on the West and Earth faces for the same range of inclinations (0°, 30° and 60°) as the case of eccentricities = 0.2 or 0.4 .

Low inclination orbits have lower fluxes on the RAM end and Space face of the spacecraft than high inclination orbits. For the inclination = 0° orbits we see that there are no East face impacts. We find that for inclination 0° and 30° the anti-RAM end has a higher flux than the RAM end. If we look at East to West ratio's specifically we find that for e=30° we have a ratio of just less than 1.0 (for e=0° the East to West ratio is 0).

Again taking face 6 (South) flux level as representative of the overall flux trends we can see again that they have once more decreased but this time only by a factor of about 2.

4.3.5 Orbit With Eccentricities =0.73

Figure 4.9 is a graph of flux on LDEF's faces, at F_{max} of 1 μm for orbits of eccentricity 0.73 and apogee at 42250 km, of varying inclinations.

Orbits with low inclinations result in generally higher fluxes on the anti-RAM end than orbits with high inclinations. The inclination of 30° (almost identical to LDEF's inclination) is the orbit with the highest flux on the West and Earth faces.

This eccentricity of orbits will result in impacts on the West and Earth faces for the same range of inclinations as the case of eccentricities = 0.2, 0.4 or 0.6.

Low inclination orbits have lower fluxes on the RAM end and Space face of the spacecraft than high inclination orbits. For the inclination = 0° orbits we see that there are no East face impacts. Again we find that for inclination 30° the anti-RAM end has a higher flux than the RAM end .

If we look at East to West ratio's specifically we find that for e=30° we have a ratio of about 0.5 (for e=0° the East to West ratio is 0).

Again comparing fluxes on the South space we can see that they have been decreased. However the size decrease is very small this time showing us that the flux is beginning to level off.

4.3.6 General Points

We find, considering only the anti-RAM end of the spacecraft, that at any given eccentricity low inclination orbits will dominate. While on the RAM end of the spacecraft high inclination orbits will dominate. One of the results of this is that low inclination orbits will have lower East to West ratios than high inclination orbits. Debris in low inclination orbits are, therefore, candidates for producing the excess of debris on the West face which chemical analysis suggests exists (see Section 5.4).

If we look at the effect of orbit eccentricity we can see that higher eccentricity orbits will result in generally lower flux levels and also lower East to West ratios of the fluxes.

Despite this there are few of the sampled orbits where the East face flux does not hugely dominate over the West face flux. In general, to achieve West fluxes which are either comparable to or greater than East face fluxes, the graphs suggest that the inclination must be between 0° and a little over 30° and eccentricities must be not much less than 0.4 .

4.4 Impact Angles

It is possible to use the model to look at these results in more depth . Figures 4.10 to 4.13 show a break down of the impact angles from 0° inclination, circular orbit for each of LDEF's cardinal faces.

The number of possible interaction scenarios between debris in a given orbit and LDEF can be surprisingly large. Although there are eight impact

scenarios mentioned earlier in Section 4.2 this was for LDEF at a specific latitude . These eight cases can result in different impact angles at different latitudes. In reality debris in any orbit could result in an infinite number of minutely different impact scenarios. However, for modelling purposes, this is limited by the size of the latitude steps chosen in the calculations (in this case 1°).

A full set of these plots, for all the debris orbits discussed earlier, are contained in Appendix 3.

The radial distance from the centre of the plot represents impact incidence angle (points near the centre are near normal impacts and points on the edge are grazing impacts), and azimuthal directions are indicated with respect to other LDEF pointing directions.

Note: The height of the columns represent relative levels within that plot. The absolute level of each plot is arbitrary and therefore, in order to compare absolute flux levels between plots, Appendix 3 should be used in conjunction with Figures 4.5 to 4.9 . The purpose of Appendix 3 is purely to allow analysis of the distribution of impact directions on individual faces .

4.4.1 East

All the impacts on the East face occur close to the North/South line. For Low inclination orbits the impacts are grazing (on both the North and South edges), but as the inclination increases the impact directions become less grazing until for high inclination orbits we have only near normal incidence impacts.

The eccentricity of the orbits appears to have no effect on the impact angles.

4.4.2 South

On the South face impacts occur only on the East portion of the face. This time low inclination orbits result in near normal impacts and high inclination orbits result in grazing impacts.

At low eccentricities these impacts occur in a very tight band along the East/West line but as we increase the eccentricity the band becomes slightly broader. This effect is slightly more pronounced at low inclinations.

4.4.3 West

On the West face there are only impacts for a limited inclination range. At 0° and 60° all the impacts are grazing on the North edge of the face. However at 30°, which is very close to LDEF's inclination (LDEF = 28.5°), there are two very distinct lines of impacts from the North to the South angles of the face. These impacts range from grazing to near normal.

Changing the eccentricity of the debris orbits has no effect on the impact angles.

4.4.4 North

On the North face low inclination orbits result in near normal incidence impacts. As the inclination increases these impacts tend to come

more from the RAM direction so that for high inclination orbits we have grazing, East edge impacts.

The initial change from circular orbits to low eccentricity orbits results in a slight spread of impacts from the East West line, but further increasing the eccentricity shows no significant effect.

4.4.5 Space

The impacts on the Space face are mainly grazing , apart from at 30°. At 0° the impacts are from the North and South angles of the face. At 30°, in addition to the North and South grazing impacts there are impacts from the West angle at less oblique angles. As the inclination increases the West angle impacts disappear again and the impacts begin to come from closer to the East direction. At 150° the impacts are grazing from the East (or close to this) direction.

Changing the eccentricity of the orbits has no effect on the impact angles.

4.4.6 Earth

The distribution of impact angles on the Earth face is the same as that of the Space face and changes in the same ways with inclination and eccentricity.

4.4.7 General Conclusions

From the above analysis it becomes clear that the eccentricity of debris orbit makes very little difference to the impact angles on each face. However the orbital inclination does make significant differences.

If we had a means of identifying debris impacts amongst the impacts from natural particles and a method of then inferring impact angles, it might then be possible to calculate the proportions of low inclination and high inclination debris which was interacting with LDEF.

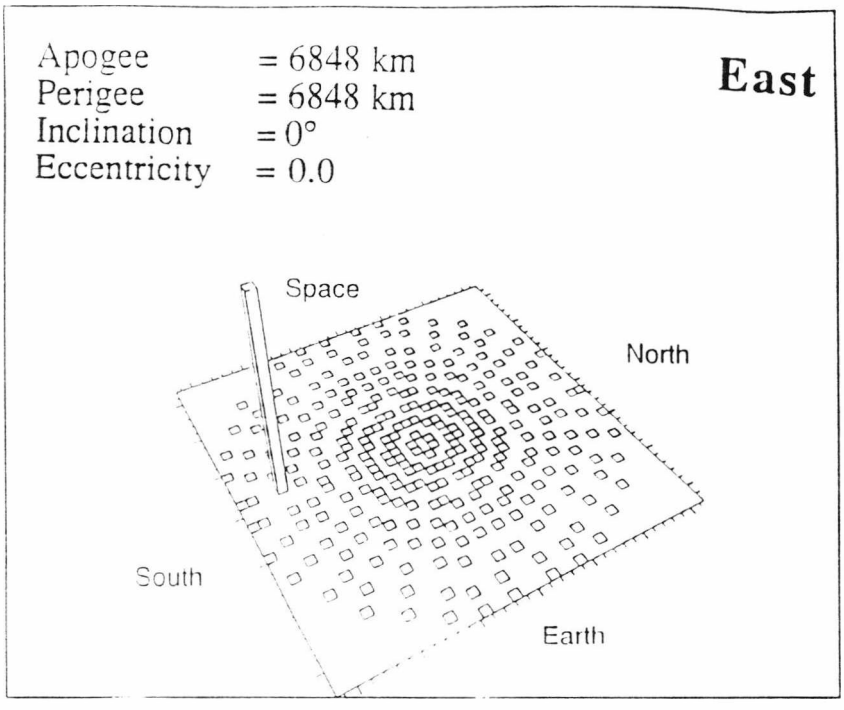

Figure 4.10. The radial distance from the centre of the plot represents impact incidence angle (points near the centre are near normal impacts and points on the edge are grazing impacts), and azimuthal directions are indicated with respect to other LDEF pointing directions.

Note: The height of the columns represent relative levels within that plot. The absolute level of each plot is arbitrary.

Impacts are near grazing from the South direction

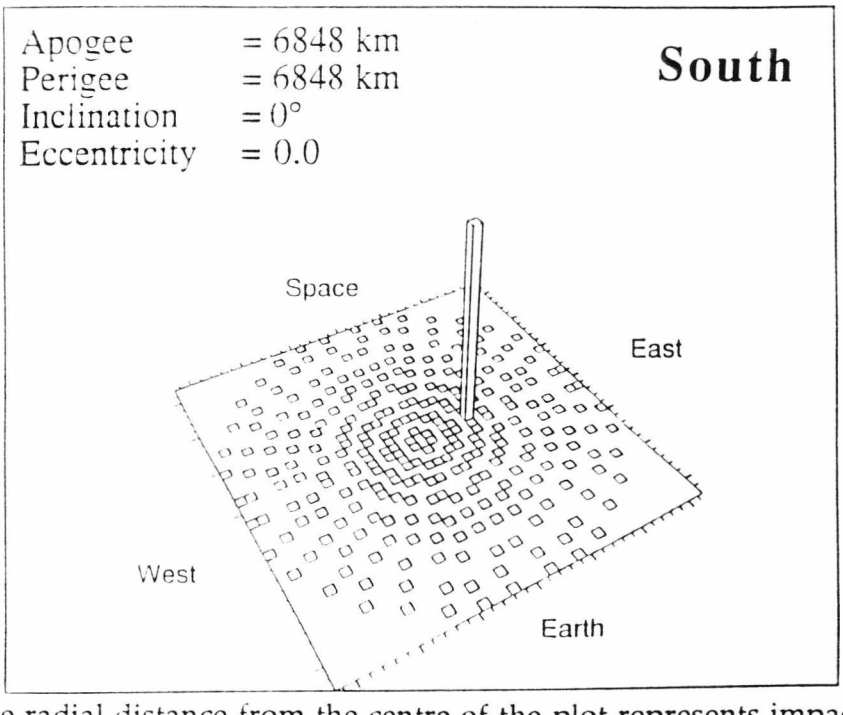

Figure 4.11. The radial distance from the centre of the plot represents impact incidence angle (points near the centre are near normal impacts and points on the edge are grazing impacts), and azimuthal directions are indicated with respect to other LDEF pointing directions.

Note: The height of the columns represent relative levels within that plot. The absolute level of each plot is arbitrary.

Impacts are near normal from the East side.

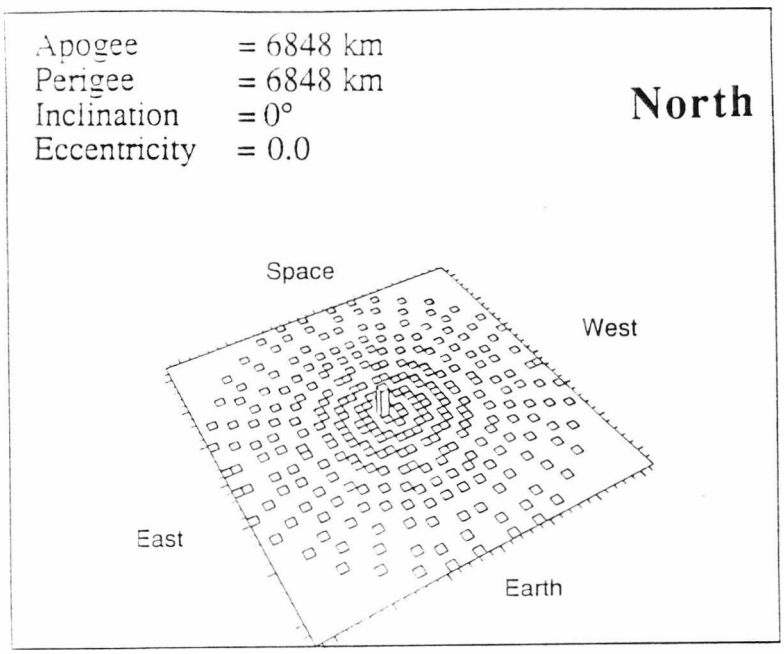

Figure 4.12. The radial distance from the centre of the plot represents impact incidence angle (points near the centre are near normal impacts and points on the edge are grazing impacts), and azimuthal directions are indicated with respect to other LDEF pointing directions.

Note: The height of the columns represent relative levels within that plot. The absolute level of each plot is arbitrary.

Impacts are near normal incidence.

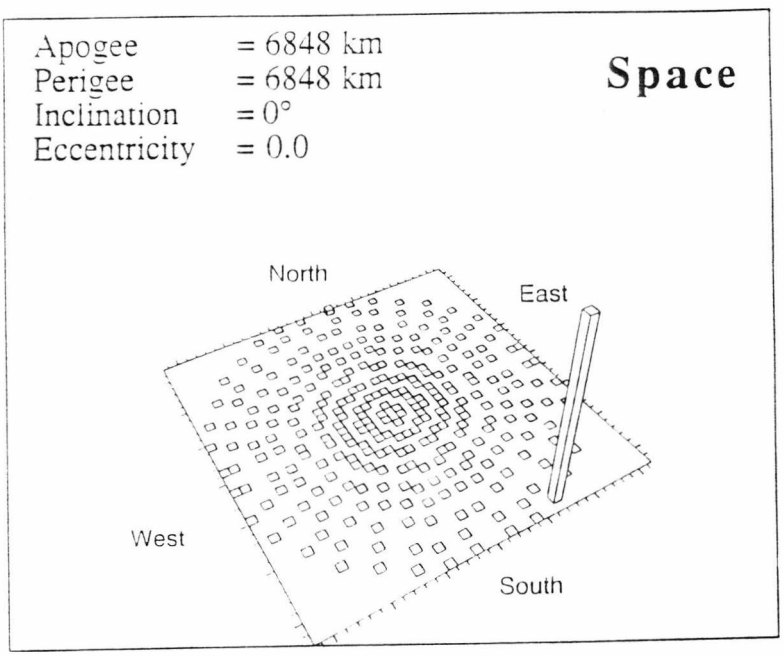

Figure 4.13. The radial distance from the centre of the plot represents impact incidence angle (points near the centre are near normal impacts and points on the edge are grazing impacts), and azimuthal directions are indicated with respect to other LDEF pointing directions.

Note: The height of the columns represent relative levels within that plot. The absolute level of each plot is arbitrary.

Impacts are grazing from the South side.

Chapter 5

The Combined Model

5.1 LDEF Data Sources

LDEF data was gathered from a variety of sources, however in order to gather a consistent data set for comparison with the modelling, restrictions were placed upon which data sets would be used. Data was only used from aluminium surfaces and the flux was calculated as a function of F_{max} (i.e.. flux of particles which will penetrate a given aluminium foil thickness) in all cases. For those instances where data was available in the form of craters rather than perforations, these data were converted to F_{max} values using the equation

$Fmax = 1.15 \times \text{crater depth}^{20}$

and crater depth/crater diameter = 0.59 for LDEF aluminium clamps (Newman, personal communication)

which gives $F_{max} = 0.68\ D_c$

Where D_c is the mean crater diameter given by

$D_c=(D_{max}\ D_{min})^{0.5}$

D_{max} is the maximum crater diameter and D_{min} the minimum perpendicular crater diameter to D_{max}

Sources of data were

1) The Micro-Abrasion Package (MAP), an experiment from the University of Kent, which used thin foil capture cells of both aluminium and brass (only aluminium results were used) to study dust and debris fluxes. For the most part each of the capture cells would give one data point on a F_{max} versus flux curve since, with one exception, only perforations had been counted on foils. The exception was one of the East foils where a small area had a crater survey performed on it. MAP foils were on East, West, North, South and Space faces.

2) LDEF clamps. These were a series of aluminium clamps which were used on LDEF to hold experimental trays in position. After recovery some of these clamps were sent to UKC in order that a crater survey could be performed. Clamps on North, South, East and Space face had surveys down to crater diameters of around 10 microns performed (complete to approximately 15 microns). In addition, one of the South clamps had a survey performed down to crater diameters of around 2 microns (estimated complete to 4 microns).

3) Space Debris Impact Experiment (SDIE, Humes 1984). This was a survey of craters on semi-infinite aluminium targets on all peripheral faces of LDEF. The size range was from a few microns to around 350 microns (complete to around 45 microns). These results were cumulatively binned in 5 micron steps, so conversions from D_c to F_{max} were performed using the lower boundary of each bin (errors were assumed to be random).

4) Intercostals. This was a crater survey performed on the LDEF aluminium frame, of all craters with a diameter greater than 500 microns (resolution was to 10 microns).

5.2 The Data

The error bars shown attached to these data are purely the statistical errors in hole and crater counts. Errors in measurements due to equipment or technique uncertainties are unknown so are not considered here.

The data sets are of differing reliability and while they overlap in some ranges, they do not cover other size ranges. In order to compare more easily the multiple LDEF data sets with the results of the modelling, one overall data set has been defined for each face. These data were defined as follows.

Firstly, an interpolated curve was drawn through all the data. The fit consisted of a simple interpolation between data points in the areas where errors were small and linear fits to the data where the errors were larger. Then points were read off this curve for a range of F_{max} values at 0.2 intervals on a log scale from 1 μm to 1 mm. The errors on these points were then defined by comparison of the statistical errors of the data in that region of the graph.

Graphs of all the data (real and interpolated) are shown in Figure 5.1 to Figure 5.5 and a summary graph of the interpolated data for all five faces being studied is shown in Figure 5.6.

5.3 Data Analysis

The LDEF fluxes were then compared with the predictions from the modelling.

Looking at Flux versus F_{max} curves would give us only a limited amount of information. This would allow us to see how far the predictions were from the actual data but would not aid us in deconvolving the relative levels of cosmic dust and space debris.
In order to attempt to estimate the relative levels a different approach was adopted.

Three sizes were chosen for more detailed analysis. These were points in the interpolated data which correspond to approximately 4 microns, 40 microns and 400 microns. At each of these sizes the relative flux levels on each face are then plotted and compared with the modelling.

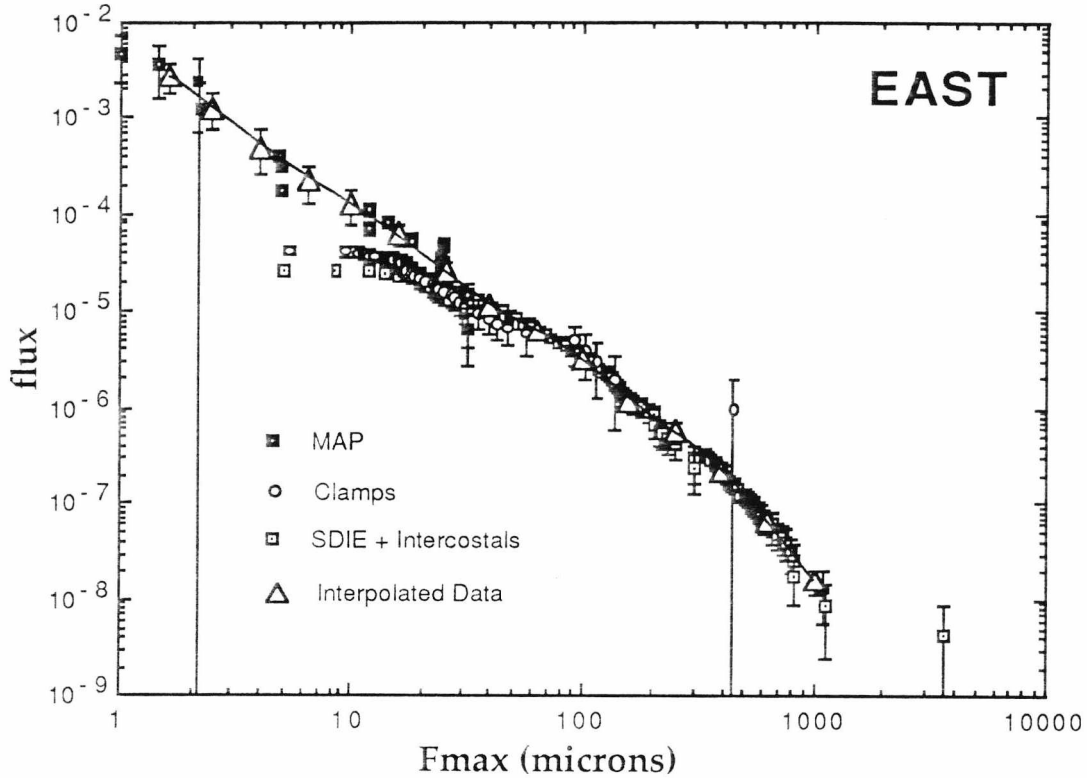

Figure 5.1. Foil perforation fluxes (m^{-2} s^{-1}) and interpolated data for LDEF face 9. Note the apparent incomplete sampling of the SDIE + Intercostals data below f_{max} ~ 30 μm and the Clamp data below f_{max} ~ 20 μm.

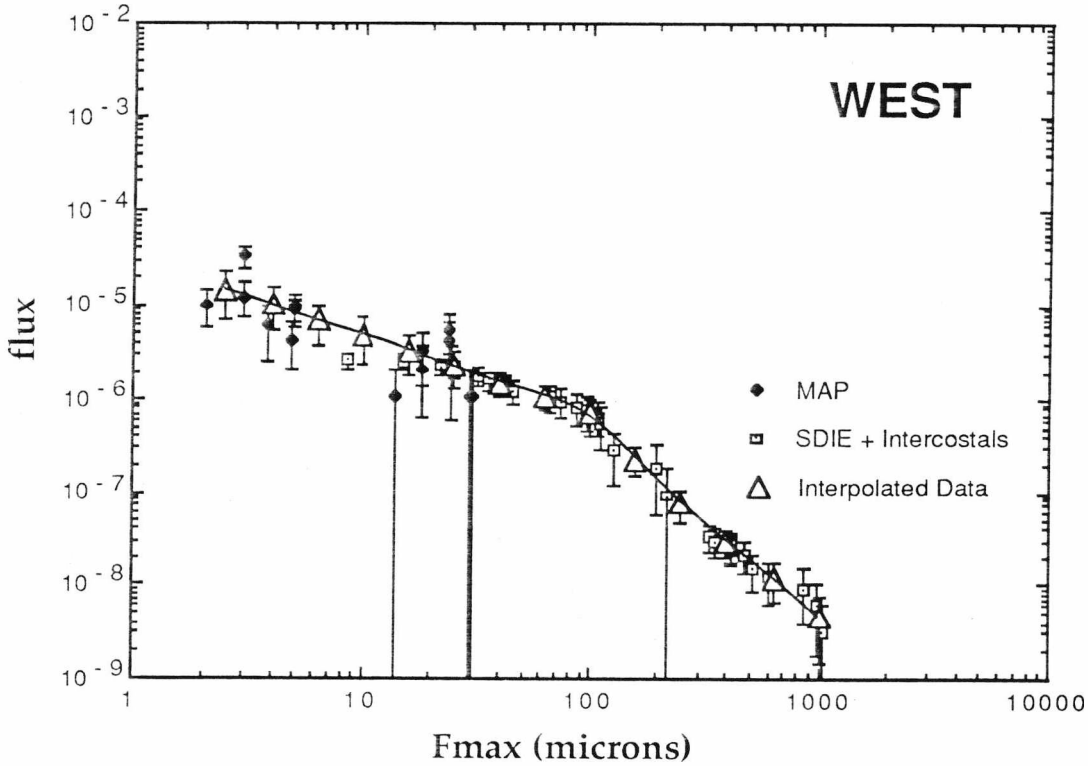

Figure 5.2. Foil perforation fluxes (m^{-2} s^{-1}) and interpolated data for LDEF face 3. Note statistics were often low on the West face hence much of the data has large error bars.

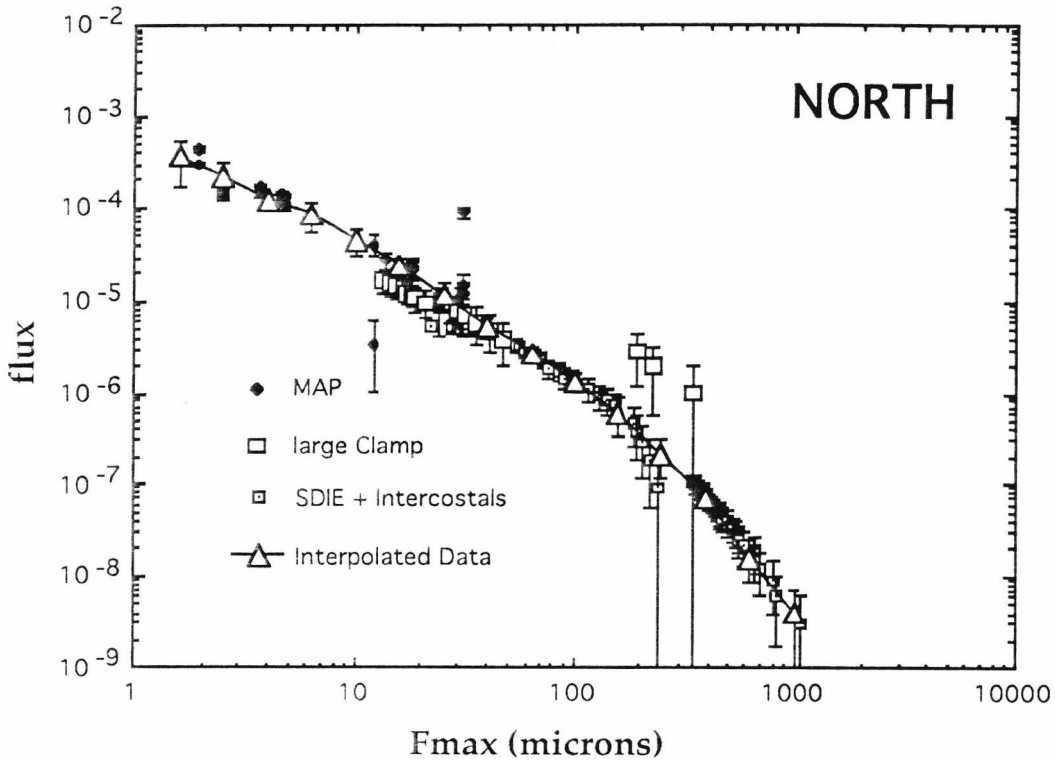

Figure 5.3. Foil perforation fluxes (m^{-2} s^{-1}) and interpolated data for LDEF face 12.

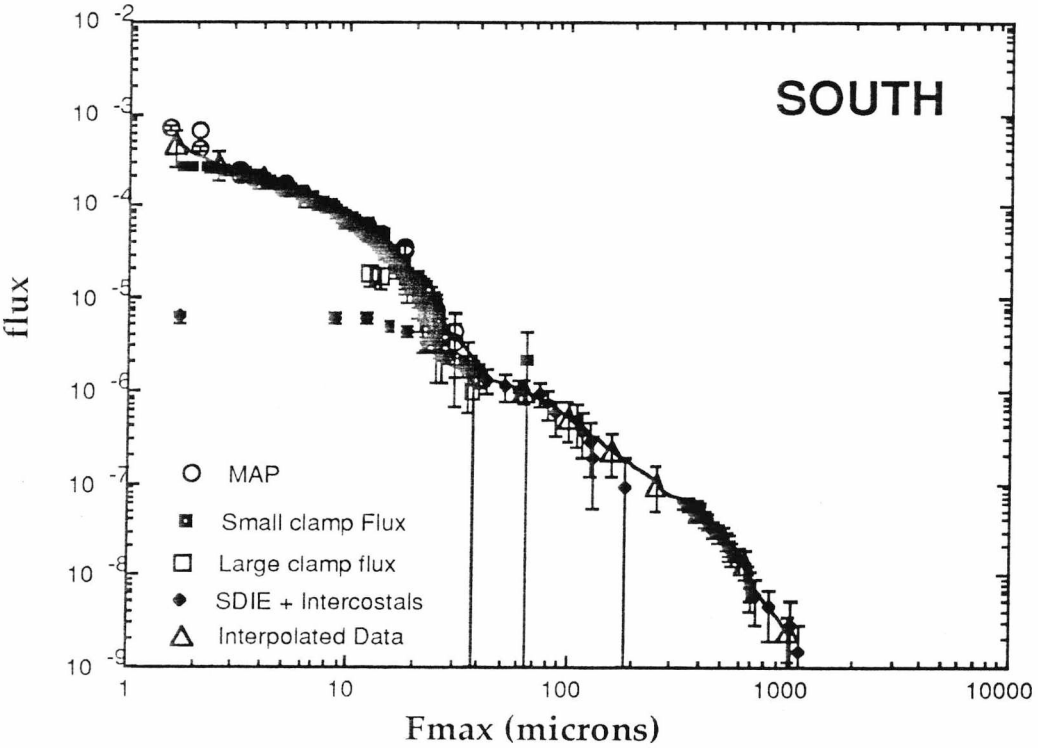

Figure 5.4. Foil perforation fluxes (m^{-2} s^{-1}) and interpolated data for LDEF face 6. Note the apparent incomplete sampling of the SDIE + Intercostals data below $f_{max} \sim 30$ μm. The thinnest MAP foils may have some contamination with secondary craters and the tray clamp data may not be complete for $f_{max}<2$ μm, hence large errors for interpolated fit.

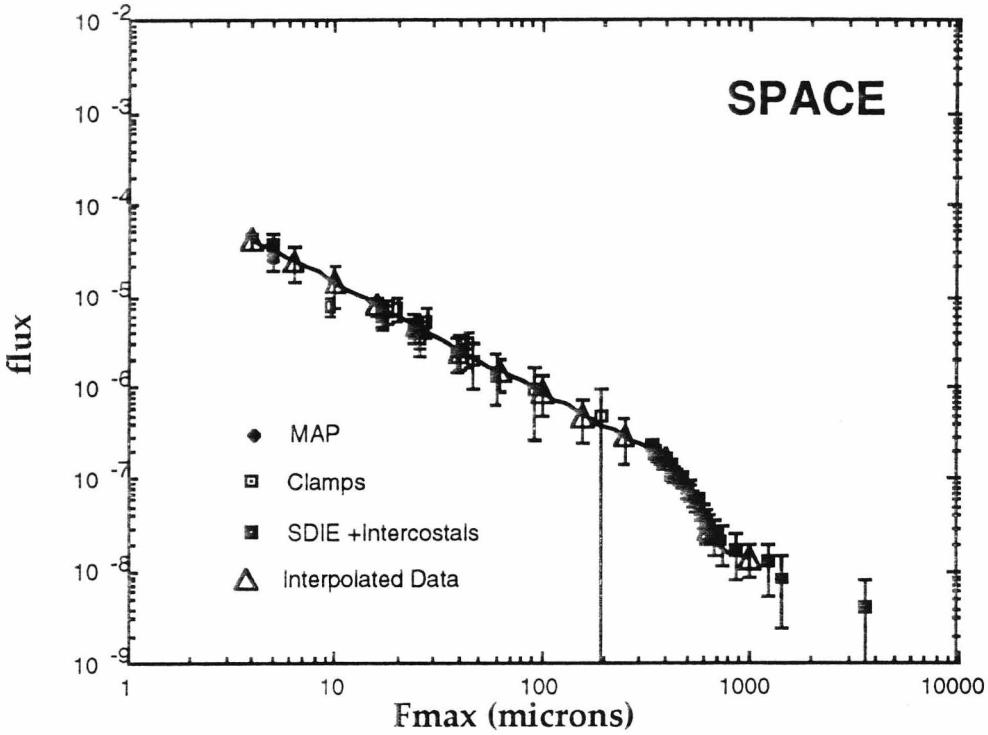

Figure 5.5. Foil perforation fluxes (m^{-2} s^{-1}) and interpolated data for LDEF Space face. Note statistics were often low on the Space face hence large error bars.

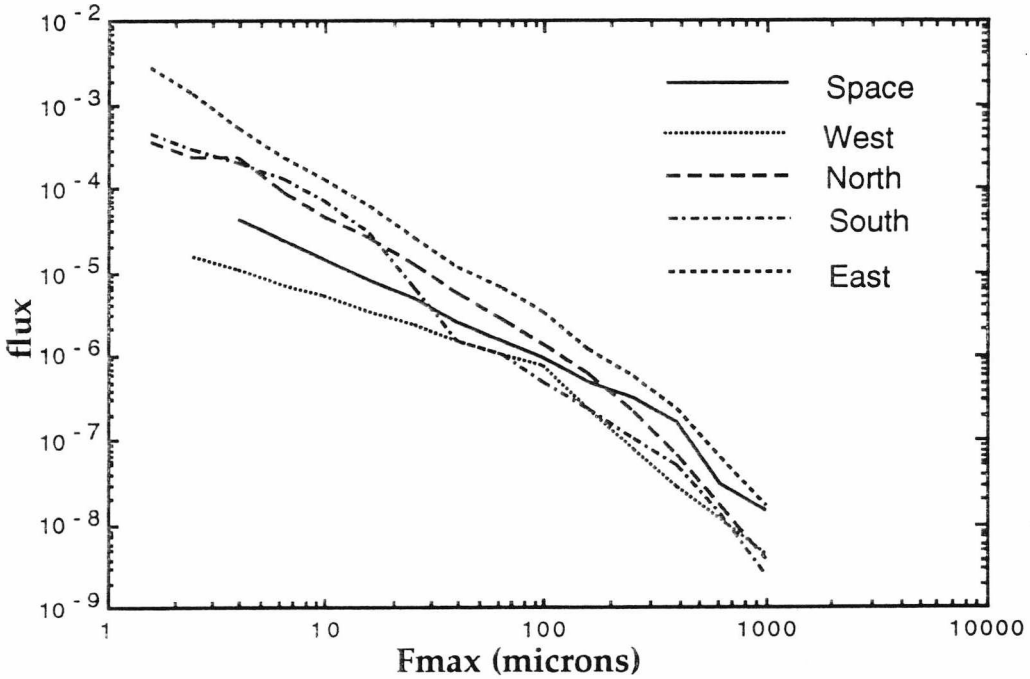

Figure 5.6 A comparison of fluxes on 5 of LDEF's cardinal faces. Note that the Earth face data is not considered here. It is seen that at large sizes (100 to 1000 μm) the East/West ratio remains fairly constant (about 10), which is what we expect for micrometeoroids, but as we go towards smaller sizes this ratio increases. This is evidence suggesting the dominance of a different population (ie. debris) in these size regimes.

Uncertainties in factors such as the absolute dust levels, the mass distribution, penetration equations and Dc to Fmax conversions, will affect the *absolute* flux levels for a given Fmax, but should not affect the relative levels around the faces. So by looking at the *shape* of these curves we can compare whether they are more representative of debris or natural impacts (assuming the validity of the assumptions made about the debris and natural particle spatial distributions and the natural particle velocity distribution).

Using the assumption that the shapes of the debris and cosmic dust distributions around the faces are correct, best fits to the data have also been calculated. There were three types of best fits calculated

1) A best fit assuming that the impacts are caused entirely by natural particles (debris levels are insignificant at this size range)
2)A best fit assuming that impacts are caused entirely by debris particles (natural dust levels are insignificant in this size range)
3)A best fit assuming a combination of dust and debris impacts

The best fits to the debris and naturals individually were chosen as follows.

i) The initial scaling factor was estimated as the actual East face flux divided by the predicted East face flux.
ii) The χ^2-values were then calculated for a series of fits going from 0.1 times the initial estimate to 10 times the initial estimate in steps of 0.1 on the Log scale (i.e. 20 steps).
iii) The fit which had the smallest χ^2-value was then selected as the best fit.

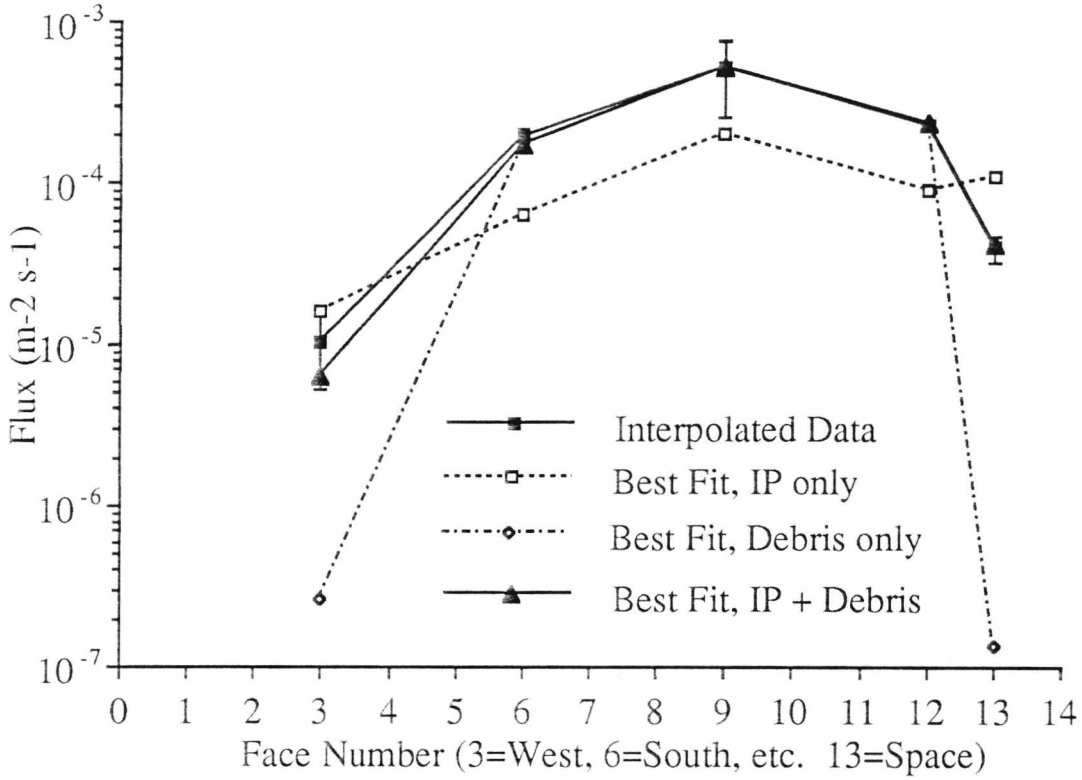

Figure 5.7. Best fit flux levels (m^{-2} s^{-1}) at 4 microns. Note there are only five faces with data in this size regime. The scaling factor for the "IP 0nly" fit is 5.2. The fit is roughly the same shape for the faces on the RAM-end but a poor match elsewhere. The scaling factor for the "Debris only" fit is 13.8. Again the shape is a good match on the RAM-end but not so good elsewhere. For the combination fit the IP coefficient is 2.0 and the debris 11.9. The combination fit is a very good match to the shape. Note that it lies inside the error bars at all points. The combination fit predicts a predominantly debris population in this size regime. natural particles will still dominate on the anti-RAM end, because the slower orbital velocities result in very little debris impacting the anti-RAM end, and on the Space face because most of the debris are in near circular orbits.

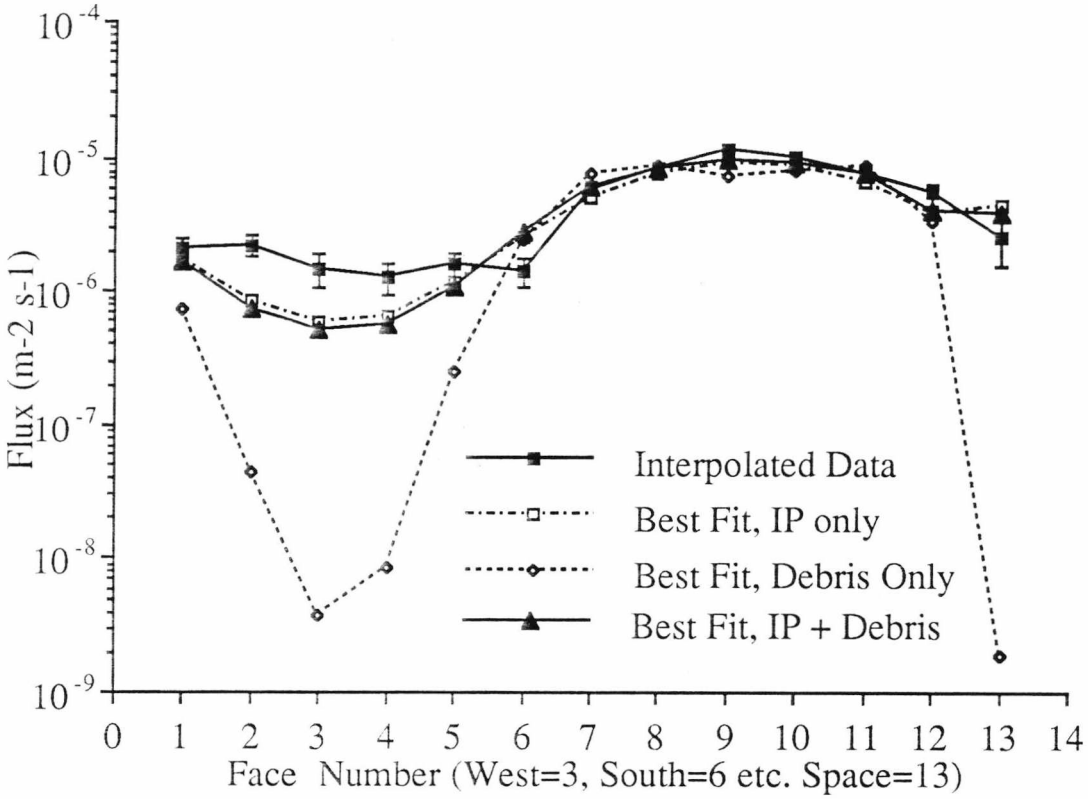

Figure 5.8. Best fit flux levels (m^{-2} s^{-1}) at 40 microns. The scaling factor for the "IP 0nly" fit is 3.0. The fit is roughly the same shape for the faces on the RAM-end but a poor match elsewhere. The scaling factor for the "Debris only" fit is 61.7. Again the shape is a good match on the RAM-end but not so good elsewhere. For the combination fit the IP coefficient is 2.6 and the debris 13.9. The combination fit is almost identical to the "IP only" fit. The combination fit predicts a predominantly IP population in this size regime (both East and West faces are over 80% IP).

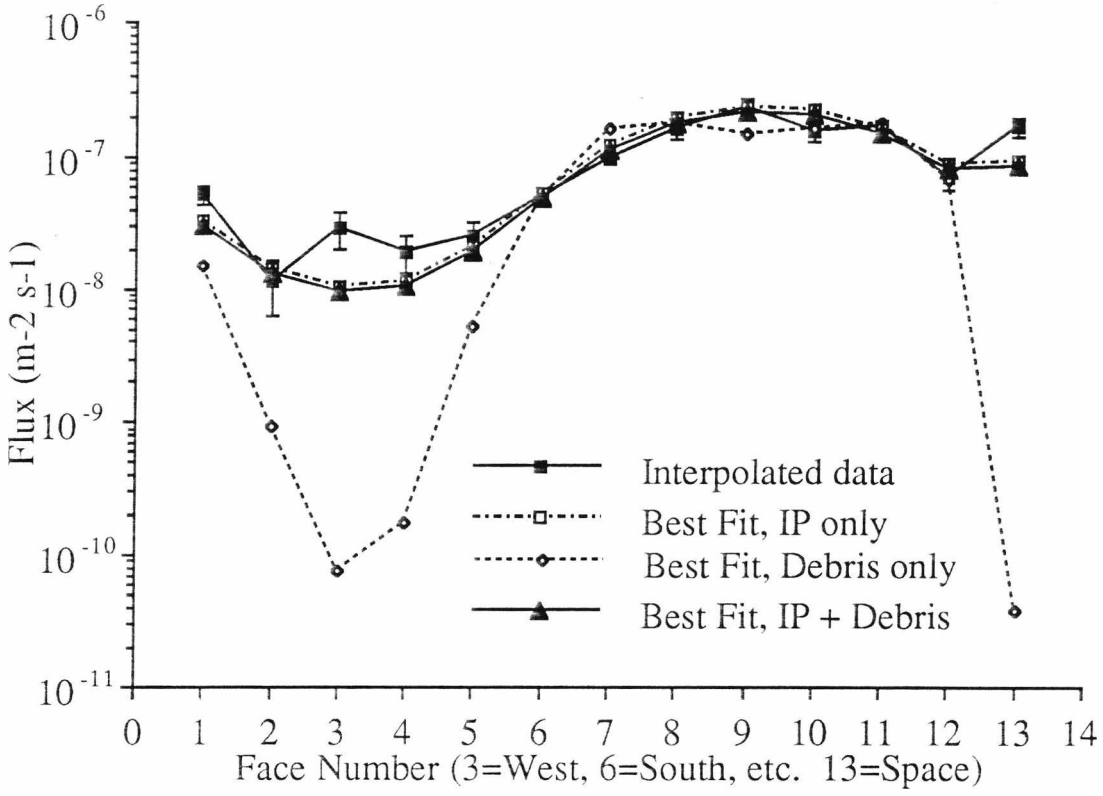

Figure 5.9. Best fit flux levels (m^{-2} s^{-1}) at 400 microns. The scaling factor for the "IP 0nly" fit is 16.7. The fit is roughly the same shape for the faces on the RAM-end and fairly good on the anti-RAM end except the West face. It is also poor on the Space Face. The scaling factor for the "Debris only" fit is 400.4. The shape is a good match on the RAM-end but not so good elsewhere. For the combination fit the IP coefficient is 15.3 and the debris 0.01. The combination fit is almost identical to the "IP only" fit. The combination fit predicts a predominantly IP population in this size regime. The scaling factor of 0.01 is the minimum possible co-efficient that the fitting program can assign. Note that the difference in the scaling factors between the "IP only " (16.7) fit and the IP scaling factor in the Combination fit (15.3) is due to the different fitting algorithms used having different starting points (and steps of 0.1 on a log scale in the 15-20 regime equate to around 4 on a linear scale).

Table 5.1. The scaling factors associated with the best fit curves shown in Figures 5.7 to 5.9. Note that 0.01 is the smallest possible scaling factor which the fitting program is capable of assigning to the debris in the combination fit.

	IP Only	Debris Only	IP + Debris	
4 micron	5.2	13.8	2.0	11.9
40 micron	3.0	61.7	2.6	13.9
400 micron	16.7	400.4	15.3	0.01

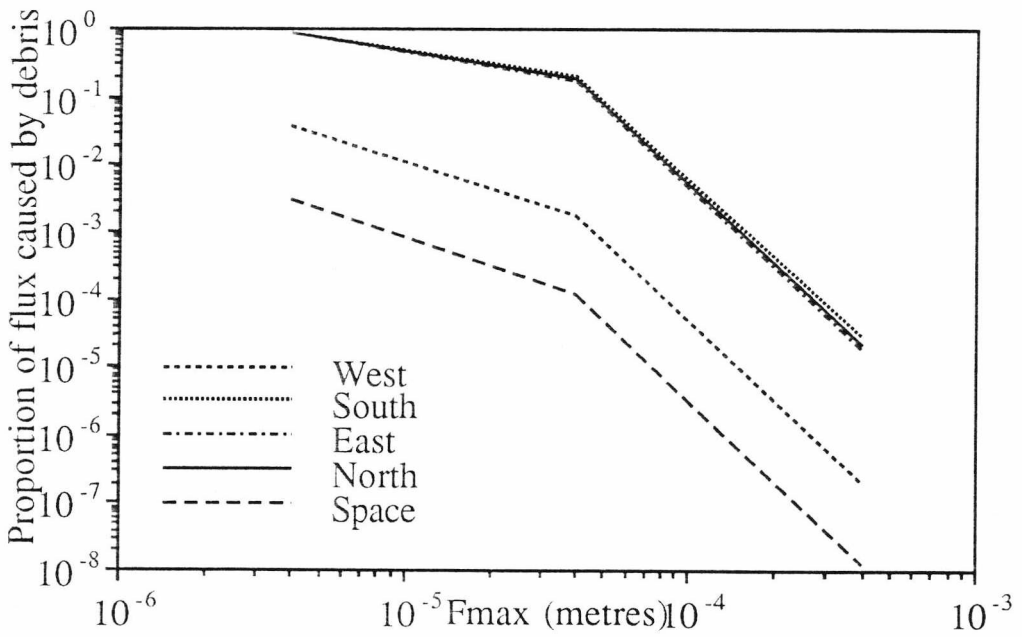

Figure 5.10 A plot of the proportion of the total LDEF flux which the combination fit for the modelling predicts is caused by debris.

For the best combination fit of debris and naturals a slightly different technique was used.

i) A rough calculation of the best fit is performed by trying all combinations of IP and debris coefficients as follows. IP coefficients range between 0.1 and 100 in 30 steps on a log scale and debris coefficients from 0.01 to 1000 in 500 steps on a log scale.

ii) The fit with the minimum χ^2-value is found and is taken as a rough estimate.

iii) Then the χ^2-values are calculated for a range of co-efficients between the one immediately below and immediately above the rough estimate coefficients, in 20 steps on a log scale.

iv) The fit with the minimum χ^2-value is selected as the best fit.

The results are shown in Figure 5.7 to Figure 5.9.

5.3.1 The 4 Micron Regime

The data sources in the 4 micron size range were MAP foils and one of the South facing Clamps. As a result of this, data is only available for the Cardinal faces of LDEF (excluding the Earth face) since none of the intermediate peripheral faces had MAP foils.

The fits even on the limited data set are still very useful. Looking at the individual fits we can see that neither the debris or interplanetary distributions produce a very good match with the shape found on LDEF. Although both curves are a fairly good match on the East, North and South faces, the IP model fit predicts too high a flux on West and Space while the debris model fit predicts too low a flux on the same faces. This is reflected in the overall best fit which contains significant amounts of both space debris

and interplanetary dust. It is worth noting however that the fit suggests that although the IP model is fairly accurate, requiring only 2.0 times the predicted fluxes, the debris model underestimates the debris level by a factor of 11.9 (Table 5.1). The flux levels suggested by these scaling factors result in a generally much larger debris than IP flux but because of the lower debris velocities, the IP will still dominate on the anti-ram side of the Spacecraft (Figure 5.10). Also, because most of the debris are in near circular orbits, the IP will dominate on the Space face.

5.3.2 The 40 Micron regime

At 40 microns we have fluxes for all but the Earth face. In this case the individual model best fits once again straddle the data on the Space face. However in this case both models are too low on the anti-RAM side of the spacecraft.

In order to reach the kind of flux levels suggested by the LDEF data the debris model requires a very large scaling factor, 61.7, while the IP need only be scaled by 3.0. When the combination best fit is calculated, however, it implies that only about 1/5 of the impacts at this size are due to debris and 4/5 from interplanetary dust (scaling factors of 13.9 and 2.6 respectively). The best fit thus created results in an only slightly better fit than the IP only. On the anti-ram side of the spacecraft the IP model fit alone is more accurate than the combined fit but since neither of the fits resemble the correct shape anyway, this could be considered less important. From looking at the shape of the flux distribution on the anti-RAM side of the spacecraft there is evidence that another flux source, not accounted for by either model, dominates here in this size regime.

5.3.3 The 400 Micron Regime

Again at 400 microns the only face for which we have no data is the Earth face. Both the individual model fits match the shape quite well for the ram side of the spacecraft, but this time IP fit is much closer than the debris fit for the anti-RAM side and the Space face.

On the anti-ram side of the spacecraft the IP fit is still reasonably good apart from the anomalously high flux in the West face data. The scaling factors required for both fits here are very high (IP = 16.7, debris = 400.4).

The superiority of the IP model fit is reflected in the combination fit. The scaling factors here are 15.3 and 0.01 for IP and debris respectively. The smallest possible scaling factor which the fitting program can give to the debris is 0.01, so this implies that the best fit is one consisting entirely of interplanetary dust. The reason for the difference between the IP scaling factors for the individual and combination fits is simply a result of the different fitting programs (for the individual fits the step of 0.1 in log space correspond to about 4 in linear space at around 15). The combination fit, is the more accurate as a result of the algorithms used.

5.3.4 General Points

The 400 micron IP fit seems to be a good approximation to the actual data but the scaling factor required is very large. If this inaccuracy were a result of assumptions made in the IP model then a similar size of inaccuracy might be expected in the smaller size regimes. However the size of the scaling

factor required for IP in the combination fits, increases with the size range from 2.0 to 2.6 then to 15.3. There are several possible reasons for this.

1) The penetration equation is invalid.

   The penetration equation chosen for the modelling (see chapter 2) does not have a dimensional scaling factor. Some of the alternative equations[21] have a scaling factor of $d_p^{1.056}$. The result is that an increase in F_{max} of a factor of 10 does not require an increase of a factor of 10 in d_p (in fact an increase of about 8.85). Therefore if the flux at F_{max} = 4 μm were assumed to be correct, an equation with this dimensional scaling would not result in such a rapid decrease in flux as we increase F_{max}. This is, however a very weak dimensional scaling and does not account for the large changes in the coefficients.

2) The Grun mass distribution has a smaller gradient than estimated.

   This would have the effect of increasing the flux of large meteoroids in comparison to smaller meteoroids and may account for the range of coefficients.

3) The velocity distribution is unrepresentative in these size regimes.

   This would not effect the 4 micron regime very much since the debris dominates there. In the 400 micron size regime this could be expected to have a very large effect, because of the very distinct dominance of the IP, however in the 40 micron size regime the effect would not be nearly as pronounced since there are significant quantities of both debris and IP here. This could be a realistic reason for the change in scaling factors found here.

The debris scaling factor does not vary all that much from the 4 to 40 micron combination best fits (from 11.9 to 13.9, approx. 15%) and although it

goes to zero in the 400 micron fit, a similar factor of about 12 would not significantly alter the overall fit due to the enormous dominance of the IP in this size regime. The scaling factors for the debris suggest that the actual flux is underestimated by as much as an order of magnitude. debris level estimates, in large size regimes, were made from observational data and were extrapolated downwards to smaller sizes using collisional fragmentation models. Both the completeness of the observations (some debris orbits are more difficult to detect than others and there is generally little definite information on factors such as debris albedoes) and the accuracy of the fragmentation models, are unknown. In addition to this there may be temporal variations of the debris population over such small time scales as 5 years, due to solar activity.

5.4 The Expanded Debris Model

The Chemistry of Micrometeoroids Experiment [22] on LDEF was flown with the purpose of performing chemical analysis on residues of impacting particles after LDEF's return. Results, so far published, on the East face show debris and natural particles in roughly the proportions expected. However on the West face there appears to be an excess of debris that cannot be accounted for by the existing debris models.

Of the 199 West face crater sites analysed, 149 have diameters in the region of 20 to 80 microns. This is converted for comparison with East face Aluminium craters by Horz[23], assuming average velocities for East and West faces, using

$$0.5\ d_c = 5.24 (d_p)^{19/18} H^{-0.25} (\rho_p/\rho_t)^{0.5} (V/V_\odot)^{2/3} \qquad \text{Equation 5.1}$$

Where d_c= crater diameter, d_p= projectile diameter, H = Brinnell hardness of target, ρ_p = density of projectile, ρ_t= density of target, V = impact velocity and Vc = speed of sound in target material

If we do not assume any velocities then we can use this for a gold to aluminium conversion on the West face. It gives us

$$\frac{d_{c_{Al}}}{d_{c_{Au}}}=(H_{Al}/H_{Au})^{-0.25}\,(\rho_{Au}/\rho_{Al})^{0.5}\,(V_{c_{Au}}/V_{c_{Al}})^{2/3} \qquad \text{Equation 5.2}$$

ρ_{Al} = 2700 kg m^{-3}, ρ_{Au} = 19300 kg m^{-3}, V_{cAl} = 6.374 Km s^{-1} V_{cAu} = 3.24 km s^{-1}, H_{Au} = 25 (for wrought gold) and assuming an average value of 90 for the Brinnell Hardness of Aluminium (H_{Al} varies from 60 to 120 for cast Aluminium), gives us

$$d_{c_{Al}}=1.235\,d_{c_{Au}} \qquad \text{Equation 5.3}$$

and using $F_{max}=0.68d_c$ from section 5.1 we get

$$F_{max_{Al}}=0.84\,d_{c_{Au}} \qquad \text{Equation 5.4}$$

(Note that deriving the same relationship from PODS[24] , equation 21, assuming projectile densities of between 100 kg m-3 and 5000 kg m-3 gives a scaling factor for F_{max} on aluminium from d_c on Gold of between 0.19 and 0.24. POD's equations were derived from a purely theoretical standpoint, although factors have been introduced to bring them more into line with actual results. The equation stated above was derived empirically from experimental data. It is not clear why these equations produce such different results but this does demonstrate the difficulties associated with interpreting impact data.)

This equates the gold craters to Aluminium craters in the F_{max} range of 16.8 microns to 67.2 microns.

Of these craters approximately 13% of the total (30% of those with identifiable residues) were debris and 29% of the total (70% of those with identifiable residues) were of natural origins. On the West face, debris impacts are at very low velocities and therefore are far more likely to leave residues than on other faces. So although 13% is a minimum estimate for debris on the West face the true figure may not be much greater than this.

These craters are in a similar size range to the 40 micron plot shown above. In order to attempt to explain the excess of debris on the West face Kessler[25] suggests that the population of particles in high ellipticity , low inclination orbits (orbits with apogee greater than 10000 km and inclinations less than 50°) is far larger than had been previously estimated. His calculations suggest that 20 times more debris would have to be in such orbits to account for the excess.

In order to test this theory to find out if it would also give a better fit to the observed LDEF flux distributions, a new debris data set was created. This data set included the basic 6600 DISCOS orbits (see chapter 3) but all high eccentricity low inclination orbits were included 20 times. Fits to the actual LDEF data were then calculated in exactly the same way as with the basic DISCOS data.

The results are shown in Figure 5.11 to Figure 5.13.

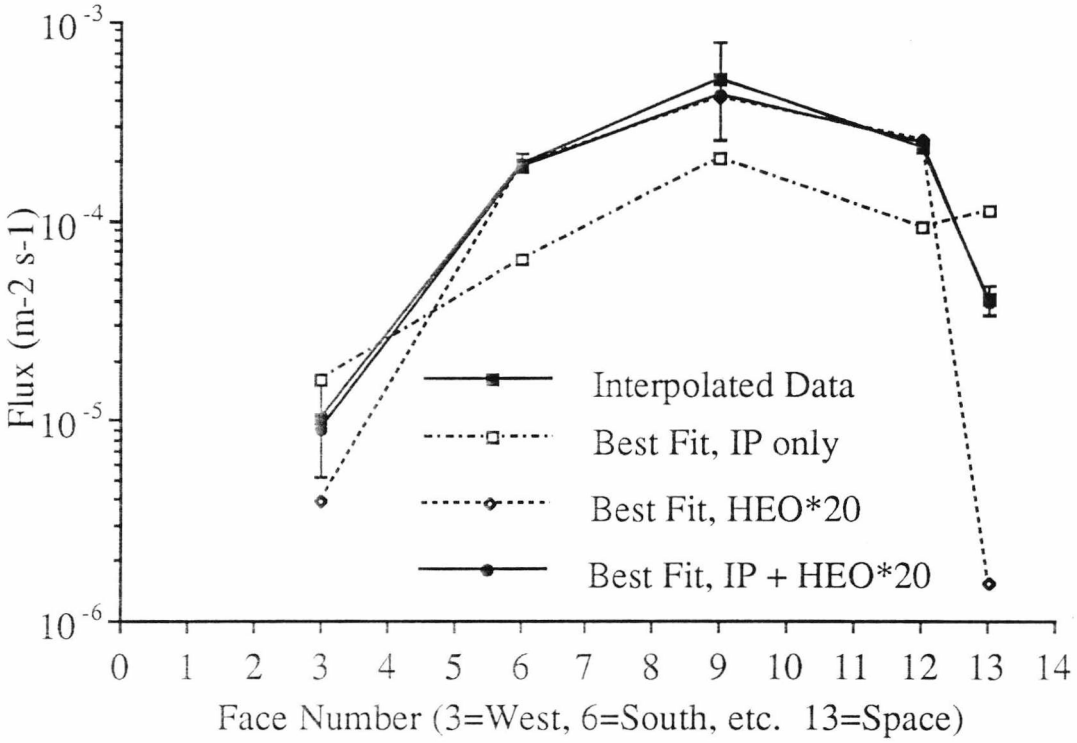

Figure 5.11. Best fit flux levels (m^{-2} s^{-1}) at 4 microns using the HEO*20 expanded debris data set. The scaling factor for the "IP 0nly" fit is 5.2. The fit is roughly the same shape for the faces on the RAM-end but a poor match elsewhere. The scaling factor for the "HEO*20 " fit is 10.8. The shape is a much improved fit, this time the debris is a fairly good match everywhere except the Space face. For the combination fit the IP coefficient is 2.0 and the HEO*20 10.0. The combination fit is a very good match to the shape. Note that it again lies inside the error bars at all points, however since the combination fit with the original debris distribution was within the error bars this cannot be considered to be a significant improvement. The combination fit predicts a predominantly debris population in this size regime, but once more the IP will still dominate on the anti-RAM end and the Space face.

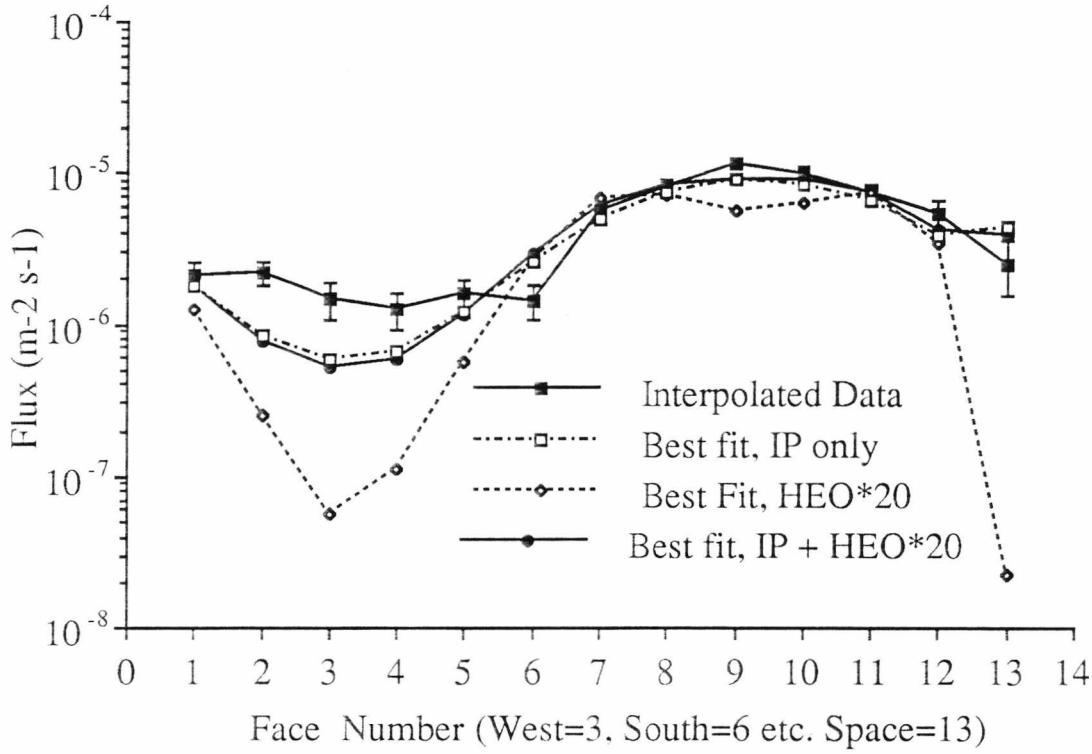

Figure 5.12. Best fit flux levels (m^{-2} s^{-1}) at 40 microns using the HEO*20 expanded debris data set. The scaling factor for the "IP 0nly" fit is 3.0. The fit is roughly the same shape for the faces on the RAM-end but a poor match elsewhere. The scaling factor for the "HEO*20" fit is 48.2. Again the shape is a good match on the RAM-end but although it is much improved it is still quite a poor fit elsewhere. For the combination fit the IP coefficient is 2.6 and the HEO*20 11.9. The combination fit is almost identical to the "IP only" fit. The combination fit predicts a predominantly IP population in this size regime.

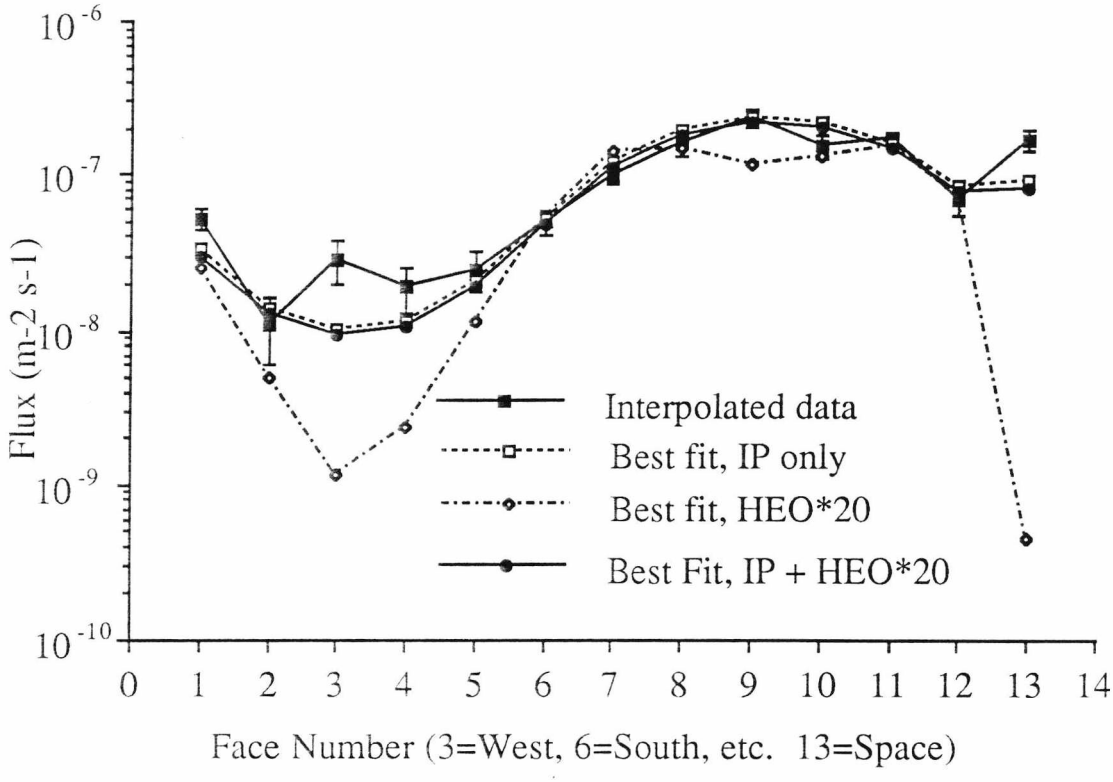

Figure 5.13. Best fit flux levels (m^{-2} s^{-1}) at 400 microns using the HEO*20 expanded debris data set. The scaling factor for the "IP 0nly" fit is 16.7. The fit is roughly the same shape for the faces on the RAM-end and fairly good on the anti-RAM end except the West face. It is also poor on the Space Face. The scaling factor for the "HEO*20 " fit is 313.2. Again the shape is a good match on the RAM-end but although it is much improved it is still quite a poor fit elsewhere. For the combination fit the IP coefficient is 15.2 and the HEO*20 0.01. The combination fit is almost identical to the "IP only" fit. The combination fit predicts a predominantly IP population in this size regime. The scaling factor of 0.01 is the minimum possible co-efficient that the fitting program can assign. Note the difference in the scaling factors between the "IP only " fit and the IP scaling factor in the Combination fit is due to the different fitting algorithms used having different starting points (and steps of 0.1 on a log scale in the 15-20 regime equate to around 4 on a linear scale).

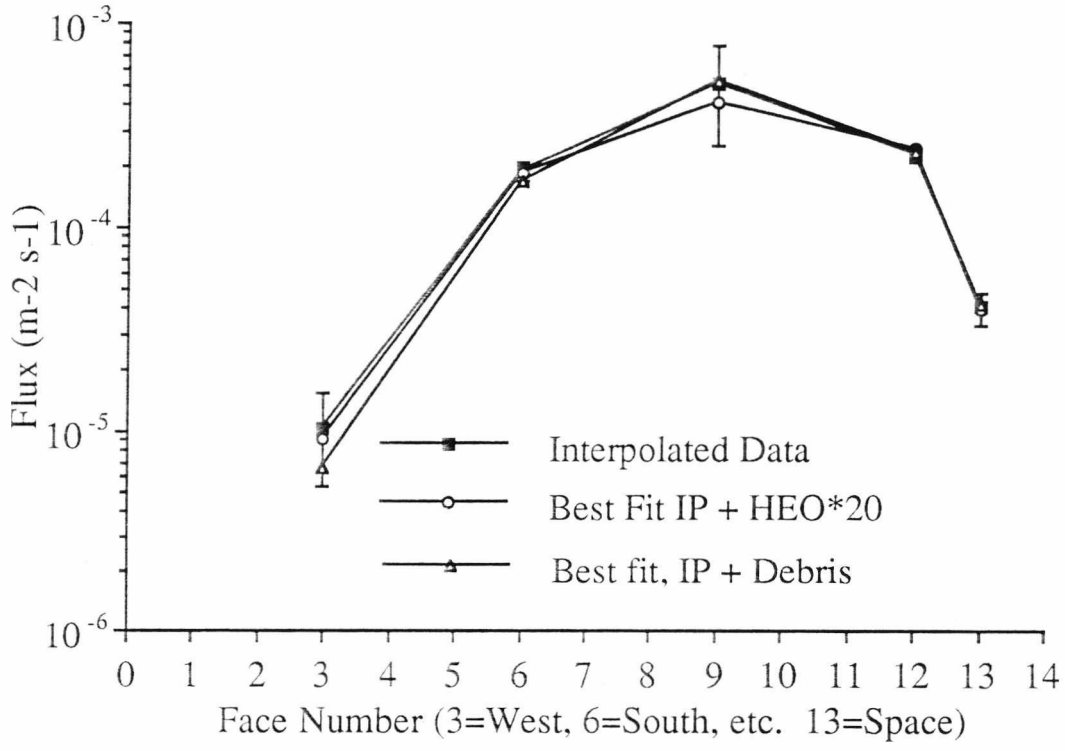

Figure 5.14. Best fit flux levels (m^{-2} s^{-1}) at 4 microns of the basic data and the HEO*20 expanded debris data set. For the IP + Debris combination fit the IP coefficient is 2.0 and the debris 11.9. For the IP + HEO*20 combination fit the IP coefficient is 2.0 and the HEO*20 10.0. The HEO*20 combination fit is not significantly different from the basic debris combination fit.

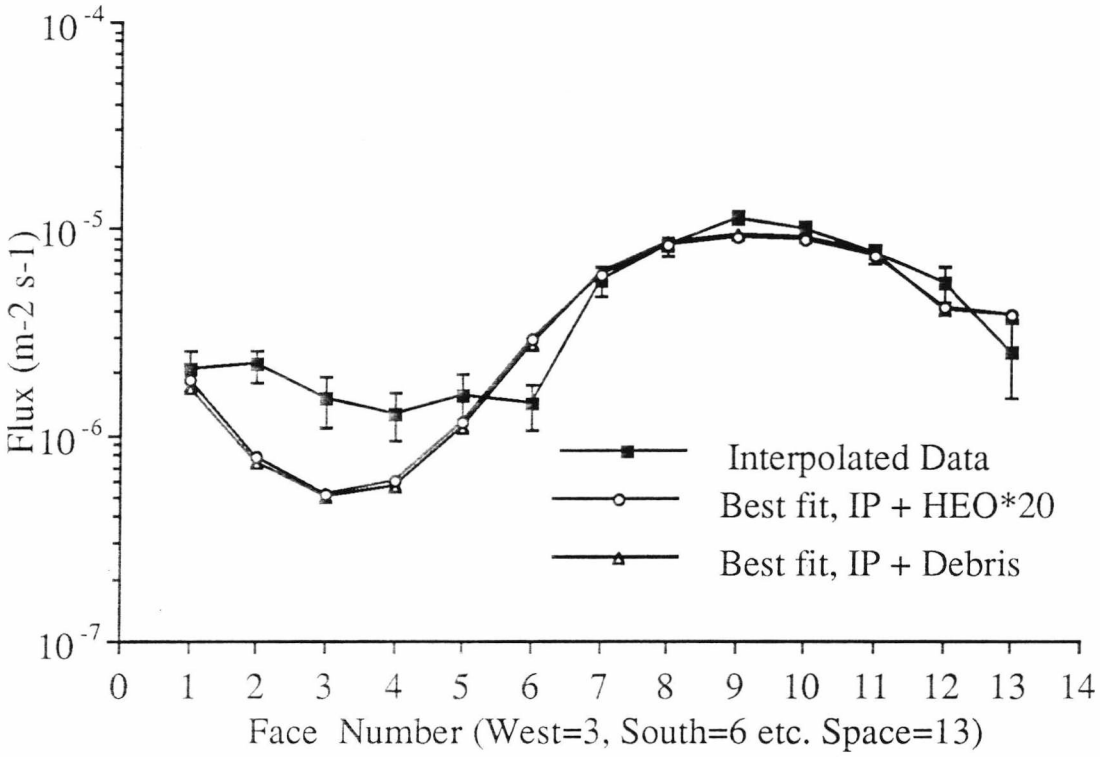

Figure 5.15. Best fit flux levels (m^{-2} s^{-1}) at 40 microns of the basic data and the HEO*20 expanded debris data set. For the IP + Debris combination fit the IP coefficient is 2.6 and the debris 13.9. For the IP + HEO*20 combination fit the IP coefficient is 2.6 and the HEO*20 11.9. The HEO*20 combination fit is virtually indistinguishable from the basic debris combination fit.

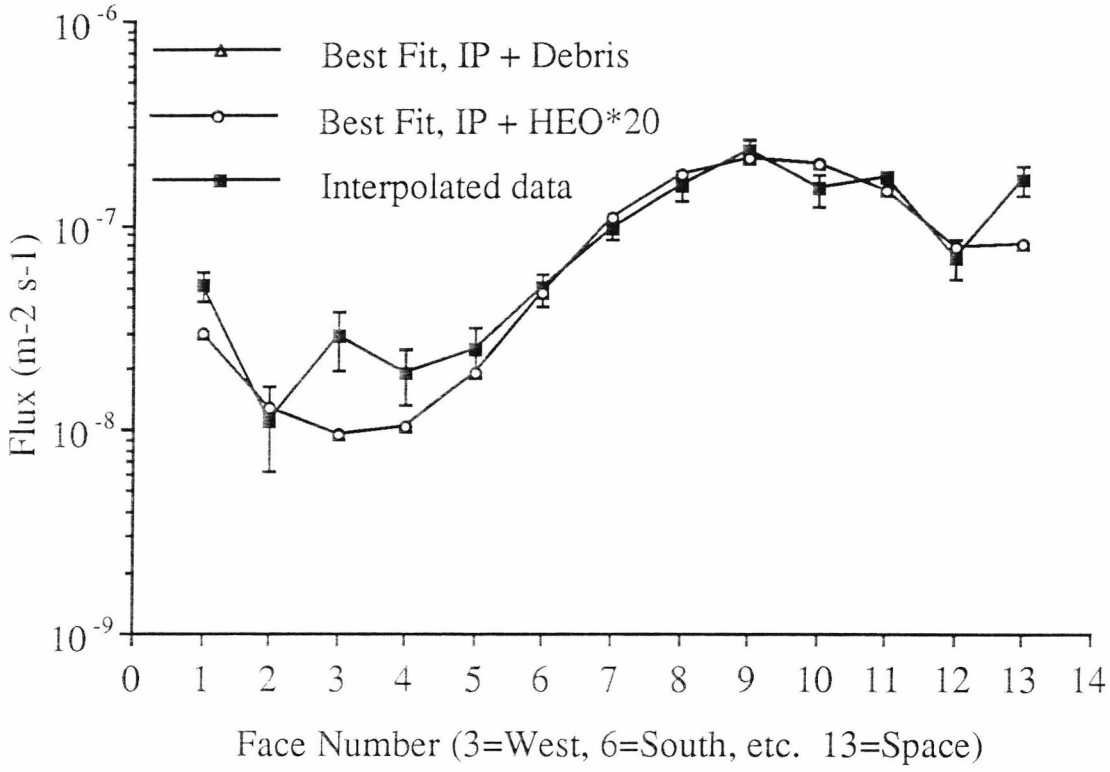

Figure 5.16. Best fit flux levels (m^{-2} s^{-1}) at 40 microns of the basic data and the HEO*20 expanded debris data set. For the IP + Debris combination fit the IP coefficient is 15.3 and the debris 0.01. For the IP + HEO*20 combination fit the IP coefficient is 15.2 and the HEO*20 0.01. The HEO*20 combination fit is virtually identical to the basic debris combination fit.

Table 5.2 The scaling factors associated with the best fit curves shown in Figures 5.11 to 5.13. Note that 0.01 is the smallest possible scaling factor which the fitting program is capable of assigning to the debris in the combination fit.

	IP Only	HEO	IP + HEO	
4 micron	5.2	10.8	2.0	10.0
40 micron	3.0	48.2	2.6	11.9
400 micron	16.7	313.2	15.2	0.01

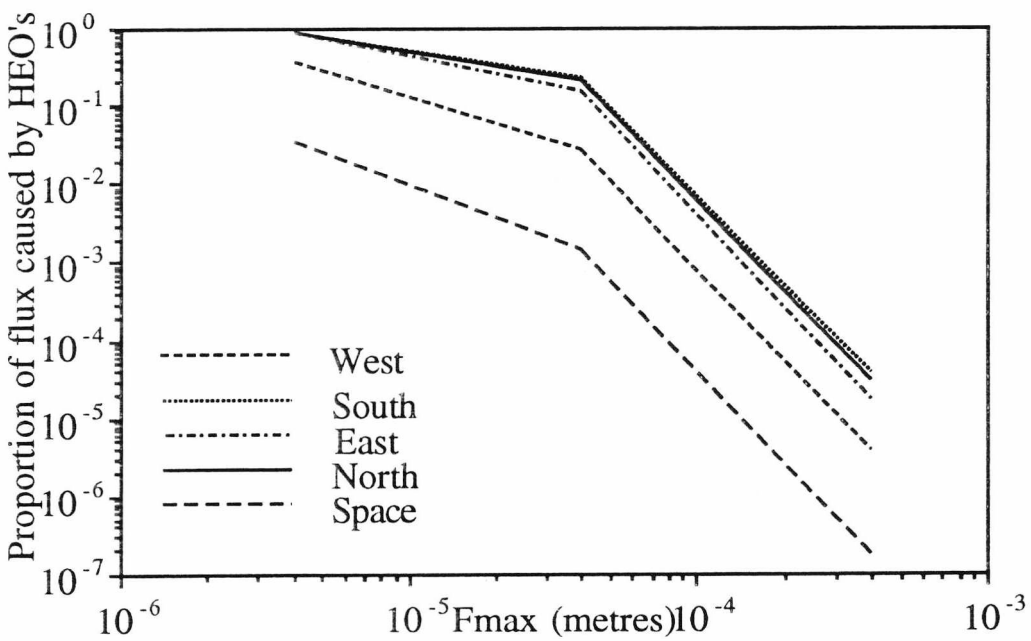

Figure 5. 17 A plot of the proportion of the total LDEF flux which the combination fit for the modelling predicts is caused by HEO's.

5.4.1 The 4 Micron Regime

At the 4 micron size regime the HEO*20 fit is a little better than the debris was on it's own. The West face point now lies considerably closer to the data point than the basic debris fit. The scaling factor is still significant though and has only reduced by about 20% to 10.8.

The combined fit may be slightly better but since the combined fit with the basic debris set was inside the error bars anyway the difference is not very important. The debris scaling factor in this case has again reduced (HEO*20 factor = 10.0), but the IP still requires a factor of 2.0. This is an even larger debris dominance than for the basic DISCOS data but since the debris scaling factor has not been reduced by very much this does not seem like much of an improvement.

A direct comparison between the combined fits is shown in Figure 5.14 to Figure 5.16. The extra HEO debris does not produce a significant improvement in the model fits in this size regime.

5.4.2 The 40 Micron regime

At 40 microns the individual debris fit is vastly improved by the extra HEO debris. Once more the actual scaling factor is only reduced by about 20% (to 48.2) but the West face fit is increased by almost two orders of magnitude (although still falling an order of magnitude short of the actual flux).

The combined fit is, again, not significantly better than the combined fit with the basic DISCOS data. The direct comparison is once more shown in

Figure 5.15 and we can see that the two fits are virtually indistinguishable. This must lead us to question the validity of the extra HEO debris as a source of the excess impacts on the West face.

5.4.3 The 400 Micron Regime

The results in the 400 micron size regime are even less impressive. The individual debris fit is again improved by the introduction of the extra HEO debris and the scaling factor is once more reduced by about 25%. However this time in the case of the combined fit the extra HEO debris makes virtually no difference whatsoever. The fit is 15.2 times the IP (compared to 15.3 for the basic data set) and 0.01 times the debris.

5.4.4 General Points

In the case of the 40 micron fits, the individual fits (IP, debris and HEO*20) all have too high an East to West face ratio. In order to have an improved fit we need to find a source of impacts with a much lower East to West ratio.

5.5 Faster Natural Particles

The interplanetary dust velocity distribution used in the simulations was chosen since it was considered to be the best of the existing distributions analysed. However this distribution was calculated using data in a much larger size regime than would produce the craters analysed on LDEF. If this velocity distribution were invalid at these sizes then we might find that the

true interplanetary dust distribution produced a much smaller (or larger) East to West ratio at 40 microns. It is also worth noting that a change in the IP velocity distribution would not be so readily apparent in the 4 micron regime since the debris appears to dominate here anyway. From the analysis performed in Chapter 3 we observe that higher particle velocities result in a lower East to West ratio.

Figure 5.19 to Figure 5.21 shows best fits to the data assuming a single interplanetary dust velocity of 30 km s^{-1} and Figure 5.22 to Figure 5.24 a comparison with the basic IP + Debris best fit and IP + HEO*20 best fit.

The average velocity of the Erickson velocity distribution was 16.7 km s^{-1}, but Taylor[26] shows that this distribution is equivalent to a far higher velocity (approx. 26.7 km s^{-1}) when converting to constant crater depth. Therefore a single velocity of 30 km s^{-1} does not represent such a large change in the velocity distribution as it might first appear.

In addition Taylor found that Southworth and Sekanina[8] (see chapter 3) underestimated the velocity of meteoroids in there sample. The result is an equivalent constant crater depth velocity for the corrected Southworth and Sekanina distribution of 23.6 km s^{-1}, bringing it more into line with the Erickson distribution. It is interesting to note , however, that the Southworth and Sekanina data include a smaller size range of particles than the Erickson distribution, thus contradicting the theory of smaller particles being faster.

Table 5.3 The scaling factors associated with the best fit curves shown in Figures 5.19 to 5.21.

	IPv=30 Only	Debris Only	IPv=30 +	Debris
4 micron	3.2	13.8	1.2	12.4
40 micron	1.68	61.7	1.2	31.2
400 micron	6.3	400.4	5.3	47.2

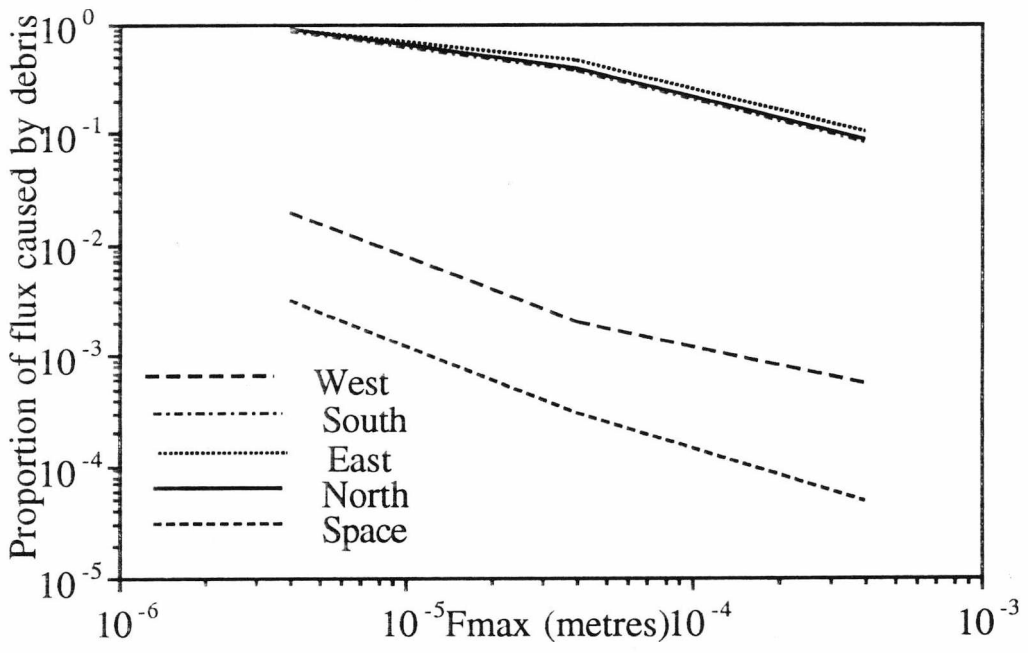

Figure 5.18 A plot of the proportion of the total LDEF flux which the combination fit for the modelling predicts is caused by debris.

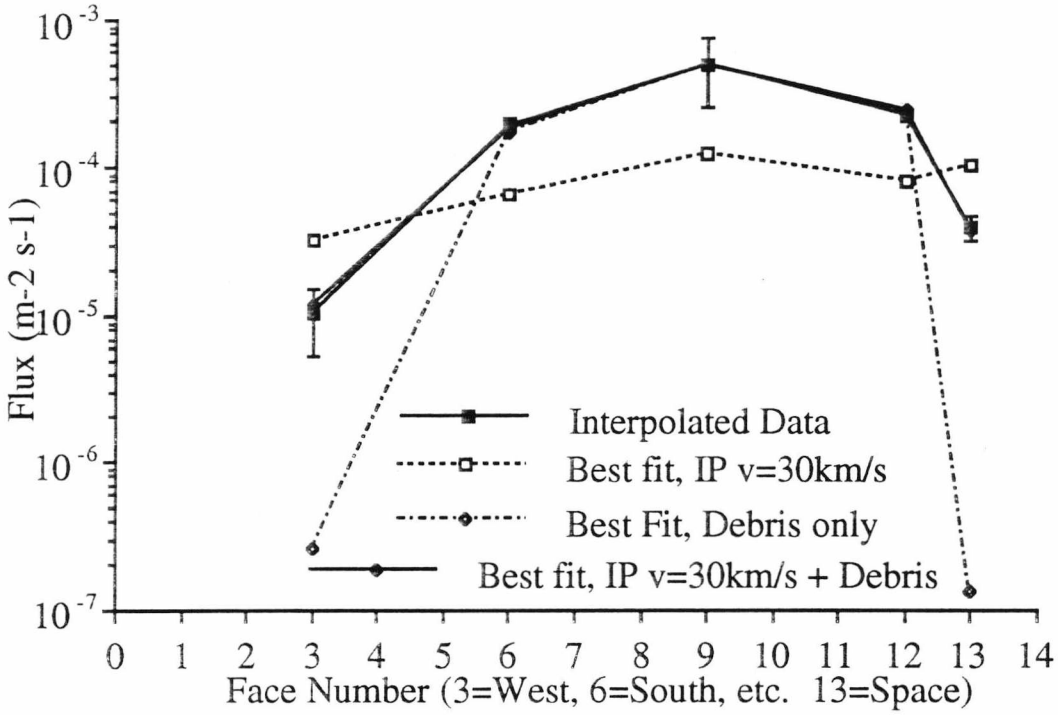

Figure 5.19. Best fit flux levels (m^{-2} s^{-1}) at 4 microns using the IP V=30 km s^{-1} single velocity. The scaling factor for the "IPv=30 km s^{-1}" fit is 3.2. The fit is roughly the same shape for the faces on the RAM-end but a poor match elsewhere. The scaling factor for the "Debris only " fit is 13.8. Again the shape is a good match on the RAM-end but not so good elsewhere. For the combination fit the IP coefficient is 1.2 and the debris 12.4. The combination fit this time almost identical to the shape of the LDEF data. Note that it again lies inside the error bars at all points, however since the combination fit with the original debris distribution was within the error bars this cannot be considered to be a significant improvement. The combination fit predicts still a predominantly debris population in this size regime, although the anti-RAM end and Space face will still be dominated by IP impacts.

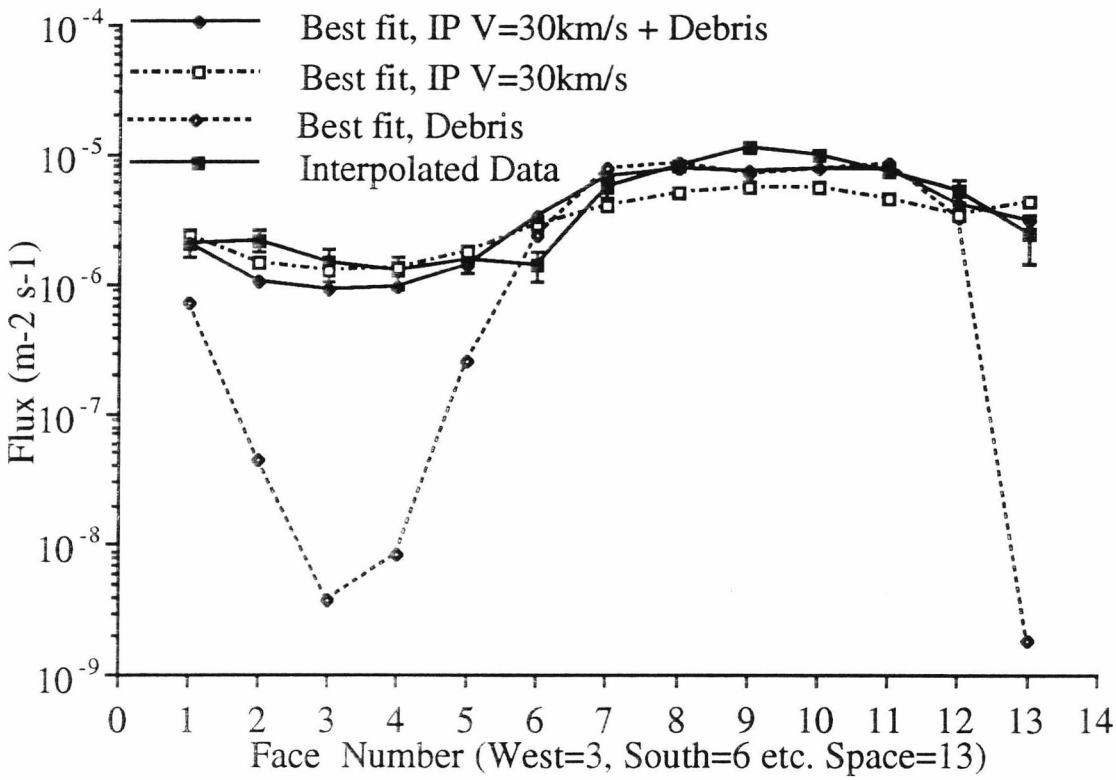

Figure 5.20. Best fit flux levels (m^{-2} s^{-1}) at 40 microns using the IP V=30 km s^{-1} single velocity. The scaling factor for the "IPv=30 km s^{-1}" fit is 1.68. The East to West ratio is much reduced . In fact now the IPv=30 km s^{-1} fit has to small a East/West ratio to account for the LDEF flux on it's own. The scaling factor for the "Debris only " fit is 61.7. This is a fairly good fit on the RAM end but very poor fit on the anti-RAM end, with much too high an East/West ratio. For the combination fit the IPv=30 km s^{-1} coefficient is 1.2 and the debris 31.2. This fit is a vast improvement on the other combination fits . The model still does not exactly match the rather erratic behaviour of the fluxes on the anti-RAM end but is at least much closer than any of the earlier fits.

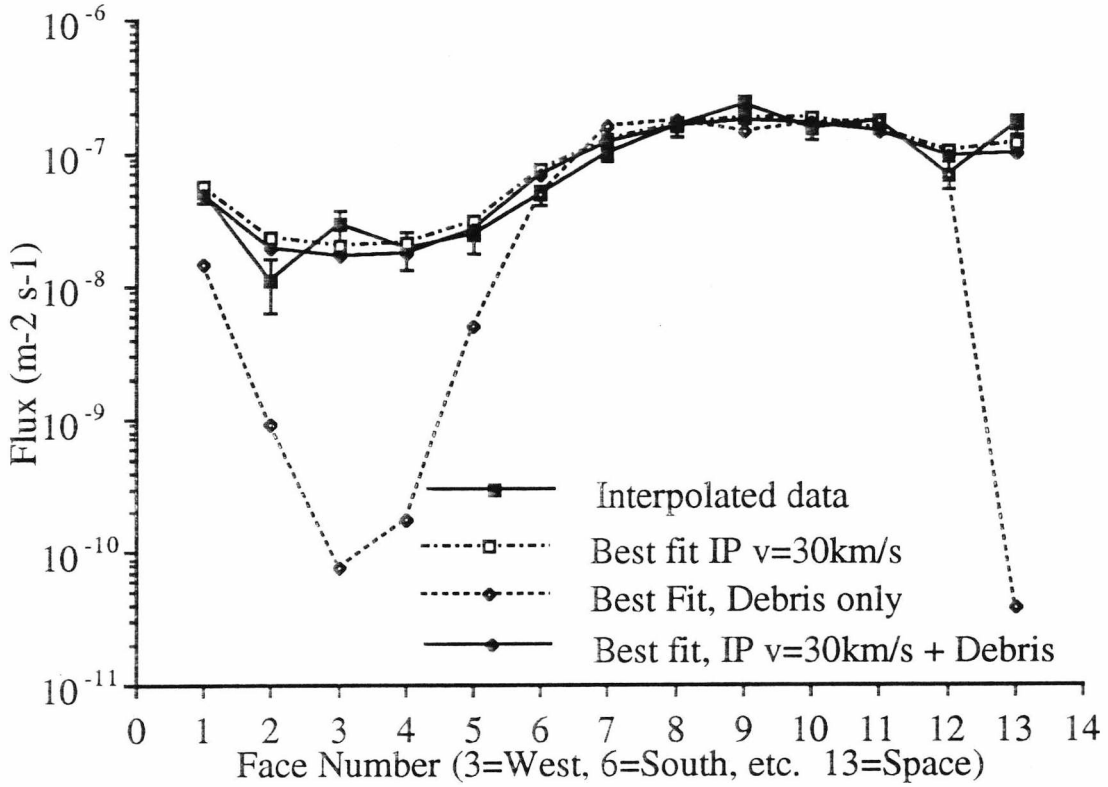

Figure 5.21. Best fit flux levels (m^{-2} s^{-1}) at 400 microns using the IP V=30 km s^{-1} single velocity. The scaling factor for the "IPv=30 km s^{-1}" fit is 6.3. The East to West ratio is much reduced . The scaling factor for the "Debris only " fit is 400.4. This is a fairly good fit on the RAM end but very poor fit on the anti-RAM end, with much too high an East/West ratio. For the combination fit the IPv=30 km s^{-1} coefficient is 5.3 and the debris 47.2. This time the combination fit goes right through the data (although not a perfect match at all points).

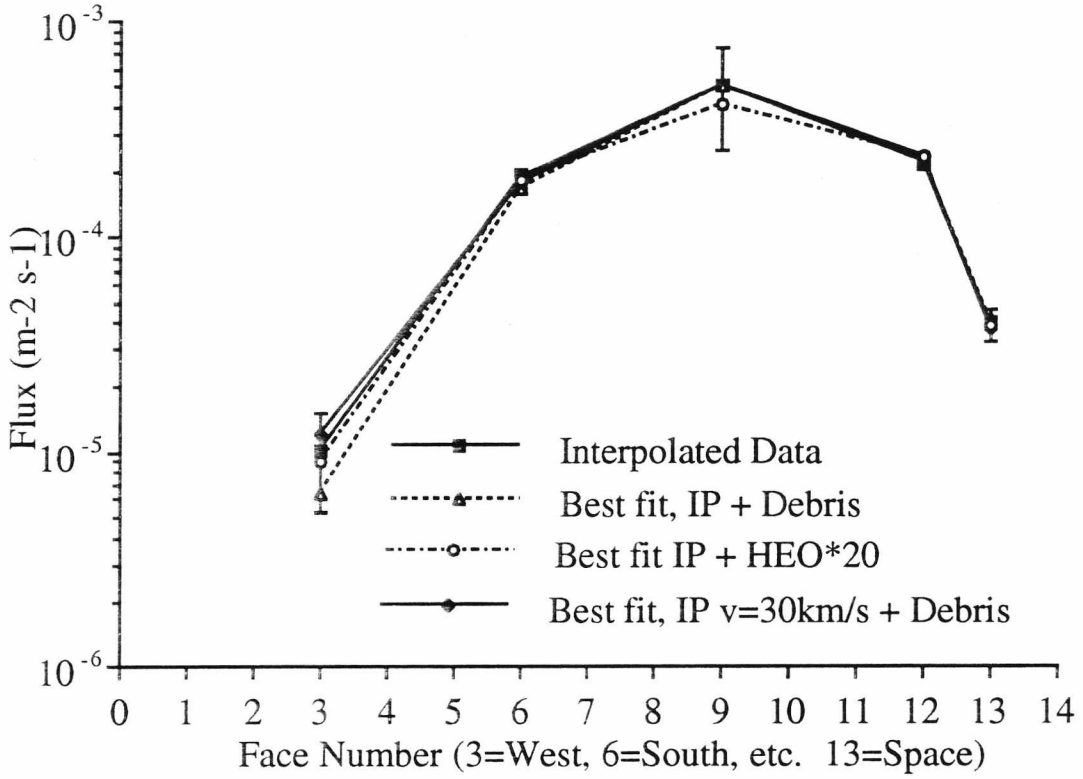

Figure 5.22. Comparison of all the combination best fit flux levels (m^{-2} s^{-1}) at 4 microns. The IP + Debris combination has scaling factors of 2.0 for the IP and 11.9 for the debris. The IP + HEO*20 has scaling factors of 2.0 for the IP and 10.0 for the HEO*20. The IPv=30 km s^{-1} + Debris has scaling factors of 1.2 for the IPv=30 km s^{-1} and 12.4 for the debris. All of the fits shown lie within the error bars of the data so although the IPv=30 km s^{-1}+ Debris is the closest match to the data, none of the fits can be said to be significantly better than the others.

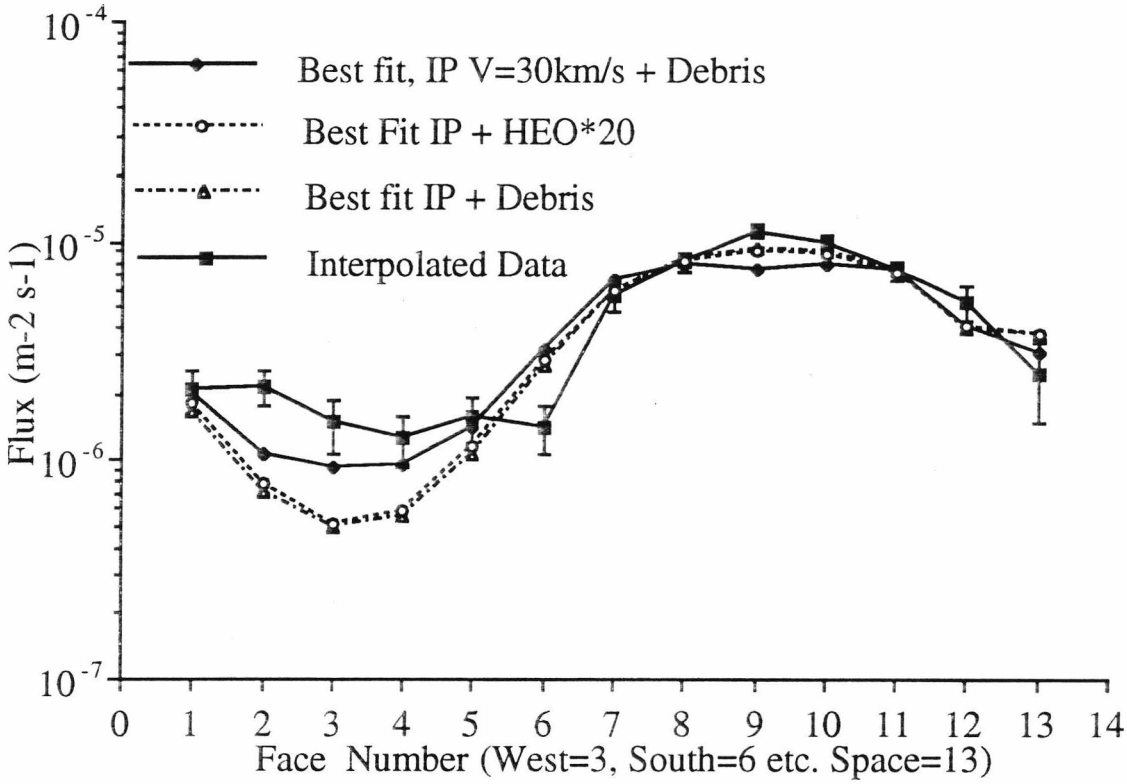

Figure 5.23. Comparison of all the combination best fit flux levels (m^{-2} s^{-1}) at 40 microns. The IP + Debris combination has scaling factors of 2.6 for the IP and 13.9 for the debris. The IP + HEO*20 has scaling factors of 2.6 for the IP and 11.9 for the HEO*20. The IPv=30 km s^{-1} + Debris has scaling factors of 1.2 for the IPv=30 km s^{-1} and 31.2 for the debris. The IPv=30 km s^{-1} + Debris is considerably better than the other two fits. The only place where it seems to be noticeably poorer is on the East face.

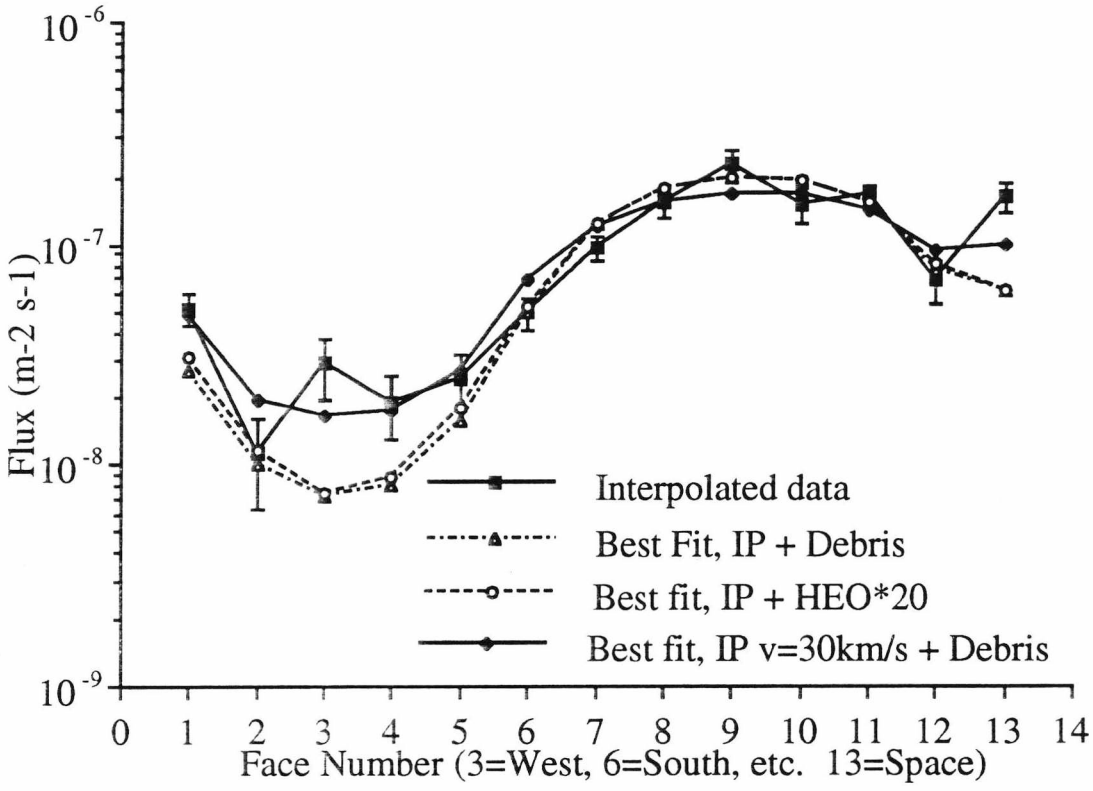

Figure 5.24. Comparison of all the combination best fit flux levels (m^{-2} s^{-1}) at 400 microns. The IP + Debris combination has scaling factors of 15.3 for the IP and 0.01 for the debris. The IP + HEO*20 has scaling factors of 15.2 for the IP and 0.01 for the HEO*20. The IPv=30 km s^{-1} + Debris has scaling factors of 5.3 for the IPv=30 km s^{-1} and 47.2 for the debris. The IPv=30 km s^{-1} + debris is considerably better than the other two fits. The IPv = 30 km s^{-1} scaling factor is considerably less than that required for the other fits.

5.5.1 The 4 micron Regime

At 4 microns the best fit for the IP V = 30 km s^{-1} + Debris is once more no worse (or better) than the original fit (in fact the West face is once more a slightly closer to the data but since the original data was inside the error bar this is not considered to be an improvement). Note that the scaling factor now required for the IP is 1.2 while the debris factor is not significantly altered.

5.5.2 The 40 micron Regime

At 40 microns the fit to the anti-RAM end of the spacecraft is considerably improved (though it still cannot match the erratic shape of the curve). Once more the IP scaling factor is reduced to 1.2, although this time the debris contribution is increased to 31.2.

If we assume that the IP contribution to the 40 micron flux represented by the IP v = 30 km s^{-1} only fit (including the scaling factor of 1.68) and that the excess is caused by debris (i.e.. in the case of the West face this may be caused by a localised event in this size regime). Then the results are shown in Table 5.5 .

A similar calculation is shown using the results with the original Erickson velocity distribution in Table 5.4.

Using the v=30 km s^{-1} single velocity, the debris contribution on the West face would be approximately 12.2 % of the total flux. This is much closer to the value of 12.8% found by the CME experiment than the original velocity

distribution gave us (applying the same reasoning on the original velocity distribution gives a debris proportion of approximately 60%).

Looking at the CME data in an equivalent size regime on the East face (this converts simply by $D_C = F_{max}/0.68$ since the East face targets are Aluminium), we find that 20% of the craters are caused by debris 38% are caused by natural impacts and 42% are of unknown origins. This size regime contains only about 1/4 of the data for the East Face but these percentages are reasonably consistent over the whole data set. This East face data shows no significant deviation from predictions made using the original velocity distribution.(see table 5.4).

In the case of the East face, debris impacts may have quite high velocities. Therefore a larger proportion of the craters of unknown origin are likely to be caused by debris than on the West face. As a result the actual debris contribution may be considerably higher than 20% (assuming half the unknown impacts on the East face were debris would give us a debris proportion of 41%) . So although not as close a fit is found here the prediction is not as inconsistent as it first appears and may in fact be a better estimate of the true situation than the 20% prediction using the original velocity distribution.

5.5.3 The 400 micron Regime

At 400 microns the fit is once more greatly improved. This time the IP scaling factor is still substantial, 5.3, although this is more than a 50 % reduction. The debris factor is still very high , 47.2, but it is worth noting that the IP v=30 km s^{-1} only fit only differs very slightly from the combined fit, suggesting that reducing the debris scaling factor would hardly be significant.

Table 5.4 A calculation of the percentage debris on the East and West faces assuming that the IP contribution is represented by the "IP only" fit .

	West Face	East Face
LDEF flux	1.48 e-06	1.12 e-05
IP (Erickson) (*3.00)	5.80 e-07	8.90 e-06
Remainder (= debris)	0.90 e-06	2.3 e-06
Percentage (debris)	60.1%	20.5%

Table 5.5 A calculation of the percentage debris on the East and West faces assuming that the IP contribution is represented by the "IPv=30 km s^{-1}" fit .

	West Face	East Face
LDEF flux	1.48 e-06	1.12 e-05
IP v=30 km s-1 (*1.68)	1.30 e-06	5.61 e-06
Remainder (= debris)	0.18 e-06	5.59 e-06
Percentage (debris)	12.2%	50%

5.5.4 General Points

The true situation would of course not be a single particle velocity. The modelling does however suggest that a velocity distribution with a bias towards higher velocities than represented by the Erickson velocity distribution, would be more representative for the size regime considered here.

5.6 Conclusions

From considering the shape of the Flux versus Face curves alone there appears to be very little evidence supporting the excess HEO's hypothesis.

At 4 and 400 microns the existing models can account for the shape of the curves fairly well. However there is a very large disparity in the IP scaling factors required to achieve these fits.

In the 40 micron regime (the same regime as the bulk of the CME data) there seems to be evidence of an additional source of impacts on the anti-ram end of the spacecraft but this shape is not satisfied by the HEO*20 enhanced DISCOS data set.

There is evidence to support the hypothesis of a velocity distribution with a higher average velocity than Erickson's for these smaller particles. This does not, however, account for the irregular shape of the distribution found on the anti-RAM end of the spacecraft in this size regime.

In general a velocity distribution with a bias towards higher velocities would also bring the scaling factors required more into line with each other. Although the 400 micron regime still requires a substantially higher factor than the smaller sizes.

Chapter 6

Elliptical Craters

6.1 Introduction

LDEF was essentially a series of flat plate detectors in a gravity gradient stabilised orbit. As a result of this, although LDEF offers us an immense amount of impact data, simple hole or crater counts will only restrict impact directions to a solid angle of 2π steradians. If a means could be found of further deconvloving impact angles of individual craters then this could be used in conjunction with modelling to further tie down the distributions of natural and man-made particles.

During scanning of LDEF surfaces a number of non-circular craters were noticed . It is known that low velocity impacts at large angles of incidence relative to the normal to the surface produce craters which are elongated along the direction of impact with a characteristic shape. It was hypothesised that this might be a source from which some directional information, about individual impacts, could be gleaned.

6.2 Crater Morphology

A Philips 525M Scanning Electron Microscope was used for scanning LDEF surfaces in order to search for elliptical craters. Images of each impact site were taken from normal to the clamp surface and at $\pm$ 7.5° to the normal. The two off axis images were then examined using a stereo viewer, enabling positive identification of true hypervelocity impact sites.

The stereo reconstruction's of these impacts allowed the depth and the maximum and minimum diameters of each crater to be measured, using the plane of the surface as a reference point. For "elliptical" craters , an estimate

of the direction of impact can also be made using criteria obtained from experimental impact studies at oblique angles. Such impacts form elliptical craters with high raised lips on the side from which the impact occurred (the entrance side) and flattened lips on the exit side. The crater walls are steeper and sometimes undercut on the entrance side. The shape of the crater is not truly elliptical but egg-shaped, being deeper and wider at the entrance side [27,28] (see Figure 2) "Ellipticity" (e) used here is determined from the major and minor axis, a and b

$$e = \left(1 - \frac{b^2}{a^2}\right)^{0.5}$$

Equation 6.1

Craters on LDEF surfaces have been placed in three categories.

"Circular" - Irregularities in the surface and uncertainties in the exact crater edge result in ellipticities smaller than 0.3 being indistinguishable from circular.

"Elliptical" - Craters with morphology characteristics of oblique impacts . The direction of impact can be estimated with an accuracy of approximately 20°.

"Undefined"- Craters with elliptical shapes but unusual morphology. It is not possible to determine which was the entrance or exit side or even if the crater was the result of an oblique impact. Such craters could be produced by low velocity irregularly shaped or heterogeneous particles.

Representative craters are illustrated in Figures 6.1- 6.3.

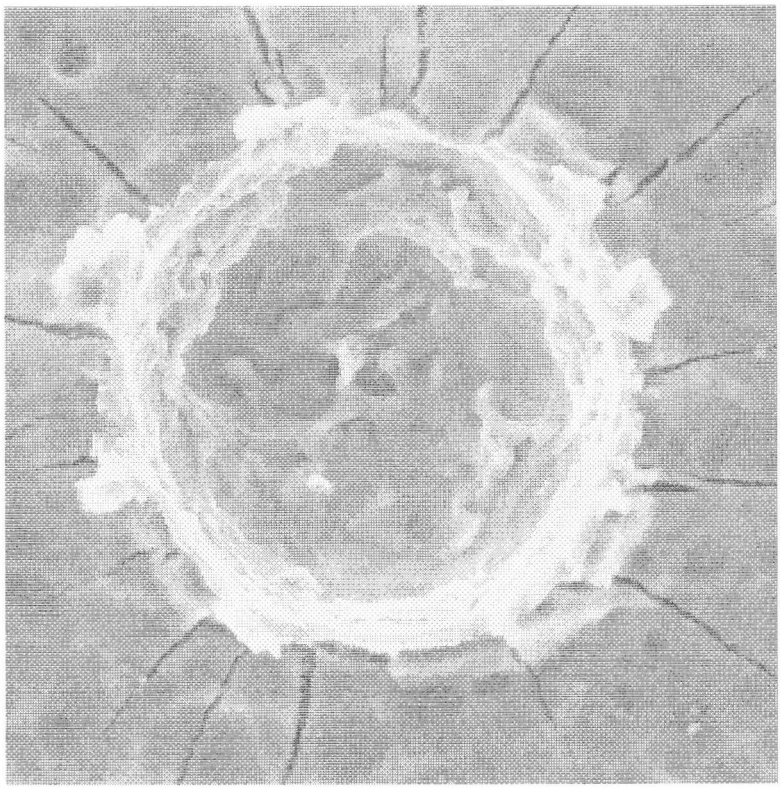

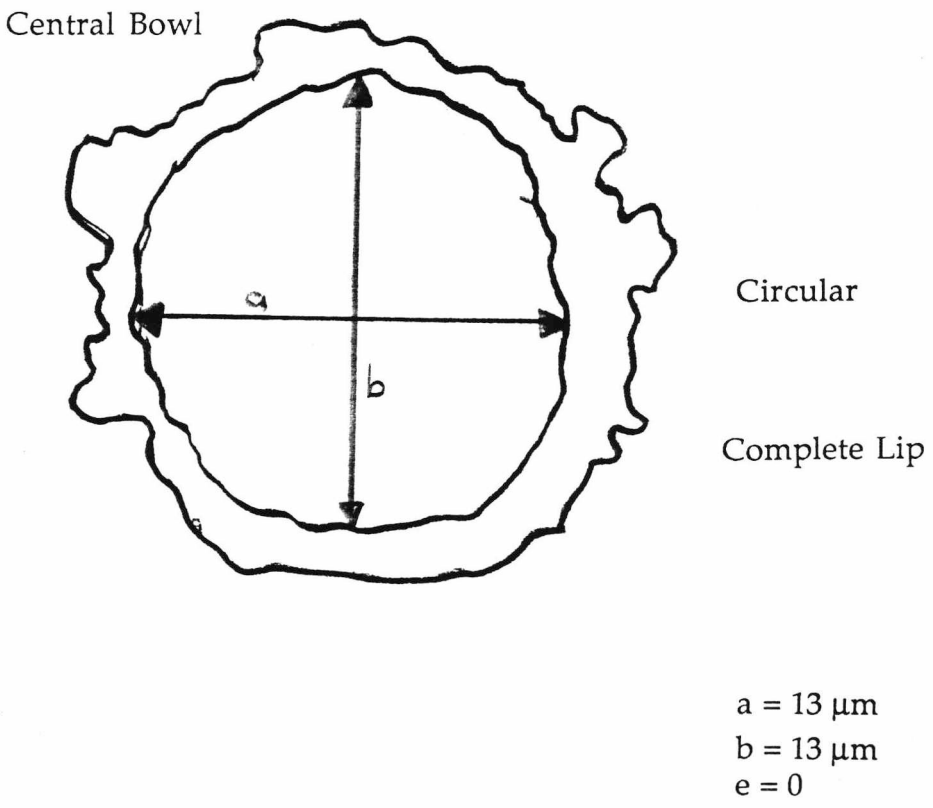

Figure 6.1. A crater classified as "circular" detected on a South face clamp from LDEF.

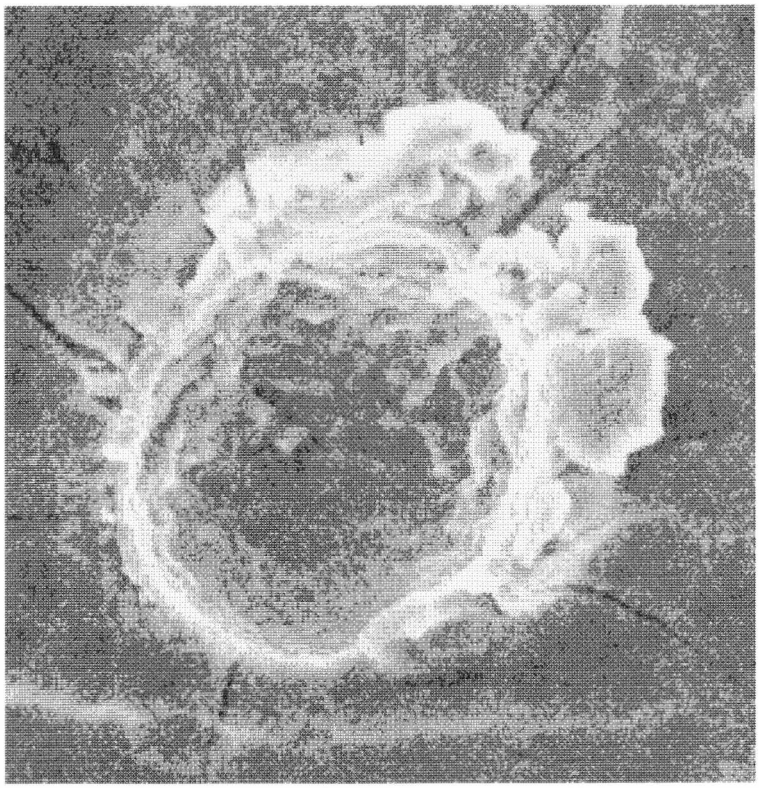

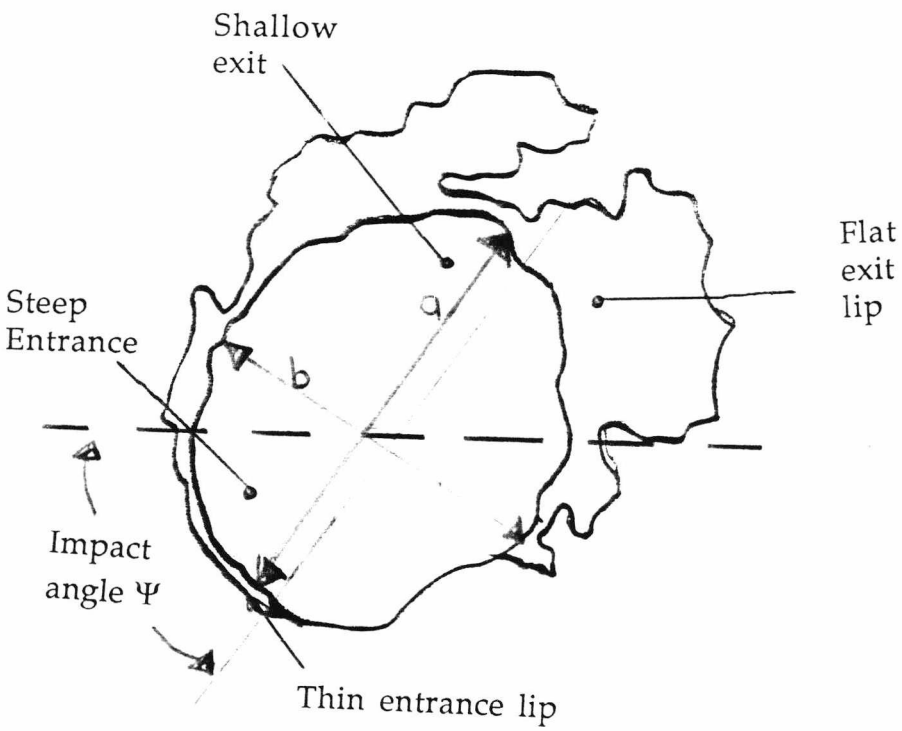

a = 14 μm
b = 11.8 μm
e = 0.54

Figure 6.2. A crater classified as "elliptical detected on a South face clamp from LDEF.

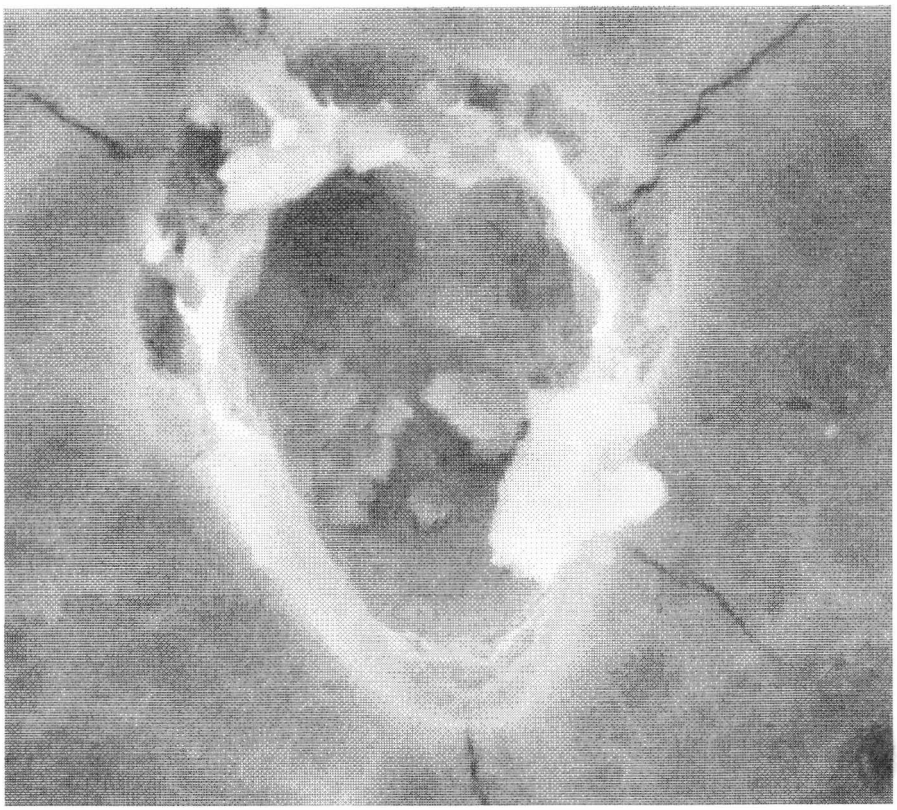

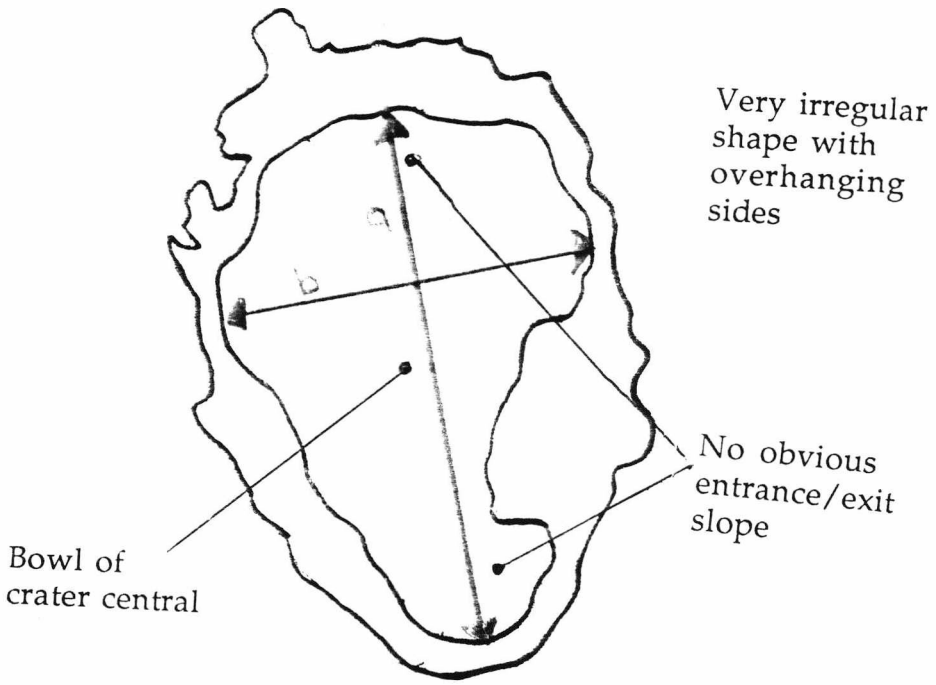

Figure 4.3 A crater classified as "undefined" detected on a South face clamp from LDEF.

6.3 Data Sources

The aluminium clamps (see chapter 2) used to support each experiment tray provide suitable surfaces for study of elliptical craters since they are available for all faces of LDEF. Data presented here is from clamps as listed in table 6.1.

The South clamp with completeness to 4 mm represents the limit of resolution possible on clamp surfaces due to there surface roughness. The technique would be applicable to smaller craters on prepared surfaces such as foils of the Micro-Abrasion Package (MAP).

Table 6.2 contains a summary of the numbers of each categories of craters found for each of the clamps examined.

6.4 Derivation of Impact Angle

Impact experiments into metal[1] indicate that craters are circular for impact angles up to a critical angle, above which they exhibit the properties described above [2]. As the particle velocity is increased, the critical angle increases[29]. For material with no cohesive strength, the critical angle is large (>60 from the normal) and dependant on velocity and physical properties of the target and projectile [30]. These experimental results apply to a range of materials and velocity and impact angle regimes but the relationship between crater ellipticity and such properties is not well quantified. For this analysis a simple relationship between impact angle and ellipticity, independent of

Table 6.1. Details of data sources for LDEF's elliptical craters.

Clamp's Pointing Direction	Area Scanned (cm^2)	Smallest Crater Found (μm)	Completeness Threshold (μm)
South	27	2	4
South	58	4	20
East	58	4	20
East	4.7	2	4
North	58	4	20

Table 4.2. Summary of craters located.

Clamp's Pointing Direction	Circular	Elliptical	Irregular
South	26	31	50
East	35	23	15
North	10	5	3

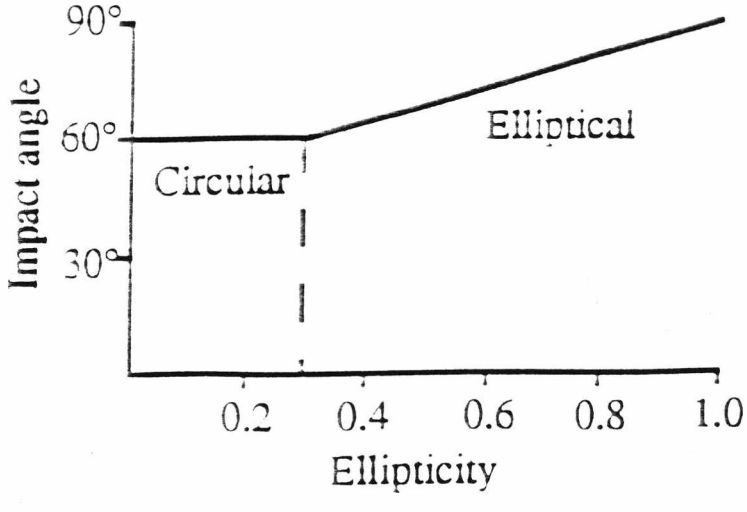

Figure 6.4 Simple Relationship between crater ellipticity and angle of incidence adopted for this analysis.

impact velocity and particle properties was adopted (Figure 6.4). Although this is physically un-realistic , a more sophisticated approach is not yet possible , and trends in the data are still easily identifiable.

Much of the experimental data have been obtained in relatively low velocity regimes which favour non circular crater production, whereas typical velocities in space are considerably larger. However, a significant number of craters on LDEF are non-circular and therefore contain information on the direction of impact. One would intuitively expect space debris impacts, which occur at lower velocities than interplanetary particles, to produce a larger fraction of the elliptical craters than of the total number of impacts.

Figures 6.5 - 6.7 Illustrate the LDEF clamp data analysed so far on a three dimensional diagram representing azimuthal and incidence angles and particle flux.

6.5 Interpretation of Elliptical Crater Data

Figures 6.8 - 6.13 illustrate the data for the models for a number of faces showing impact azimuthal and incidence angle fluxes. The models are calculated for impacts into aluminium with fluxes derived at a crater diameter of 4 microns or larger. For comparisons between the predicted fluxes and the observed crater counts see chapter 5. Despite the uncertainty in the relative numbers of space debris and interplanetary dust demonstrated in chapter 5 the following results are apparent.

6.5.1 South Face

The interplanetary dust impacts (Figure 6.8) are predominantly from the Space and East directions as would be expected from LDEF's orbital motion and Earth shielding. There are significant numbers of highly oblique impacts in this quadrant which may produce elliptical craters despite the high impact velocity.

The space debris model (using the basic dataset as outlined in chapter 4) (Figure 6.9) predicts impacts only from directions close to the East (RAM) direction at angles of incidence ranging from near normal to near grazing. The lower velocity of space debris implies a possible source of elliptical craters in the East direction.

The measured South face data (Figure 6.5) show a concentration in the East direction as would be expected for debris, but also a large number striking from the Earth direction.

Neither of the models predict impacts from the Earth direction and the analysis of debris orbits performed in chapter 4 does not produce any candidate orbits. This, again, is evidence of a source of impacts on LDEF not accounted for by any of the models (possibly a localised event, see chapter 5).

6.5.2 North Face

The interplanetary dust impacts (Figure 6.10) are again predominantly from the Space and East directions. As with the South face, there are significant numbers of highly oblique impacts in this quadrant which may produce elliptical craters despite the high impact velocity.

The space debris model (Figure 6.11) predicts impacts only from directions close to the East (RAM) direction at angles of incidence ranging from near normal to near grazing. The lower velocity of space debris implies a possible source of elliptical craters in the East direction.

The measured North face data (Figure 6.6) has much lower statistics than the South face but seems to show a concentration of impacts from the Space/East direction. This East component is consistent with the debris model but the overall distribution is consistent with the interplanetary dust predictions.

This time there is no Earth component to the data. This would be consistent with a localised source of impacts on the South face which would be unlikely to impact the North face.

6.5.3 East Face

The interplanetary dust impacts (Figure 6.12) are from almost all possible directions above the North/South line, with a slight bias towards the North. The peak of the data is at an angle of incidence of around 45 with very few grazing impacts.

The space debris model (Figure 6.13) predicts impacts only from directions close to the North South line. The distribution of incidence angles is similar, in this case, to the interplanetary dust but the lower velocity of space debris means it is more likely to result in elliptical craters.

The measured East face data (Figure 6.7) show a concentration above the North/South line as would be expected for debris. Although the impacts are not in as tight a band around the North/South line as the debris model suggests there is a drop in the intensity from the directly Space direction. There are also a few impacts from the Earth direction.

6.5.4 General Points

Analysis such as this can be performed for any or all of LDEF's faces given a sufficiently large sample of impacts. The value of this type of analysis is apparent, however the process would be much more useful if a more accurate relationship between ellipticity of impact crater, angle of incidence, velocity of impact and material properties could be established

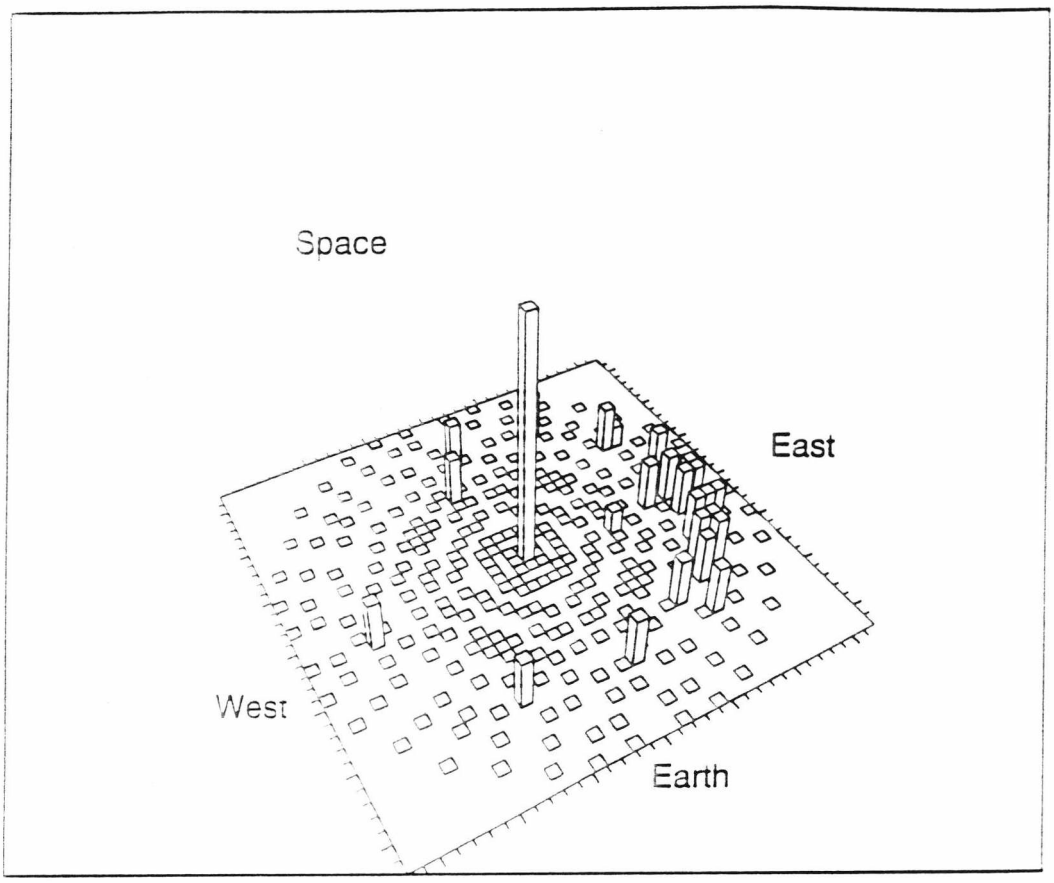

Figure 6.5. Elliptical crater data from an LDEF experimental tray clamp from the South face. Radial distance from the centre of the plot represents impact incidence angle, with the azimuthal directions indicated with respect to other LDEF pointing directions. The height of each column represents the flux. The central peak contains all craters with elliptical characteristics but with ellipticities smaller than the nominal measurable limit of 0.3. These data can be compared with model predictions shown in Figures 6.8 and 6.9.
Note impacts from the Earth direction.
Flux Scale 0 $\rightarrow$ 1045 x 10^{-8} m^{-2} s^{-1}

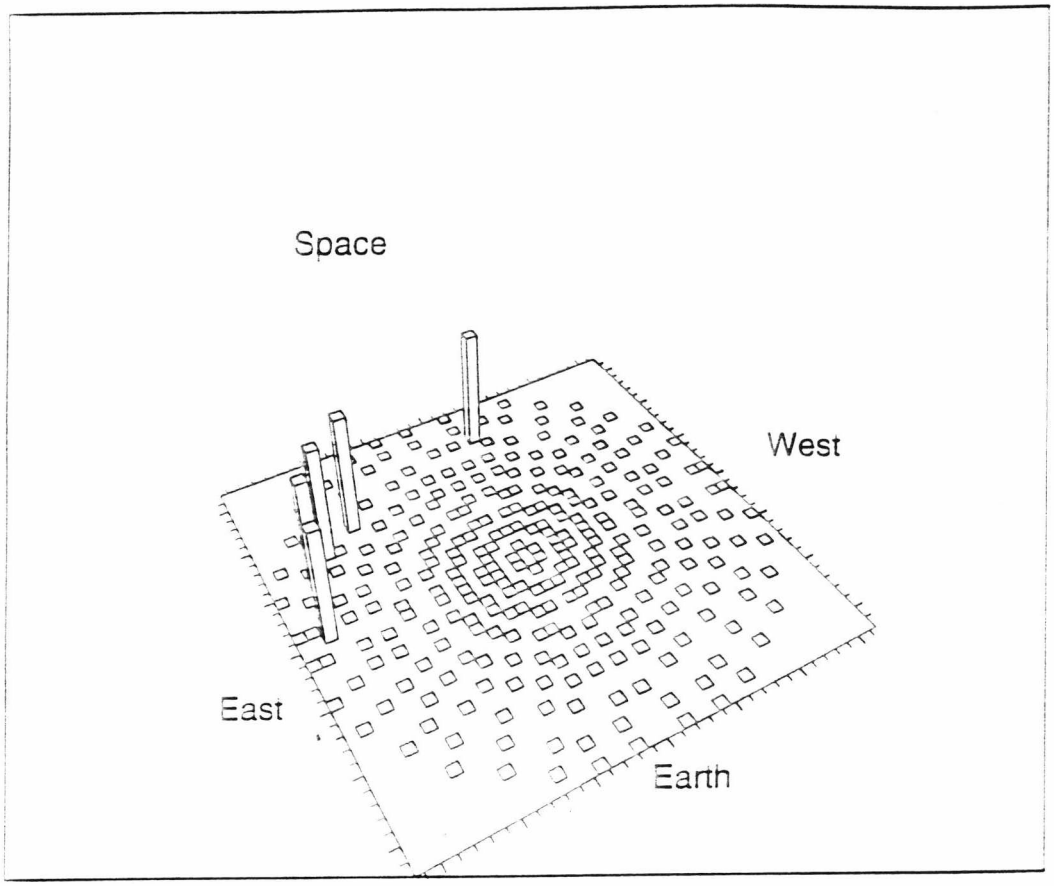

Figure 6.6. Elliptical crater data from an LDEF experimental tray clamp from the North face. Radial distance from the centre of the plot represents impact incidence angle, with the azimuthal directions indicated with respect to other LDEF pointing directions. The height of each column represents the flux. These data can be compared with model predictions shown in Figures 6.10 and 6.11.
Impacts are from the East/Space direction.
Flux Scale 0 $\rightarrow$ 96.4 x 10^{-8} m^{-2} s^{-1}

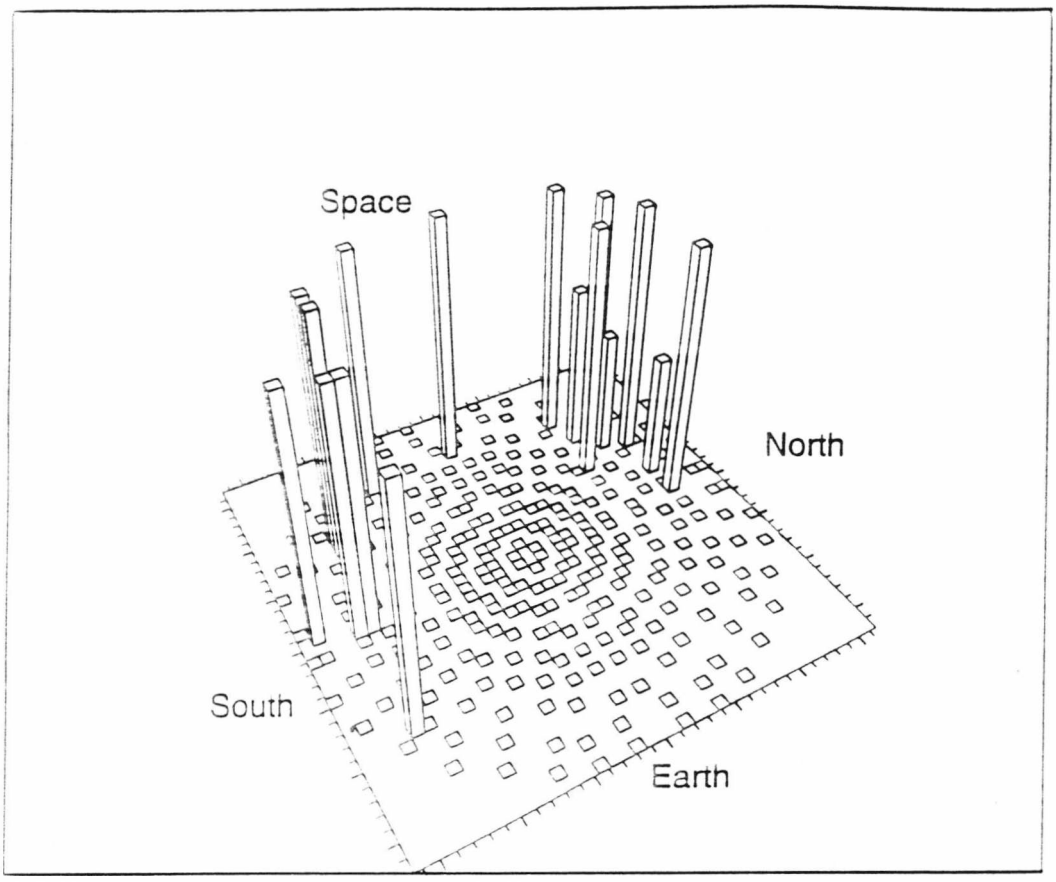

Figure 6.7. Elliptical crater data from an LDEF experimental tray clamp from the East face. Radial distance from the centre of the plot represents impact incidence angle, with the azimuthal directions indicated with respect to other LDEF pointing directions. The height of each column represents the flux. Impacts are coming from the Space/North and Space/South directions, with a few from the Earth directon.

Flux Scale 0 $\rightarrow$ 96.4 x 10^{-8} m^{-2} s^{-1}

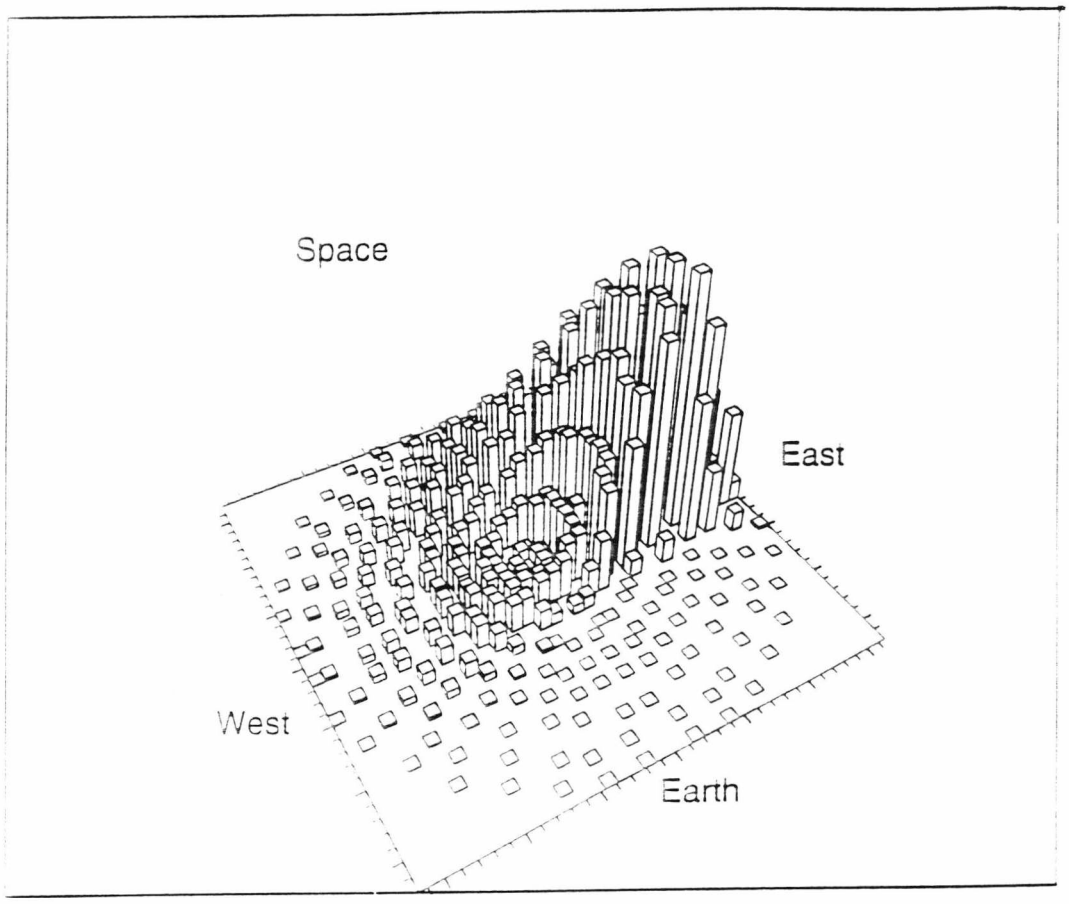

Figure 6.8. Predicted directional flux distribution for interplanetary dust on the South face of LDEF at an F_{max} of 20 μm. Radial distance from the centre of the plot represents impact incidence angle, with azimuthal directions indicated with respect to other LDEF pointing directions. The height of each column represents the flux.
Impacts are from the East and Space direction.
Flux Scale 0 → 1045 x 10^{-8} m^{-2} s^{-1}

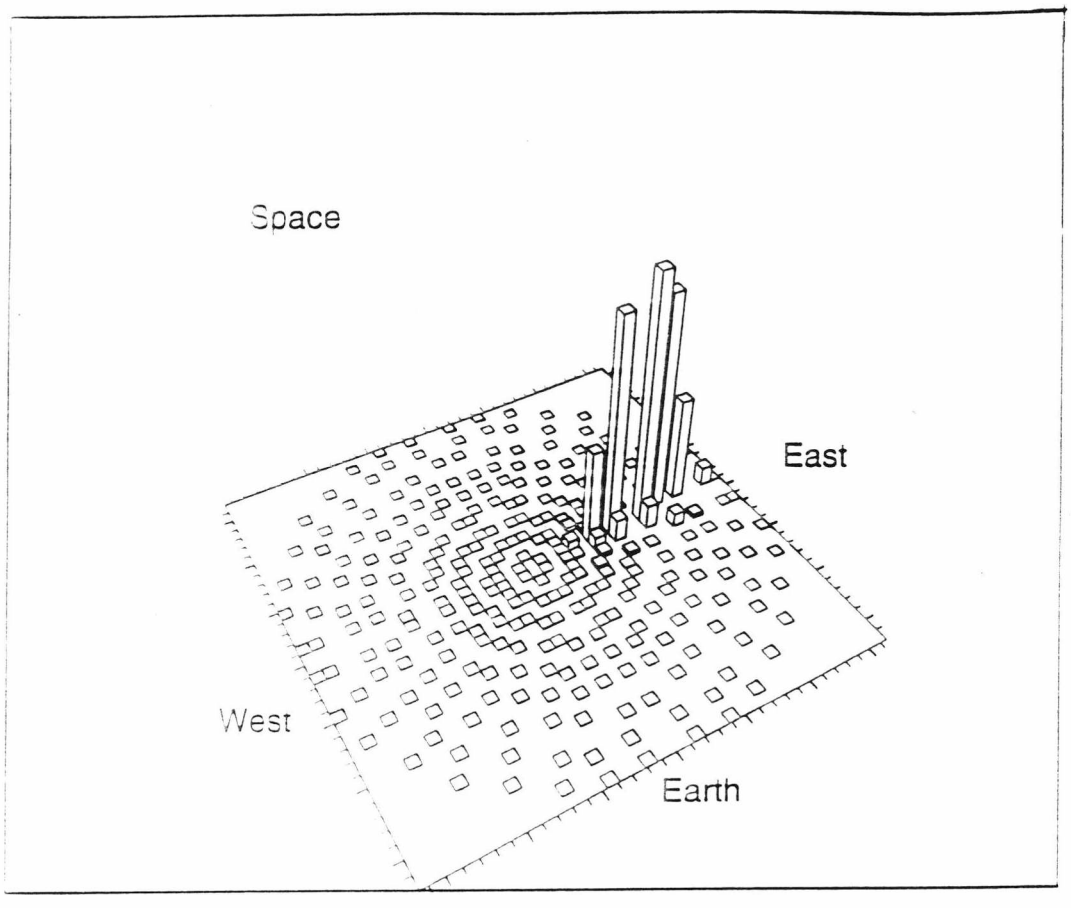

Figure 6.9. Predicted directional flux distribution for space debris on the South face of LDEF at an F_{max} of 20 μm. Radial distance from the centre of the plot represents impact incidence angle, with azimuthal directions indicated with respect to other LDEF pointing directions. The height of each column represents the flux.
Impacts are near grazing from the East direction.
Flux Scale 0 → 1150 x 10^{-8} m^{-2} s^{-1}

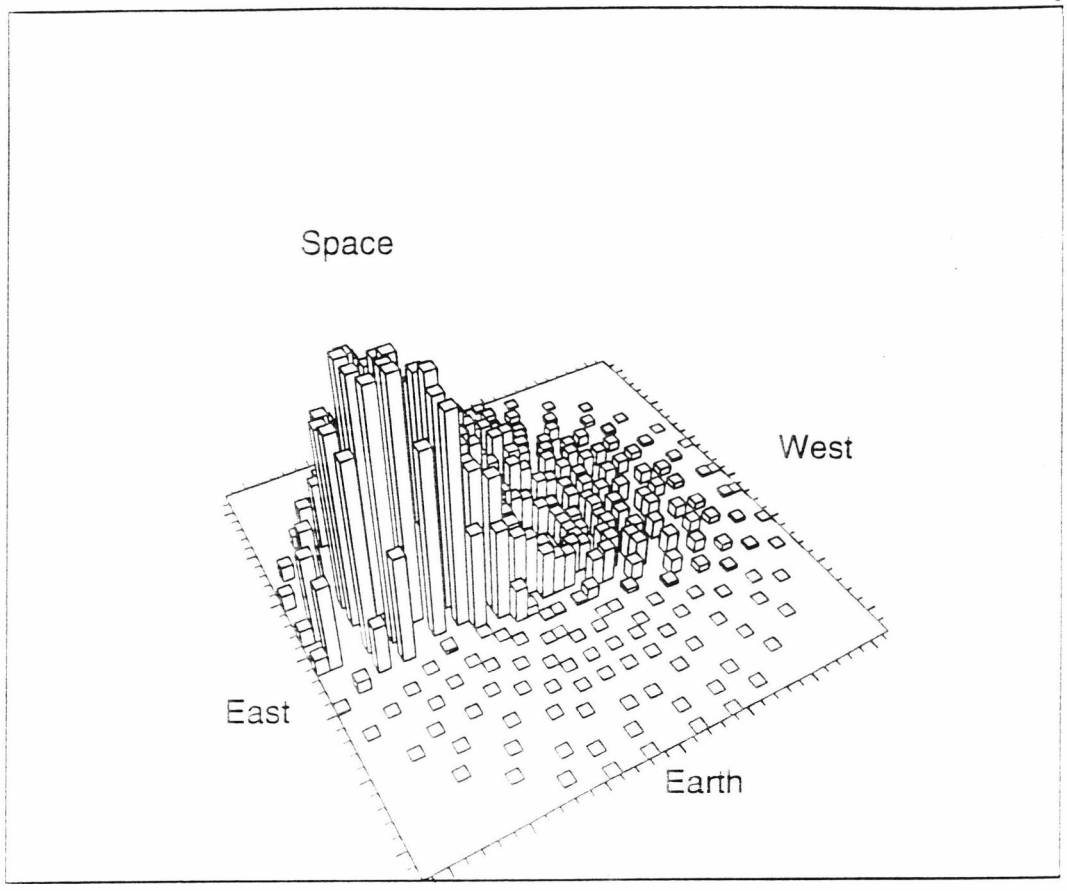

Figure 6.10. Predicted directional flux distribution for interplanetary dust on the North face of LDEF at an F_{max} of 20 μm. Radial distance from the centre of the plot represents impact incidence angle, with azimuthal directions indicated with respect to other LDEF pointing directions. The height of each column represents the flux.
Impacts are from the East and Space direction.
Flux Scale 0 $\rightarrow$ 64 x 10^{-8} m^{-2} s^{-1}

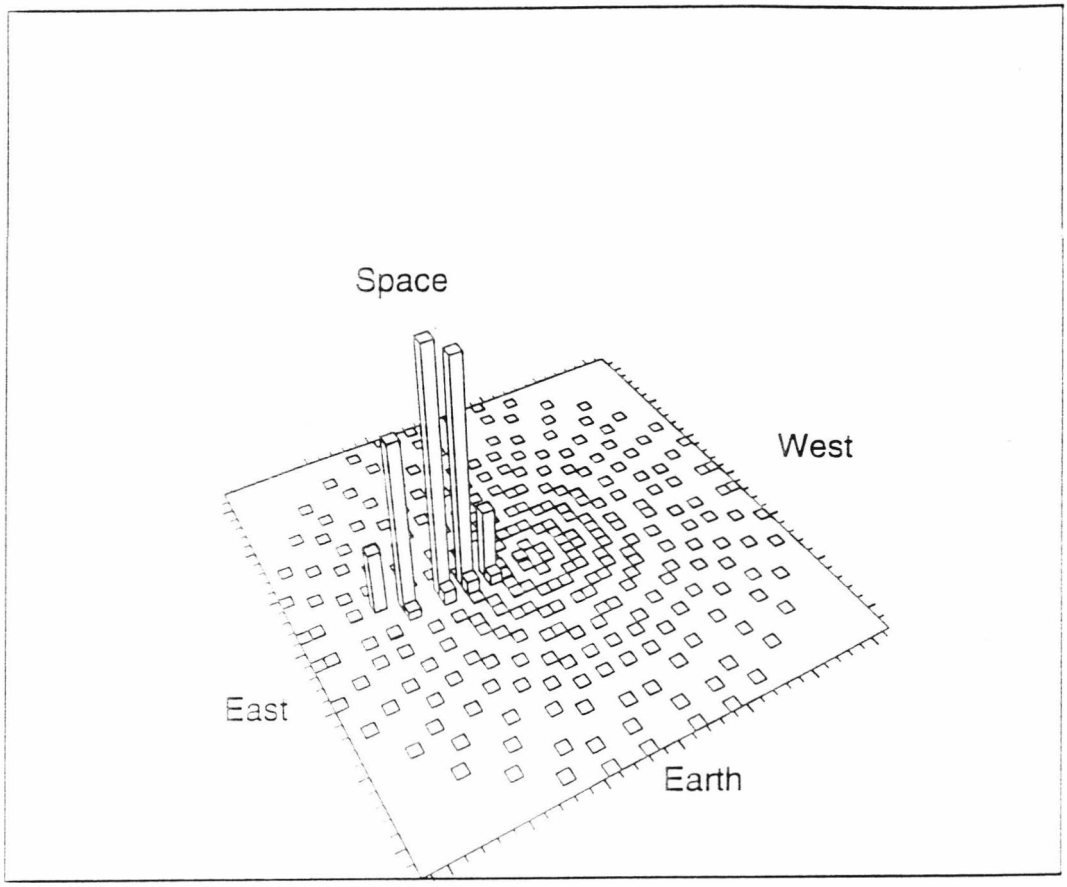

Figure 6.11. Predicted directional flux distribution for space debris on the North face of LDEF at an F_{max} of 20 μm. Radial distance from the centre of the plot represents impact incidence angle, with azimuthal directions indicated with respect to other LDEF pointing directions. The height of each column represents the flux.
Impacts are non-grazing from the East direction.
Flux Scale 0 $\rightarrow$ 3650 x 10^{-8} m^{-2} s^{-1}

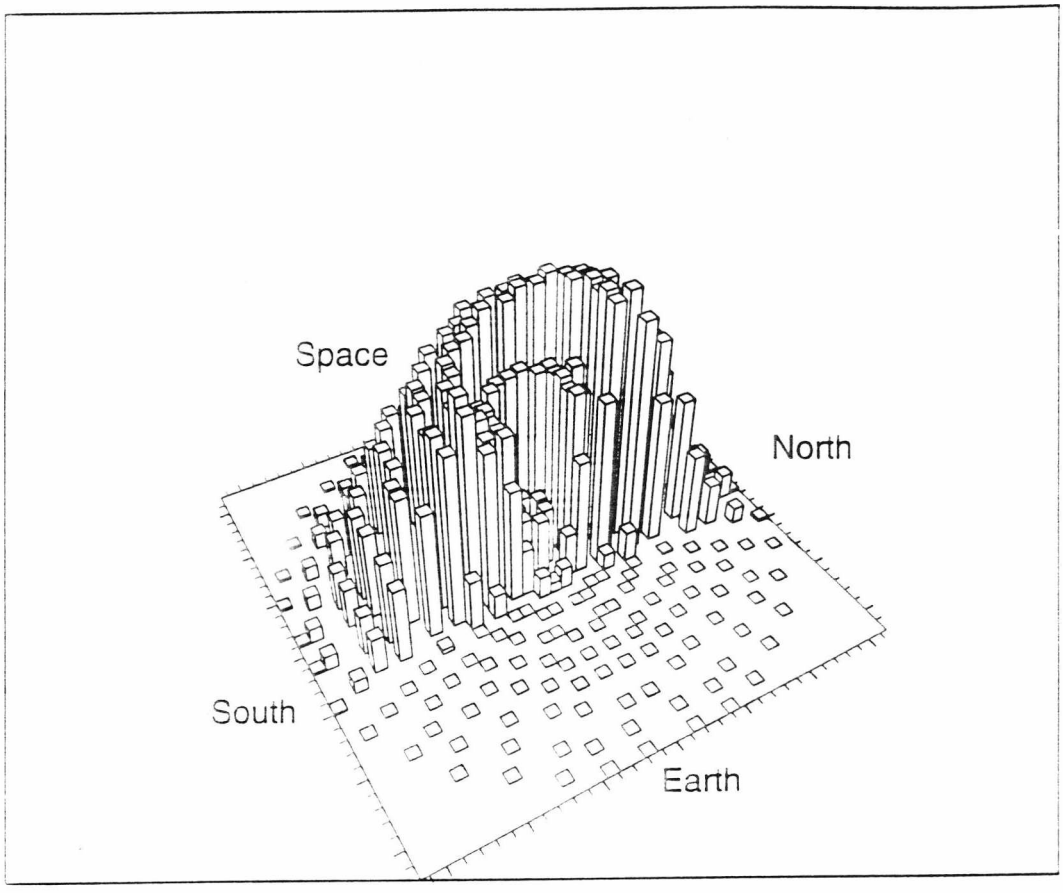

Figure 6.12. Predicted directional flux distribution for interplanetary dust on the East face of LDEF at an F_{max} of 20 μm. Radial distance from the centre of the plot represents impact incidence angle, with azimuthal directions indicated with respect to other LDEF pointing directions. The height of each column represents the flux.
Impacts are from the above the East/West line.
Flux Scale 0 $\rightarrow$ 86 x 10^{-8} m^{-2} s^{-1}

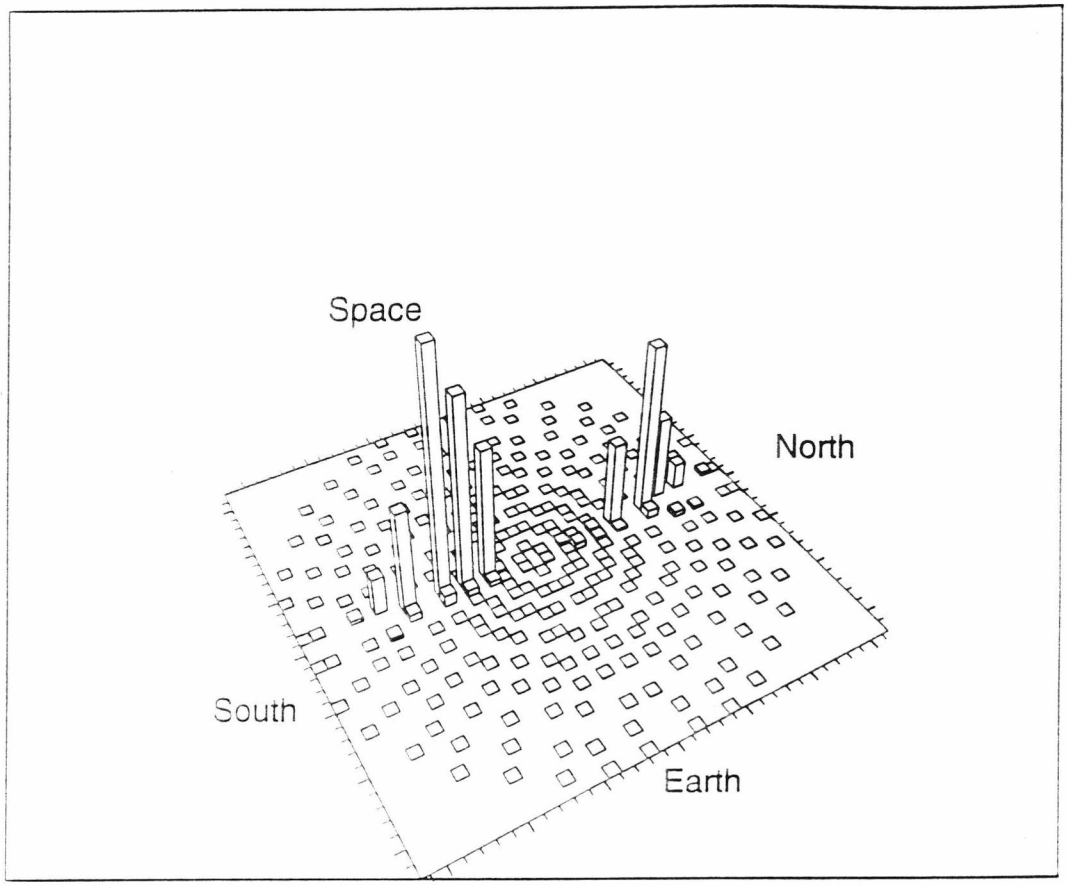

Figure 6.13. Predicted directional flux distribution for space debris on the East face of LDEF at an F_{max} of 20 μm. Radial distance from the centre of the plot represents impact incidence angle, with azimuthal directions indicated with respect to other LDEF pointing directions. The height of each column represents the flux.
Impacts are non-grazing along the North/South line.
Flux Scale 0 $\rightarrow$ 3310 x 10^{-8} m^{-2} s^{-1}

Chapter 7

The Experimental Program

7.1 The Light Gas Gun

7.1.1 Theory

There is a theoretical limit to the velocities which can be realised by using rifle powder alone as a means of accelerating projectiles. This velocity is defined by the mean velocity of the molecules in the exploding powder. The upper limit for this velocity can be calculated using Equation 7.1.

$$E\,M = E_m = 0.5\,M\,v^2 \qquad \text{Equation 7.1}$$

Where

E is the energy per unit mass of the rifle powder

M is the molecular mass of the gas produced

E_m is the energy per molecule of the gas

and v is the velocity of the gas

Even assuming that pure nitro-glycerine (rifle powder is a mixture of this and lower energy explosives) is used in the explosive and that no energy is lost, the upper limit on the velocity of the gas thus calculated is 3.5 km s^{-1}, in reality the actual velocity is likely to be considerably lower than this. In order to achieve higher velocities another mechanism must be used.

The UKC Light Gas Gun is a two stage accelerator which utilises rifle powder in the first stage and Hydrogen gas in the second.

Rifle powder, held in a shotgun cartridge is used in order to accelerate a piston, along a pump tube (see Figure 7.1) full of hydrogen, (initially at a pressure of 45 bars) to a velocity of about 1.3 km s^{-1}. This in turn causes an

adiabatic compression of the hydrogen, which due to it's much lighter molecular mass, can achieve velocities of around 5 km s^{-1}, at 2000K (or higher velocities at higher temperatures).

When a critical hydrogen pressure is reached, a small aluminium disc (or diaphragm) ruptures, upon the other side of which is the sabot (either solid or containing a projectile). The second stage of the accelerator utilises the explosive expansion of the hydrogen gas to accelerate the sabot along the launch tube to velocities of as much as 6 km s^{-1}.

If the sabot is not solid, (i.e.. it contains a separate projectile) it should be stripped off in the blast tank. The velocity of the projectile can then be measured in the flight chamber before the projectile impacts on the target which can be mounted in either of the target chambers.

7.1.2 Light Gas Gun Development Program

At the start of our experimental program on the Light Gas Gun, the development of the Gun into a fully working tool had not been completed. The Gun's firings were infrequent and the first problem was that more often than not when a shot was attempted there would be several misfires before a successful shot.

The second problem was with the pump tube and central breech, (see Figure 7.2) as a result of the use of leaded pistons, both the Central breech and the end of the pump tube were gradually being stretched which would result in reduced performance as hydrogen gas could escape round the piston. Also this would weaken both the components gradually rendering them unsafe for use and therefore necessitating their costly replacement.

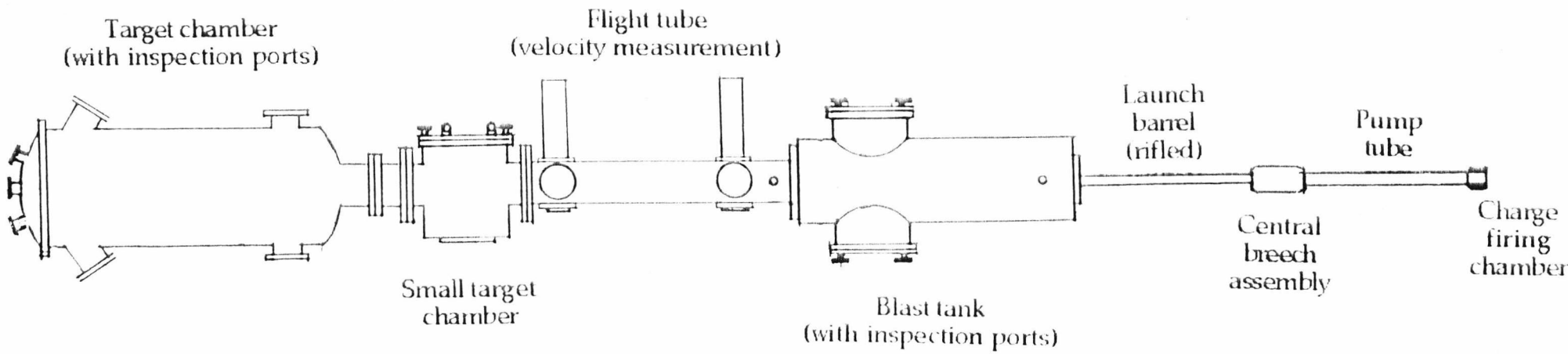

Figure 7.1. The Light Gas Gun

Further to this the piston would extrude down the launch tube and frequently sheer off at high velocity, follow the projectile along it's path and impact the target after the projectile disrupting experimental results. Also the leaded piston was a very 'dirty' technique causing the interior of the pump tube and the central breech to become coated in lead which had to be removed before the next shot could be fired. This was a time consuming process which in the case of the central breech this involved drilling out the area filled with lead.

The next problem was with the use of split sabots. These were intended to separate due to the rotation caused by the rifling of the launch tube, fly off axis and impact on the stop plate while the projectile passed through the hole in the middle and impacted on the target (Figure 7.3). However the sabot would invariably not split properly and parts of the sabot would pass through the hole following the projectile (as with the piston) and impacting on the target (although the sabot impact was sometimes far enough offset and distinctive enough from the projectile impact that it could be identified).

The final problem was with the velocity measuring system (see Figure 7.4). This very rarely worked and on the occasions when it did trigger, the traces produced on the oscilloscope were often off the scale and indecipherable. This was at the time hypothesised to be caused by the photomultipliers picking up a signal from very fast, glowing hydrogen gas overtaking the sabot in the flight chamber.

The first problem we tackled was that of the misfiring, since experimentation of the other problems required the ability, at the very least to

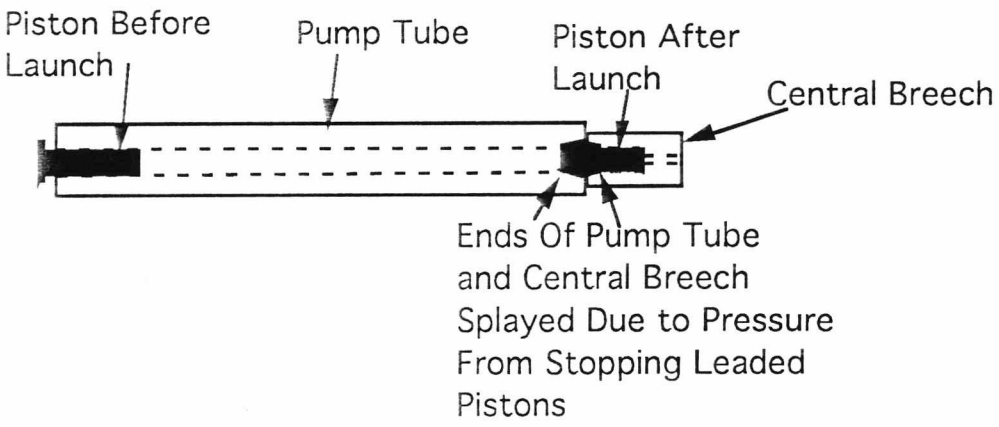

Figure 7.2 The effect of leaded pistons on the Pump Tube and enthral Breech

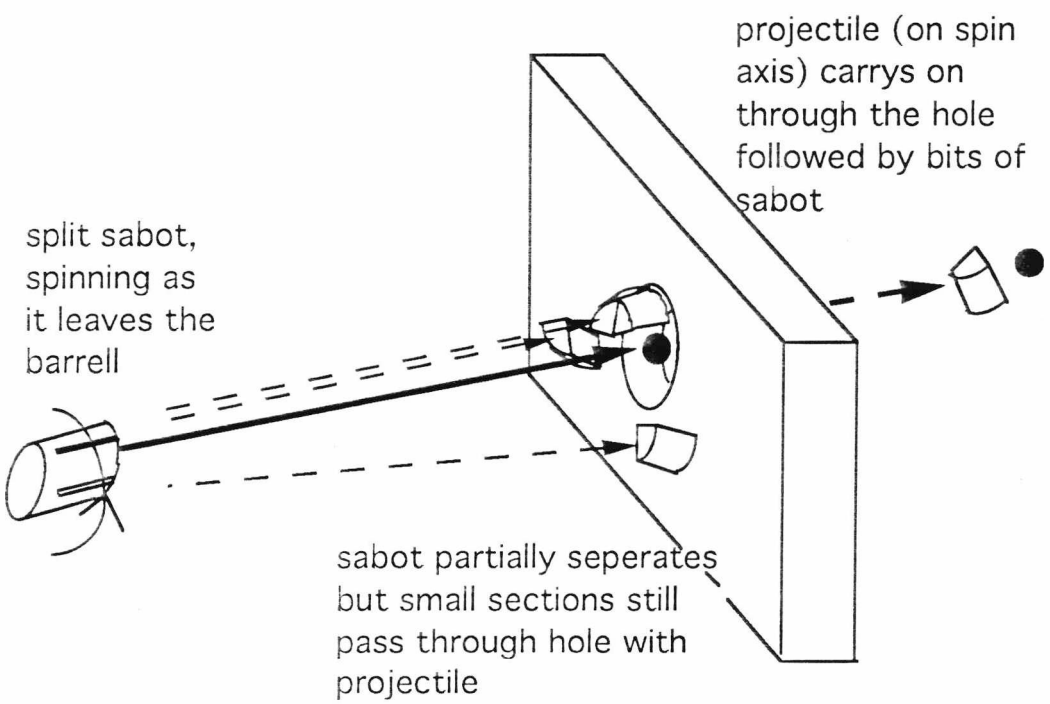

Figure 7.3 The Stop Plate

accelerate the piston. At first we assumed that the consumable which were supplied with the gun (i.e.. the cartridges, primers, rifle powder and wadding) were appropriate for the task in hand. So we investigated with a number of styles of packing the cartridge to find the most effective. The result was an apparent slight improvement in success rate but still not to a satisfactory level. On enquiring after professional advice we discovered that the rifle powder and the primers with which we had been supplied were in fact incompatible. On purchase of the appropriate materials we found we had no further problems with the misfires, a situation which has continued with subsequent purchases of combustibles.

Next we tackled the problem of the piston extrusion. This was simply a case of increasing the initial hydrogen gas progressively over a series of shots until we achieved an initial pressure which slowed down the piston enough before the diaphragm burst. When we started work on the Light Gas Gun the recommended pressure on record was 22 bar, however we found that initial pressures of higher than 40 bar were required to stop the piston. Even this is not effective all the time, probably due to some of the hydrogen gas escaping round the piston as it passes through the broader part of the pump tube (caused by use of leaded pistons as mentioned earlier).

At around the same time we began to investigate the use of solid nylon pistons. Some of these had been made by past researchers but there was no record of them ever having been used. We found that the solid nylon pistons achieved a combination of things. Firstly and most importantly the nylon pistons were light enough that they did not cause the pump tube or the central breech to expand any further than they already had and secondly these turned out to cause far less mess, making it a simple job to remove the piston and clean both the central breech and the pump tube.

Our next task was to try and identify and rectify the problems with the velocity measuring system. The system was set up as shown in Figure 7.4. In theory any object passing through the beams of white light should scatter light to the sides and be picked up by the photomultipliers. The photomultipliers were, however, thought to be false triggering on light emitted by the hydrogen plasma.

The first steps we took was to try to identify the wavelengths of emissions from the plasma (it was expected to be more than just the pure hydrogen emission wavelengths due to the existence of any contaminants in the flight chamber and blast tank). In order to do this we removed one of the photomultipliers and installed a spectrograph in its place. After a series of shots had been fired and we had been unable to detect any emissions whatsoever we concluded that any emissions from the hydrogen plasma were of an order too small to be significantly interfering with the scattered light from the projectile.

At this point we began to look for another source of the problems. On further investigation we discovered that the optics of the system had been incorrectly adjusted and that both the beams of white light were focused out of the plane through which the projectiles were passing. In addition to this, one of the slits was skewed so that it was almost parallel to the line of flight.

Having corrected and cleaned the optics we performed a further series of experiments to test the system. We found that with a solid sabot the system would trigger correctly most of the time (although still not all of the time), but when using a split sabot and smaller projectiles we only very occasionally achieved a successful velocity measurement. However having now established that the velocity appeared to remain fairly consistent (between 4.3 and 4.9 km s-1) as long as we didn't change any of the parameters involved

we began to perform our experimental program while continuing to attempt to improve the velocity measurements.

We at this point considered using a laser instead of a white light source and to detect obscuration from below rather than from side scattered light (this would prevent confusing any emissions from other sources). In addition to this, over a period of time, a detector at the muzzle of the launch tube (again looking for obscuration as the sabot left the tube), then a PZT on the target to detect the impact and finally a PZT on the stop plate to detect the impact of the split sabot when it was used, were tested (Figure 7.5). To date the system used is

For a solid sabot

1) Laser system looking for obscuration of a photodiode
2) White light source looking for obscuration on a photodiode
(these systems are being compared for efficiency and when we have established which is the best be will convert the other to match
3) A PZT on the target to detect the impact

Any two of the above triggering will give us a velocity measurement. Usually all three trigger, giving us a corroborative measurement.

For a split sabot

1) PZT on the stop plate to detect sabot impact
2) Laser system
3) White light system
4) PZT on the target

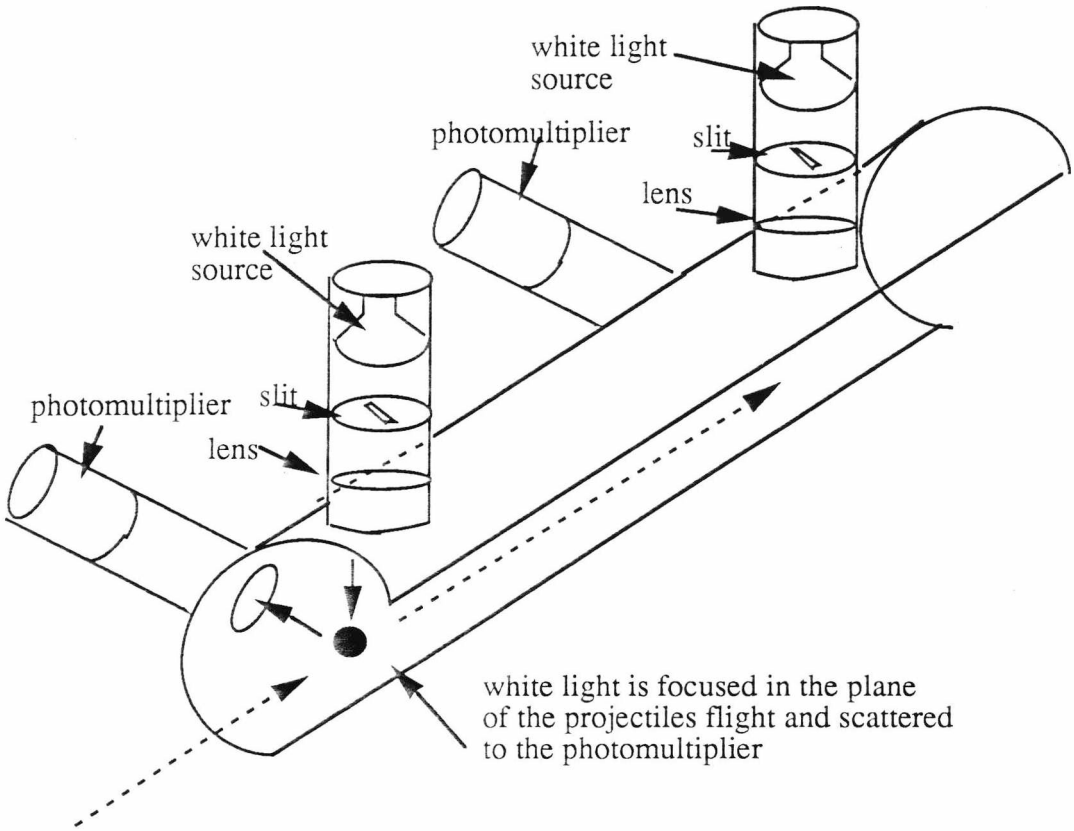

Figure 7.4 The original velocity measuring system

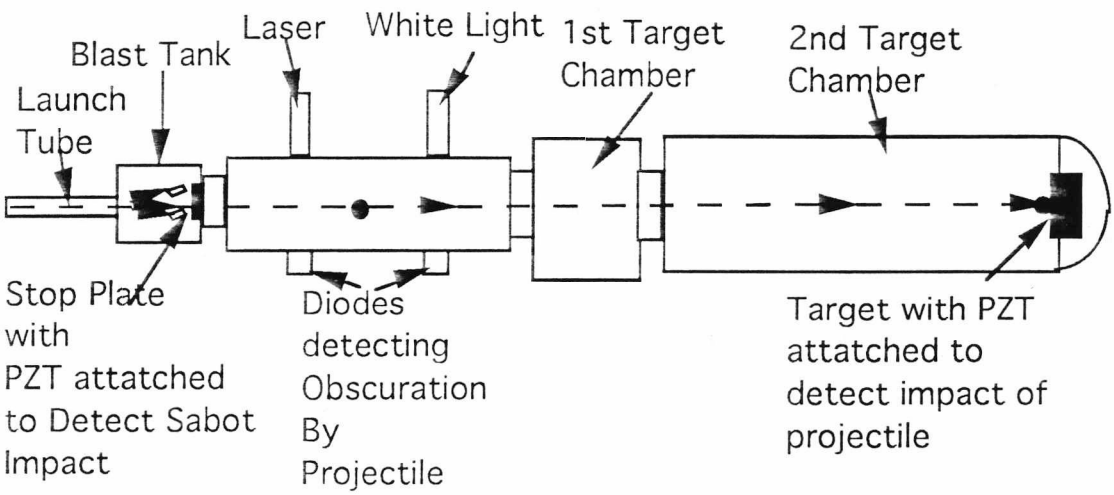

Figure 7.5 The existing velocity measuring system

In this case the two PZTs trigger very reliably and sometimes, with the larger projectiles we can get readings from the two light systems to give us a corroborative measurement.

The final problem of the split sabots was again tackled over an extended period of time. The initial design (Figure 7.6) of split sabot which was already in existence was of a sabot which had four cuts down it's length but was still joined at the end. The rifling in the barrel was meant to cause the sabot to be spinning fast enough when it left the barrel that the sabot would split in flight due to the centripetal force and impact the stop plate allowing the projectile (who's centre of mass would be on the axis of rotation) to pass through the hole in the middle and reach the target.

This was partially successful but most of the time parts of the sabot would also pass through the hole and impact the target. While mostly such sabot impacts were distinct and easily distinguishable from projectiles, such a situation was obviously not ideal. Several alterations were made to the sabot design in an attempt to overcome this problem by harnessing the hydrogen gas pressure to force the sabot quadrants further off axis, these were however all unsuccessful.

Advice was sought from other Light Gas Gun researchers and as a result of a visit to the Light Gas Gun facility at the Johnson Space Centre a quantity of sabot material as shown in Figure 7.6 was acquired. These sabots come in four complete parts and can be assembled, tooled to the appropriate size and then have the required size of hole drilled in them. This sabot design has been highly successful, the sabot parts splitting sufficiently in flight that they do not pass through the hole in the stop plate. As a result this is the design of split sabot which has been permanently adopted.

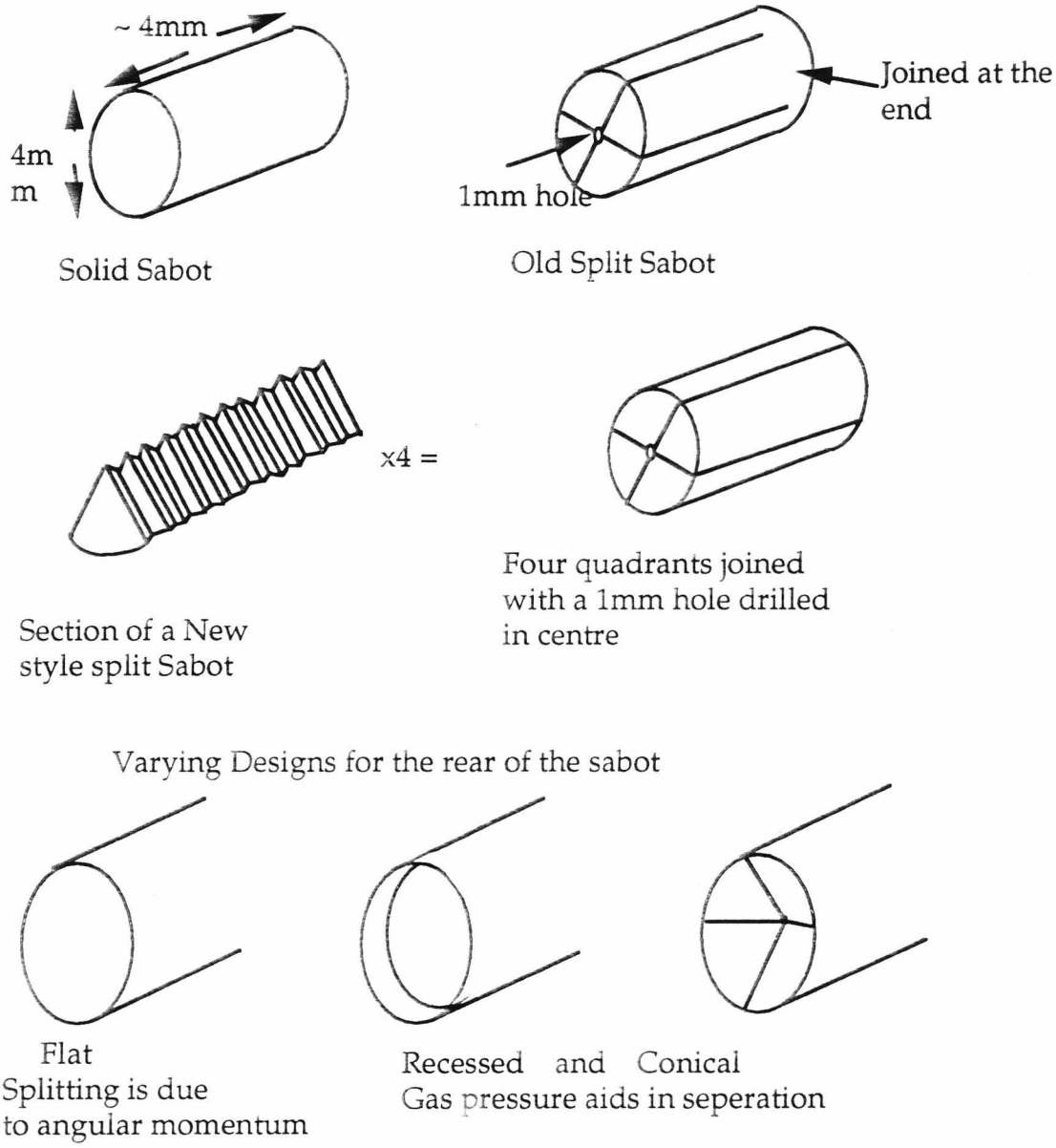

Figure 7.6 A Variety of Sabot Designs

7.2 Experimental Program

During analysis of LDEF surfaces, a large number of elliptical craters were observed. These have been interpreted as due to impacts from interplanetary dust or space debris at highly oblique angles[31,32] although it has been suggested that they were caused by irregularly shaped impactors. If the former interpretation is valid then these impact sites provide an invaluable diagnostic tool for determination of impact directions and hence orbital distribution of space debris particles impacting LDEF surfaces.

A series of experiments have been performed in order to investigate the relationship between impact parameters and crater morphology. If a relationship of this nature can be established, it will be possible to use this to help deconvolve the dust/debris environment.
Previous experiments which have been performed by other researchers have included

1) Oblique impacts into rock and rock dust
2) Oblique impacts into glass
3) Oblique impacts into lead
4) Oblique impacts into bumper shields

Most of the experiments into semi-infinite targets were investigating factors such as depth to diameter ratios or volume of the crater excavated, although the bumper shield studies did include hole shapes and angles. The majority of space exposed surfaces suitable for dust particle impact studies are effectively smooth metal semi-infinite or foil targets. We are therefore investigating the effects of impactors of known speed direction and composition onto such targets.

7.2.1 Experiments on The Light Gas Gun

In this case steel ball bearings of 400 μm (AISI420C) and 1 mm diameter were used as projectiles. These were fired at a series of discrete angled (55°, 65°, 70°, 75°, 85°) aluminium (HE30), Stainless Steel (304 St. St.) and lead targets (see Figure 7.7). The accuracy of the target frame in defining the impact direction was measured and was found to be within 0.5° .

The targets were then removed from the target frame and the analysis was performed using an optical microscope.

7.2.2 The Electrostatic Accelerator

In addition to the experiments performed on the Light Gas Gun an additional experiment was performed on a 2MV Van de Graaff accelerator[33].

The accelerator contains a dust source of spherical iron (I1068) particles which are typically less than 10 μm in diameter. The dust is charged with an electric field and accelerated along an evacuated flight tube to velocities from 0.5 km s^{-1} to upwards of 25 km s^{-1} before impacting the target.

In this case the target was an aluminium foil curved round a target frame in order to expose the full range of angles of 0° - 90° to the impacting projectiles (as shown in Figure 7.8).

After exposure in the accelerator the foil was removed from the mounting, flattened, and placed on a microscope stub. An analysis of it was performed using a Philips 525 SEM.

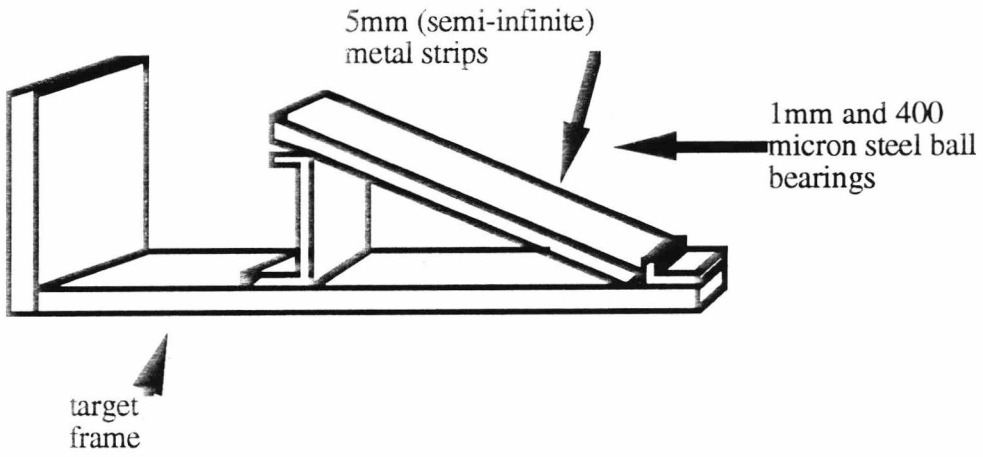

Figure 7.7: Target frame and target used for Light Gas Gun experiment.

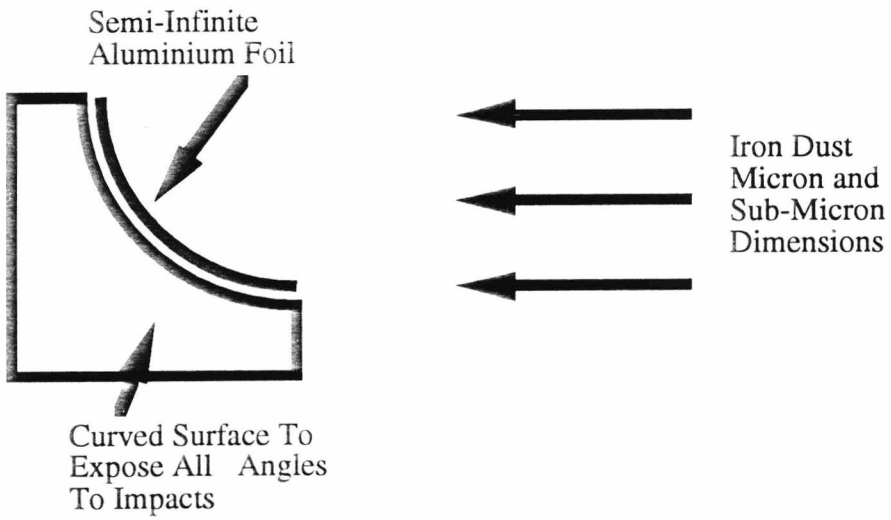

Figure 7.8. Experimental set-up in the Van de Graaff accelerator.

A strip down the length of the foil was examined, covering a range of angles from 90° to about 40°. Each crater located was classified according to it's source (I.e.. hypervelocity or non-hypervelocity) and the quality of image achieved. Those craters from a non-hypervelocity source or too poor an image to be useful were discarded and the remainder were then measured along both axes.

7.3 Experimental Results

7.3.1 The Van de Graaff Accelerator

Results from the Van de Graaff accelerator experiment are shown in Figure 7.9. The error bars shown are due to uncertainties in measurements. Although the accelerator is capable of producing a large range of velocities, these consist of small fast projectiles or larger slower ones. As a result of this it is difficult to analyse impacts from very fast projectiles since they are very small and therefore produce craters which are too small to resolve with sufficient accuracy to determine ellipticity. In the case of the craters analysed so far the velocities were in the range 1-3 km s^{-1} . The craters are still noticeably elliptical at angles as small as 45° for these slow velocities. The trend is very distinctly towards increased ellipticity with increased impact obliquity and in the range of 75-80° the craters become extremely long and thin.

7.3.2 The Light Gas Gun

7.3.2.1 Aluminium Targets

Results of Light Gas Gun experiments into aluminium targets are shown in Figure 7.10. Once more the error bars are due to uncertainties in measurements. The scatter shown represents a real dispersion in crater properties. The velocities of the projectiles in most of these experiments was approximately 4.6 ± 0.4 km s-1 which is slightly faster than the impacts measured from the accelerator experiment. The actual raw data is given in appendix 4.

7.3.2.2 Stainless Steel Targets

Results of the Light Gas Gun experiments into stainless steel targets are shown in Figure 7.11. This data once more shows a very broad scatter in results. Much of the results at each angle come from only one 'buckshot' style shot, so will be at virtually identical velocities (the raw data is once more given in appendix 4). So this spread of crater ellipticities was achieved from impacts under as near identical conditions as could be achieved using the Light gas Gun.

7.3.2.3 Lead Targets

Results of Light Gas Gun experiments into lead targets are shown in Figure 7.12. Again this data shows the general trends observed in the other materials and the same large spread of results at each impact angle.

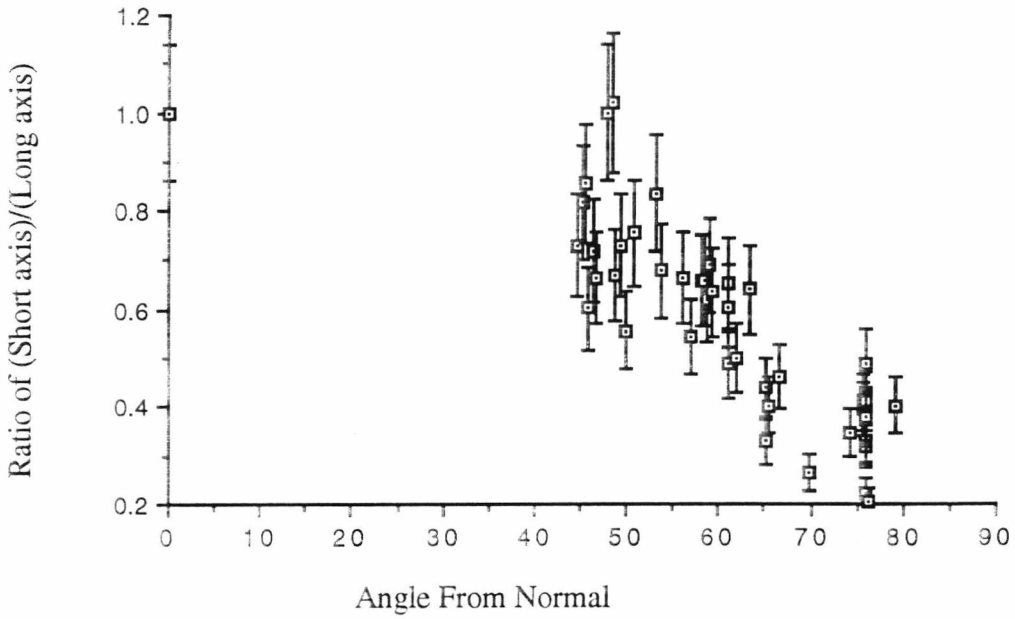

Figure 7.9. The variance of the ratio of short axis to long axis with angle of impact for craters produced by impacts from the Van de Graaff accelerator.

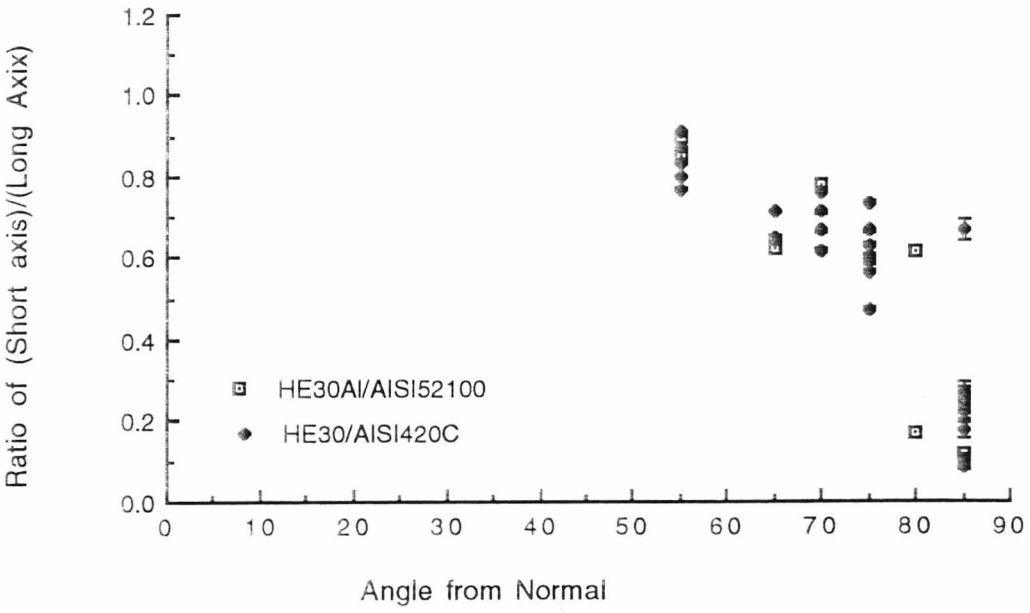

Figure 7.10 The variance of the ratio of short axis to long axis with angle of impact for craters produced by impacts from stainless steel ball bearings onto aluminium (HE30) targets using the Light Gas Gun.

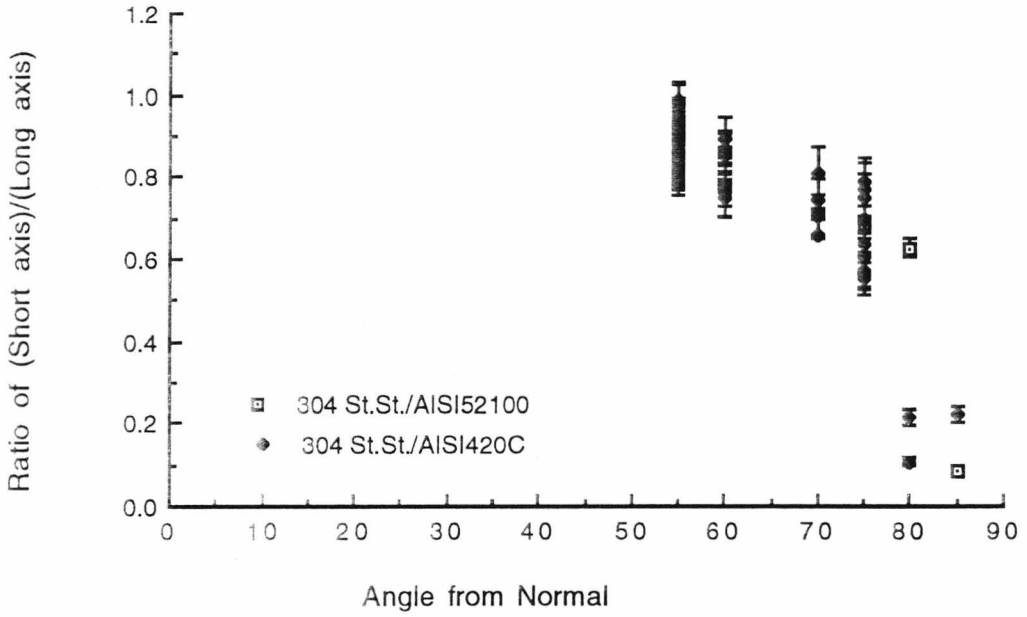

Figure 7.11 The variance of the ratio of short axis to long axis with angle of impact for craters produced by impacts from stainless steel ball bearings onto stainless steel (304 st. st.) targets using the Light Gas Gun.

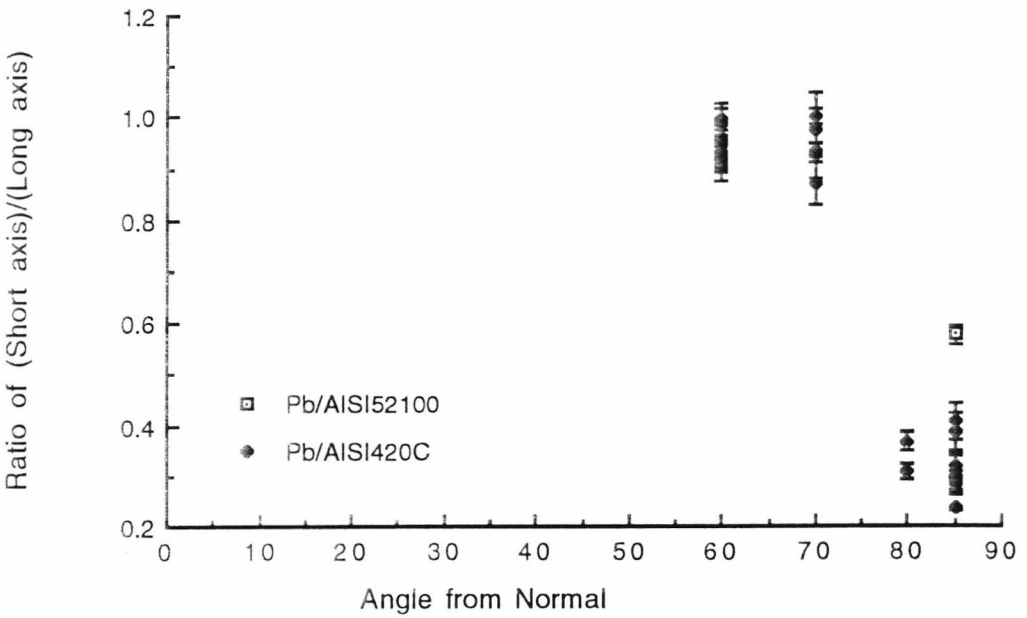

Figure 7.12 The variance of the ratio of short axis to long axis with angle of impact for craters produced by impacts from stainless steel ball bearings onto lead targets using the Light Gas Gun.

7.3.3 General Points

Figure 7.13 shows average values for the impacts from the AISI420C 400 μm stainless steel ball bearings (the bulk of the Light Gas Gun experimental data) and average values for the accelerator data which has been binned in 5° steps for this purpose, this allows us to more easily compare the results. We can see that the slower impacts from the accelerator are generally the most elliptical. For the faster Light Gas Gun experiments we find that the data shows a general trend suggesting that the less dense target materials produce a higher ellipticity.

7.4 Normal Incidence Impacts

In addition to the experiments outlined earlier a few experiments were performed, on the Light Gas Gun to study the craters produced by non-spherical projectiles impacting at normal incidence. The experiments performed consisted of

a) Polyester hexagonal projectiles, approximately 500 μm across and a few microns thick being fired at a lead target.

b) Small lengths of copper wire (ratio of diameter to length approximately 7) being fired at a lead target and a mild steel target.

Results of these experiments are shown in Figure 7.14 and the raw data is listed in appendix 4. It is apparent from these experiments that relatively high ellipticities can be achieved by normal incidence impacts of non spherical projectiles at velocities as high as 5 km s^{-1}. In addition a few of the

craters examined also had lip formations which might be considered indicative of an oblique angle impact.

7.5 Conclusions

The oblique angle experiments do suggest general trends in the relationship between factors such as angle of incidence, velocity of impact, target material properties and eccentricity of the impact crater. However the spread of the ellipticities achieved for near identical impact conditions is very large. This in itself would make it very difficult to establish an impact equation which would predict ellipticities with enough accuracy to be useful in deconvolving the angle of incidence from any given impact

These experiments were performed at relatively low velocities in comparison with the bulk of the collisions expected in space and higher velocities are likely to make elliptical craters from irregular particles less likely. However higher velocities would also make elliptical craters from oblique angle impacts less likely. This would narrow down the range of possible impact angles for any elliptical craters but is likely to only yield information as to whether the impact was higher or lower than the critical angle. So even at higher velocities we are unlikely to be able to deconvolve impacts with any real accuracy.

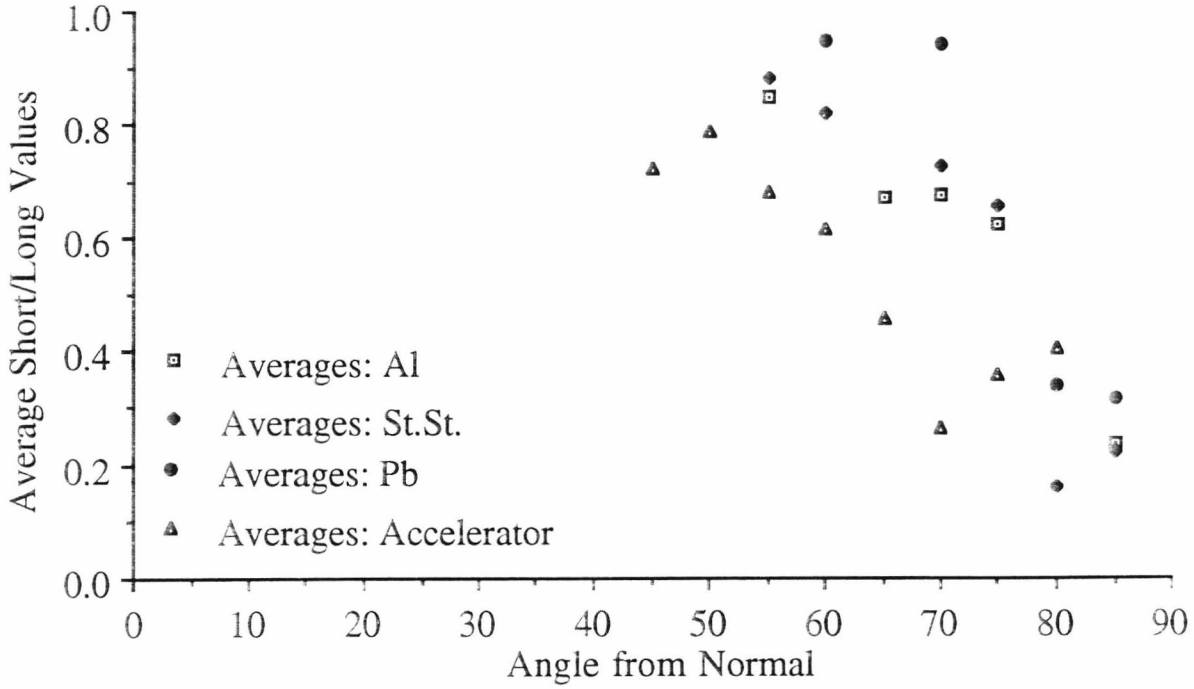

Figure 7.13 The average values for variance of the ratio of short axis to long axis with angle of impact for the light gas gun and accelerator data. In the case of the accelerator, the data is binned in 5° for the purpose of calculating the average values shown in the graph.

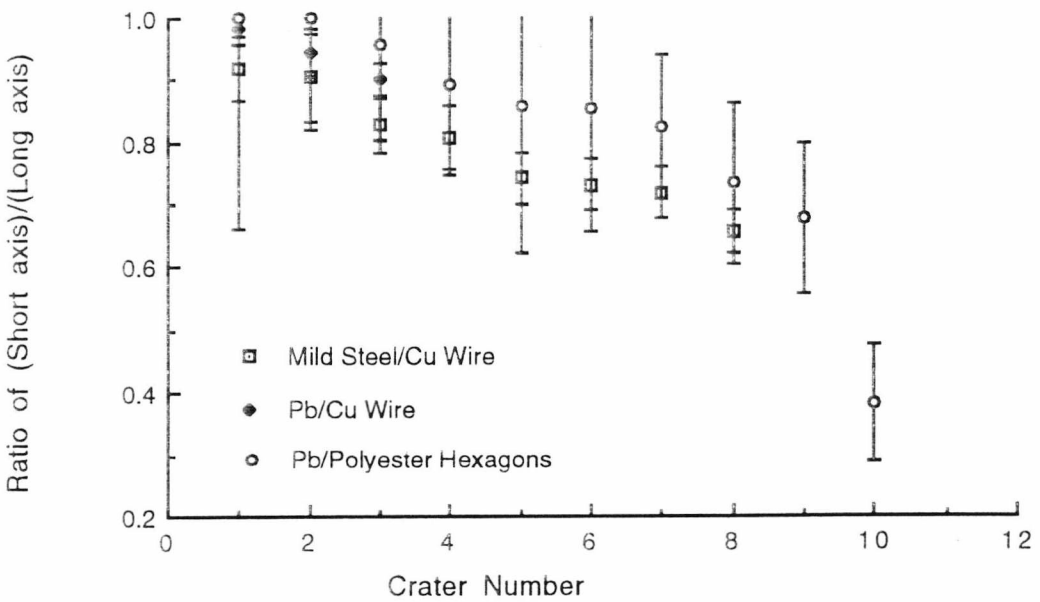

Figure 7.14 The ratio of short axis to long axis for normal incidence impacts from non-spherical projectiles into lead and mild steel targets using the Light Gas Gun.

Chapter 8

Conclusions and Future Work

8.1 Conclusions

8.1.1 Interplanetary Dust Modelling

A model was created to simulate the interactions of the natural dust population with the LDEF satellite. This model was then used in order to gain an understanding of the interactions between the velocities of natural particles and the distribution of impacts on LDEF.

8.1.2 Space Debris

A model was also created to simulate the space debris population and it's interactions with the LDEF spacecraft. Using this as a tool an understanding of the flux contributions made from different classes of debris orbits was achieved. Typical signatures of classes of debris orbits, in terms of angular distributions of impacts on individual LDEF faces, were established. The theoretical use of these signatures as a means of establishing relative levels of low and high inclination orbits was suggested, and the inappropriateness of these signatures for discriminating between high and low eccentricity orbits was established.

8.1.3 Combined Modelling

A comparison of the LDEF data with the results of the LDEF modelling was performed at a number of size regimes (4 μm, 40 μm, 400 μm) in order to test the validity of existing estimates of both the interplanetary dust and space debris populations. The existing estimates of the space debris and IP

populations were found to fairly accurately predict the flux encountered by LDEF in very small size regimes (the space debris population being found to be dominant there) but could not satisfy the shape of the flux distribution and required very large scaling factors to account for the flux levels in the 40 and 400 μm regimes.

Evidence supporting the hypothesis that there existed a far higher population of debris in highly eccentric orbits was searched for, but none was found in terms of best fits to flux levels for the LDEF data (although the best fits still did not explain the results of the chemical analysis which led to the excess HEO's hypothesis).

The suggestion was made that the interplanetary dust population may have a bias towards higher velocities than previous researchers have found. Supporting evidence for this theory was presented in terms of fits to LDEF data. A higher velocity was found to result in a more satisfactory fit to the shape of the flux distribution at 400 μm and considerably lower the scaling factors required to account for the LDEF fluxes in both the 40 and 400 μm size regimes.

The suggestion was also made that the very irregular shape of the flux distribution at 40 μm (the same size regime at which the chemical data used to support the theory of an excess in the HEO population was taken), which could not be explained by any of the scenarios tested, could have been caused by a localised debris event (although there is no firm evidence to support this at this time).

An attempt to further analyse directionality of impacts on LDEF was made by comparison of interplanetary dust and space debris modelling with elliptical craters found on LDEF aluminium tray clamps. The conclusion was

reached that this might be a powerful diagnostic tool if a relationship could be established between the velocity and angle of impact, the material properties of the projectile and target and the ellipticity of the hypervelocity impact crater. In order to investigate this relationship, an experimental program using the Unit for Space Sciences Light Gas Gun was proposed.

8.1.4 The Light Gas Gun Development and Experimental Program

The Light Gas Gun was developed from its initial highly unreliable state into a useful working tool on which a number of experimental programs are now being performed. The Light Gas Gun now has

1)A very low misfire rate.

2) The capability to measure projectile velocity for both solid and split sabots.

3)A highly successful design of split sabots.

4) A much cleaner piston design which puts much less strain on the equipment.

5) No Piston extrusion.

6) A much faster turn around time.

An experimental program was performed on the Light Gas Gun and the Van de Graaff accelerator to investigate the velocity/angle/material properties/ellipticity, relationship. Although basic trends could be observed in the resulting data, a large spread of ellipticities were observed to occur under as near identical impact conditions as could be achieved using the Light Gas Gun. It was also demonstrated that at velocities in the regime produced by the Light Gas Gun elliptical craters could be created by the use of non spherical projectiles impacting targets at normal incidence. As a result

of both of these factors it was concluded that any equation derived from the experimental program would be of little practical use in decoding the elliptical craters found on LDEF.

8.2 Future Work

8.2.1 Modelling

Different interplanetary dust velocity distributions could be defined and iteratively compared with LDEF fluxes in order to investigate the validity of existing velocity distributions in the small size regimes. Meteor streams could be incorporated on top of the sporadic background flux which has been modelled in this research program[34]. Also the validity of the randomness of the sporadics assumption could be investigated.

More observations of the space debris population are required in order to better define input to the space debris model. Also the accuracy of the "randomness of nodes" assumption could be further investigated.

More chemical analysis in a wider range of size regimes would be very useful in helping to deconvolve the interplanetary dust and space debris contributions on LDEF.

8.2.2 The Light Gas Gun

A number of things could still be done to optimise the Light Gas Guns usefulness.

1) Finalise the light obscuration velocity measurement system (probably two lasers)

2) Investigate the maximum velocity which can be achieved by the gun

3) Gain better control of the velocity by varying powder types and quantities, hydrogen pressures and bursting disc materials

4) A means of preventing the sheared part of the bursting disc from impacting the target when a solid sabot is used

5) An investigation of the guns operation for modelling purposes (piston speeds, burst time for the diaphragm etc.)

6) More equipment in the target chamber to analyse impacts (a high speed camera, flash X-ray facilities)

I feel that if the above suggestions were implemented then the Light Gas Gun would be a far more powerful experimental tool.

References

[1] ESA. 1988 Space Debris - A Report of The Space Debris Working Group. ESA SP-1109, 1988.

[2] Kessler D. J., Reynolds R.C., Anz-Meador P. D. 1989. Orbital debris Environment for Spacecraft Designed to Operate in Low Earth Orbit. NASA Technical Memorandum 100 471

[3] Drolshagen C., Borde J. 1992 ESABASE/Debris. Meteoroid/Debris Impact Analysis. Technical Description. Issue 1 for ESABASE Version 9.0. ESABASE - GD - 01/1

[4] Fucke W., Sdunnus H. 1993 Population Model of Small Size Space Debris. ESOC Contract No. 9266/90/MD

[5] Green S. F., Optical Detection Of Space Debris , Workpackage 2100 Report,,Debris Characterisation , 7/7/91

[6] Green S. F., Optical detection of Space Debris, Workpackage 4300 Report, Debris detection Concept Performance Analysis, Nov. 1991

[7] McDonnell J.A.M., Deshpande S.P., Green S.F., Newman P.J., Paley M. T., Ratcliff P.R., Stevenson T. J., and Sullivan K., First Results of Particulate Impacts and Foil Perforations on LDEF. COSPAR 1990

[8] Southworth, R.B. and Sekanina, Z. (1973) Physical and dynamical studies of meteors. NASA CR-2313, 108 pp.

[9] Dohnanyi, J.S. (1966) Model distribution of photographic meteors. Bellcom TR-66-340-1, Bellcomm, Inc.

[10] Erickson, J.E. (1968) Velocity distribution of sporadic photographic meteors. J. Geophys. Res. 73, 3721-3726

[11] Kessler, D.J. (i969) Average relative velocity of sporadic meteoroids in interplanetary space. AIAA J. 7, 2337-2338.

[12] Zook, H.A. (1975) The State of Meteororic Material on the Moon. Proc. Lunar Sci. Conf. 6th pp. 1653-1672

[13] Grun, E., Zook, H.A., Fechtig, H., Giese, H. (1984) Collisional Blance of the Meteoric Complex. ICARUS 62, 244-272 (1985)

[14] Zook, H.A., Flaherty, R.E., Kessler, D.J. (1970). Meteoroid Impacts on the Gemini Windows. Planet. Space Sci. 18,953-964

15 Fechtig, H., Gentner, W., Hartung, J.B., Nagel, K., Neukum, G., Storzer, D. Lunar Microcrater Studies, Derived Meteoroid Fluxes, and Comparison with Satellite Borne Experiments. Proc. Lunar Sci. Conf. 5th 3, 2463-2474

16 McDonnell, J.A.M. (1978). Microparticles Studies by Space Instrumentation. Cosmic Dust (J.A.M. McDonnell, Ed.), pp. 337-426. Wiley, Chichester.

17 Le Sergeant d'Hendecourt, L.B., Lamy, P.L.(1980). On the Size Distribution and Physical Properties of Interplanetary Dust Grains. Icarus 43, 350-372

18 Humes, D.H. (1991). Large Craters on the Meteoroid and Space Debris Impact Experiment. Proc. of LDEF First Post Retrieval Symposium Pt. 1 .
19 Kessler D.J. , 1990 Orbital Debris Environment for Spacecraft in Low Earth Orbit. AIAA 90-1353 AIAA/NASA/DOD Orbital Debris Conference: Technical Issues, 1990, Baltimore, MD.

20 McDonnell, J.A.M. 1970, Factors affecting the choice of Foils for Penetration Experiments in Space. Space Res., X, 314-325

21 McDonnell J.A.M., Sullivan K. Hypervelocity Impacts on Space Detectors: Decoding the Projectile Parameters. Hypervelocity Impacts in Space ed. J.A.M. McDonnell, Unit for Space Sciences, University of Kent at Canterbury, UK, p39-47, 1992.

22 Bernhard R.P., Horz F., Zolensky M.E., See T.H., Barrett R.A., Composition and Frequency of Impact Residues Detected On LDEF Surfaces. Proc. First European Conference on Space Debris. 1993

23 Horz F., Bernhard R.P., Warren J., See T., Brownlee D., Laurance M., Messenger S., Preliminary Analysis of LDEF Instrument A0187-1, the Chemistry of Micrometeoroids Experiment (CME), Hypervelocity Impacts in Space. 1991.

24 Watts A., Atkinson D., Rieco S., Dimensional Scaling for Impact Cratering and Perforation. POD Associates Inc. (i993)

25 Kessler D.J. Origin of Orbital Debris Impacts on LDEF's Trailing Surfaces. In LDEF - 69 Months in Space, Second LDEF Post-retrieval Symposium, NASA Conf. Publ. 3194, pt 2, 585-593.

26 Taylor A. D., The Harvard Radio Meteor Project Velocity Distribution Reappraised, ICARUS, Manuscript 6174N, 1994
27 Kineke, J.H. Jr., 1960 An experimental Study of Crater Formation in Metallic Targets. Hypervelocity Impacts, 4th Symposim, Air Proving Centre, Eglin Air Force Base Florida, APGC-TR-60-39(I), Section4.

[28] Bryan, G.M.,.. 1960. A Model of Oblique Impact . Hypervelocity Impacts, 4th Symposim, Air Proving Centre, Eglin Air Force Base Florida, APGC-TR-60-39(III), Section33.

[29] Culp, F.L., 1959. Volume-Energy Relation for Craters Formed by High-Velocity rojectiles. Hypervelocity Impact 3rd Symposium, Armour Research Foundation of Illinois Inst. of Technology, Chicago.

[30]Gault, D.E. and Wedekind, J. A. , 1978. Experimental studies of Oblique Impact. Proc. 9th Lunar Plant Sci. Conf., 3843-3875.

[31] Mackay, N.G., Green, S.F., Deshpande, S.P., and Newman, P.J., 1993. Interpretation of Impact Crater Morphology and Residues on LDEF using 3-D Space Debris and Micrometeoroid models. Proc. 1st European Conference on Space Debris , Darmstadt, 5-7 Apr. 1993.

[32] Newman P.J., Mackay N., Deshpande S.P., Green S.F. and McDonnell J.A.M., 1993. Derivation of Particulate Directional Information from Analysis of Elliptical Impact Craters. Proc. Second LDEF Post-retrieval Conference, in press

[33] Green S. F., Clarke D. D., Stevenson T. J., 1988. A 2MV Van de Graaff Accelerator for Cosmic Dust Simulation. JBIS Vol. 41 No. 9, Sept 1988.

[34] McBride N., Taylor A.D., Green S.F., McDonnell J.A.M., 1994. Asymmetries in the natural meteoroid population as sampled by LDEF . Planet. Space Sci. In Press.

Appendix 1

A listing of the code of the Interplanetary dust model.

```
      PROGRAM IMPACT19
*This version reads data from file but calculates the averag impact
*velocities on the faces as well as everything else
*produces ellipticity data for constant mass
*allows you to choose output data
*slightly faster version since it loops only for theta up to 180
*instead of 360
*Numbers LDEF's faces correctly 9=EAST (RAM) etc
*Performs mass loop for mass distribution and calculates the
*perforation limit for given target and particle types
*Has mass and perforation depths bins in a logarithmic scale
*Output bins are cumulative
*Calculates maximum impact velocity on each face
*The perforation depths are calculated in metres
* NGM PRODUCTIONS *
*   4/8/92


*Declaration of constants.
      PARAMETER (IVBIN=80
     +,IPOBIN=17,IEQBIN=35,IPO2=179,
     +IEQ2=179,IVBIN2=800,RADIUS=6378,ATMOS=150,IFACE=12)
*IVCON,IPOCON,IEQCON,IVC2,IPOC2,IEQC2 are the maximum  upper limits
*for the velocity and angular arrays for results and calculations .
*RADIUS,ATMOS are the radius and atmospheric height of the Earth.
*IFACON is the maximum number of peripheral faces on the satellite.
      LOGICAL WHICH(1:14)

*Declaration of arrays

      COMMON /CALCARRAY/ OMFLUX(0:IPO2),PHI(0:IPO2),DOMEGA(0:IPO2),
     +THETA(0:IEQ2)
     +,DPHI,DTHETA
      COMMON /CALCARRAY2/ BIN(0:IVBIN,0:IEQBIN,0:IPOBIN)
      COMMON /SPHRES/VELDIS(0:IVBIN),ANGDIS(0:IEQBIN,0:IPOBIN),
     +THEDIS(0:IEQBIN),PHIDIS(0:IPOBIN),SPHTOT
      COMMON /RESARRAY/
FACTOT(0:IFACE),SVFDIS(0:IVBIN),SCRVEL(0:IVBIN)
     +,EVFDIS(0:IVBIN),ECRVEL(0:IVBIN)
     +,RVFDIS(0:IFACE,0:IVBIN),PCRVEL(0:IFACE,0:IVBIN),SANDIS(0:8)
     +,EANDIS(0:8),SBIN(0:IVBIN,0:8),EBIN(0:IVBIN,0:8)
     +,PBIN(0:IFACE,0:IVBIN,0:8),
     +RANDIS(0:IFACE,0:8)
     +,ELIP1(0:IVBIN,0:36,0:9,0:IFACE)
     +,SPELI1(0:IVBIN,0:36,0:9),EAELI1(0:IVBIN,0:36,0:9)
     +,ELIP2(0:36,0:IFACE)
     +,ELIP4(0:36,0:IFACE),ANGNV(0:IVBIN,0:36,0:IFACE)
     +,SELIP4(0:36),SANGNV(0:IVBIN,0:36)
     +,EELIP4(0:36),EANGNV(0:IVBIN,0:36)
     +,SPELI2(0:36),EAELI2(0:36)
     +,ELIP3(0:36,0:9,0:IFACE)
     +,SPELI3(0:36,0:9),EAELI3(0:36,0:9)
     +,SPTN(0:30),EPTN(0:30),PTN(0:IFACE,0:30)
     +,PMAXV(0:IFACE)
     +,AVTOT,EARTH,SPACE
     +,VELMAX,SMAXV,EMAXV
      REAL NF,MFLUX
      COMMON /DATAARRAY/ DIAM(1:30),MFLUX(1:30),NF(1:3,0:IFACE)
*OMFLUX,DOMEGA are the area of one of the angular bins on the spherical
```

```
*satellite and the fraction of the flux which effects that area.
*PHI,THETA,PHI2,THETA2 are the centre points of these bins for results
*and calculations.
*BIN,VELDIS,ANGDIS,THEDIS,PHIDIS are the results arrays for the spherical
*satellite.
*SVFDIS,SCRVEL,EVFDIS,ECRVEL,RVFDIS,PCRVEL,SANDIS,EANDIS,SBIN,EBI
N,PBIN
*,RANDIS are the velocity an angular
*results arrays for the actual satellite.
*FACTOT are the total number of particles hitting the peripheral
*faces of the satellite


*Variable declarations
      COMMON /REALCALC1/ SATVEL
      COMMON /REALCALC2/ VBISIZ
      COMMON /REALCALC3/ BETA,ROEP,ROET,SIGAL,SIGT
       COMMON /REAL9/ slimit
      COMMON /REALCALC4/ OFFSET,TILT
      COMMON /REALCALC5/ PARVEL,FLUX
      COMMON /REAL6/ PI
      COMMON /REAL7/ HAPI,PI2
      COMMON /REAL8/ PI4
*SATVEL,PARVEL are the velocity of the satellite and of the IP dust.
*FLUX is the flux through which the satellite is moving.
*VBISIZ is the size if the velocity bins for the results arrays.
*BETA is the angle associated with Earth shielding.
*OFFSET,TILT are the offset and tilt of the satellite.
*DPHI,DTHETA are the size of the angular results bin.
*EARTH,SPACE are the total number of
*impacts on the Earth and
*and space of the satellite.
*SPHTOT is the total number of impacts on the spherical satellite.
*PI,PI2,PI4,HAPI are pi,2xpi,4xpi and pi/2

      COMMON /INTCALC/ IPOUS,IEQUS,
     +IPOUS2,IEQUS2
      COMMON /INTDAT/ MST
*      COMMON /INTCALC2/
*     +IVBIN,IPOBIN,IEQBIN,IPO2,IEQ2,IFACE
*     +,IVBIN2
*IEQBIN,IPOBIN,IVBIN,IEQ2,IPO2,IVBIN2 are the upper limits of the
*velocity and angular results and calculations arrays.
*IPOUS,IEQUS,IPOUS2,IEQUS2 are the size of these arrays (this is different
*since the arrays have been taken to start at zero instead of one)
*ie. IEQBIN=IEQUS-1.
*IFACE is the number of peripheral faces on the satellite.

*Define the values of PI ect.
      IEQUS=IEQBIN+1
      IPOUS=IPOBIN+1
      IEQUS2= 5*IEQUS
      IPOUS2= 10*IPOUS
      PI=4.0*ATAN(1.0)
      PI2=2*PI
      PI4=4*PI
      HAPI=0.5*PI
*Open the results file.
       OPEN(15,FILE='info.dat',STATUS='OLD')
```

```
      OPEN(14,FILE='dis.res',STATUS='NEW',RECL=1200)
      OPEN(16,FILE='eli.res',STATUS='NEW',RECL=1200)
      OPEN(17,FILE='pen.res',STATUS='NEW',RECL=1200)
      OPEN(18,FILE='siz.dis',STATUS='OLD')
*Main part of program
*Read in the user input data
    CALL REDATA()
    CALL whatout(WHICH)
*Initialise all the totals and results arrays to zero.

    SPACE=0
    EARTH=0
    EMAXV=0
    SMAXV=0
    DO 41 K=0,IFACE,1
      PMAXV(K)=0
      FACTOT(K)=0
41  CONTINUE
    DO 42 I=0,IVBIN,1
       SVFDIS(I)=0
       SCRVEL(I)=0
       EVFDIS(I)=0
       ECRVEL(I)=0
       DO 43 J=0,IFACE,1
          RVFDIS(J,I)=0
43     CONTINUE
42  CONTINUE
    DO 44 I=0,8,1
      SANDIS(I)=0
      EANDIS(I)=0
      DO 45 J=0,IFACE,1
         RANDIS(J,I)=0
45     CONTINUE
44  CONTINUE
    SPHTOT=0
    VELMAX=0
    I=1
555 CONTINUE
    READ(18,*,END=888) DIAM(I),MFLUX(I)          (Read in size distribution)
    I=I+1
    GOTO 555
888 CONTINUE
    MST=I-1
*For each dust velocity.
666 CONTINUE
      READ(15,*,END=999) PARVEL,FLUX             (Read in velocity distribution)

      IF (PARVEL.GT.VELMAX)  VELMAX=PARVEL       (locate maximum velocity in
                                                  distribution)
*       IVBIN=INT((SATVEL+VELMAX)/VBISIZ)+1
*       IVBIN2=INT((SATVEL+VELMAX)/VBI2)
*Initialise the results bins.
    DO 80 I=0,IVCON,1
      DO 81 J=0,IEQCON,1
        DO 82 K=0,IPOCON,1
          BIN(I,J,K)=0.0
82      CONTINUE
81    CONTINUE
80  CONTINUE
```

```
*Perform necessary transformations on data.


      CALL CALC()
*Work out the velocity and angular distributions.
      CALL DBTN()
      GOTO 666
 999  CONTINUE
*Output results to file.
      CALL  RESULT(WHICH)
*Close results file.
      CLOSE(15)
      CLOSE(14)
      END



      SUBROUTINE RELVEL(PHI,THETA,PHIREL,THEREL,VPAR)
*Takes in the dust data relative to a stationary satellite and outputs
*data relative to moving satellite

      COMMON /REALCALC1/ VSAT
      COMMON /CALCLOC/ VREL
      COMMON /CALCLOC2/ X1,X2,X3
      REAL PHI,THETA,PHIREL,THEREL
      COMMON /REAL7/ HAPI,PI2

      REAL TEST1,TEST2
*VREL is the velocity of the particle relative to the satellite.
*VSAT,VPAR are the velocity of the satellite and of the IP dust.
*PHI,THETA,PHIREL,THEREL are the angles of approach of a particle
*relative to the stationary and moving satellite.
*X1,X2,X3 are the approach vector of the particle in cartesian co_ordinates.
*TEST1,TEST2 are dummy variables.

*Resolve input data to cartesian co_ordinates .
      X1=VPAR*COS(PHI)*COS(THETA)+VSAT
      X2=VPAR*COS(PHI)*SIN(THETA)
      X3=VPAR*SIN(PHI)
*Calculates relative velocities and approach angles.
      VREL=SQRT(X1**2+X2**2+X3**2)
*Tests for computer inaccuracies before executing the inverse trig
*functions.
      TEST1=X3/VREL
      IF ((TEST1 .GT. 1.0) .AND. (TEST1 .LT. 1.0001))
     + TEST1= 1.0
      IF ((TEST1 .LT. -1.0) .AND. (TEST1 .GT. -1.0001))
     + TEST1=-1.0
      PHIREL=ASIN(X3/VREL)
*Compensate for cos function only returning a 0-PI value
      TEST2=X1/(VREL*COS(PHIREL))

      IF ((TEST2 .GE. 1.0) .AND. (TEST2 .LT. 1.001)) THEN
            TEST2=1.0
            IF (THETA .GT. PI) THETA=0.0
      END IF
      IF ((TEST2 .LT. -1.0) .AND. (TEST2 .GT. -1.001))
```

```
     + TEST2=-1.0
      IF (THETA.GT.PI) THEN
                THEREL=PI2-ACOS(TEST2)
                 ELSE
                THEREL=ACOS(TEST2)
      END IF
      END



      SUBROUTINE DBTN()
*Calculates velocity and angular distributions and outputs results.   (for spherical satellite)
      PARAMETER (IVBIN=80
     +,IPOBIN=17,IEQBIN=35)
*IEQBIN,IPOBIN,IVBIN are the upper limits of the
*velocity and angular results arrays.
          COMMON /CALCARRAY2/ BIN(0:IVBIN,0:IEQBIN,0:IPOBIN)
      COMMON /SPHRES/VELDIS(0:IVBIN),ANGDIS(0:IEQBIN,0:IPOBIN),
     +THEDIS(0:IEQBIN),PHIDIS(0:IPOBIN),SPHTOT

*BIN,VELDIS,ANGDIS,THEDIS,PHIDIS are the results arrays for the spherical
*satellite.


* Calculate velocity distribution and output to a file.
      DO 15 I=0,IVBIN,1
        DO 10 J=0,IEQBIN,1
          DO 11 K=0,IPOBIN,1
            VELDIS(I)=VELDIS(I)+BIN(I,J,K)
 11       CONTINUE
 10     CONTINUE
 15   CONTINUE
*Calculate angular distribution and output to same file.
      DO 25 J=0,IEQBIN,1
        DO 26 K=0,IPOBIN,1
          DO 20 I=0,IVBIN,1
            ANGDIS(J,K)=ANGDIS(J,K)+BIN(I,J,K)
 20       CONTINUE
 26     CONTINUE
 25   CONTINUE
      DO 27 I=0,IEQBIN,1
        DO 28 J=0,IPOBIN,1
          THEDIS(I)=THEDIS(I) + ANGDIS(I,J)
 28     CONTINUE
 27   CONTINUE
      DO 37 J=0,IPOBIN,1
        DO 38 I=0,IEQBIN,1
          PHIDIS(J)=PHIDIS(J) + ANGDIS(I,J)
 38     CONTINUE
 37   CONTINUE


      END
```

```
      SUBROUTINE REDATA()
*Read in user input parameters.
            COMMON /REALCALC1/ SATVEL
            COMMON /REALCALC2/ VBISIZ
            COMMON /REALCALC3/ BETA,ROEP,ROET,SIGAL,SIGT
            COMMON /REALCALC4/ OFFSET,TILT
            COMMON /REAL7/ HAPI,PI2
          COMMON /REAL9/ slimit
         PARAMETER (IVBIN=80
        +,IPOBIN=17,IEQBIN=35,IPO2=179,
       +IEQ2=179,IVBIN2=800,RADIUS=6378,ATMOS=150,IFACE=12)
            COMMON /INTCALC/ IPOUS,IEQUS,
       +IPOUS2,IEQUS2

      REAL ALPHA,HEIGHT
*Request and read in parameters.
      PRINT *,'Please enter the speed  of the satellite, and the speed
     +of the IP dust.'
      READ(15,*) SATVEL
      WRITE (14,*) 'Velocity of satellite=',SATVEL
      PRINT *,'Please enter the size of the velocity bins.'
      READ(15,*) VBISIZ
      WRITE (14,*) 'Size of velocity bins=',VBISIZ
*Calculate appropriate velocity array size.
      VBI2=VBISIZ/10
      PRINT *,'Please enter the height of the satellites orbit'
      READ(15,*) HEIGHT
      WRITE (14,*) 'Height of satellite=',HEIGHT
*Calculate  the angle associated with Earth shielding.
      ALPHA=ASIN((RADIUS+ATMOS)/(RADIUS + HEIGHT))
      slimit=ALPHA - HAPI
       WRITE (14,*) 'Earth shielding =',beta,'radians'
      PRINT *,'Please enter the no. of faces round satellite, it"s
     +offset and tilt.'
      READ(15,*) OFF,TIL
      OFFSET=OFF*PI2/360
      TILT=TIL*PI2/360
      WRITE (14,*) 'Number of lateral faces =',IFACE
       WRITE (14,*) 'Offset =',OFFSET
       WRITE (14,*) 'Tilt =',TILT
      WRITE (14,*)
      READ (15,*) ROEP,ROET,SIGAL,SIGT
      RETURN
      END



      SUBROUTINE CALC()
*Performs transformations on input data.
      PARAMETER (IVBIN=80
     +,IPOBIN=17,IEQBIN=35,IPO2=179,
     +IEQ2=179,IVBIN2=800,RADIUS=6378,ATMOS=150,IFACE=12)
            COMMON /REALCALC1/ SATVEL
            COMMON /REALCALC2/ VBISIZ
            COMMON /REALCALC3/ BETA,ROEP,ROET,SIGAL,SIGT
          COMMON /REAL9/ slimit
            COMMON /REALCALC4/ OFFSET,TILT
            COMMON /REALCALC5/ PARVEL,FLUX
```

```
      COMMON /REAL6/ PI
      COMMON /REAL7/ HAPI,PI2
      COMMON /REAL8/ PI4
     COMMON /CALCLOC/ VREL
    COMMON /CALCLOC3/ ADD
*    COMMON /INTCALC2/
     COMMON /INTDAT/ MST
*    +IVBIN,IPOBIN,IEQBIN,IPO2,IEQ2,IFACE
*    +,IVBIN2

     REAL DPHI2,DTHET2,POFAC2,EQFAC2
*VREL is the velocity of the particle relative to the satellite.
*SATVEL,PARVEL are the velocity of the satellite and of the IP dust.
*FLUX is the flux through which the satellite is moving.
*VBISIZ is the size if the velocity bins for the results arrays.
*BETA is the angle associated with Earth shielding.
*OFFSET,TILT are the offset and tilt of the satellite.
*DPHI,DTHETA are the size of the angular results bin.
*EARTH,SPACE are the total  number of
*impacts  on the Earth and
*and space of the satellite.
*SPHTOT is the total number of impacts on the spherical satellite.
*X1,X2,X3 are the approach vector of the particle in cartesian co_ordinates.
      COMMON /INTCALC/ IPOUS,IEQUS,
    +IPOUS2,IEQUS2
     COMMON /CALCLOC2/ X1,X2,X3
     COMMON /SPHRES/VELDIS(0:IVBIN),ANGDIS(0:IEQBIN,0:IPOBIN),
    +THEDIS(0:IEQBIN),PHIDIS(0:IPOBIN),SPHTOT

*IEQBIN,IPOBIN,IVBIN,IEQ2,IPO2, are the upper limits of the
*velocity and angular results and calculations arrays.
*IPOUS,IEQUS,IPOUS2,IEQUS2 are the size of these arrays (this is different
*since the arrays have been taken to start at zero instead of one)
*ie. IEQBIN=IEQUS-1.
*IFACE is the number of peripheral faces on the satellite.
     COMMON /CALCARRAY/ OMFLUX(0:IPO2),PHI(0:IPO2),DOMEGA(0:IPO2),
    +THETA(0:IEQ2)
    +,DPHI,DTHETA
     COMMON /CALCARRAY2/ BIN(0:IVBIN,0:IEQBIN,0:IPOBIN)

     COMMON /RESARRAY/
FACTOT(0:IFACE),SVFDIS(0:IVBIN),SCRVEL(0:IVBIN)
    +,EVFDIS(0:IVBIN),ECRVEL(0:IVBIN)
    +,RVFDIS(0:IFACE,0:IVBIN),PCRVEL(0:IFACE,0:IVBIN),SANDIS(0:8)
    +,EANDIS(0:8),SBIN(0:IVBIN,0:8),EBIN(0:IVBIN,0:8)
    +,PBIN(0:IFACE,0:IVBIN,0:8),
    +RANDIS(0:IFACE,0:8)
    +,ELIP1(0:IVBIN,0:36,0:9,0:IFACE)
    +,SPELI1(0:IVBIN,0:36,0:9),EAELI1(0:IVBIN,0:36,0:9)
    +,ELIP2(0:36,0:IFACE)
    +,ELIP4(0:36,0:IFACE),ANGNV(0:IVBIN,0:36,0:IFACE)
    +,SELIP4(0:36),SANGNV(0:IVBIN,0:36)
    +,EELIP4(0:36),EANGNV(0:IVBIN,0:36)
    +,SPELI2(0:36),EAELI2(0:36)
    +,ELIP3(0:36,0:9,0:IFACE)
    +,SPELI3(0:36,0:9),EAELI3(0:36,0:9)
    +,SPTN(0:30),EPTN(0:30),PTN(0:IFACE,0:30)
    +,PMAXV(0:IFACE)
    +,AVTOT,EARTH,SPACE
```

```
     +,VELMAX,SMAXV,EMAXV
       REAL NF,MFLUX
         COMMON /DATAARRAY/ DIAM(1:30),MFLUX(1:30),NF(1:3,0:IFACE)

*OMFLUX,DOMEGA are the area of one of the angular bins on the spherical
*satellite and the fraction of the flux which effects that area.
*PHI,THETA are the centre points of these bins for results.
*BIN is the results arrays for the spherical satellite.
*SVFDIS,SCRVEL,EVFDIS,ECRVEL,RVFDIS,PCRVEL,SANDIS,EANDIS,SBIN
*,EBIN,PBIN,RANDIS are the velocity an angular
*results arrays for the actual satellite.
*FACTOT are the total number of particles hitting the peripheral
*faces of the satellite
*     Calculate bin dimensions and shift factors.          (to locate centre of bins)
      DTHETA=PI2/IEQUS
      DPHI=PI/IPOUS
      DPHI2=PI/IPOUS2
      DTHET2=PI/IEQUS2
      EQFAC2=DTHET2/2
      POFAC2=(PI-DPHI2)/2
*     Initialise the PHI array.
*     Calculate size of bins and the relavent flux .
      DO 30 I=0,IPO2,1
        PHI(I)=REAL(I)*DPHI2-POFAC2
        DOMEGA(I)=DPHI2*COS(PHI(I))*DTHET2
        OMFLUX(I)=(FLUX*DOMEGA(I))/PI4
 30   CONTINUE

*     Initialise the THETA array.
      DO 40 I=0,IEQ2,1
        THETA(I)=REAL(I)*DTHET2+EQFAC2
 40   CONTINUE
*     For each angle of approach.
      DO 50 I=0,IPO2,1
        DO 51 J=0,IEQ2,1
*       If vector is not coming from Earths shielding cone then,
        IF (.NOT.(PHI(I) .LT. slimit)) THEN
           CALL RELVEL(PHI(I),
     +       THETA(J),PHIREL,THEREL,PARVEL)
*            IF ((X1/VREL.GT.0.9).AND.(X3/VREL.LT.0.1).AND.(I.GT.72))
*     +PRINT *,X1/VREL,X2/VREL,X3/VREL
*       Calculate approach vector relative to moving spherical satellite.
*          Calculate the effective flux for a moving satellite.
           ADD=OMFLUX(I)*(VREL/PARVEL)
*          Check which of the faces the particle can impact on.
           CALL FACE(X1,X2,X3)
           CALL FACE(X1,-X2,X3)
*          Put appropriate value in appropriate bin location for
*          spherical satellite results.
           IVEL=INT((VREL/VBISIZ))
           IEQ=INT((THEREL/DTHETA))
           IPO=INT(((PHIREL+HAPI)/DPHI))
           BIN(IVEL,IEQ,IPO)=BIN(IVEL,IEQ,IPO)+ADD
           BIN(IVEL,(IEQBIN-IEQ),IPO)=BIN(IVEL,(IEQBIN-IEQ),IPO)
     +      +ADD
           SPHTOT=SPHTOT+2*ADD
         END IF
 51     CONTINUE
 50   CONTINUE
```

```
      END



      SUBROUTINE FACE(X1,X2,X3)

*IFACE is the number of peripheral faces on the satellite.
*IVBIN is the size of the velocity results arrays
      PARAMETER (IVBIN=80
     +,IPOBIN=17,IEQBIN=35,IPO2=179,
     +IEQ2=179,IVBIN2=800,RADIUS=6378,ATMOS=150,IFACE=12)
           COMMON /REALCALC3/ BETA,ROEP,ROET,SIGAL,SIGT
           COMMON /REALCALC4/ OFFSET,TILT
           COMMON /REALCALC2/ VBISIZ
          COMMON /CALCLOC/ VREL
      COMMON /CALCLOC3/ ADD

           COMMON /REAL6/ PI
      REAL COSPSI,ADDON
       REAL N1(1:3),N2(1:3),N3(1:3),NSP(1:3),X(1:3)
*N1,N2,N3,N1SPA,N2SPA,N3SPA are the normal vectors to the space and
*the peripherel faces (Normal to Earth face is negative the normal to
*the space face.
*VREL is the velocity of the particle relative to the satellite.
*VBISIZ is the size if the velocity bins for the results arrays.
*OFFSET,TILT are the offset and tilt of the satellite.
*EARTH,SPACE are the total  number of
*impacts  on the Earth and
*and space of the satellite.
*X1,X2,X3 are the approach vector of the particle in cartesian co_ordinates.

     COMMON /RESARRAY/
FACTOT(0:IFACE),SVFDIS(0:IVBIN),SCRVEL(0:IVBIN)
    +,EVFDIS(0:IVBIN),ECRVEL(0:IVBIN)
    +,RVFDIS(0:IFACE,0:IVBIN),PCRVEL(0:IFACE,0:IVBIN),SANDIS(0:8)
     +,EANDIS(0:8),SBIN(0:IVBIN,0:8),EBIN(0:IVBIN,0:8)
     +,PBIN(0:IFACE,0:IVBIN,0:8),
    +RANDIS(0:IFACE,0:8)
    +,ELIP1(0:IVBIN,0:36,0:9,0:IFACE)
    +,SPELI1(0:IVBIN,0:36,0:9),EAELI1(0:IVBIN,0:36,0:9)
    +,ELIP2(0:36,0:IFACE)
    +,ELIP4(0:36,0:IFACE),ANGNV(0:IVBIN,0:36,0:IFACE)
    +,SELIP4(0:36),SANGNV(0:IVBIN,0:36)
    +,EELIP4(0:36),EANGNV(0:IVBIN,0:36)
    +,SPELI2(0:36),EAELI2(0:36)
    +,ELIP3(0:36,0:9,0:IFACE)
    +,SPELI3(0:36,0:9),EAELI3(0:36,0:9)
     +,SPTN(0:30),EPTN(0:30),PTN(0:IFACE,0:30)
    +,PMAXV(0:IFACE)
    +,AVTOT,EARTH,SPACE
    +,VELMAX,SMAXV,EMAXV
      REAL NF,MFLUX
         COMMON /DATAARRAY/ DIAM(1:30),MFLUX(1:30),NF(1:3,0:IFACE)
      COMMON /INTDAT/ MST
          COMMON /REAL7/ HAPI,PI2

*SVFDIS,SCRVEL,EVFDIS,ECRVEL,RVFDIS,PCRVEL,SANDIS,EANDIS,SBIN
```

```
*,EBIN,PBIN,RANDIS are the velocity an angular
*results arrays for the actual satellite.
*FACTOT are the total number of particles hitting the peripheral
*faces of the satellite

*Calculate the angle between the normals to the peripheral faces.
      DFACE=PI2/IFACE
      TOTHIR=2.0/3.0
      X(1)=X1
      X(2)=X2
      X(3)=X3
*Calculate the normal vector to the space face.
      NSP(1)=SIN(TILT)*COS(OFFSET)
      NSP(2)=SIN(OFFSET)*SIN(TILT)
      NSP(3)=COS(TILT)
      DO 155 K=0,(IFACE-1),1
        THEFAC=DFACE*K
*Calculate the normal vector to the peripheral faces.

        NF(1,K)=COS(THEFAC)*COS(TILT)*COS(OFFSET)-
     +SIN(THEFAC)*SIN(OFFSET)
        NF(2,K)=COS(THEFAC)*COS(TILT)*SIN(OFFSET)+
     +SIN(THEFAC)*COS(OFFSET)
        NF(3,K)=-SIN(TILT)*COS(THEFAC)
 155    CONTINUE
*Calculate the cosine of the angle between the normal and the approach vector.
        COSPSI=(X1*NSP(1)+X2*NSP(2)+X3*NSP(3))/VREL
*If the particle hits the face.
        IF (COSPSI.GT.0)  THEN
*Add the appropriate value to the appropriate totals.
        DO 47 I=1,MST,1
        ADDON=ADD*COSPSI*MFLUX(I)          (Define contribution from this
                                                direction, speed,size)
        SPACE=SPACE + ADDON                (total flux on face)
        ABV=ABS(VREL)
        IF (ABV.GT.SMAXV) SMAXV=ABV        (maximum impact velocity on face)
          LNORM=INT((VREL*COSPSI)/VBISIZ)       (calculate velocity distribution
          N=INT(VREL/VBISIZ)                          and normal velocity
          SVFDIS(LNORM)=SVFDIS(LNORM)+ADDON           distribution
          SCRVEL(N)=SCRVEL(N)+ADDON                   on face)
        PSI=ACOS(COSPSI)                   (calculate impact incidence angle)
        M= PSI*9/HAPI
        SANDIS(M)= SANDIS(M) + ADDON       (calculate distribution of impact angles)
        SBIN(N,M)= SBIN(N,M) + ADDON       (calc vel/ang distribution)
        BETA=0.69*((ROEP/ROET)**0.09)
        PTNDTH=0.6*((ROEP/ROET)**0.26)*((SIGT/80)**-0.08)*        (calc. Fmax)
     +DIAM(I)*((VREL*COSPSI)**BETA)
         IF (PTNDTH.NE.0) THEN
          MPTN=INT((log10(PTNDTH)+7)/0.2)
          IF (MPTN.GE.0) SPTN(MPTN)=SPTN(MPTN)+ADDON(distribution of Fmax)
         ENDIF
        DO 49 L=1,3,1
        N1(L)=NSP(L)
        N2(L)=NF(L,0)
        N3(L)=NF(L,9)
 49     CONTINUE
           CALL elip(N1,N2,N3,X,EPSI,PI,IFACE)    (source direction in plane of face)
           MM=INT(EPSI*36/PI2)
            IF (PTNDTH.GT.0.2e-5) THEN                (set fmax threshold)
```

```
            SPELI1(N,MM,M)=SPELI1(N,MM,M)+ADDON  (vel/ang1/ang2 distribution)
            SPELI2(MM)=SPELI2(MM)+ADDON*SIN(PSI)      (ellipticity estimate,
                                                      NEVER USED)
            SPELI3(MM,M)=SPELI3(MM,M)+ADDON     (ang1/ang2 distribution)
             DO 38 L=1,3,1
              N1(L)=NSP(L)
              N2(L)=-NF(L,0)
              N3(L)=-NF(L,9)
 38               CONTINUE
             CALL elip(N3,N1,N2,X,SI,PI,IFACE)        (ang in a plane perpendicular
             KLM=INT(SI*36/PI2)                       to direction of motion,
             SELIP4(KLM)=SELIP4(KLM)+ADDON            for a different coord. system
             SANGNV(LNORM,KLM)=SANGNV(LNORM,KLM)+ADDON NEVER
           ENDIF                                                    USED)


 47     CONTINUE
        END IF
*Calculate the cosine of the angle between the normal and the approach vector,
*For the Earth face (note: Normal to Earth face is the negative
*of the normal to the space face.
        COSPSI=(X1*(-NSP(1))+X2*(-NSP(2))+X3*(-NSP(3)))/VREL
*If the particle hits the face.

(Comments for the next section are as above but for the Earth face)

       IF (COSPSI.GT.0) THEN
*Add the appropriate value to the appropriate totals.
        DO 57 I=1,MST,1
        ADDON=ADD*COSPSI*MFLUX(I)
           EARTH=EARTH + ADDON
        ABV=ABS(VREL)
        IF (ABV.GT.EMAXV) EMAXV=ABV
       IF (EMAXV.LT.0) PRINT *, ABV
          LNORM=INT((VREL*COSPSI)/VBISIZ)

          N=INT(VREL/VBISIZ)
          EVFDIS(LNORM)=EVFDIS(LNORM)+ADDON
          ECRVEL(N)=ECRVEL(N)+ADDON
        PSI=ACOS(COSPSI)
        M= PSI*9/HAPI

       EANDIS(M)= EANDIS(M) + ADDON
       EBIN(N,M)= EBIN(N,M) + ADDON
       BETA=0.69*((ROEP/ROET)**0.09)
       PTNDTH=0.6*((ROEP/ROET)**0.26)*((SIGT/80)**-0.08)*
  +DIAM(I)*((VREL*COSPSI)**BETA)
         IF (PTNDTH.NE.0) THEN
          MPTN=INT((log10(PTNDTH)+7)/0.2)
          IF (MPTN.GE.0) EPTN(MPTN)=EPTN(MPTN)+ADDON

         ENDIF
        DO 59 L=1,3,1
         N1(L)=-NSP(L)
         N2(L)=NF(L,6)
         N3(L)=NF(L,9)
 59      CONTINUE
             CALL elip(N1,N2,N3,X,EPSI,PI,IFACE)
            MM=INT(EPSI*36/PI2)
```

```
            IF (PTNDTH.GT.0.2e-5) THEN
           EAELI1(N,MM,M)=EAELI1(N,MM,M)+ADDON
           EAELI2(MM)=EAELI2(MM)+ADDON*SIN(PSI)
           EAELI3(MM,M)=EAELI3(MM,M)+ADDON
                 DO 37 L=1,3,1
                  N1(L)=NSP(L)
                  N2(L)=-NF(L,6)
                  N3(L)=-NF(L,9)
37               CONTINUE
                 CALL elip(N3,N1,N2,X,SI,PI,IFACE)
                  KLM=INT(SI*36/PI2)
                  EELIP4(KLM)=EELIP4(KLM)+ADDON
                  EANGNV(LNORM,KLM)=EANGNV(LNORM,KLM)+ADDON
                ENDIF

57     CONTINUE
     END IF
     DO 150 K=0,(IFACE-1),1
*Calculate the cosine of the angle between the normal and the approach vector,
*For the peripheral faces.
          COSPSI=(X1*NF(1,K)+X2*NF(2,K)+X3*NF(3,K))/VREL
*If the particle hits the face.
*Add the appropriate value to the appropriate totals.
```

(Comments for the next section are as above but for the peripheral faces)

```
          IF (COSPSI.GT.0) THEN
           DO 27 I=1,MST,1
           ADDON=ADD*COSPSI*MFLUX(I)
           ABV=ABS(VREL)
           IF (ABV.GT.PMAXV(K)) PMAXV(K)=ABV
       IF (PMAXV(K).LT.0) PRINT *, ABV
           FACTOT(K)=FACTOT(K) + ADDON
           LNORM=INT((VREL*COSPSI)/VBISIZ)
           NVEL=INT(VREL/VBISIZ)
           PSI=ACOS(COSPSI)
           M=INT(PSI*9/HAPI)

           RANDIS(K,M)= RANDIS(K,M) + ADDON
           PCRVEL(K,NVEL)= PCRVEL(K,NVEL) + ADDON
           RVFDIS(K,LNORM)=RVFDIS(K,LNORM)+ADDON
           PBIN(K,NVEL,M)= PBIN(K,NVEL,M) + ADDON
           BETA=0.69*((ROEP/ROET)**0.09)
           PTNDTH=0.6*((ROEP/ROET)**0.26)*((SIGT/80)**
  +-0.08)*DIAM(I)*((VREL*COSPSI)**BETA)

        IF (PTNDTH.NE.0) THEN
            MPTN=INT((log10(PTNDTH)+7)/0.2)
         IF (MPTN.GE.0) PTN(K,MPTN)=PTN(K,MPTN)+ADDON

          ENDIF
           IF (K.GT.2) THEN
           LL=K-3
          ELSE
           LL=K+9
          ENDIF
          DO 39 L=1,3,1
           N1(L)=NF(L,K)
           N2(L)=NF(L,LL)
```

```
 39          CONTINUE
             CALL elip(N1,N2,NSP,X,EPSI,PI,IFACE)
            MM=INT(EPSI*36/PI2)
             IF (PTNDTH.GT.0.2e-5) THEN
            ELIP3(MM,M,K)=ELIP3(MM,M,K) + ADDON
            ELIP1(NVEL,MM,M,K)=ELIP1(NVEL,MM,M,K)+ADDON
            ELIP2(MM,K)=ELIP2(MM,K)+ADDON*SIN(PSI)
             DO 36 L=1,3,1
              N1(L)=NF(L,K)
              N2(L)=-NF(L,LL)
              N3(L)=-NSP(L)
 36           CONTINUE
             CALL elip(N3,N1,N2,X,SI,PI,IFACE)
              KLM=INT(SI*36/PI2)
              ELIP4(KLM,K)=ELIP4(KLM,K)+ADDON
            ANGNV(LNORM,KLM,K)=ANGNV(LNORM,KLM,K)+ADDON
            ENDIF
 27          CONTINUE
          END IF
 150  CONTINUE
     RETURN
     END



      SUBROUTINE RESULT(WHICH)
(Print out selected result sets)
      PARAMETER (IVBIN=80
     +,IPOBIN=17,IEQBIN=35,IPO2=179,
     +IEQ2=179,IVBIN2=800,RADIUS=6378,ATMOS=150,IFACE=12)
      LOGICAL WHICH(1:14)
      REAL DUM,TIMP,SPHTOT
*TIMP is the total number of impacts on the satellite.
*EARTH,SPACE are the total  number of
*impacts on the Earth and
*and space of the satellite.
      COMMON /RESARRAY/
FACTOT(0:IFACE),SVFDIS(0:IVBIN),SCRVEL(0:IVBIN)
     +,EVFDIS(0:IVBIN),ECRVEL(0:IVBIN)
     +,RVFDIS(0:IFACE,0:IVBIN),PCRVEL(0:IFACE,0:IVBIN),SANDIS(0:8)
     +,EANDIS(0:8),SBIN(0:IVBIN,0:8),EBIN(0:IVBIN,0:8)
     +,PBIN(0:IFACE,0:IVBIN,0:8),
     +RANDIS(0:IFACE,0:8)
     +,ELIP1(0:IVBIN,0:36,0:9,0:IFACE)
     +,SPELI1(0:IVBIN,0:36,0:9),EAELI1(0:IVBIN,0:36,0:9)
     +,ELIP2(0:36,0:IFACE)
     +,ELIP4(0:36,0:IFACE),ANGNV(0:IVBIN,0:36,0:IFACE)
     +,SELIP4(0:36),SANGNV(0:IVBIN,0:36)
     +,EELIP4(0:36),EANGNV(0:IVBIN,0:36)
     +,SPELI2(0:36),EAELI2(0:36)
     +,ELIP3(0:36,0:9,0:IFACE)
     +,SPELI3(0:36,0:9),EAELI3(0:36,0:9)
     +,SPTN(0:30),EPTN(0:30),PTN(0:IFACE,0:30)
     +,PMAXV(0:IFACE)
     +,AVTOT,EARTH,SPACE
     +,VELMAX,SMAXV,EMAXV
      COMMON /SPHRES/VELDIS(0:IVBIN),ANGDIS(0:IEQBIN,0:IPOBIN),
     +THEDIS(0:IEQBIN),PHIDIS(0:IPOBIN),SPHTOT
```

```
*VELDIS,THEDIS,PHIDIS are the results arrays for the spherical
*satellite.
*PHI,THETA are the centre points of these bins for results.
*SVFDIS,SCRVEL,EVFDIS,ECRVEL,RVFDIS,PCRVEL,SANDIS,EANDIS,SBIN
*,EBIN,PBIN,RANDIS are the velocity an angular
*results arrays for the actual satellite.
*FACTOT, are the total number of particles hitting the peripheral
*faces of the satellite and their effective total taking into account
*their angle of approach.
        COMMON /REALCALC2/ VBISIZ
       COMMON /INTCALC/ IPOUS,IEQUS,
     +IPOUS2,IEQUS2
      REAL PAVIMP(0:IFACE),PAVNOR(0:IFACE)
*IEQBIN,IPOBIN,IVBIN are the upper limits of the
*velocity and angular results  arrays.
*IPOUS,IEQUS are the size of these arrays (this is different
*since the arrays have been taken to start at zero instead of one)
*ie. IEQBIN=IEQUS-1.
*IFACE is the number of peripheral faces on the satellite.
    L=IFACE-1
    IF (WHICH(6)) THEN
     SAVIMP=0
     EAVIMP=0
     DO 3  I=0,L,1
      PAVIMP(I) = 0
 3   CONTINUE
     DO 16 I=0,IVBIN,1
      SAVIMP=SAVIMP+(SCRVEL(I)*(I*VBISIZ+(VBISIZ/2.0)))      (calculate average
      EAVIMP=EAVIMP+(ECRVEL(I)*(I*VBISIZ+(VBISIZ/2.0)))       impact velocities
       DO 19 K=0,L,1                                          on faces)
        PAVIMP(K)=PAVIMP(K)+(PCRVEL(K,I)*
   +     (I*VBISIZ+(VBISIZ/2.0)))
19     CONTINUE
16    CONTINUE
     WRITE(14,*) 'Average Impact velocities on faces'
       WRITE(14,50) ((mod((21-I),12)+1),I=1,IFACE,1)
     WRITE(14,40)((PAVIMP(K)/FACTOT(K)),K=0,L,1),(SAVIMP/SPACE)
   + ,(EAVIMP/EARTH)
    ENDIF

    IF (WHICH(7)) THEN
     DO 2  I=0,L,1
      PAVNOR(I) = 0
 2   CONTINUE
     WRITE(14,*) 'Average NORMAL velocities on faces'
     SAVNOR=0
     EAVNOR=0
     DO 26 I=0,IVBIN,1
      SAVNOR=SAVNOR+(SVFDIS(I)*(I*VBISIZ+(VBISIZ/2.0)))      (calculate average
      EAVNOR=EAVNOR+(EVFDIS(I)*(I*VBISIZ+(VBISIZ/2.0)))       normal impact
       DO 29 K=0,L,1                                          velocities)
        PAVNOR(K)=PAVNOR(K)+(RVFDIS(K,I)*
   +     (I*VBISIZ+(VBISIZ/2.0)))
29     CONTINUE
26    CONTINUE
     WRITE(14,50) ((mod((21-I),12)+1),I=1,IFACE,1)
     WRITE(14,40)((PAVNOR(K)/FACTOT(K)),K=0,L,1),(SAVNOR/SPACE)
   + ,(EAVNOR/EARTH)
```

```
      ENDIF

      IF (WHICH(1)) THEN
        OPEN(10,FILE='sph.res',STATUS='NEW',RECL=1200)
       DEGA=360/(IEQUS*2)
       DEGB=180/(IPOUS*2)
       WRITE(10, *) 'Velocity Distribution (Spherical Satellite)'
       WRITE(10,*)
       DO 10 I=0,IVBIN,1
         DUM=((I+I+1.0)/2.0)
         WRITE(10,60) DUM,(VELDIS(I)/SPHTOT)
10     CONTINUE
       WRITE(10,*)
       WRITE(10,*)
       WRITE(10,*) 'Angular Distribution'
       WRITE(10,*)
       WRITE(10,*) 'THETA DISTRIBUTION'
       DO 20 I=0,IEQBIN,1
         WRITE(10,*) ((2*I+1)*DEGA),',',(THEDIS(I)/SPHTOT)
20     CONTINUE
       WRITE(10,*)
       WRITE(10,*) 'PHI DISTRIBUTION'
       DO 30 I=0,IPOBIN,1
        WRITE(10,* ) ((2*I+1)*DEGB-90),',',(PHIDIS(I)/SPHTOT)
30     CONTINUE
      ENDIF

      IF (WHICH(2)) THEN
       TIMP=0
       TIMP = TIMP + SPACE + EARTH
       DO 17 K=0,IFACE,1
        TIMP = TIMP + FACTOT(K)          (calculate total impacting flux on all faces)
17     CONTINUE
       tumble=timp/14                    (average for a tumbling plate)
       WRITE(14,*)
       WRITE(14,*)
       WRITE(14,*) '  Flux On Faces'
       WRITE(14,50) ((mod((21-I),12)+1),I=1,IFACE,1)
       WRITE(14,40)((FACTOT(K)),K=0,L,1),(SPACE)
     +,(EARTH)
      ENDIF

      IF (WHICH(8)) THEN
       AVTOT=0
       DO 18 K=0,IVBIN,1
        AVTOT=AVTOT+(VELDIS(K)*(K*VBISIZ+(VBISIZ/2.0)))      (calculate
18     CONTINUE                                              average impact velocity
       WRITE(14,*) 'Average impact velocity=',AVTOT/SPHTOT   on spherical spacecraft)
      ENDIF

      IF (WHICH(4)) THEN
       WRITE(14,*) 'Distribution Of Normal Components Of'
       WRITE(14,*) ' Velocity  On Faces'
       DO 65 I=0,L,1
        WRITE(14,40) ((J*VBISIZ+(VBISIZ/2.0)),J=0,IVBIN,1)
        WRITE(14,40) ((RVFDIS(I,J)),J=0,IVBIN,1)
65     CONTINUE

       WRITE(14,40) ((J*VBISIZ+(VBISIZ/2.0)),J=0,IVBIN,1)
```

```
      WRITE(14,40)  ((SVFDIS(I)),I=0,IVBIN,1)
      WRITE(14,40) ((J*VBISIZ+(VBISIZ/2.0)),J=0,IVBIN,1)
      WRITE(14,40) ((EVFDIS(I)),I=0,IVBIN,1)
     ENDIF

     IF (WHICH(5)) THEN
      WRITE(14,*) 'Distribution Of Actual Impact'
      WRITE(14,*) ' Velocity  On Faces'
      DO 67 I=0,L,1
        WRITE(14,40) ((J*VBISIZ+(VBISIZ/2.0)),J=0,IVBIN,1)
        WRITE(14,40) ((PCRVEL(I,J)),J=0,IVBIN,1)
 67   CONTINUE
      WRITE(14,40) ((J*VBISIZ+(VBISIZ/2.0)),J=0,IVBIN,1)
      WRITE(14,40)  ((SCRVEL(I)),I=0,IVBIN,1)
      WRITE(14,40) ((J*VBISIZ+(VBISIZ/2.0)),J=0,IVBIN,1)
      WRITE(14,40) ((ECRVEL(I)),I=0,IVBIN,1)
     ENDIF

     IF (WHICH(3)) THEN
      WRITE(14,*) 'Angular Distribution On Faces'
      DO 66 I=0,L,1
        WRITE(14,50) (J,J=5,85,10)
        WRITE(14,40) ((RANDIS(I,J)),J=0,8,1)
 66   CONTINUE
      WRITE(14,50) (J,J=5,85,10)
      WRITE(14,40)  ((SANDIS(I)),I=0,8,1)
      WRITE(14,50) (J,J=5,85,10)
      WRITE(14,40) ((EANDIS(I)),I=0,8,1)
     ENDIF

     IF (WHICH(9)) THEN
      DO 121 K=0,L,1
        WRITE(16,50) ((360-J),J=5,355,10)
        WRITE(16,40) (ELIP2(J,K),J=0,35,1)
       WRITE(16,*)
 121   CONTINUE
      WRITE(16,50) ((360-J),J=5,355,10)
      WRITE(16,40) (SPELI2(J),J=0,35,1)
     WRITE(16,*)
      WRITE(16,50) ((360-J),J=5,355,10)
      WRITE(16,40) (EAELI2(J),J=0,35,1)
     ENDIF
     IF (WHICH(10)) THEN
        DO 77 I=29,0,-1
          DO 76 K=0,L,1
                PTN(K,I)=PTN(K,I)+PTN(K,(I+1))          (calculate cumulative fmax
 76       CONTINUE                                          distributions)
          SPTN(I)=SPTN(I)+SPTN((I+1))
          EPTN(I)=EPTN(I)+EPTN((I+1))
 77     CONTINUE

      WRITE(17,50) ((mod((21-I),12)+1),I=1,IFACE,1)
     DO 42 I=0,30,1
        WRITE (17,40) (10**((I/5.0)-7.0)),(PTN(K,I),K=0,L,1)
    +,SPTN(I),EPTN(I)
 42  CONTINUE
     ENDIF
     IF (WHICH(11)) THEN
      WRITE(14,50) ((mod((21-I),12)+1),I=1,IFACE,1)
```

```
      WRITE(14,40) (PMAXV(K), K=0,L,1),SMAXV,EMAXV
     ENDIF

     IF (WHICH(12)) THEN
      WRITE (16,*)
      WRITE(16,*) 'Directional information'
      DO 191 K=0,L,1
        WRITE(16,50) ((J),J=5,175,10)
        WRITE(16,40) (ELIP4(J,K),J=0,35,1)
       WRITE(16,*)
191    CONTINUE
       WRITE(16,50) ((J),J=5,175,10)
       WRITE(16,40) (SELIP4(J),J=0,35,1)
       WRITE(16,50) ((J),J=5,175,10)
       WRITE(16,40) (EELIP4(J),J=0,35,1)
     ENDIF
     IF (WHICH(14)) THEN
*       DO 127 K=0,L,1
*        Do 129 J=0,35
*        DO 124 N=0,8
*          ELIP3(J,N,K)=0
*         DO 128 I=0,IVBIN,1
*           ELIP3(J,N,K)=ELIP3(J,N,K)+ELIP1(I,J,N,K)
128      CONTINUE
124      CONTINUE
129      CONTINUE
127     CONTINUE


       WRITE(16,*) 'Absolute Directions'
       DO 134 K=0,L,1
        WRITE(16,55) ((360-J),J=5,355,10)
       DO 133 I=0,8,1
         WRITE(16,45) ((90-(I*10+5))),((ELIP3(J,I,K)),J=0,35,1)
133      CONTINUE
      WRITE(16,*)
134    CONTINUE
       WRITE(16,55) ((360-J),J=5,355,10)
       DO 131 I=0,8,1
         WRITE(16,45) ((90-(I*10+5))),((SPELI3(J,I)),J=0,35,1)
131      CONTINUE
      WRITE(16,*)
       WRITE(16,55) ((360-J),J=5,355,10)
       DO 132 I=0,8,1
         WRITE(16,45) ((90-(I*10+5))),((EAELI3(J,I)),J=0,35,1)
132      CONTINUE
      WRITE(16,*)
     ENDIF
     IF (WHICH(13)) THEN
      WRITE (16,*)
      WRITE(16,*) 'Velocity/Directional information'
      DO 197 K=0,L,1
        WRITE(16,55) ((360-J),J=5,355,10)
       DO 196 I=0,IVBIN,1
        WRITE(16,40) ((I*VBISIZ+(VBISIZ/2.0))),(ANGNV(I,J,K),J=0,35,1)
      WRITE(16,*)
196    CONTINUE
197   CONTINUE
       WRITE(16,55) ((360-J),J=5,355,10)
```

```
      DO 193 I=0,IVBIN,1
       WRITE(16,40) (I*VBISIZ+(VBISIZ/2.0)),(SANGNV(I,J),J=0,35,1)
      WRITE(16,*)
193     CONTINUE
       WRITE(16,55) ((360-J),J=5,355,10)
      DO 194 I=0,IVBIN,1
       WRITE(16,40) ((I*VBISIZ+(VBISIZ/2.0))),(EANGNV(I,J),J=0,35,1)
      WRITE(16,*)
194     CONTINUE
   ENDIF
40     FORMAT (E10.4,85(',',E10.4))
50     FORMAT (I10,85(',',I10))
55     FORMAT (' ',I10,85(',',I10))
45     FORMAT (' ',I10,85(',',E10.4))
60     FORMAT (1X,F4.1,',',F10.3)
    RETURN
    END



   SUBROUTINE mult(mat,vec1,vec2)

   REAL MAT(1:3,1:3),VEC1(1:3),VEC2(1:3)

   DO 20 I=1,3,1
   VEC2(I)=MAT(I,1)*VEC1(1)+MAT(I,2)*VEC1(2)+MAT(I,3)*VEC1(3)
20 CONTINUE      (routine performs transformations between different cartesian
   RETURN                coordinate systems)
   END



   SUBROUTINE elip(N1,N2,N3,X,EPSI,PI,IFACE)

   REAL N1(1:3),N2(1:3),N3(1:3)
  +    , MAT(1:3,1:3),FX(1:3)

   REAL EPSI

   DO 20 I=1,3,1          (takes a set of axis and a vector and calculates the angle from
    MAT(1,I)=N1(I)        the vector to the plane of the Y-Z axis)
    MAT(2,I)=N2(I)
    MAT(3,I)=N3(I)
20 CONTINUE
   call mult(MAT,X,FX)
   IF (FX(3).EQ.0) THEN
         IF (FX(2).LT.0) THEN
               EPSI= 1.5*PI
             ELSE
               EPSI= 0.5*PI
        ENDIF
       ELSE
        EPSI=atan(FX(2)/FX(3))
   ENDIF
    IF ((EPSI.LT.0).AND.(FX(3).GT.0)) THEN
         EPSI=EPSI+PI*2
       ELSE
```

```
      IF (FX(3).LT.0) EPSI=EPSI+PI
ENDIF
RETURN
END



 SUBROUTINE whatout(which)
                                    (allows user to select output)

CHARACTER*1 D

LOGICAL WHICH(1:14)


PRINT *,'Which data sets would you like as outputs'
PRINT *, 'Spherical satellite data (y/n).'
READ *,D
  WHICH(1)=((D.EQ.'y').OR.(D.EQ.'Y'))
PRINT *, 'The total  flux on each face (y/n).'
READ *,D
  WHICH(2)=((D.EQ.'y').OR.(D.EQ.'Y'))
PRINT *, 'The distribution in angle from the normal'
 PRINT *,'for each face (y/n).'
READ *,D
  WHICH(3)=((D.EQ.'y').OR.(D.EQ.'Y'))
PRINT *, 'The distribution of normal component of velocity'
 PRINT *, 'for each face (y/n).'
READ *,D
  WHICH(4)=((D.EQ.'y').OR.(D.EQ.'Y'))
PRINT *, 'The distribution of impact velocities on'
 PRINT *,'each face (y/n).'
READ *,D
  WHICH(5)=((D.EQ.'y').OR.(D.EQ.'Y'))
PRINT *, 'The average impact velocities on each face (y/n)'
READ *,D
  WHICH(6)=((D.EQ.'y').OR.(D.EQ.'Y'))
PRINT *, 'The average normal velocities on each face (y/n)'
READ *,D
  WHICH(7)=((D.EQ.'y').OR.(D.EQ.'Y'))
PRINT *, 'The maximum impact velocity on each face (y/n)'
READ *,D
  WHICH(11)=((D.EQ.'y').OR.(D.EQ.'Y'))
PRINT *, 'The average impact velocity on S/C (y/n)'
READ *,D
  WHICH(8)=((D.EQ.'y').OR.(D.EQ.'Y'))
PRINT *, 'The crater ellipticity data (y/n)'
READ *,D
  WHICH(9)=((D.EQ.'y').OR.(D.EQ.'Y'))
PRINT *, 'The penetration data (y/n)'
READ *,D
  WHICH(10)=((D.EQ.'y').OR.(D.EQ.'Y'))
PRINT *, 'The 2d directional information  (y/n)'
READ *,D
  WHICH(12)=((D.EQ.'y').OR.(D.EQ.'Y'))
PRINT *, 'The Velocity/directional information  (y/n)'
READ *,D
  WHICH(13)=((D.EQ.'y').OR.(D.EQ.'Y'))
```

```
PRINT *, 'The Absolute directional information  (y/n)'
READ *,D
  WHICH(14)=((D.EQ.'y').OR.(D.EQ.'Y'))
RETURN
END
```

Appendix 2

A listing of the code of the Space Debris model.

```
      PROGRAM impact
C----===============
C----calculates relative impact fluxes and angles due to
C----space debris on an orbiting spacecraft
C----SFG 17/6/91
C----Commented , subroutined and converted to LDEF by
C----This version works out ellipticity data for constant mass
C----Lets you choose the output data and numbers LDEF's faces
C----correctly
C---- Also works out penetrarion data and stores results in a
C----logarithmic array.
C---- And uses a mass distribution
C---- Uses the actual 6600 debris orbits instead of bins
C----ngm productions 28/7/92

*Declaration of constants.
          PARAMETER (IVBIN=80
     +,IPOBIN=17,IEQBIN=35,IPO2=179,
     +IEQ2=179,IVBIN2=800,RADIUS=6378,ATMOS=150,IFACE=12
     +,INC=36,IN2C=19,IA=8)

      LOGICAL WHICH(1:12)
      DIMENSION
     -        Q(IA),ZNBIN(7,IA),ALT1(IA),ALT2(IA),
     -        zv(0:25),zvr(0:25),zvc(0:25),
     -        zgam(-18:18),ZTHETA(-13:13),
     -        tzv(0:25),tzvr(0:25),tzvc(0:25),
     -        tzgam(-18:18),tzthet(-13:13)
C----E = midpoint of the four eccentricity bins
C----ORBIN = fraction of the debris in each "eccentricity X
C----Inclinatiuon X Altitude" bin.
C----B = lower boundary of lattitude bins
C----B1 = midpoint of lattitude bins
C----B2 = upper boundary of lattitude bins
C----ALT1,ALT2 = lower and upper bound of altitude bins
C----ZI = lower bound of inclination bins
C----Q = is a weighted average of the altitude bins
C----ZNBIN = sum over all debris orbits ofdebris in
C----altitude-latitude bin
C----VOL = the volume of the altitude-lattitude bin
C----zv = debris velocity
C----zvc = component of debris velocity which lies in sphere
C----zvr = radial coponent of debris velocity
C----zgam = the angle between zv and zvc
C----ZTHETA = angle between zvc and polar component of zvc

          COMMON /CALCARRAY/ OMFLUX(0:IPO2),PHI(0:IPO2),DOMEGA(0:IPO2),
     +THETA(0:IEQ2)
     +,DPHI,DTHETA
          COMMON /CALCARRAY2/ BIN(0:IVBIN,0:IEQBIN,0:IPOBIN)
          COMMON /SPHRES/VELDIS(0:IVBIN),ANGDIS(0:IEQBIN,0:IPOBIN),
     +THEDIS(0:IEQBIN),PHIDIS(0:IPOBIN),SPHTOT
          COMMON /RESARRAY/
FACTOT(0:IFACE),SVFDIS(0:IVBIN),SCRVEL(0:IVBIN)
     +,EVFDIS(0:IVBIN),ECRVEL(0:IVBIN)
     +,RVFDIS(0:IFACE,0:IVBIN),PCRVEL(0:IFACE,0:IVBIN),SANDIS(0:8)
     +,EANDIS(0:8),SBIN(0:IVBIN,0:8),EBIN(0:IVBIN,0:8)
     +,PBIN(0:IFACE,0:IVBIN,0:8),
     +RANDIS(0:IFACE,0:8)
```

```
     +,ELIP1(0:IVBIN,0:36,0:9,0:IFACE)
     +,SPELI1(0:IVBIN,0:36,0:9),EAELI1(0:IVBIN,0:36,0:9)
     +,ELIP2(0:36,0:IFACE)
     +,ELIP4(0:36,0:IFACE),ANGNV(0:IVBIN,0:36,0:IFACE)
     +,SELIP4(0:36),SANGNV(0:IVBIN,0:36)
     +,EELIP4(0:36),EANGNV(0:IVBIN,0:36)
     +,SPELI2(0:36),EAELI2(0:36)
     +,ELIP3(0:36,0:9,0:IFACE)
     +,SPELI3(0:36,0:9),EAELI3(0:36,0:9)
      +,SPTN(0:30),EPTN(0:30),PTN(0:IFACE,0:30)
     +,PMAXV(0:IFACE)
     +,AVTOT,EARTH,SPACE
     +,VELMAX,SMAXV,EMAXV
          REAL NF,MFLUX
          COMMON /DATAARRAY/ DIAM(1:30),MFLUX(1:30),NF(1:3,0:IFACE)

*SVFDIS,SCRVEL,EVFDIS,ECRVEL,RVFDIS,PCRVEL,SANDIS,EANDIS,SBIN,EBI
N,PBIN
*,RANDIS are the velocity an angular
*results arrays for the actual satellite.
*FACTOT, are the total number of particles hitting the peripheral
*faces of the satellite
*Variable declarations
          COMMON /REALCALC1/ SATVEL
          COMMON /REALCALC2/ VBISIZ
          COMMON /REALCALC3/ BETA,ROEP,ROET,SIGAL,SIGT
                COMMON /REAL9/ slimit
          COMMON /REALCALC4/ OFFSET,TILT
          COMMON /REALCALC5/ PARVEL,FLUX
          COMMON /REAL6/ PI
          COMMON /REAL7/ HAPI,PI2
          COMMON /REAL8/ PI4
*VBISIZ is the size if the velocity bins for the results arrays.
*BETA is the angle associated with Earth shielding.
*OFFSET,TILT are the offset and tilt of the satellite.
*EARTH,SPACE are the total number of
*impacts  on the Earth and
*and space of the satellite.
*SPHTOT is the total number of impacts on the spherical satellite.
*PI,PI2,PI4,HAPI are pi,2xpi,4xpi and pi/2
          COMMON /INTCALC/ IPOUS,IEQUS,
     +IPOUS2,IEQUS2
                COMMON /INTDAT/ MST

*IEQBIN,IPOBIN,IVBIN,IEQ2,IPO2, are the upper limits of the
*velocity and angular results and calculations arrays.
*IPOUS,IEQUS,IPOUS2,IEQUS2 are the size of these arrays (this is different
*since the arrays have been taken to start at zero instead of one)
*ie. IEQBIN=IEQUS-1.
*NFACE is the number of peripheral faces on the satellite.

C---- Initialise the data arrays
C---- Define Earths radius (in Km),the mass*gravity constant
C---- and the total volume of all the latitude bins
     DATA RE,ZMU,VOLTOT /6367.5,3.98E14,2.0E14/

C---- Open data and results files
      OPEN (10,STATUS='NEW')
       OPEN(15,FILE='info2.dat',STATUS='OLD')
```

```
      OPEN(18,FILE='siz.dis',STATUS='OLD')
      OPEN(19,FILE='orb.dis',STATUS='OLD')
      OPEN(14,FILE='dis2.res',STATUS='NEW',RECL=1200)
      OPEN(16,FILE='eli.res',STATUS='NEW',RECL=1200)
      OPEN(17,FILE='pen.res',STATUS='NEW',RECL=1200)


C---- Define Pi and the degrees-radians and radians-degrees
C---- Convertion factors
        IEQUS=IEQBIN+1
        IPOUS=IPOBIN+1
        IEQUS2= 5*IEQUS
        IPOUS2= 10*IPOUS

    PI=4.0*ATAN(1.0)
    DEGR=PI/180.0
    RDEG=180.0/PI
     PI2=2*PI
     PI4=4*PI
     HAPI=0.5*PI
C---- Read in initial data
    CALL REDAT(ALSIZ,SCA,Q,RE,SCALT,SCI,SCP,PI,
    +SCV,SCVR,SCVC,BINTOT,ZMU,IA,IN2,FUINC)
    HAINC=FUINC/2


    CALL whatout(which)
    CALL REDATA(SCALT)

    I=1
555  CONTINUE
    READ(18,*,END=888) DIAM(I),MFLUX(I)
       I=I+1
    GOTO 555
888  CONTINUE
    MST=I-1
    SPACE=0
    EARTH=0
    DO 41 K=0,NFACE,1
      FACTOT(K)=0
41   CONTINUE
    DO 42 I=0,IVBIN,1
       SVFDIS(I)=0
       SCRVEL(I)=0
       EVFDIS(I)=0
       ECRVEL(I)=0
       DO 43 J=0,NFACE,1
          RVFDIS(J,I)=0
43     CONTINUE
42   CONTINUE
    DO 44 I=0,8,1
      SANDIS(I)=0
      EANDIS(I)=0
      DO 45 J=0,NFACE,1
         RANDIS(J,I)=0
45     CONTINUE
44   CONTINUE
    SPHTOT=0
    VELMAX=0
```

```
C---- SET ALTITUDE, LATITUDE BIN
C---- ONLY PERFORM CALCULATIONS FOR BINS ENTERED BY S/C
      DO 2000 IB=1,IN2
        PRINT*,' STARTING IALT=',IALT,'  IB=',IB
C----   Calculate centre and boundaries of the altitude bin
        R1=SCA-(ALSIZ*500)
        R2=SCA+(ALSIZ*500)
        R=SCA
        B=(IB-1)*FUINC          (define midpoint of lattitude bin)
        IF (IB.EQ.1) THEN
          B1=0.0
              ELSE              (define lower boundary of lattitude bin)
          B1=B-HAINC
        ENDIF
        B2=B+HAINC              (define upper boundary of lattitude bin
C----   Calculate the angle between the spherical velocity of
C----   the spacecraft and the north direction
        CALL ZEETA(SCI,SCZETA,PI,SCSINTN,B,DEGR,SCTN,CSCZET,IB
     +,IN2)
C----   If the S/C never enters the lattitude bin then goto the
C----   end of the loop
        IF (SCI.LT.B1.OR.SCI.GT.180.0-B1) GOTO 2000
C----   Calculate the time the spacecraft spends in the latitude bin
        CALL latime(SCI,SCTN1,B1,DEGR,PI,B2,SCTN2,SCFB,IB,IN2)

C----   INITIALISE ARRAYS
       DO 51 I51=0,25
        ZV(I51)=0.0
        ZVC(I51)=0.0
        ZVR(I51)=0.0
   51   CONTINUE
       DO 52 I52=-18,18
        ZGAM(I52)=0.0
   52   CONTINUE
       DO 53 I53=-IN,IN
*        ZTHETA(I53)=0.0
   53   CONTINUE
*       ZNBIN(IB,IALT)=0.0
  111   CONTINUE
       READ(19,*,END=333) APO,PERI,ZINC,E     (read in debris orbital parameters)
          APO=APO*1000
          PERI=PERI*1000                      (convert to metres)
          PERC=1.0/6600.0    (define the proportion of the total, which one orbit represents)
          IF (PERI.GT.R2) GOTO 111          (check debris enters altitude bin)
          IF (APO.LT.R1) GOTO 111           ( andlattitude bins)
           IF ((ZINC.LT.B1).OR.(ZINC.GT.180.0-B1)) GOTO 111
          A=APO/(1.0+E)
          CALL ALTIM(E,FALT,R1,PERI,TP1,R2,APO,PI,TP2,A)          (calculate time
C---        For each possible debris inclination calculate the          spent in altitude bin)
C----       FRACTION OF TIME SPENT IN LATITUDE BIN (FB)
           CALL latime(ZINC,TN1,B1,DEGR,PI,B2,TN2,FB,IB,IN2)
C----       CALCULATE CONTRIBUTION TO BIN FROM THIS ORBIT
C----       DEN IS FRACTION OF TOTAL POPULATION PER M3
C----       The fraction of the debris in the bin
C----       is the amount of debris on given orbit  times the fraction
C----       of time spent in the bin
          FRAC=FB*FALT*PERC
C----       The density of debris in the bin is the fraction in the bin
```

```
C----         divided by the volume of the bin
                VOL=2*PI*(((SCALT+RE+ALSIZ/2)**3)-((SCALT+RE-ALSIZ
   +/2)**3))*(SIN(B2*DEGR)-SIN(B1*DEGR))/3

           DEN=FRAC*1.0E-9/VOL
C----        Add fraction from this orbit to the total in the altitude
C----        latitude bin
*            ZNBIN(IB,IALT)=ZNBIN(IB,IALT)+FRAC
C----O
C----        CALCULATION OF VELOCITIES
C----        (DO NOT INCLUDE IF APO.LT.R)
           IF (APO.GE.R) THEN
C----         Calculate the components of the debris velocity
            CALL CALVEL(E,R,I2,V,ZMU,A,VR,VC)
C----         Calculate the angle from the spherical component of
C----         the debris velocity to the north direction
            CALL ZEETA(ZINC,ZETA,PI,SINTN,B,DEGR,TN,CZETA,IB
   +,IN2)
c----         take 2 cases
           zeta2=pi-zeta                                    (see chap 4)
C----         Calculate the velocity of the debris relative to S/C
c----         case 1 (zeta)
            CALL RESVEL(VC,VR,SCVC,SCZETA,ZETA,RDEG,IV,IVC,IVR,
   + IGAM,ITHETA,ZV,ZVC,ZVR,ZGAM,ZTHETA,DEN,SCFB,FUINC,HAINC)

C----         case 2 (zeta2)
            CALL RESVEL(VC,VR,SCVC,SCZETA,ZETA2,RDEG,IV,IVC,IVR,
   + IGAM,ITHETA,ZV,ZVC,ZVR,ZGAM,ZTHETA,DEN,SCFB,FUINC,HAINC)
C----
           ENDIF
    GOTO 111
 333  CONTINUE
   REWIND(19)
C----    Compensate for only having done calculations for the upper
C----    half of the sphere
C----    DETERMINE MIRROR IMAGE BIN CONTENTS
*       ZTHETA(0)=ZTHETA(0)*2.0
       ZGAM(0)=ZGAM(0)*2.0
       DO 350 I35=1,18
        ZGAM(-I35)=ZGAM(I35)
 350    CONTINUE
       DO 360 I36=1,IN
*        ZTHETA(-I36)=ZTHETA(I36)
 360    CONTINUE
C----
 400  CONTINUE

C---- Tests of results
C    -          ALT2(IALT),Q(IALT),ZNBIN(IB,IALT),
C 9040  FORMAT(1X,'DISTRIBUTION OF IMPACT VELOCITIES OF SPACE
DEBRIS',//,
C    -      18X,'LATITUDE BIN = ',I1,/,
C    -       16X,'LATITUDE RANGE = ',F5.2,' TO ',F5.2,/,
C    -      18X,'ALTITUDE BIN = ' I1,/,
C    -       16X,'ALTITUDE RANGE = ',F6.0,' TO ',F6.0,' KM',/,
C    -      17X,'MEAN ALTITUDE = ',F6.0,' KM',/,
C    -      1X,'FRACTION OF POPULATION IN BIN = ',E9.3,/,
C    -      17X,'VOLUME OF BIN = ',E9.3,' KM**3',/,
C    -      15X,'FRACTION OF SKY = ',E9.3,/,
```

```
C     -      9X,'FRACTION PER CUBIC KM = ',E9.3,/
C     -       11X,'SPACECRAFT ALTITUDE = ',F8.1,' KM',/
C     -      8x,'SPACECRAFT INCLINATION = ',F5.2,' DEGREES',///)
C       WRITE(10,9050)
C 9050  FORMAT(1X,'IMPACT VELOCITY (KM.S-1)  V       VC     ABS(VR)')
C       DO 500 I5=0,25
C         WRITE (10,9051) FLOAT(I5)-0.5,FLOAT(I5)+0.5,ZV(I5),
C     -             ZVC(I5),ZVR(I5)
C  500  CONTINUE
C       WRITE(10,9060)
C 9060  FORMAT(//,1X,'IMPACT ANGLE (DEGREES)  GAMMA           ',
C     -          'ANGLE (DEGREES)  THETA')
C       DO 600 I6=-18,6
C         WRITE (10,9061) (FLOAT(I6)-0.5)*5.0,(FLOAT(I6)+0.5)*5.0,
C     -             ZGAM(I6),(FLOAT(I6)+5.5)*15.0,
C     -             (FLOAT(I6)+6.5)*15.0,ZTHETA(I6+6)
C  600  CONTINUE
C       DO 610 I61=7,18
C         WRITE (10,9062) (FLOAT(I61)-0.5)*5.0,(FLOAT(I61)+0.5)*5.0,
C     -             ZGAM(I61)
C  610  CONTINUE
c 9051   FORMAT (8X,F4.1,' - ',F4.1,3X,3(1X,E9.3))
c 9061    FORMAT(8X,F5.1,' - ',F5.1,3X,E9.3,10X,F6.1,' - ',F6.1,3X,E9.3)
c 9062   FORMAT(8X,F5.1,' - ',F5.1,3X,E9.3)
C----
c       BINTOT=BINTOT+ZNBIN(IB,IALT)
C----
C----   INCREMENT BINS FOR WHOLE OF S/C ORBIT
       DO 710 I71=0,25                          (spherical satellite)
         TZV(I71)=TZV(I71)+ZV(I71)
         TZVR(I71)=TZVR(I71)+ZVR(I71)
         TZVC(I71)=TZVC(I71)+ZVC(I71)
  710   CONTINUE
       DO 720 I72=-18,18
         TZGAM(I72)=TZGAM(I72)+ZGAM(I72)
  720   CONTINUE
       DO 730 I73=-IN,IN
*        TZTHET(I73)=TZTHET(I73)+ZTHETA(I73)
  730   CONTINUE
C----
 2000 CONTINUE
C---- ********************
C---- Write the results to a file
      CALL RESULTS(TZV,TZVC
     +,TZVR,TZGAM,TZTHET,SCALT,SCI,IN)
*Output results to file.
       CALL  RESULT(WHICH)

      STOP
      END

C*****************************************************************
C*****************************************************************



      SUBROUTINE RESULTS(TZV,TZVC
     +,TZVR,TZGAM,TZTHET,SCALT,SCI,IN)
C---- Writes the results to  a file              (spherical satellite)
```

```
      DIMENSION
     -      tzv(0:25),tzvr(0:25),tzvc(0:25),
     -      tzgam(-18:18),tzthet(-IN:IN)

C---- WRITE OUT RESULTS
      WRITE(10,9140) SCALT,SCI
 9140 FORMAT(1X,'DISTRIBUTION OF IMPACT VELOCITIES OF SPACE
DEBRIS',//,
     -    1X,'BINS CONTAIN FRACTION OF TOTAL DEBRIS POPULATION ',
     -    'IMPACTING PER M**2 PER S',//,
     -     11X,'SPACECRAFT ALTITUDE = ',F8.1,' KM',/
     -     8x,'SPACECRAFT INCLINATION = ',F5.2,' DEGREES',///)
      WRITE(10,9150)
 9150 FORMAT(1X,'IMPACT VELOCITY (KM.S-1)  V      VC     ABS(VR)')
      DO 810 I81=0,25
        WRITE (10,9151) FLOAT(I81)-0.5,FLOAT(I81)+0.5,TZV(I81),
     -          TZVC(I81),TZVR(I81)
  810 CONTINUE
      WRITE(10,9160)
 9160 FORMAT(//,1X,'IMPACT ANGLE (DEGREES)  GAMMA          ',
     -       'ANGLE (DEGREES)  THETA')
      DO 820 I82=-18,6
        WRITE (10,9161) (FLOAT(I82)-0.5)*5.0,(FLOAT(I82)+0.5)*5.0,
     -          TZGAM(I82),(FLOAT(I82)+5.5)*15.0,
     -          (FLOAT(I82)+6.5)*15.0,TZTHET(I82+6)
  820 CONTINUE
      DO 830 I83=7,18
        WRITE (10,9162) (FLOAT(I83)-0.5)*5.0,(FLOAT(I83)+0.5)*5.0,
     -          TZGAM(I83)
  830 CONTINUE
 9151  FORMAT (8X,F4.1,' - ',F4.1,3X,3(1X,E9.3))
 9161  FORMAT(8X,F5.1,' - ',F5.1,3X,E9.3,10X,F6.1,' - ',F6.1,3X,E9.3)
 9162  FORMAT(8X,F5.1,' - ',F5.1,3X,E9.3)
C----
      END




      SUBROUTINE REDAT(ALSIZ,SCA,Q,RE,SCALT,SCI,SCP,PI,
     +SCV,SCVR,SCVC,BINTOT,ZMU,IA,IN2,ANG)
C---- Reads in the initial data

C---- READ S/C ORBIT DATA
      WRITE (6,*) ' SPACECRAFT ORBIT PARAMETERS'
      WRITE (6,*) ' ORBIT ALTITUDE ? (in km)'
      READ (5,*) SCALT
      WRITE (6,*) ' Altitude bin size ? (in km)'

      READ *,ALSIZ
      WRITE (6,*) 'Angle bin size ? (in degrees)'
      READ (5,*) ANG
      TIN2=(90.0/ANG)
      IF (TIN2.NE.INT(TIN2)) THEN
```

```
        IN2=INT(TIN2+1)
                ELSE
        IN2=INT(TIN2)
      ENDIF
      PRINT *,TIN2,ANG
      ANG=90.0/REAL(IN2)
      WRITE (6,*) 'Angle taken as ',ANG

C---- Calculate radius of orbit im metres.
      SCA=(SCALT+RE)*1000.0
C---- Assign the altidude to the orbit
      WRITE (6,*) ' INCLINATION (DEG)?'
      READ (5,*) SCI
C---- Calculate the period of the orbit
      SCP=2.0*PI*SQRT(SCA**3/ZMU)
C---- Calculate the orbital velocity at this altitude.
      SCV=SQRT(ZMU/SCA)
C---- Set the radial component of velocity to zero
      SCVR=0.0
C---- Set the spherical component to be the same as the orbital
C---- velocity (no radial component)
      SCVC=SCV

C----
C----
      BINTOT=0.0
C----
      END




      SUBROUTINE ZEETA(XI,ZET,PI,SNT,B,DEGR,T,CSZET,IB,IN2)
C---- Calculate the angle between the spherical component of an
C---- objects velocity and the north direction


C---- If the inclination of the orbit is zero
      IF (XI.EQ.0.0) THEN
C---- Then angle between velocity and north pole direction is Pi/2
       ZET=PI/2.0
      ELSE
C----  Otherwise calculate  sin(2*Pi*T/P) where T is the time
C----  , from node, at which the object reaches the midpoint of the
C----  latitude bin and P is the period of orbit (equation 2.5.4.4)
       SNT=SIN(B*DEGR)/SIN(XI*DEGR)
C----  Compensate for rounding errors
       IF (SNT.GT.1.0) SNT=1.0
C----  Calculate (2*Pi*T/P), the length of the arc up to the point
C----  of entering the latitude bin.
       T=ASIN(SNT)
C----  Calculate the Cos of the angle between the objects
C----  velocity and the North direction (equation 2.5.4.3)
       CSZET=(SIN(XI*DEGR)/COS(B*DEGR)*COS(T))
C----  Check for errors and print a warning
```

```
      IF (CSZET.GT.1.0.OR.CSZET.LT.-1.0) THEN
        PRINT*,'***',CSZET
         PRINT*,'SCI,IB,SCTN',XI,IB,T
      ENDIF
C---- Compensate for rounding errors and calculate the actual angle
      IF (CSZET.GT.1.0) CSZET=1.0
      ZET=ACOS(CSZET)
C---- Check which sector the object was in and adjust zeta
C---- accordingly
      IF (XI.GT.90.0) ZET=-ZET
    ENDIF

    END




    SUBROUTINE RESVEL(VC,VR,SCVC,SCZETA,ZETA,RDEG,IV,IVC,IVR,IGAM
    + ,ITHETA,ZV,ZVC,ZVR,ZGAM,ZTHETA,DEN,SCFB,FUINC,HAINC)
C---- Calculate the relative velocity of the debri on the S/C

        PARAMETER (IVBIN=80
   +,IPOBIN=17,IEQBIN=35,IPO2=179,
   +IEQ2=179,IVBIN2=800,RADIUS=6378,ATMOS=150,IFACE=12
   +,INC=36,IN2C=19,IA=8)
    DIMENSION ZV(0:25),ZVC(0:25),ZVR(0:25),ZGAM(-18:18)
   +,ZTHETA(-13:13)
     COMMON /CALCLOC/ VREL
        COMMON /CALCLOC3/ ADD

        COMMON /SPHRES/VELDIS(0:IVBIN),ANGDIS(0:IEQBIN,0:IPOBIN),
   +THEDIS(0:IEQBIN),PHIDIS(0:IPOBIN),SPHTOT
        COMMON /RESARRAY/
FACTOT(0:IFACE),SVFDIS(0:IVBIN),SCRVEL(0:IVBIN)
   +,EVFDIS(0:IVBIN),ECRVEL(0:IVBIN)
   +,RVFDIS(0:IFACE,0:IVBIN),PCRVEL(0:IFACE,0:IVBIN),SANDIS(0:8)
   +,EANDIS(0:8),SBIN(0:IVBIN,0:8),EBIN(0:IVBIN,0:8)
   +,PBIN(0:IFACE,0:IVBIN,0:8),
   +RANDIS(0:IFACE,0:8)
   +,ELIP1(0:IVBIN,0:36,0:9,0:IFACE)
   +,SPELI1(0:IVBIN,0:36,0:9),EAELI1(0:IVBIN,0:36,0:9)
   +,ELIP2(0:36,0:IFACE)
   +,ELIP4(0:36,0:IFACE),ANGNV(0:IVBIN,0:36,0:IFACE)
   +,SELIP4(0:36),SANGNV(0:IVBIN,0:36)
   +,EELIP4(0:36),EANGNV(0:IVBIN,0:36)
   +,SPELI2(0:36),EAELI2(0:36)
   +,ELIP3(0:36,0:9,0:IFACE)
   +,SPELI3(0:36,0:9),EAELI3(0:36,0:9)
   +,SPTN(0:30),EPTN(0:30),PTN(0:IFACE,0:30)
   +,PMAXV(0:IFACE)
   +,AVTOT,EARTH,SPACE
   +,VELMAX,SMAXV,EMAXV
        REAL NF,MFLUX
        COMMON /DATAARRAY/ DIAM(1:30),MFLUX(1:30),NF(1:3,0:IFACE)
```

```
C---- DETERMINE RESULTANT VELOCITIES ON S/C
C---- DEFINE THETA AS ANGLE IN L-B PLANE FROM S/C VELOCITY VECTOR
C---- (The angle between the spacecraft orbuital velocity and the
C---- orbital impact velocity)
C---- Calculate the relative orbital velocity between S/C and debris
      XVC=SQRT((VC*VC)+(SCVC*SCVC)-(2.0*VC*SCVC*COS(SCZETA-ZETA)))
      IF (XVC.EQ.0.0) THEN
       COSTHT=1.0
      ELSE
C---- Calculate Cos theta
       COSTHT=((XVC*XVC)+(SCVC*SCVC)-(VC*VC))/(2.0*XVC*SCVC)
      ENDIF
C---- Check for rounding error and print out error message
      IF (COSTHT.GT.1.0) THEN
       COSTHT=1.0
        PRINT*,' ROUNDING ERROR, COSTHETA=1.0'
      ENDIF
      IF (COSTHT.LT.-1.0) THEN
       COSTHT=-1.0
      ENDIF
C---- Calculate theta
      THETA=ACOS(COSTHT)
C---- The relative radial velocity is the debris radial velocity
      XVR=VR
C---- Calculate the total relative velocity
      XV=SQRT(XVC*XVC+XVR*XVR)
      IF (XV.EQ.0.0) THEN
C----  If the total relative velocity equals zero then the angle to
C----  the radial component is zero
       XGAM=0.0
      ELSE
C----  Otherwise calculate the angle to the radial component
       XGAM=ACOS(XVC/XV)
      ENDIF
C----
C---- INCREMENT BINS
C---- FLUX(NUMBER M-2 HITTING S/C PER SEC)= SUM DEN*XV*SCFB
C---- Calculate the index numbers to increment the 3 velocity bins
C---- and the two angular bins
      IV=INT(XV/1000.0+0.5)
      IVC=INT(XVC/1000.0+0.5)
      IVR=INT(XVR/1000.0+0.5)
      IGAM=INT((XGAM*RDEG+2.5)/5.0)
      ITHETA=INT((THETA*RDEG+HAINC)/FUINC)
C---- Increment the bins appropriately
      ZV(IV)=ZV(IV)+DEN*XV*SCFB*0.5
      ZVC(IVC)=ZVC(IVC)+DEN*XV*SCFB*0.5
      ZVR(IVR)=ZVR(IVR)+DEN*XV*SCFB*0.5
      ZGAM(IGAM)=ZGAM(IGAM)+DEN*XV*SCFB/4.0
*      ZTHETA(ITHETA)=ZTHETA(ITHETA)+DEN*XV*SCFB/4.0
      ADD=DEN*XV*SCFB/8.0
      SPHTOT=SPHTOT+DEN*XV*SCFB
(for 4 cases below see chapter 4)
      VREL=XV/1000
      X1=XVC*COSTHT/1000
      X2=XVC*SIN(THETA)/1000
      X3=XVR/1000
      IF (VREL.NE.0) THEN
          CALL FACE(X1,X2,X3)
```

```
      X1=XVC*COSTHT/1000
      X2=XVC*SIN(-THETA)/1000
      X3=XVR/1000
          CALL FACE(X1,X2,X3)
      X1=XVC*COSTHT/1000
      X2=XVC*SIN(THETA)/1000
      X3=-XVR/1000
      IF (VREL.NE.0) THEN
          CALL FACE(X1,X2,X3)
      X1=XVC*COSTHT/1000
      X2=XVC*SIN(-THETA)/1000
      X3=-XVR/1000
          CALL FACE(X1,X2,X3)
      ENDIF
      ENDIF
      END



      SUBROUTINE latime(XI,T1,B1,DEGR,PI,B2,T2,FR,IB,IN2)
C---- Calculate the time an object spends in a latitude bin
C---- If the inclination is zero then the object enters the
C---- latitude bin at T1=0
      IF (XI.EQ.0.0) THEN
       T1=0.0
C---- Otherwise calculate the time round the orbit at which
C---- the object enters the latitude biun
      ELSE
       T1=ASIN(SIN(B1*DEGR)/SIN(XI*DEGR))/(2.0*PI)
      ENDIF
C---- If object leaves the latitude bin then calculate the time
C---- at which it leaves it
      IF (XI.GT.B2.AND.XI.LT.(180.0-B2)) THEN
       T2=ASIN(SIN(B2*DEGR)/SIN(XI*DEGR))/(2.0*PI)
      ELSE
C----   Otherwise set the time to 1/4 of the period
       T2=0.25
      ENDIF
C---- Calculate the time spent in each latitude bin
      FR=2.0*(T2-T1)

      END



      SUBROUTINE ALTIM(E,FALT,R1,PERI,TP1,R2,APO,PI,TP2,A)
C---- Calculate the amount of time spent in the altitude bin

C---- FRACTIONAL TIME SPENT IN ALTITUDE BIN (FALT)
C---- If the eccentricity of the objects orbit is zero then the
C---- object spends it's whole orbit in the same altitude bin
      IF (E.EQ.0.0) THEN
```

```
      FALT=1.0
     ELSE
C----  If the perigee of the object is greater than the lower
C----  bound of the altitude bin then the time for entering
C----  that bin is zero
      IF (R1.LE.PERI) THEN
       TP1=0.0
C----    Otherwise calculate the time for entering that bin
      ELSE
       EANOM1=ACOS((1.0-R1/A)/E)
       TP1=(EANOM1-E*SIN(EANOM1))/(2.0*PI)
      ENDIF
C----  If the apogee is less than the upper bound of the altitude
C----  bin then set the time for leaving to be 0.5
      IF (R2.GE.APO) THEN
       TP2=0.5
      ELSE
C----    Otherwise calculate the time for leaving the altitude bin
       EANOM2=ACOS((1.0-R2/A)/E)
       TP2=(EANOM2-E*SIN(EANOM2))/(2.0*PI)
      ENDIF
C----  Calculate the amount of time spent in the altitude bin
C----  (going up and down)
      FALT=2.0*(TP2-TP1)
     ENDIF

     END



     SUBROUTINE CALVEL(E,R,I2,V,ZMU,A,VR,VC)
C---- Calculate the components of an objects velocity

C---- Calculate the velocity of the object in the qei-bin
     V=SQRT(ZMU*(2.0/R-1.0/A))
C---- Calculate Cos of angle between the velocity vector and the
C---- tangential plane
     COSGAM=SQRT(A*A*(1.0-E*E)/
    -          (R*(2.0*A-R)))
C---- Test for rounding errors and print a warning
      IF (COSGAM.GT.1.0) THEN
*       PRINT*,'ROUNDING ERROR, COSGAM=',COSGAM
       COSGAM=1.0
      ENDIF
      IF (COSGAM.LT.0.0) THEN
       PRINT*,'ROUNDING ERROR, COSGAM=',COSGAM
      ENDIF
C---- Calculate the actual angle
     GAM=ACOS(COSGAM)
C---- Calculate the radial component of the velocity
     VR=V*SIN(GAM)
C---- Calculte the spherical component of the velocity
     VC=V*COSGAM
     END
```

```
      SUBROUTINE REDATA(SCALT)
*Read in user input parameters.
            COMMON /REALCALC1/ SATVEL
            COMMON /REALCALC2/ VBISIZ
            COMMON /REALCALC3/ BETA,ROEP,ROET,SIGAL,SIGT
            COMMON /REALCALC4/ OFFSET,TILT
            COMMON /REAL7/ HAPI,PI2
            COMMON /REAL9/ slimit
           PARAMETER (IVBIN=80
     +,IPOBIN=17,IEQBIN=35,IPO2=179,
     +IEQ2=179,IVBIN2=800,RADIUS=6378,ATMOS=150,IFACE=12)
            COMMON /INTCALC/ IPOUS,IEQUS,
     +IPOUS2,IEQUS2


      REAL ALPHA,HEIGHT
*Request and read in parameters.
*Calculate appropriate angular array sizes.
      PRINT *,'Please enter the size of the velocity bins.'
      READ(15,*) VBISIZ
*Calculate appropriate velocity array size.
      VBI2=VBISIZ/10
      HEIGHT=SCALT
*Calculate  the angle associated with Earth shielding.
      ALPHA=ASIN((RADIUS+ATMOS)/(RADIUS + HEIGHT))
      slimit=ALPHA - HAPI
      PRINT *,'Please enter the no. of faces round satellite, it''s
     +offset and tilt.'
      READ(15,*) OFF,TIL
      READ(15,*) ROEP,ROET,SIGAL,SIGT
      OFFSET=OFF*PI2/360
      TILT=TIL*PI2/360
      RETURN
      END
```

(For comments on the rest of the subroutines see the appropriate sections of the IP dust model)

```
      SUBROUTINE FACE(X1,X2,X3)

*IFACE is the number of peripheral faces on the satellite.
*IVBIN is the size of the velocity results arrays
      PARAMETER (IVBIN=80
     +,IPOBIN=17,IEQBIN=35,IPO2=179,
     +IEQ2=179,IVBIN2=800,RADIUS=6378,ATMOS=150,IFACE=12)
           COMMON /REALCALC3/ BETA,ROEP,ROET,SIGAL,SIGT
           COMMON /REALCALC4/ OFFSET,TILT
           COMMON /REALCALC2/ VBISIZ
          COMMON /CALCLOC/ VREL
      COMMON /CALCLOC3/ ADD

           COMMON /REAL6/ PI
      REAL COSPSI,ADDON
       REAL N1(1:3),N2(1:3),N3(1:3),NSP(1:3),X(1:3)
*N1,N2,N3,N1SPA,N2SPA,N3SPA are the normal vectors to the space and
*the peripherel faces (Normal to Earth face is negative the normal to
*the space face.
*VREL is the velocity of the particle relative to the satellite.
*VBISIZ is the size if the velocity bins for the results arrays.
*OFFSET,TILT are the offset and tilt of the satellite.
*EARTH,SPACE are the total  number of
*impacts  on the Earth and
*and space of the satellite.
*X1,X2,X3 are the approach vector of the particle in cartesian co_ordinates.

     COMMON /RESARRAY/
FACTOT(0:IFACE),SVFDIS(0:IVBIN),SCRVEL(0:IVBIN)
    +,EVFDIS(0:IVBIN),ECRVEL(0:IVBIN)
    +,RVFDIS(0:IFACE,0:IVBIN),PCRVEL(0:IFACE,0:IVBIN),SANDIS(0:8)
    +,EANDIS(0:8),SBIN(0:IVBIN,0:8),EBIN(0:IVBIN,0:8)
    +,PBIN(0:IFACE,0:IVBIN,0:8),
    +RANDIS(0:IFACE,0:8)
    +,ELIP1(0:IVBIN,0:36,0:9,0:IFACE)
    +,SPELI1(0:IVBIN,0:36,0:9),EAELI1(0:IVBIN,0:36,0:9)
    +,ELIP2(0:36,0:IFACE)
    +,ELIP4(0:36,0:IFACE),ANGNV(0:IVBIN,0:36,0:IFACE)
    +,SELIP4(0:36),SANGNV(0:IVBIN,0:36)
    +,EELIP4(0:36),EANGNV(0:IVBIN,0:36)
    +,SPELI2(0:36),EAELI2(0:36)
    +,ELIP3(0:36,0:9,0:IFACE)
    +,SPELI3(0:36,0:9),EAELI3(0:36,0:9)
    +,SPTN(0:30),EPTN(0:30),PTN(0:IFACE,0:30)
    +,PMAXV(0:IFACE)
    +,AVTOT,EARTH,SPACE
    +,VELMAX,SMAXV,EMAXV
      REAL NF,MFLUX
        COMMON /DATAARRAY/ DIAM(1:30),MFLUX(1:30),NF(1:3,0:IFACE)
      COMMON /INTDAT/ MST
           COMMON /REAL7/ HAPI,PI2
```

```
*SVFDIS,SCRVEL,EVFDIS,ECRVEL,RVFDIS,PCRVEL,SANDIS,EANDIS,SBIN
*,EBIN,PBIN,RANDIS are the velocity an angular
*results arrays for the actual satellite.
*FACTOT are the total number of particles hitting the peripheral
*faces of the satellite

*Calculate the angle between the normals to the peripheral faces.

      DFACE=PI2/IFACE
      TOTHIR=2.0/3.0
      X(1)=X1
      X(2)=X2
      X(3)=X3
*Calculate the normal vector to the space face.
      NSP(1)=SIN(TILT)*COS(OFFSET)
      NSP(2)=SIN(OFFSET)*SIN(TILT)
      NSP(3)=COS(TILT)
      DO 155 K=0,(IFACE-1),1
        THEFAC=DFACE*K
*Calculate the normal vector to the peripheral faces.

        NF(1,K)=COS(THEFAC)*COS(TILT)*COS(OFFSET)-
     +SIN(THEFAC)*SIN(OFFSET)
        NF(2,K)=COS(THEFAC)*COS(TILT)*SIN(OFFSET)+
     +SIN(THEFAC)*COS(OFFSET)
        NF(3,K)=-SIN(TILT)*COS(THEFAC)
 155    CONTINUE
*Calculate the cosine of the angle between the normal and the approach vector.
         COSPSI=(X1*NSP(1)+X2*NSP(2)+X3*NSP(3))/VREL
       IF ((COSPSI.GT.1.0).AND.(COSPSI.LT.1.000001)) COSPSI=1.0
*If the particle hits the face.
         IF (COSPSI.GT.0)  THEN
*Add the appropriate value to the appropriate totals.
        DO 47 I=1,MST,1
        ADDON=ADD*COSPSI*MFLUX(I)
        SPACE=SPACE + ADDON
        ABV=ABS(VREL)
        IF (ABV.GT.SMAXV) SMAXV=ABV
           LNORM=INT((VREL*COSPSI)/VBISIZ)
           N=INT(VREL/VBISIZ)
           SVFDIS(LNORM)=SVFDIS(LNORM)+ADDON
           SCRVEL(N)=SCRVEL(N)+ADDON
        PSI=ACOS(COSPSI)
        M= PSI*9/HAPI
        SANDIS(M)= SANDIS(M) + ADDON
        SBIN(N,M)= SBIN(N,M) + ADDON
        BETA=0.69*((ROEP/ROET)**0.09)
        PTNDTH=0.6*((ROEP/ROET)**0.26)*((SIGT/80)**-0.08)*
     +DIAM(I)*((VREL*COSPSI)**BETA)
          IF (PTNDTH.NE.0) THEN
           MPTN=INT((log10(PTNDTH)+7)/0.2)
           IF (MPTN.GE.0) SPTN(MPTN)=SPTN(MPTN)+ADDON

          ENDIF
        DO 49 L=1,3,1
         N1(L)=NSP(L)
         N2(L)=NF(L,0)
         N3(L)=NF(L,9)
 49     CONTINUE
```

```
            CALL elip(N1,N2,N3,X,EPSI,PI,IFACE)
           MM=INT(EPSI*36/PI2)
            IF (PTNDTH.GT.0.2e-5) THEN
           SPELI1(N,MM,M)=SPELI1(N,MM,M)+ADDON
           SPELI2(MM)=SPELI2(MM)+ADDON*SIN(PSI)
           SPELI3(MM,M)=SPELI3(MM,M)+ADDON
            DO 38 L=1,3,1
             N1(L)=NSP(L)
             N2(L)=-NF(L,0)
             N3(L)=-NF(L,9)
38               CONTINUE
            CALL elip(N3,N1,N2,X,SI,PI,IFACE)
            KLM=INT(SI*36/PI2)
            SELIP4(KLM)=SELIP4(KLM)+ADDON
            SANGNV(LNORM,KLM)=SANGNV(LNORM,KLM)+ADDON
           ENDIF


 47     CONTINUE
        END IF
*Calculate the cosine of the angle between the normal and the approach vector,
*For the Earth face (note: Normal to Earth face is the negative
*of the normal to the space face.
        COSPSI=(X1*(-NSP(1))+X2*(-NSP(2))+X3*(-NSP(3)))/VREL
         IF ((COSPSI.GT.1.0).AND.(COSPSI.LT.1.000001)) COSPSI=1.0
*If the particle hits the face.
       IF (COSPSI.GT.0) THEN
*Add the appropriate value to the appropriate totals.
        DO 57 I=1,MST,1
        ADDON=ADD*COSPSI*MFLUX(I)
           EARTH=EARTH + ADDON
        ABV=ABS(VREL)
        IF (ABV.GT.EMAXV) EMAXV=ABV
       IF (EMAXV.LT.0) PRINT *, ABV
          LNORM=INT((VREL*COSPSI)/VBISIZ)

          N=INT(VREL/VBISIZ)
          EVFDIS(LNORM)=EVFDIS(LNORM)+ADDON
          ECRVEL(N)=ECRVEL(N)+ADDON
        PSI=ACOS(COSPSI)
        M= PSI*9/HAPI

       EANDIS(M)= EANDIS(M) + ADDON
       EBIN(N,M)= EBIN(N,M) + ADDON
       BETA=0.69*((ROEP/ROET)**0.09)
       PTNDTH=0.6*((ROEP/ROET)**0.26)*((SIGT/80)**-0.08)*
  +DIAM(I)*((VREL*COSPSI)**BETA)
         IF (PTNDTH.NE.0) THEN
          MPTN=INT((log10(PTNDTH)+7)/0.2)
          IF (MPTN.GE.0) EPTN(MPTN)=EPTN(MPTN)+ADDON

         ENDIF
        DO 59 L=1,3,1
         N1(L)=-NSP(L)
         N2(L)=NF(L,6)
         N3(L)=NF(L,9)
59       CONTINUE
             CALL elip(N1,N2,N3,X,EPSI,PI,IFACE)
            MM=INT(EPSI*36/PI2)
```

```
            IF (PTNDTH.GT.0.2e-5) THEN
           EAELI1(N,MM,M)=EAELI1(N,MM,M)+ADDON
           EAELI2(MM)=EAELI2(MM)+ADDON*SIN(PSI)
           EAELI3(MM,M)=EAELI3(MM,M)+ADDON
                 DO 37 L=1,3,1
                  N1(L)=NSP(L)
                  N2(L)=-NF(L,6)
                  N3(L)=-NF(L,9)
37                CONTINUE
                  CALL elip(N3,N1,N2,X,SI,PI,IFACE)
                   KLM=INT(SI*36/PI2)
                   EELIP4(KLM)=EELIP4(KLM)+ADDON
                   EANGNV(LNORM,KLM)=EANGNV(LNORM,KLM)+ADDON
                 ENDIF

57      CONTINUE
      END IF
     DO 150 K=0,(IFACE-1),1
*Calculate the cosine of the angle between the normal and the approach vector,
*For the peripheral faces.
            COSPSI=(X1*NF(1,K)+X2*NF(2,K)+X3*NF(3,K))/VREL
         IF ((COSPSI.GT.1.0).AND.(COSPSI.LT.1.000001)) COSPSI=1.0
*If the particle hits the face.
*Add the appropriate value to the appropriate totals.
           IF (COSPSI.GT.0) THEN
            DO 27 I=1,MST,1
            ADDON=ADD*COSPSI*MFLUX(I)
            ABV=ABS(VREL)
            IF (ABV.GT.PMAXV(K)) PMAXV(K)=ABV
       IF (PMAXV(K).LT.0) PRINT *, ABV
            FACTOT(K)=FACTOT(K) + ADDON
            LNORM=INT((VREL*COSPSI)/VBISIZ)
            NVEL=INT(VREL/VBISIZ)
            PSI=ACOS(COSPSI)
            M=INT(PSI*9/HAPI)

            RANDIS(K,M)= RANDIS(K,M) + ADDON
            PCRVEL(K,NVEL)= PCRVEL(K,NVEL) + ADDON
            RVFDIS(K,LNORM)=RVFDIS(K,LNORM)+ADDON
            PBIN(K,NVEL,M)= PBIN(K,NVEL,M) + ADDON
            BETA=0.69*((ROEP/ROET)**0.09)
            PTNDTH=0.6*((ROEP/ROET)**0.26)*((SIGT/80)**
  +-0.08)*DIAM(I)*((VREL*COSPSI)**BETA)

        IF (PTNDTH.NE.0) THEN
             MPTN=INT((log10(PTNDTH)+7)/0.2)
          IF (MPTN.GE.0) PTN(K,MPTN)=PTN(K,MPTN)+ADDON

           ENDIF
            IF (K.GT.2) THEN
            LL=K-3
           ELSE
            LL=K+9
           ENDIF
           DO 39 L=1,3,1
            N1(L)=NF(L,K)
            N2(L)=NF(L,LL)
39          CONTINUE
           CALL elip(N1,N2,NSP,X,EPSI,PI,IFACE)
```

```
          MM=INT(EPSI*36/PI2)
           IF (PTNDTH.GT.0.2e-5) THEN
          ELIP3(MM,M,K)=ELIP3(MM,M,K) + ADDON
          ELIP1(NVEL,MM,M,K)=ELIP1(NVEL,MM,M,K)+ADDON
          ELIP2(MM,K)=ELIP2(MM,K)+ADDON*SIN(PSI)
           DO 36 L=1,3,1
            N1(L)=NF(L,K)
            N2(L)=-NF(L,LL)
            N3(L)=-NSP(L)
36          CONTINUE
           CALL elip(N3,N1,N2,X,SI,PI,IFACE)
            KLM=INT(SI*36/PI2)
            ELIP4(KLM,K)=ELIP4(KLM,K)+ADDON
          ANGNV(LNORM,KLM,K)=ANGNV(LNORM,KLM,K)+ADDON
          ENDIF
27          CONTINUE
        END IF
150  CONTINUE
     RETURN
     END
```

```
      SUBROUTINE mult(mat,vec1,vec2)

      REAL MAT(1:3,1:3),VEC1(1:3),VEC2(1:3)

      DO 20 I=1,3,1
       VEC2(I)=MAT(I,1)*VEC1(1)+MAT(I,2)*VEC1(2)+MAT(I,3)*VEC1(3)
20    CONTINUE
      RETURN
      END
```

```
      SUBROUTINE RESULT(WHICH)

      PARAMETER (IVBIN=80
     +,IPOBIN=17,IEQBIN=35,IPO2=179,
     +IEQ2=179,IVBIN2=800,RADIUS=6378,ATMOS=150,IFACE=12)
      LOGICAL WHICH(1:14)
      REAL DUM,TIMP,SPHTOT
*TIMP is the total number of impacts on the satellite.
*EARTH,SPACE are the total  number of
*impacts on the Earth and
*and space of the satellite.
      COMMON /RESARRAY/
FACTOT(0:IFACE),SVFDIS(0:IVBIN),SCRVEL(0:IVBIN)
     +,EVFDIS(0:IVBIN),ECRVEL(0:IVBIN)
     +,RVFDIS(0:IFACE,0:IVBIN),PCRVEL(0:IFACE,0:IVBIN),SANDIS(0:8)
     +,EANDIS(0:8),SBIN(0:IVBIN,0:8),EBIN(0:IVBIN,0:8)
     +,PBIN(0:IFACE,0:IVBIN,0:8),
     +RANDIS(0:IFACE,0:8)
     +,ELIP1(0:IVBIN,0:36,0:9,0:IFACE)
     +,SPELI1(0:IVBIN,0:36,0:9),EAELI1(0:IVBIN,0:36,0:9)
     +,ELIP2(0:36,0:IFACE)
     +,ELIP4(0:36,0:IFACE),ANGNV(0:IVBIN,0:36,0:IFACE)
     +,SELIP4(0:36),SANGNV(0:IVBIN,0:36)
     +,EELIP4(0:36),EANGNV(0:IVBIN,0:36)
     +,SPELI2(0:36),EAELI2(0:36)
     +,ELIP3(0:36,0:9,0:IFACE)
     +,SPELI3(0:36,0:9),EAELI3(0:36,0:9)
     +,SPTN(0:30),EPTN(0:30),PTN(0:IFACE,0:30)
     +,PMAXV(0:IFACE)
     +,AVTOT,EARTH,SPACE
     +,VELMAX,SMAXV,EMAXV
      COMMON /SPHRES/VELDIS(0:IVBIN),ANGDIS(0:IEQBIN,0:IPOBIN),
     +THEDIS(0:IEQBIN),PHIDIS(0:IPOBIN),SPHTOT

*VELDIS,THEDIS,PHIDIS are the results arrays for the spherical
*satellite.
*PHI,THETA are the centre points of these bins for results.
*SVFDIS,SCRVEL,EVFDIS,ECRVEL,RVFDIS,PCRVEL,SANDIS,EANDIS,SBIN
*,EBIN,PBIN,RANDIS are the velocity an angular
*results arrays for the actual satellite.
*FACTOT, are the total number of particles hitting the peripheral
*faces of the satellite and their effective total taking into account
*their angle of approach.
         COMMON /REALCALC2/ VBISIZ
        COMMON /INTCALC/ IPOUS,IEQUS,
     +IPOUS2,IEQUS2
      REAL PAVIMP(0:IFACE),PAVNOR(0:IFACE)
*IEQBIN,IPOBIN,IVBIN are the upper limits of the
*velocity and angular results  arrays.
*IPOUS,IEQUS are the size of these arrays (this is different
*since the arrays have been taken to start at zero instead of one)
*ie. IEQBIN=IEQUS-1.
*IFACE is the number of peripheral faces on the satellite.
      L=IFACE-1
      IF (WHICH(6)) THEN
```

```
      SAVIMP=0
      EAVIMP=0
      DO 3  I=0,L,1
       PAVIMP(I) = 0
    3  CONTINUE
      DO 16 I=0,IVBIN,1
       SAVIMP=SAVIMP+(SCRVEL(I)*(I*VBISIZ+(VBISIZ/2.0)))
       EAVIMP=EAVIMP+(ECRVEL(I)*(I*VBISIZ+(VBISIZ/2.0)))
       DO 19 K=0,L,1
         PAVIMP(K)=PAVIMP(K)+(PCRVEL(K,I)*
     +     (I*VBISIZ+(VBISIZ/2.0)))
   19    CONTINUE
   16   CONTINUE
      WRITE(14,*) 'Average Impact velocities on faces'
        WRITE(14,50) ((mod((21-I),12)+1),I=1,IFACE,1)
      WRITE(14,40)((PAVIMP(K)/FACTOT(K)),K=0,L,1),(SAVIMP/SPACE)
     + ,(EAVIMP/EARTH)
      ENDIF

      IF (WHICH(7)) THEN
       DO 2  I=0,L,1
        PAVNOR(I) = 0
    2  CONTINUE
      WRITE(14,*) 'Average NORMAL velocities on faces'
      SAVNOR=0
      EAVNOR=0
      DO 26 I=0,IVBIN,1
       SAVNOR=SAVNOR+(SVFDIS(I)*(I*VBISIZ+(VBISIZ/2.0)))
       EAVNOR=EAVNOR+(EVFDIS(I)*(I*VBISIZ+(VBISIZ/2.0)))
       DO 29 K=0,L,1
         PAVNOR(K)=PAVNOR(K)+(RVFDIS(K,I)*
     +     (I*VBISIZ+(VBISIZ/2.0)))
   29    CONTINUE
   26   CONTINUE
       WRITE(14,50) ((mod((21-I),12)+1),I=1,IFACE,1)
      WRITE(14,40)((PAVNOR(K)/FACTOT(K)),K=0,L,1),(SAVNOR/SPACE)
     + ,(EAVNOR/EARTH)
      ENDIF

      IF (WHICH(1)) THEN
        OPEN(10,FILE='sph.res',STATUS='NEW',RECL=1200)
       DEGA=360/(IEQUS*2)
       DEGB=180/(IPOUS*2)
       WRITE(10, *) 'Velocity Distribution (Spherical Satellite)'
       WRITE(10,*)
       DO 10 I=0,IVBIN,1
         DUM=((I+I+1.0)/2.0)
         WRITE(10,60) DUM,(VELDIS(I)/SPHTOT)
   10   CONTINUE
       WRITE(10,*)
       WRITE(10,*)
       WRITE(10,*) 'Angular Distribution'
       WRITE(10,*)
       WRITE(10,*) 'THETA DISTRIBUTION'
       DO 20 I=0,IEQBIN,1
         WRITE(10,*) ((2*I+1)*DEGA),',',(THEDIS(I)/SPHTOT)
   20   CONTINUE
       WRITE(10,*)
       WRITE(10,*) 'PHI DISTRIBUTION'
```

```
      DO 30 I=0,IPOBIN,1
       WRITE(10,* ) ((2*I+1)*DEGB-90),',',(PHIDIS(I)/SPHTOT)
30    CONTINUE
     ENDIF

     IF (WHICH(2)) THEN
      TIMP=0
      TIMP = TIMP + SPACE + EARTH
      DO 17 K=0,IFACE,1
       TIMP = TIMP + FACTOT(K)
17    CONTINUE
      tumble=timp/14
      WRITE(14,*)
      WRITE(14,*)
      WRITE(14,*) '  Flux On Faces'
      WRITE(14,50) ((mod((21-I),12)+1),I=1,IFACE,1)
      WRITE(14,40)((FACTOT(K)),K=0,L,1),(SPACE)
     +,(EARTH)
     ENDIF

     IF (WHICH(8)) THEN
      AVTOT=0
      DO 18 K=0,IVBIN,1

       AVTOT=AVTOT+(VELDIS(K)*(K*VBISIZ+(VBISIZ/2.0)))
18    CONTINUE
      WRITE(14,*) 'Average impact velocity=',AVTOT/SPHTOT
     ENDIF

     IF (WHICH(4)) THEN
      WRITE(14,*) 'Distribution Of Normal Components Of'
      WRITE(14,*) ' Velocity  On Faces'
      DO 65 I=0,L,1
       WRITE(14,40) ((J*VBISIZ+(VBISIZ/2.0)),J=0,IVBIN,1)
        WRITE(14,40) ((RVFDIS(I,J)),J=0,IVBIN,1)
65    CONTINUE

      WRITE(14,40) ((J*VBISIZ+(VBISIZ/2.0)),J=0,IVBIN,1)
      WRITE(14,40)  ((SVFDIS(I)),I=0,IVBIN,1)
      WRITE(14,40) ((J*VBISIZ+(VBISIZ/2.0)),J=0,IVBIN,1)
      WRITE(14,40) ((EVFDIS(I)),I=0,IVBIN,1)
     ENDIF

     IF (WHICH(5)) THEN
      WRITE(14,*) 'Distribution Of Actual Impact'
      WRITE(14,*) ' Velocity  On Faces'
      DO 67 I=0,L,1
       WRITE(14,40) ((J*VBISIZ+(VBISIZ/2.0)),J=0,IVBIN,1)
       WRITE(14,40) ((PCRVEL(I,J)),J=0,IVBIN,1)
67    CONTINUE
      WRITE(14,40) ((J*VBISIZ+(VBISIZ/2.0)),J=0,IVBIN,1)
      WRITE(14,40)  ((SCRVEL(I)),I=0,IVBIN,1)
      WRITE(14,40) ((J*VBISIZ+(VBISIZ/2.0)),J=0,IVBIN,1)
      WRITE(14,40) ((ECRVEL(I)),I=0,IVBIN,1)
     ENDIF

     IF (WHICH(3)) THEN
      WRITE(14,*) 'Angular Distribution On Faces'
      DO 66 I=0,L,1
```

```
      WRITE(14,50) (J,J=5,85,10)
      WRITE(14,40) ((RANDIS(I,J)),J=0,8,1)
 66   CONTINUE
      WRITE(14,50) (J,J=5,85,10)
      WRITE(14,40)  ((SANDIS(I)),I=0,8,1)
      WRITE(14,50) (J,J=5,85,10)
      WRITE(14,40) ((EANDIS(I)),I=0,8,1)
    ENDIF

    IF (WHICH(9)) THEN
     DO 121 K=0,L,1
       WRITE(16,50) ((360-J),J=5,355,10)
       WRITE(16,40) (ELIP2(J,K),J=0,35,1)
      WRITE(16,*)
 121  CONTINUE
      WRITE(16,50) ((360-J),J=5,355,10)
      WRITE(16,40) (SPELI2(J),J=0,35,1)
     WRITE(16,*)
      WRITE(16,50) ((360-J),J=5,355,10)
     WRITE(16,40) (EAELI2(J),J=0,35,1)
    ENDIF
    IF (WHICH(10)) THEN
        DO 77 I=29,0,-1
          DO 76 K=0,L,1
                PTN(K,I)=PTN(K,I)+PTN(K,(I+1))
76         CONTINUE
          SPTN(I)=SPTN(I)+SPTN((I+1))
          EPTN(I)=EPTN(I)+EPTN((I+1))
77      CONTINUE

     WRITE(17,50) ((mod((21-I),12)+1),I=1,IFACE,1)
     DO 42 I=0,30,1
        WRITE (17,40) (10**((I/5.0)-7.0)),(PTN(K,I),K=0,L,1)
    +,SPTN(I),EPTN(I)
42   CONTINUE
    ENDIF
    IF (WHICH(11)) THEN
     WRITE(14,50) ((mod((21-I),12)+1),I=1,IFACE,1)
     WRITE(14,40) (PMAXV(K), K=0,L,1),SMAXV,EMAXV
    ENDIF

    IF (WHICH(12)) THEN
     WRITE (16,*)
     WRITE(16,*) 'Directional information'
     DO 191 K=0,L,1
       WRITE(16,50) ((J),J=5,175,10)
       WRITE(16,40) (ELIP4(J,K),J=0,35,1)
      WRITE(16,*)
 191  CONTINUE
      WRITE(16,50) ((J),J=5,175,10)
      WRITE(16,40) (SELIP4(J),J=0,35,1)
      WRITE(16,50) ((J),J=5,175,10)
      WRITE(16,40) (EELIP4(J),J=0,35,1)
    ENDIF
    IF (WHICH(14)) THEN
*      DO 127 K=0,L,1
*       Do 129 J=0,35
*        DO 124 N=0,8
*          ELIP3(J,N,K)=0
```

```
*          DO 128 I=0,IVBIN,1
*            ELIP3(J,N,K)=ELIP3(J,N,K)+ELIP1(I,J,N,K)
 128       CONTINUE
 124       CONTINUE
 129      CONTINUE
 127     CONTINUE


       WRITE(16,*) 'Absolute Directions'
       DO 134 K=0,L,1
        WRITE(16,55) ((360-J),J=5,355,10)
        DO 133 I=0,8,1
         WRITE(16,45) ((90-(I*10+5))),((ELIP3(J,I,K)),J=0,35,1)
 133     CONTINUE
       WRITE(16,*)
 134    CONTINUE
        WRITE(16,55) ((360-J),J=5,355,10)
        DO 131 I=0,8,1
         WRITE(16,45) ((90-(I*10+5))),((SPELI3(J,I)),J=0,35,1)
 131     CONTINUE
       WRITE(16,*)
        WRITE(16,55) ((360-J),J=5,355,10)
        DO 132 I=0,8,1
         WRITE(16,45) ((90-(I*10+5))),((EAELI3(J,I)),J=0,35,1)
 132     CONTINUE
       WRITE(16,*)
    ENDIF
    IF (WHICH(13)) THEN
     WRITE (16,*)
     WRITE(16,*) 'Velocity/Directional information'
     DO 197 K=0,L,1
      WRITE(16,55) ((360-J),J=5,355,10)
      DO 196 I=0,IVBIN,1
       WRITE(16,40) ((I*VBISIZ+(VBISIZ/2.0))),(ANGNV(I,J,K),J=0,35,1)
      WRITE(16,*)
 196    CONTINUE
 197   CONTINUE
       WRITE(16,55) ((360-J),J=5,355,10)
      DO 193 I=0,IVBIN,1
       WRITE(16,40) (I*VBISIZ+(VBISIZ/2.0)),(SANGNV(I,J),J=0,35,1)
      WRITE(16,*)
 193    CONTINUE
       WRITE(16,55) ((360-J),J=5,355,10)
      DO 194 I=0,IVBIN,1
       WRITE(16,40) ((I*VBISIZ+(VBISIZ/2.0))),(EANGNV(I,J),J=0,35,1)
      WRITE(16,*)
 194    CONTINUE
    ENDIF
 40    FORMAT (E10.4,85(',',E10.4))
 50    FORMAT (I10,85(',',I10))
 55     FORMAT (' ',I10,85(',',I10))
 45     FORMAT (' ',I10,85(',',E10.4))
 60     FORMAT (1X,F4.1,',',F10.3)
     RETURN
     END
```

```
      SUBROUTINE whatout(which)

      CHARACTER*1 D

      LOGICAL WHICH(1:14)

*     PRINT *,'Which data sets would you like as outputs'
*     PRINT *, 'Spherical satellite data (y/n).'
*     READ *,D
      WHICH(1)=((D.EQ.'y').OR.(D.EQ.'Y'))
      PRINT *, 'The total  flux on each face (y/n).'
      READ *,D
      WHICH(2)=((D.EQ.'y').OR.(D.EQ.'Y'))
      PRINT *, 'The distribution in angle from the normal'
      PRINT *,'for each face (y/n).'
      READ *,D
      WHICH(3)=((D.EQ.'y').OR.(D.EQ.'Y'))
      PRINT *, 'The distribution of normal component of velocity'
      PRINT *, 'for each face (y/n).'
      READ *,D
      WHICH(4)=((D.EQ.'y').OR.(D.EQ.'Y'))
      PRINT *, 'The distribution of impact velocities on'
      PRINT *,'each face (y/n).'
      READ *,D
      WHICH(5)=((D.EQ.'y').OR.(D.EQ.'Y'))
      PRINT *, 'The average impact velocities on each face (y/n)'
      READ *,D
      WHICH(6)=((D.EQ.'y').OR.(D.EQ.'Y'))
      PRINT *, 'The average normal velocities on each face (y/n)'
      READ *,D
      WHICH(7)=((D.EQ.'y').OR.(D.EQ.'Y'))
      PRINT *, 'The maximum impact velocity on each face (y/n)'
      READ *,D
      WHICH(11)=((D.EQ.'y').OR.(D.EQ.'Y'))
      PRINT *, 'The average impact velocity on S/C (y/n)'
      READ *,D
      WHICH(8)=((D.EQ.'y').OR.(D.EQ.'Y'))
      PRINT *, 'The crater ellipticity data (y/n)'
      READ *,D
      WHICH(9)=((D.EQ.'y').OR.(D.EQ.'Y'))
      PRINT *, 'The penetration data (y/n)'
      READ *,D
      WHICH(10)=((D.EQ.'y').OR.(D.EQ.'Y'))
      PRINT *, 'The 2d directional information  (y/n)'
      READ *,D
      WHICH(12)=((D.EQ.'y').OR.(D.EQ.'Y'))
      PRINT *, 'The Velocity/directional information  (y/n)'
      READ *,D
      WHICH(13)=((D.EQ.'y').OR.(D.EQ.'Y'))
      PRINT *, 'The Absolute directional information  (y/n)'
      READ *,D
      WHICH(14)=((D.EQ.'y').OR.(D.EQ.'Y'))
      RETURN
```

```
      SUBROUTINE elip(N1,N2,N3,X,EPSI,PI,IFACE)

      REAL N1(1:3),N2(1:3),N3(1:3)
     +    , MAT(1:3,1:3),FX(1:3)

      REAL EPSI

      DO 20 I=1,3,1
       MAT(1,I)=N1(I)
       MAT(2,I)=N2(I)
       MAT(3,I)=N3(I)
20    CONTINUE
      call mult(MAT,X,FX)
      IF (FX(3).EQ.0) THEN
            IF (FX(2).LT.0) THEN
                  EPSI= 1.5*PI
                ELSE
                  EPSI= 0.5*PI
           ENDIF
          ELSE
           EPSI=atan(FX(2)/FX(3))
      ENDIF
       IF ((EPSI.LT.0).AND.(FX(3).GT.0)) THEN
            EPSI=EPSI+PI*2
          ELSE
            IF (FX(3).LT.0) EPSI=EPSI+PI
      ENDIF
      RETURN
      END
```

Appendix 3

All plots are of predicted directional impact distributions for individual debris orbits as shown.

The radial distance from the centre of the plot represents impact incidence angle (points near the centre are near normal impacts and points on the edge are grazing impacts), and azimuthal directions are indicated with respect to other LDEF pointing directions.

Note: The height of the columns represent relative levels within that plot. The absolute level of each plot is arbitrary and therefore, in order to compare absolute flux levels between plots, Appendix 3 should be used in conjunction with Figures 4.5 to 4.9 . The purpose of Appendix 3 is purely to allow analysis of the distribution of impact directions on individual faces .

Apogee = 6848 km
Perigee = 6848 km
Inclination = 0°
Eccentricity = 0.0

East

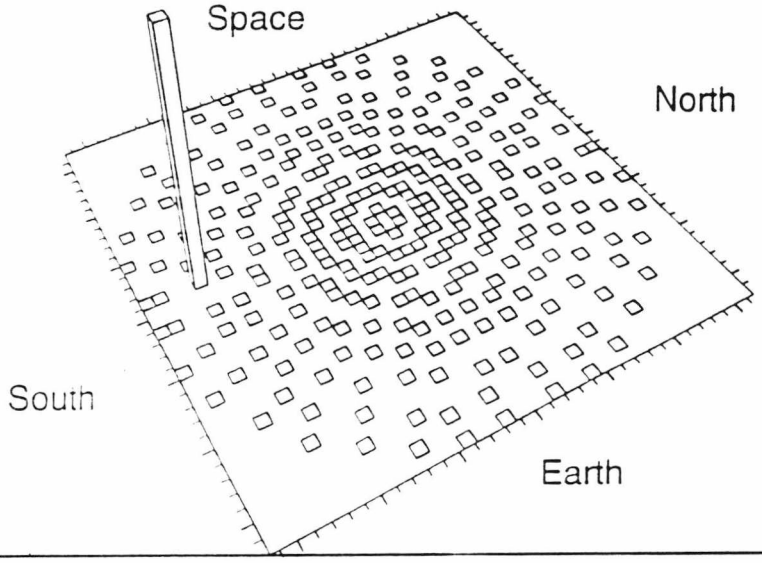

Apogee = 6848 km
Perigee = 6848 km
Inclination = 30°
Eccentricity = 0.0

East

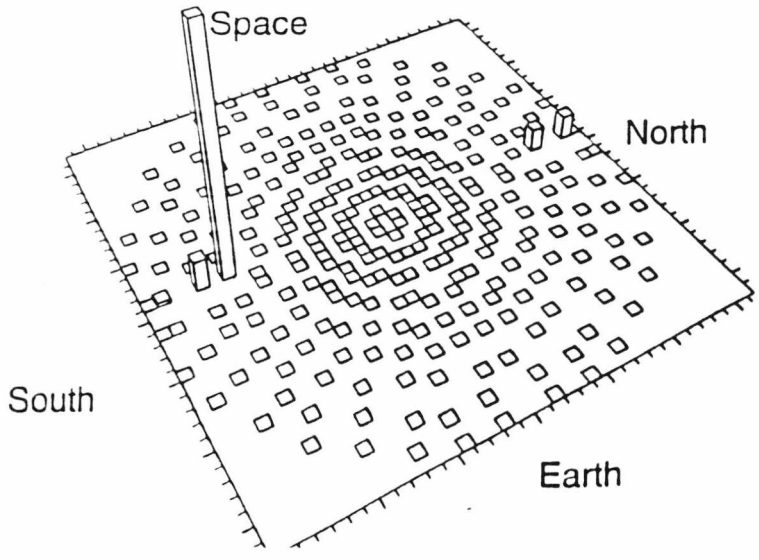

Apogee = 6848 km
Perigee = 6848 km
Inclination = 60°
Eccentricity = 0.0

East

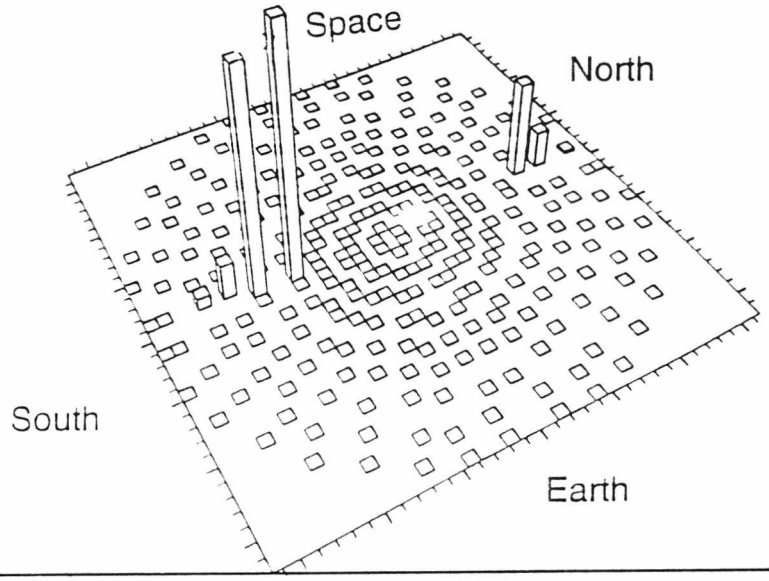

Apogee = 6848 km
Perigee = 6848 km
Inclination = 90°
Eccentricity = 0.0

East

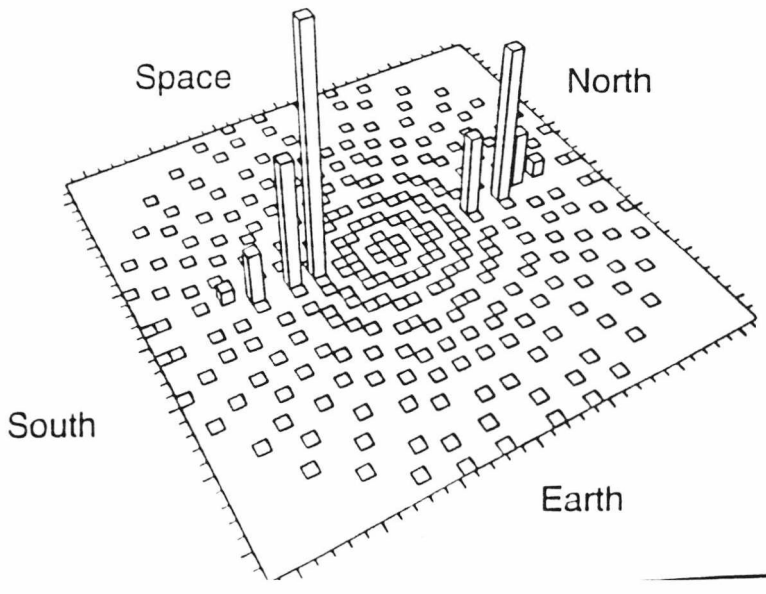

Apogee = 6848 km
Perigee = 6848 km
Inclination = 120°
Eccentricity = 0.0

East

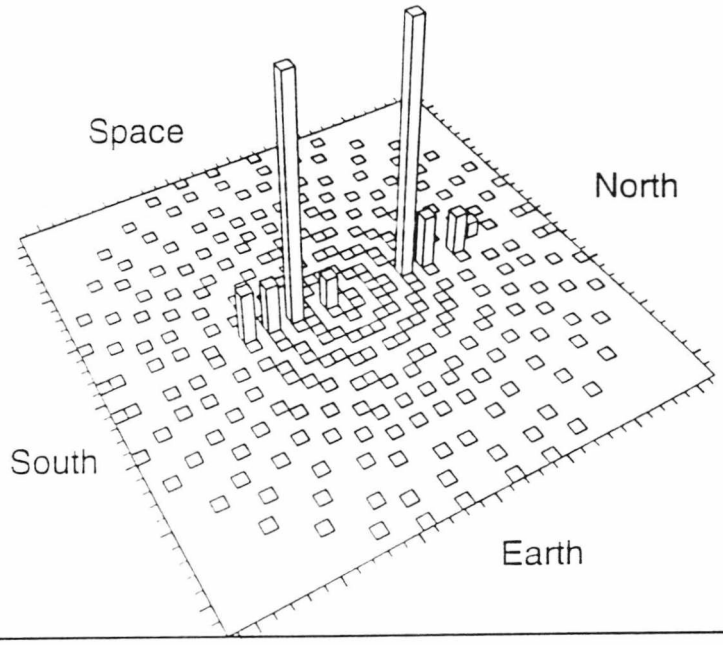

Apogee = 6848 km
Perigee = 6848 km
Inclination = 150°
Eccentricity = 0.0

East

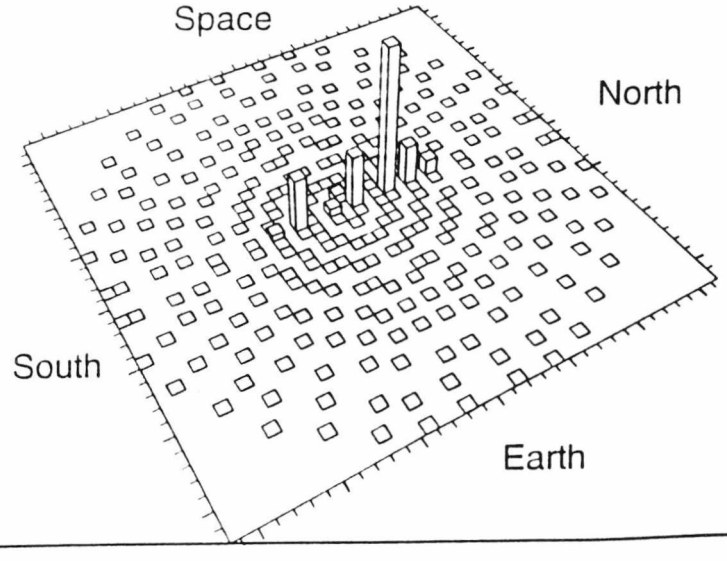

Apogee = 10005 km
Perigee = 6670 km
Inclination = 0°
Eccentricity = 0.2

East

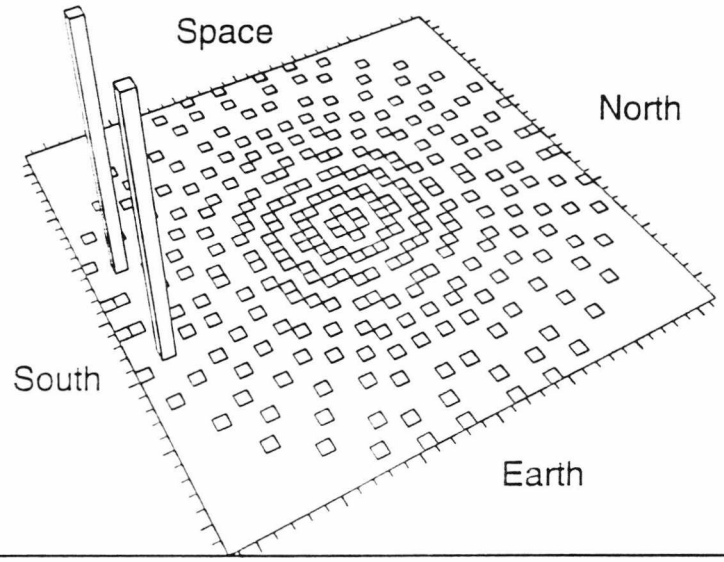

Apogee = 10005 km
Perigee = 6670km
Inclination = 30°
Eccentricity = 0.2

East

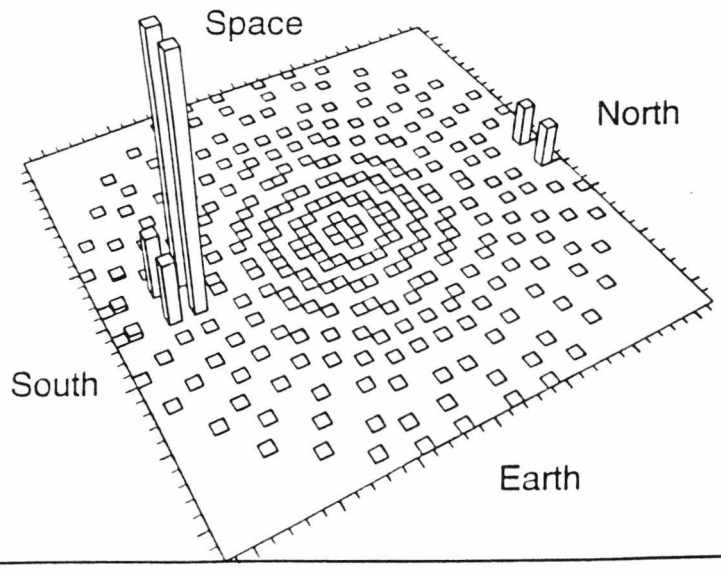

Apogee = 10005 km
Perigee = 6670 km
Inclination = 60°
Eccentricity = 0.2

East

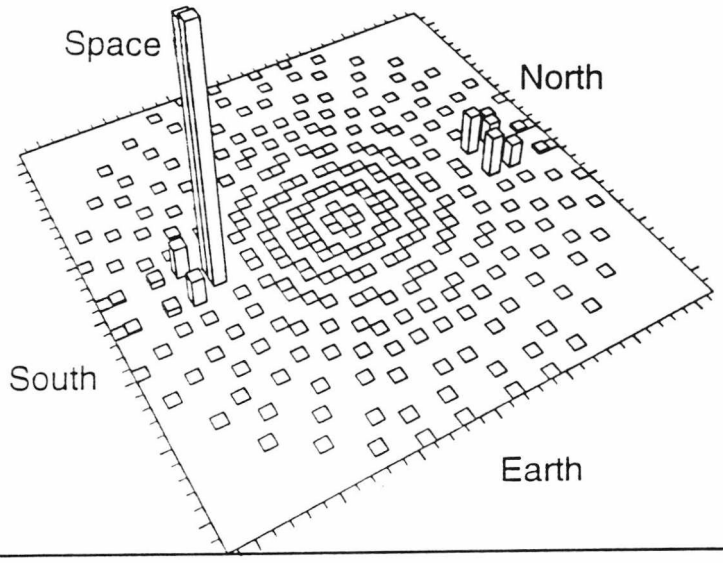

Apogee = 10005 km
Perigee = 6670km
Inclination = 90°
Eccentricity = 0.2

East

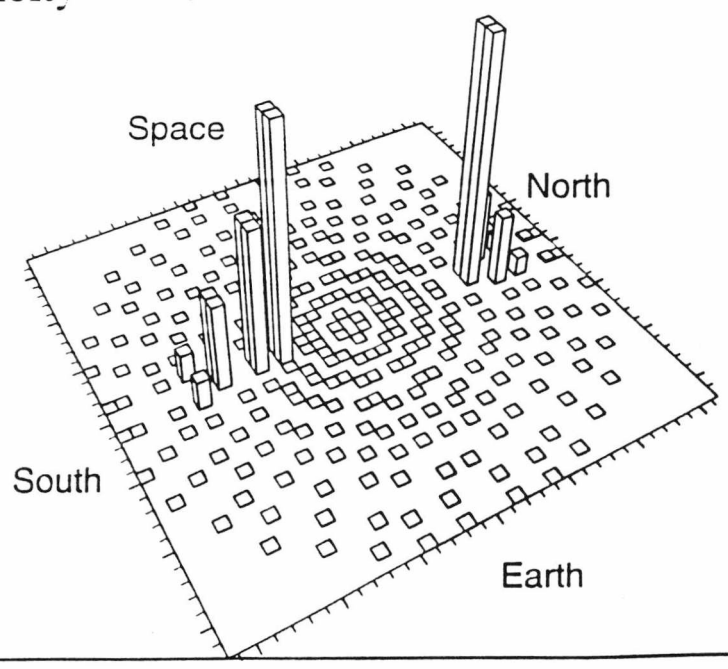

Apogee = 10005 km
Perigee = 6670 km
Inclination = 120°
Eccentricity = 0.2

East

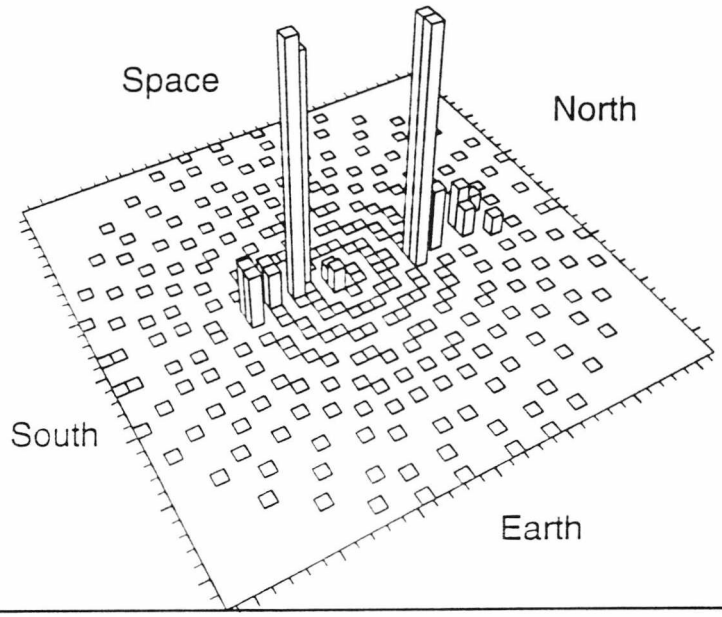

Apogee = 10005 km
Perigee = 6670km
Inclination = 150°
Eccentricity = 0.2

East

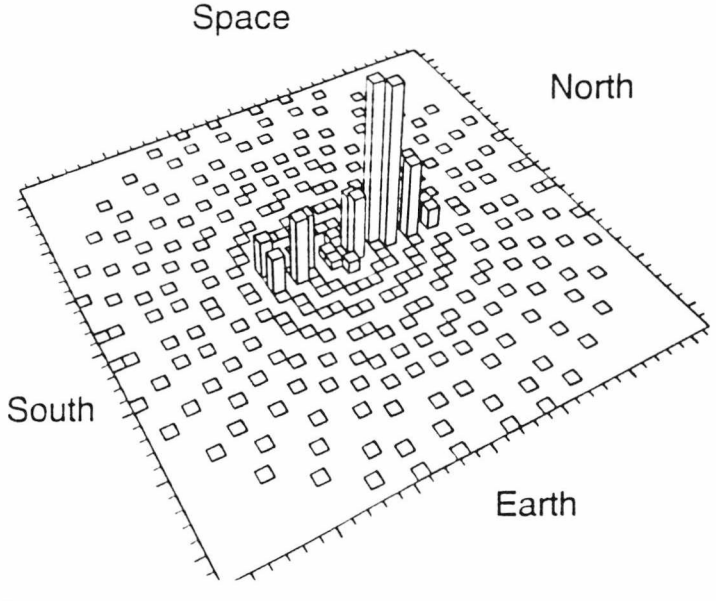

Apogee = 15470 km
Perigee = 6630 km
Inclination = 0°
Eccentricity = 0.4

East

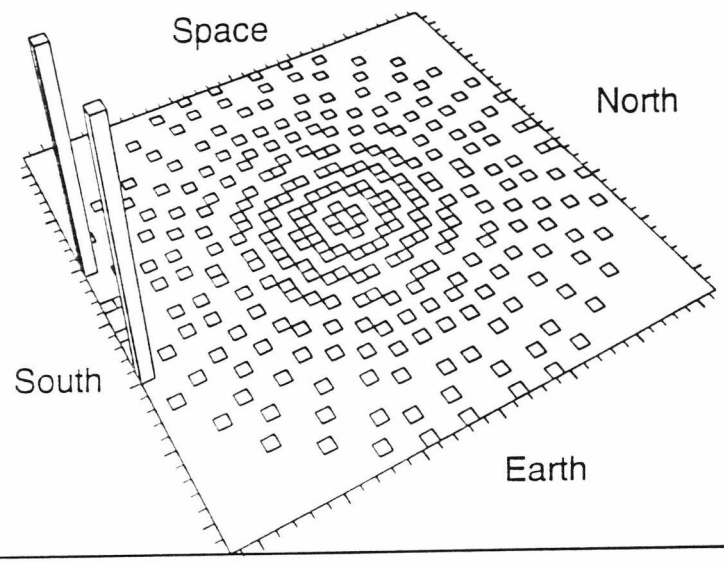

Apogee = 15470 km
Perigee = 6630km
Inclination = 30°
Eccentricity = 0.4

East

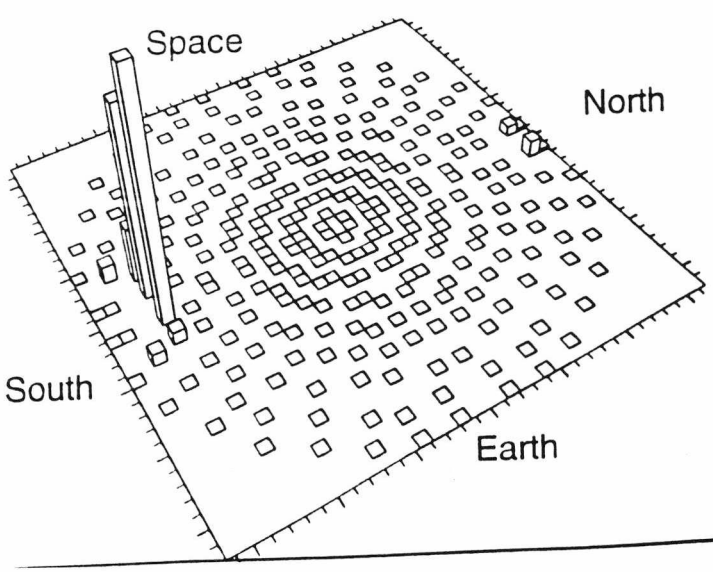

Apogee = 15470 km
Perigee = 6630 km
Inclination = 60°
Eccentricity = 0.4

East

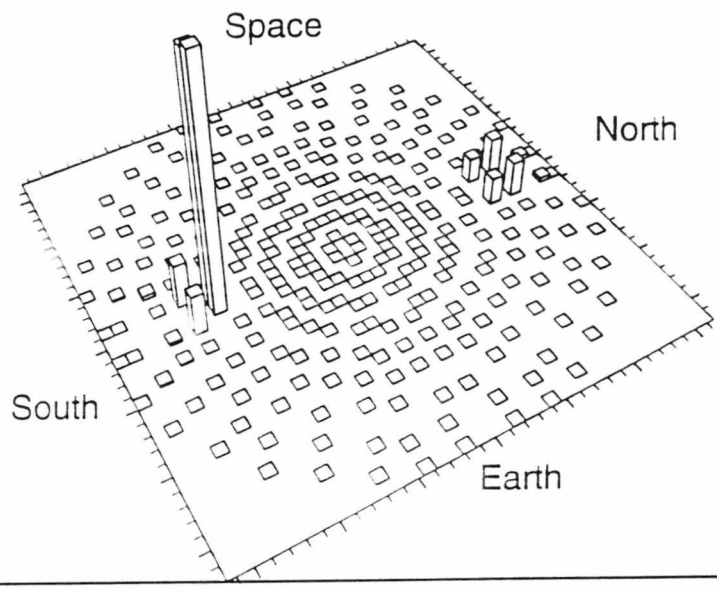

Apogee = 15470 km
Perigee = 6630km
Inclination = 90°
Eccentricity = 0.4

East

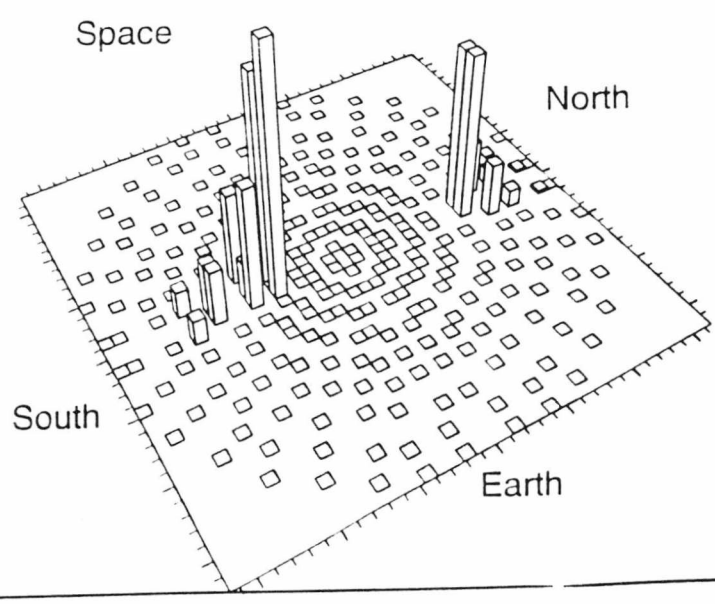

Apogee = 15470 km
Perigee = 6630 km
Inclination = 120°
Eccentricity = 0.4

East

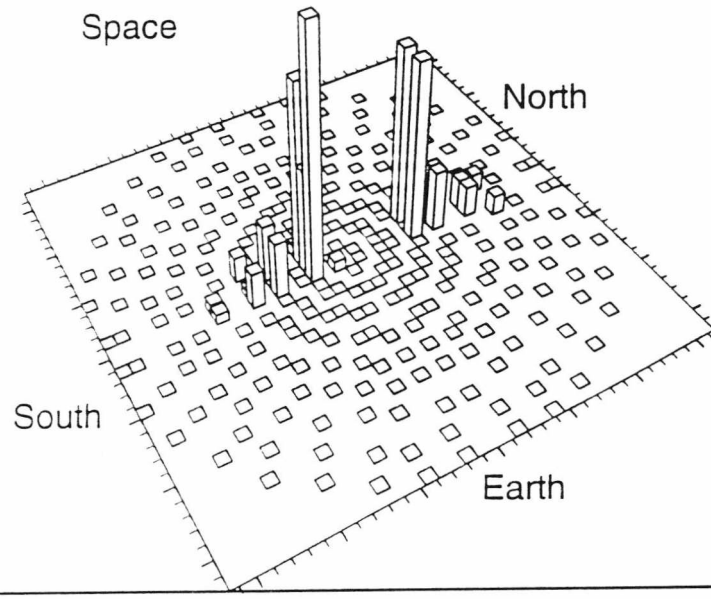

Apogee = 15470 km
Perigee = 6630km
Inclination = 150°
Eccentricity = 0.4

East

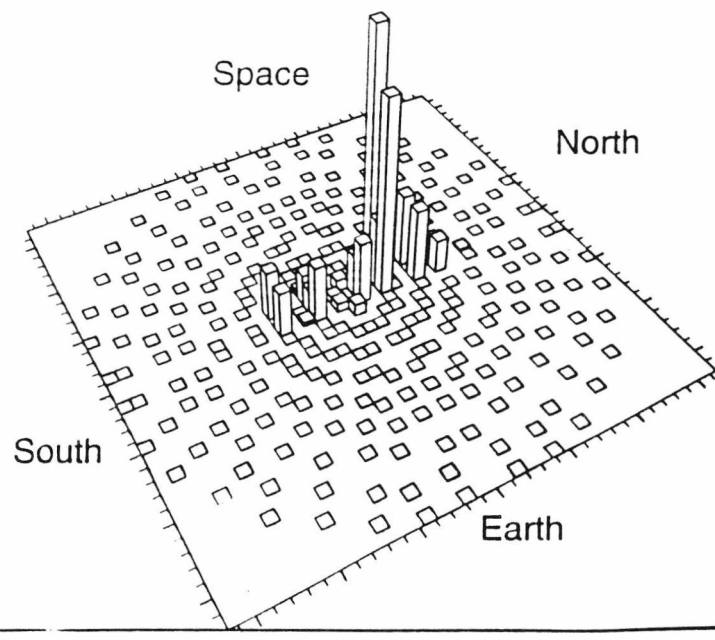

Apogee = 26400 km
Perigee = 6600km
Inclination = 30°
Eccentricity = 0.6

East

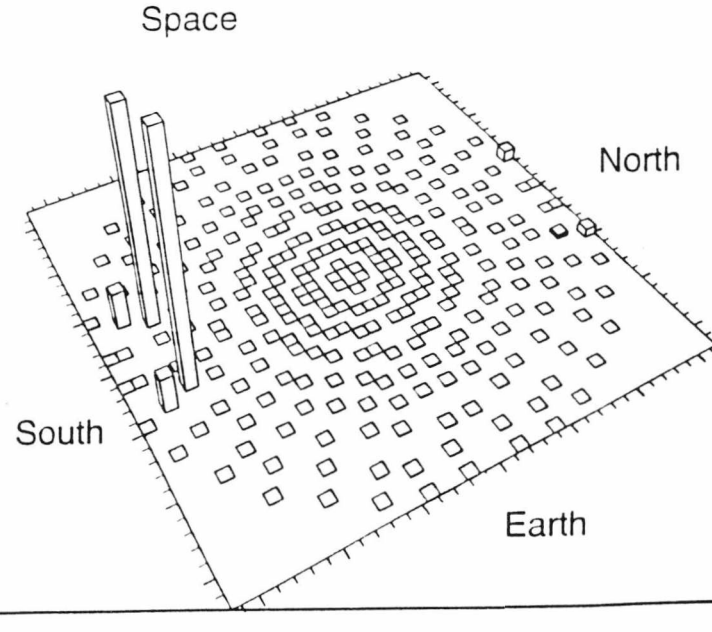

Apogee = 26400 km
Perigee = 6600 km
Inclination = 60°
Eccentricity = 0.6

East

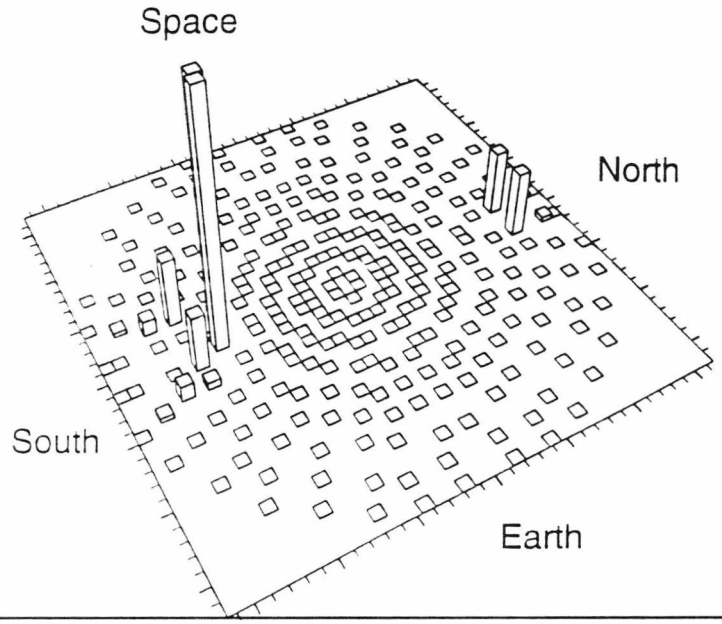

Apogee = 26400 km
Perigee = 6600km
Inclination = 90°
Eccentricity = 0.6

East

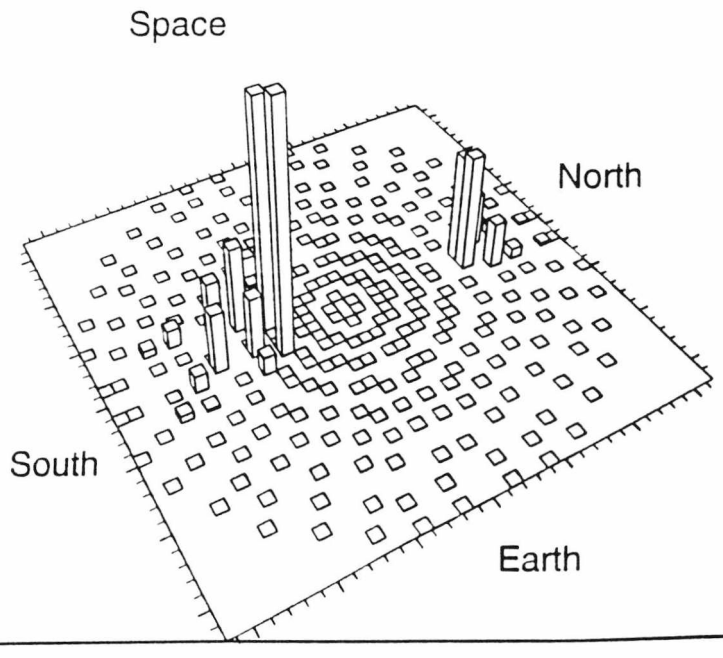

Apogee = 26400 km
Perigee = 6600 km
Inclination = 120°
Eccentricity = 0.6

East

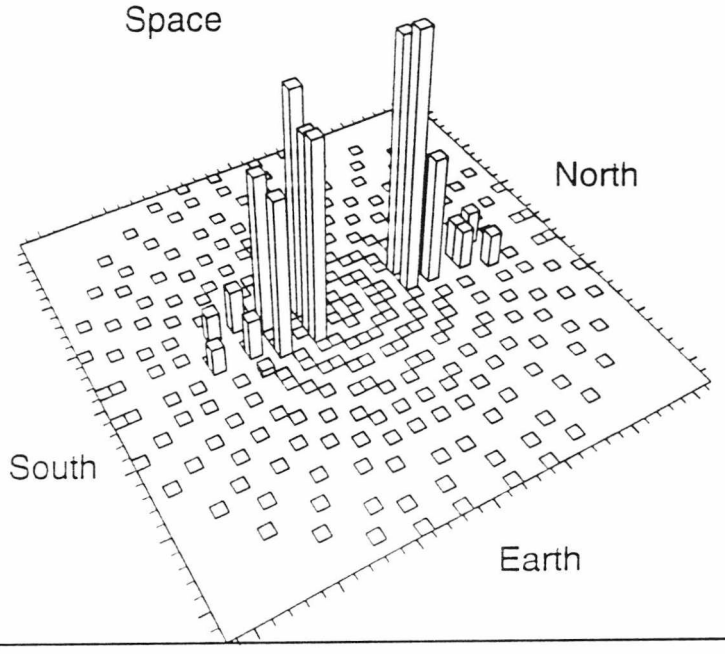

Apogee = 26400 km
Perigee = 6600km
Inclination = 150°
Eccentricity = 0.6

East

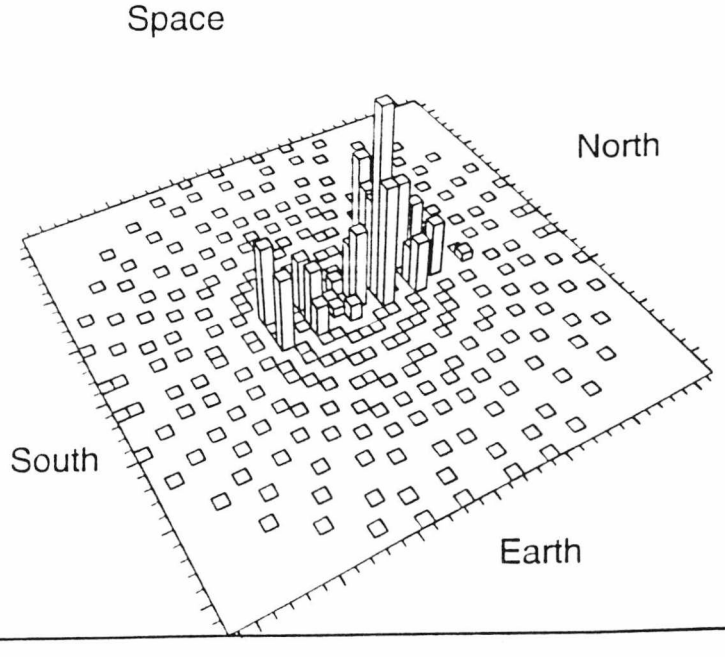

Apogee = 42250 km
Perigee = 6580km
Inclination = 30°
Eccentricity = 0.73

East

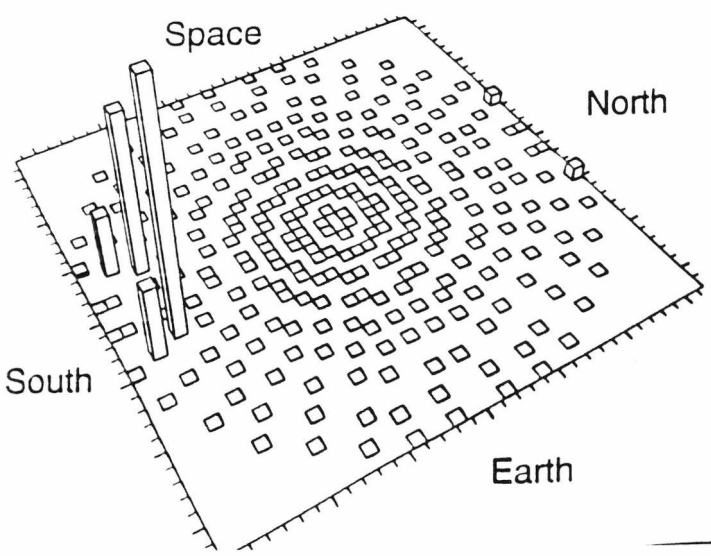

Apogee = 42250 km
Perigee = 6580 km
Inclination = 60°
Eccentricity = 0.73

East

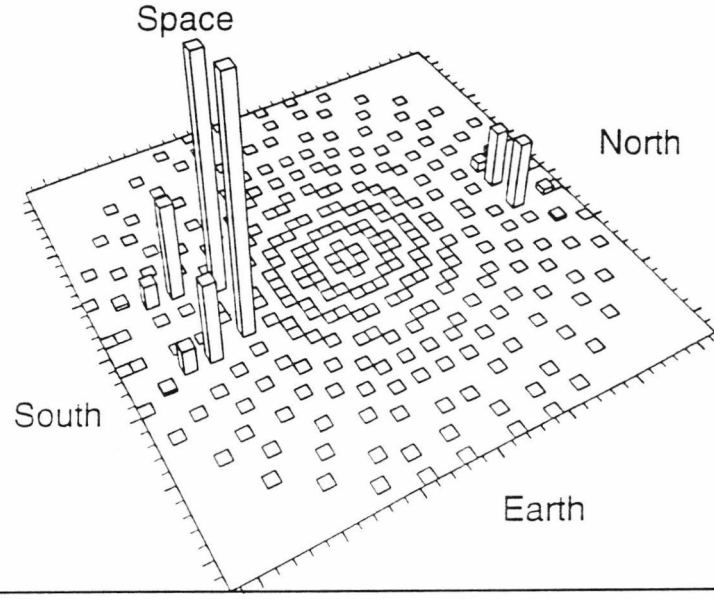

Apogee = 42250 km
Perigee = 6580km
Inclination = 90°
Eccentricity = 0.73

East

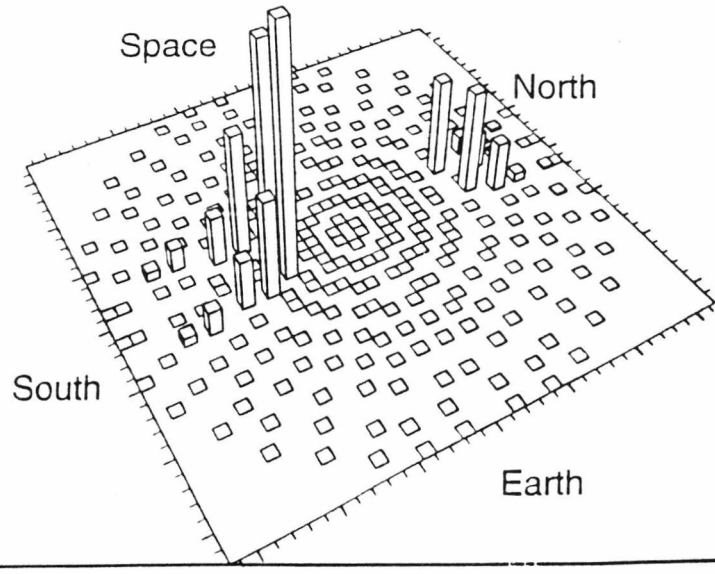

Apogee = 42250 km
Perigee = 6580 km
Inclination = 120°
Eccentricity = 0.73

East

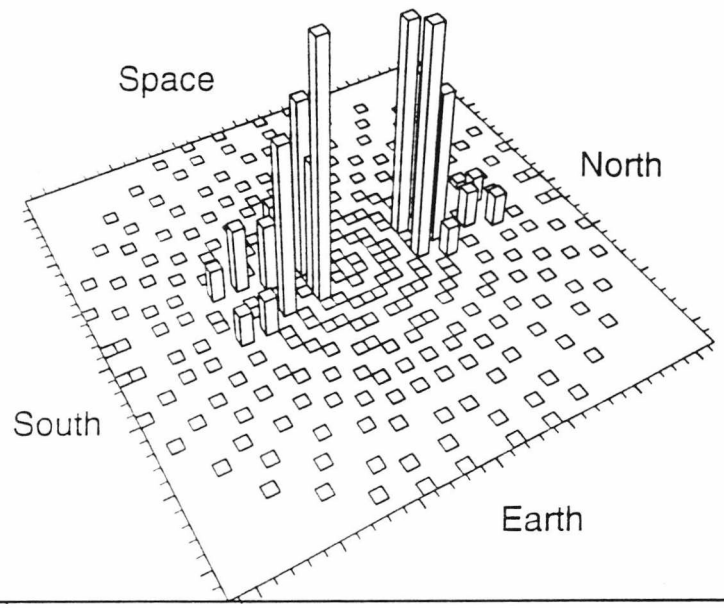

Apogee = 42250 km
Perigee = 6580km
Inclination = 150°
Eccentricity = 0.73

East

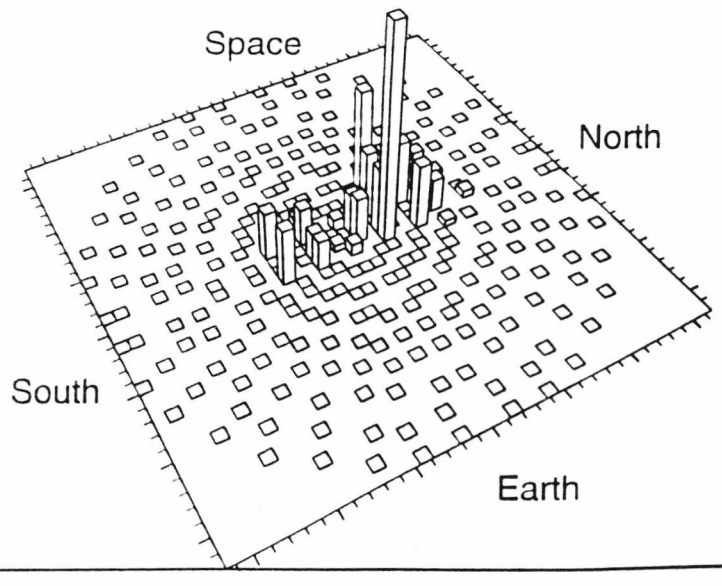

Apogee = 6848 km
Perigee = 6848 km
Inclination = 0°
Eccentricity = 0.0

South

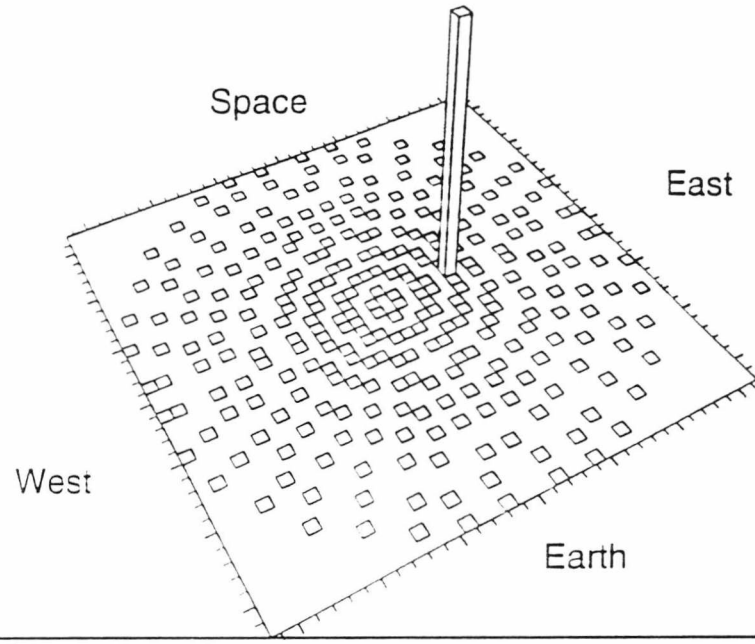

Apogee = 6848 km
Perigee = 6848 km
Inclination = 30°
Eccentricity = 0.0

South

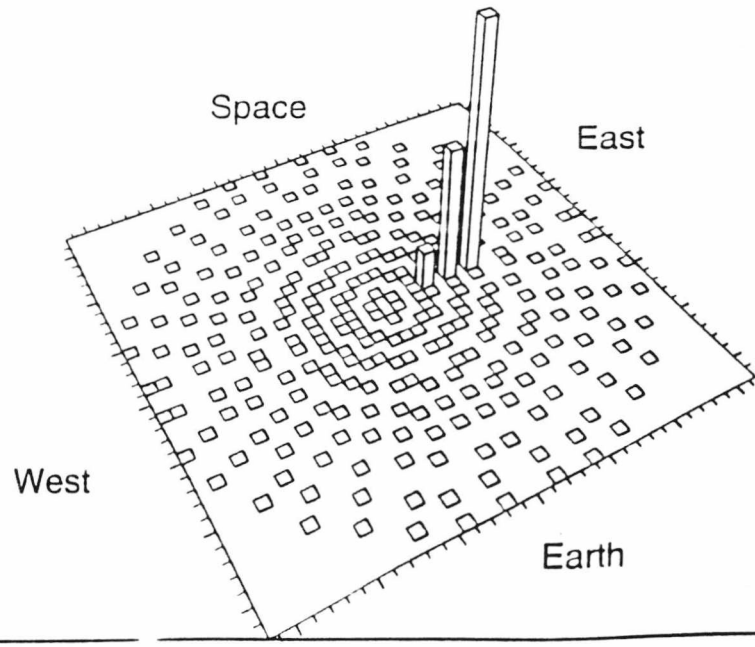

Apogee = 6848 km
Perigee = 6848 km
Inclination = 60°
Eccentricity = 0.0

South

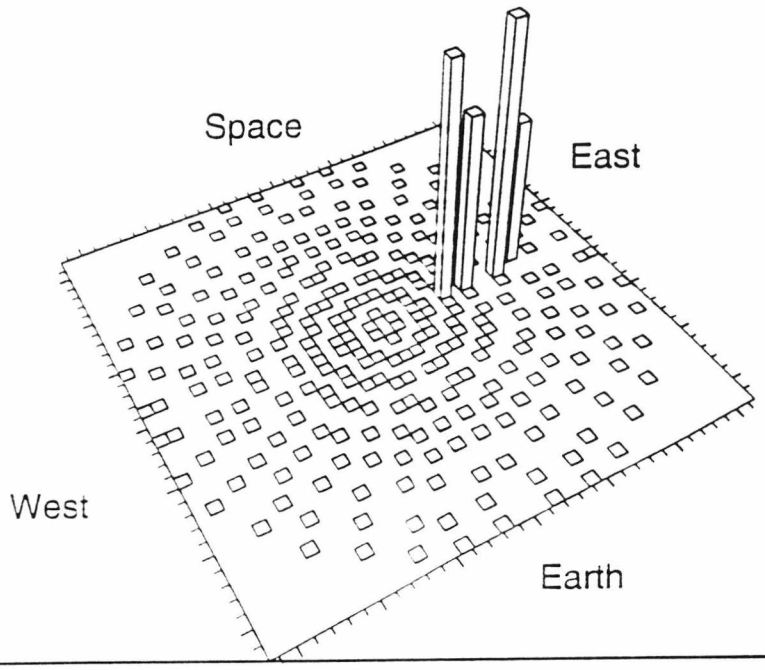

Apogee = 6848 km
Perigee = 6848 km
Inclination = 90°
Eccentricity = 0.0

South

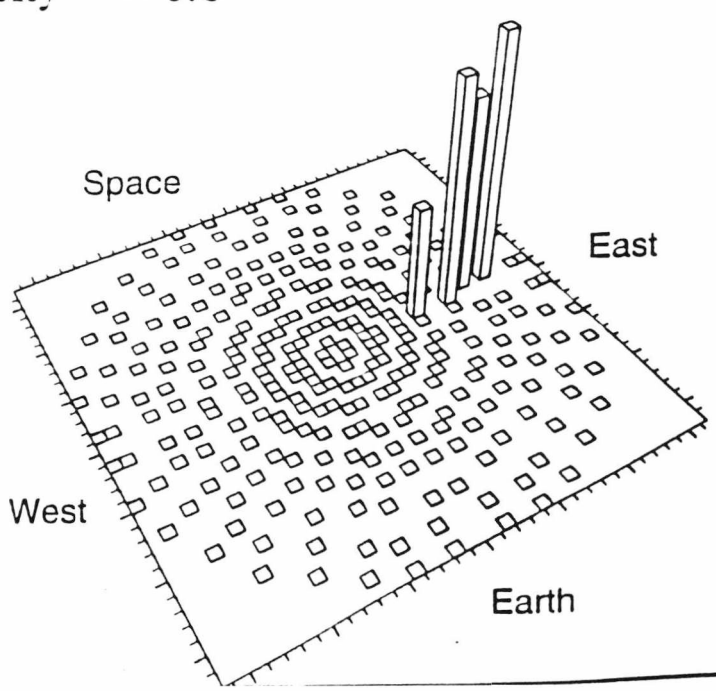

Apogee = 6848 km
Perigee = 6848 km
Inclination = 120°
Eccentricity = 0.0

South

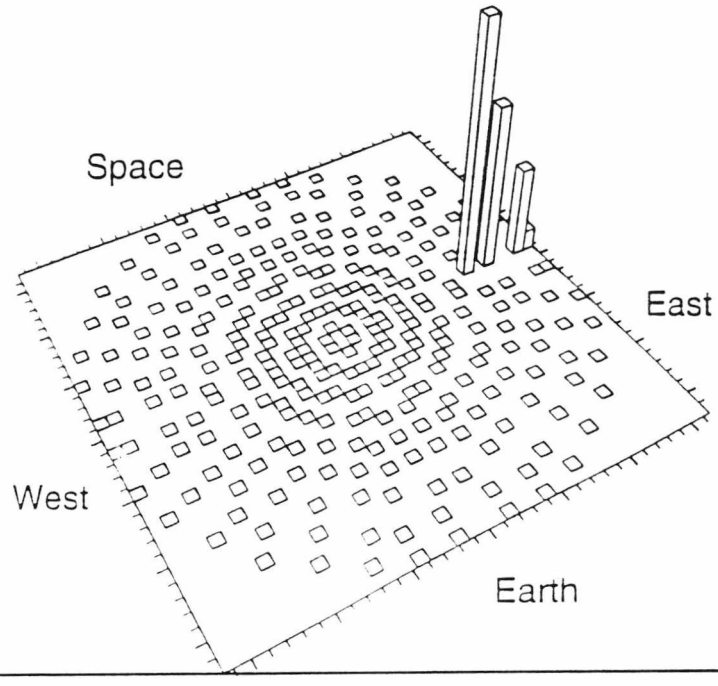

Apogee = 6848 km
Perigee = 6848 km
Inclination = 150°
Eccentricity = 0.0

South

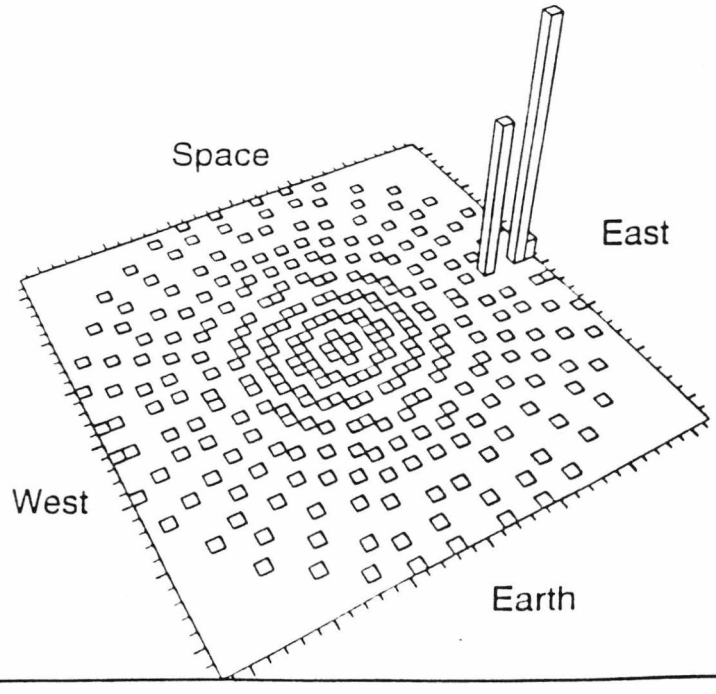

Apogee = 10005 km
Perigee = 6670 km
Inclination = 0°
Eccentricity = 0.2

South

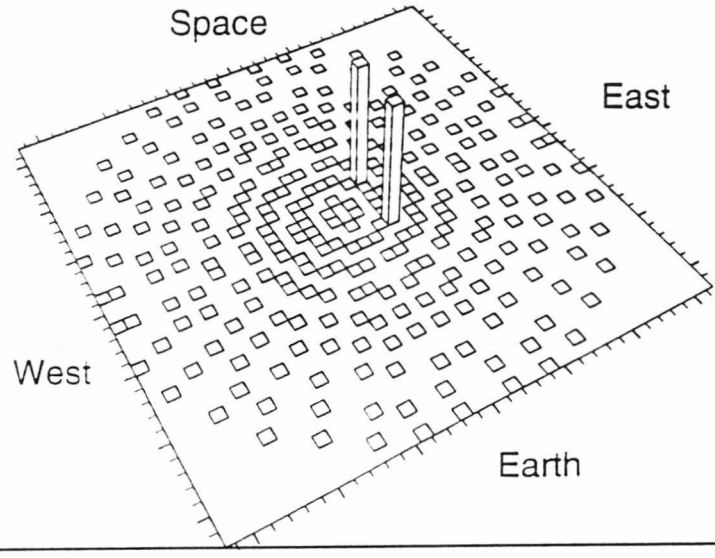

Apogee = 10005 km
Perigee = 6670km
Inclination = 30°
Eccentricity = 0.2

South

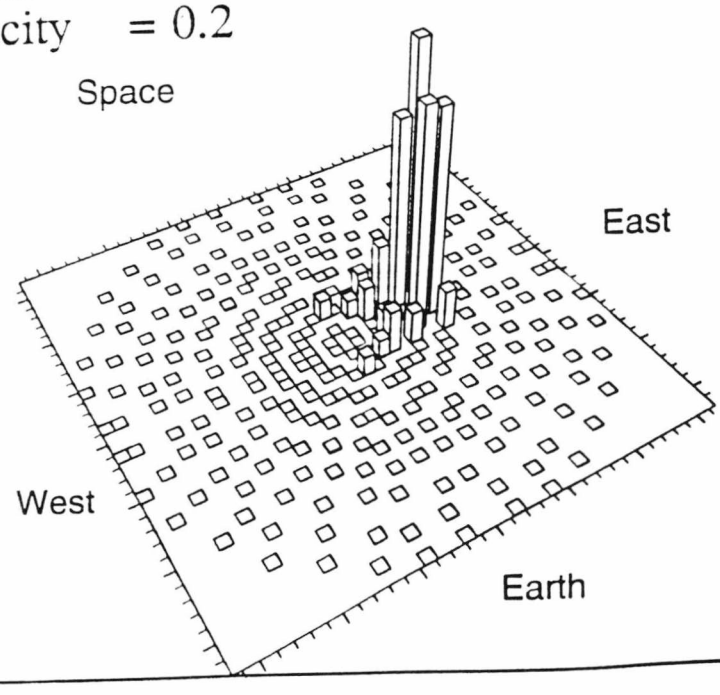

Apogee = 10005 km
Perigee = 6670 km
Inclination = 60°
Eccentricity = 0.2

South

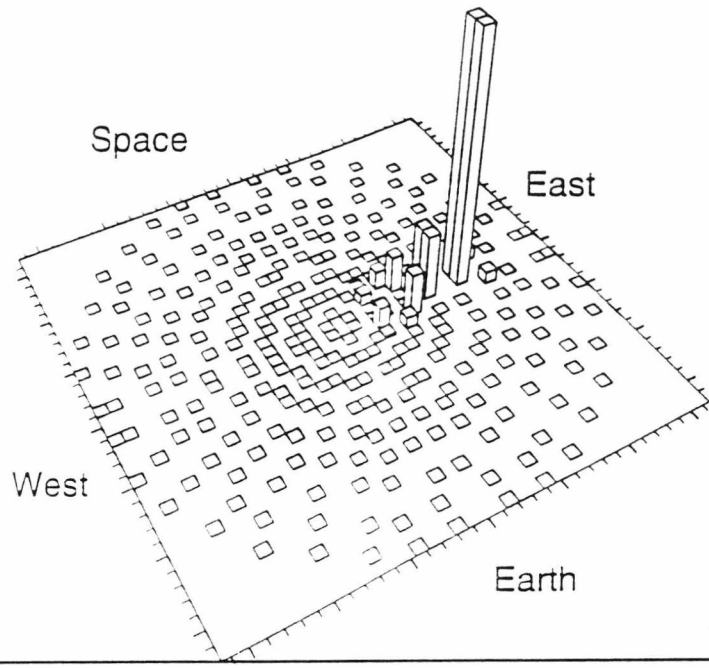

Apogee = 10005 km
Perigee = 6670km
Inclination = 90°
Eccentricity = 0.2

South

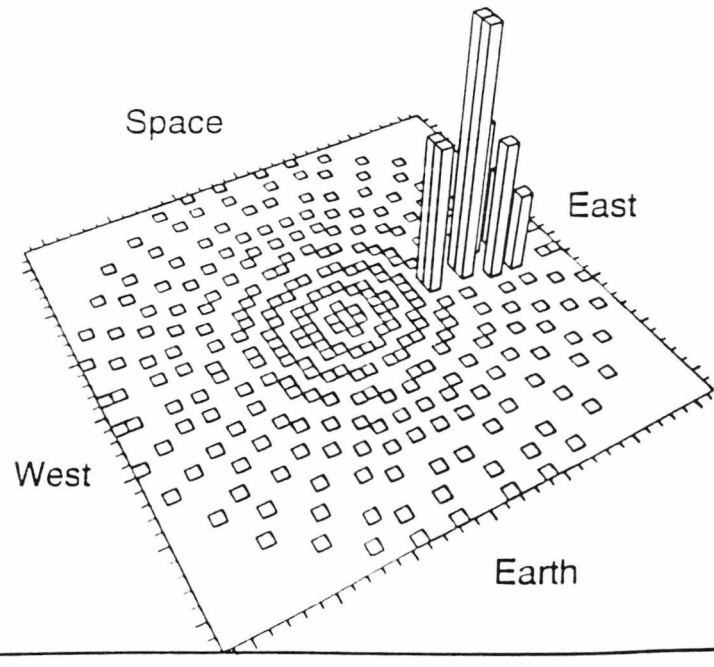

Apogee = 10005 km
Perigee = 6670 km
Inclination = 120°
Eccentricity = 0.2

South

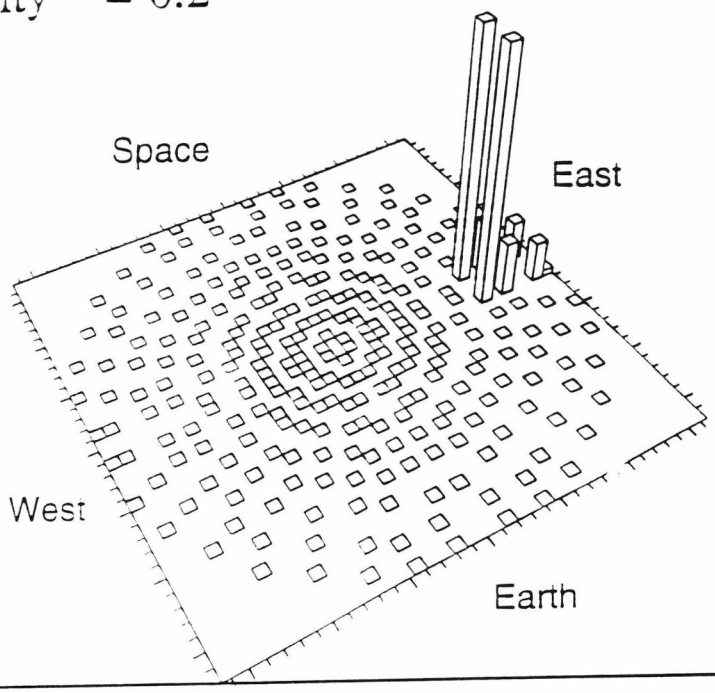

Apogee = 10005 km
Perigee = 6670km
Inclination = 150°
Eccentricity = 0.2

South

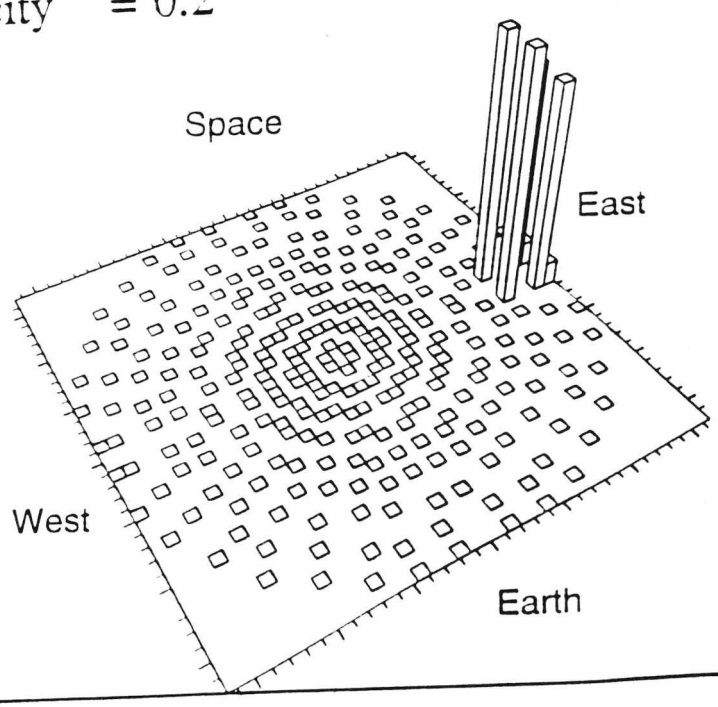

Apogee = 15470 km
Perigee = 6630 km
Inclination = 0°
Eccentricity = 0.4

South

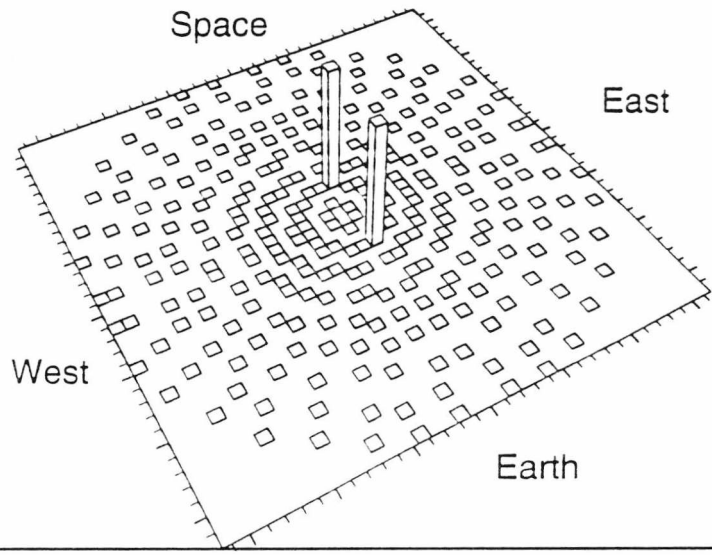

Apogee = 15470 km
Perigee = 6630km
Inclination = 30°
Eccentricity = 0.4

South

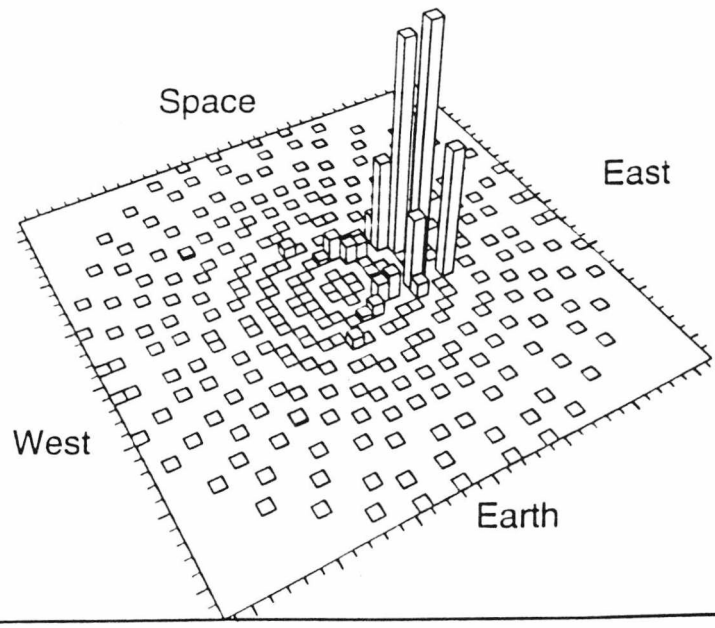

Apogee = 15470 km
Perigee = 6630 km
Inclination = 60°
Eccentricity = 0.4

South

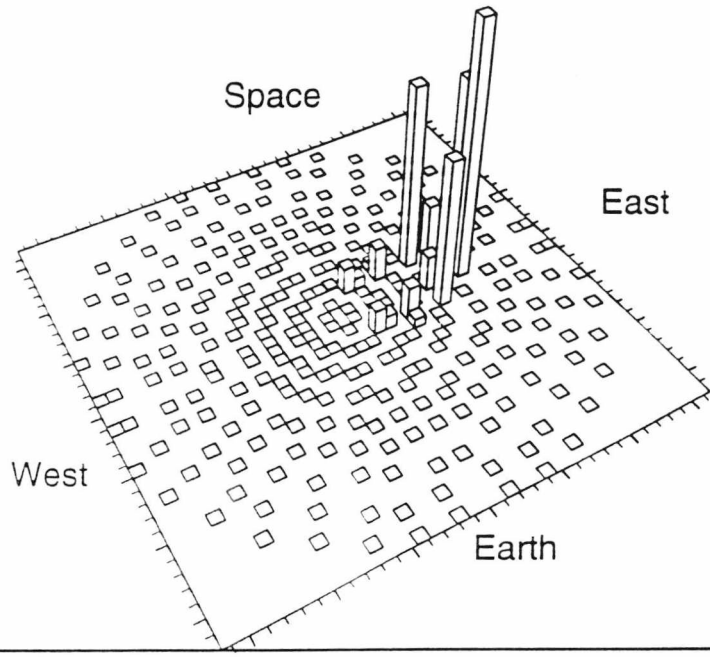

Apogee = 15470 km
Perigee = 6630km
Inclination = 90°
Eccentricity = 0.4

South

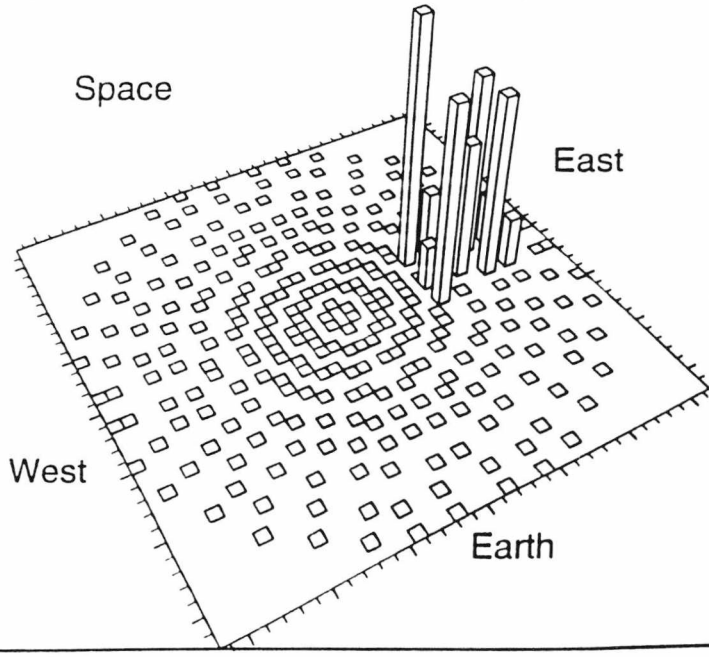

Apogee = 15470 km
Perigee = 6630 km
Inclination = 120°
Eccentricity = 0.4

South

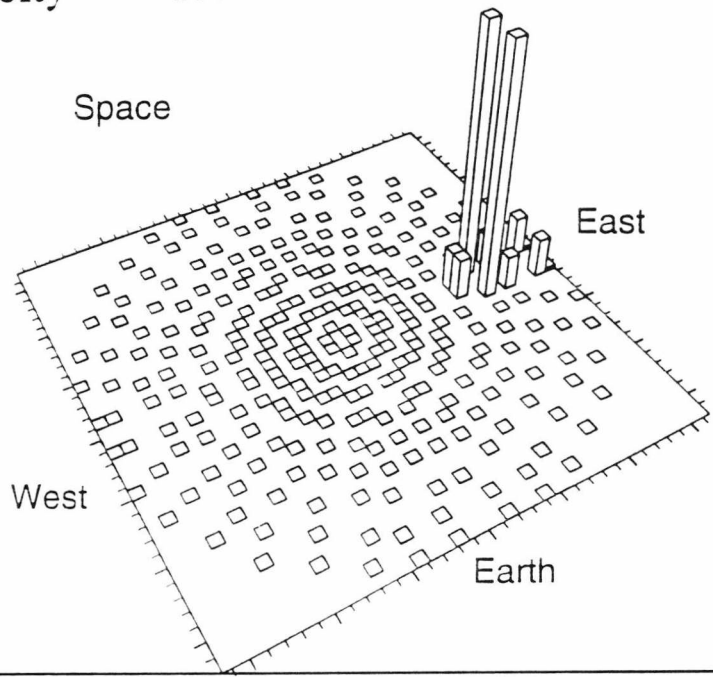

Apogee = 15470 km
Perigee = 6630km
Inclination = 150°
Eccentricity = 0.4

South

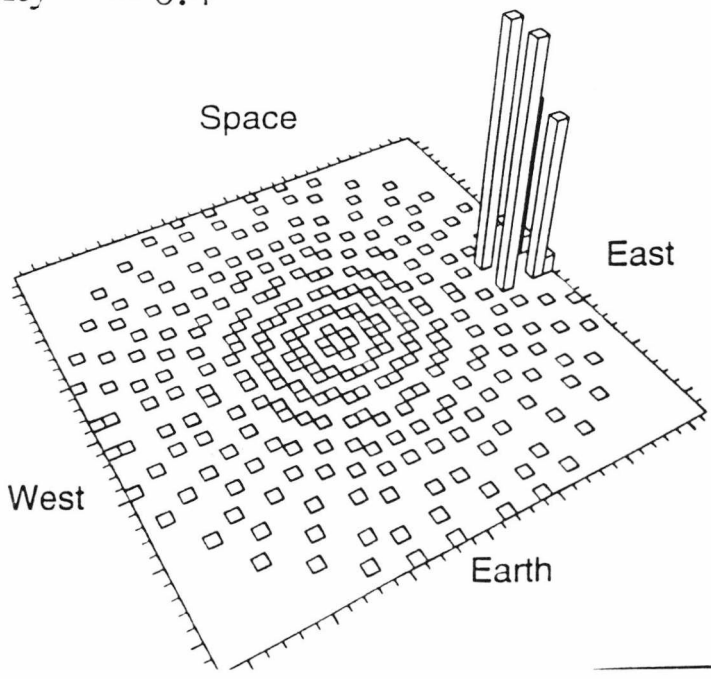

Apogee = 26400 km
Perigee = 6600 km
Inclination = 0°
Eccentricity = 0.6

South

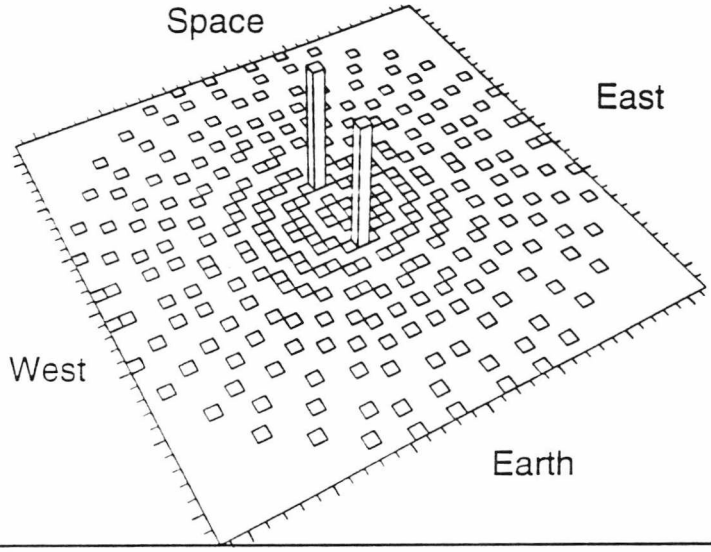

Apogee = 26400 km
Perigee = 6600km
Inclination = 30°
Eccentricity = 0.6

South

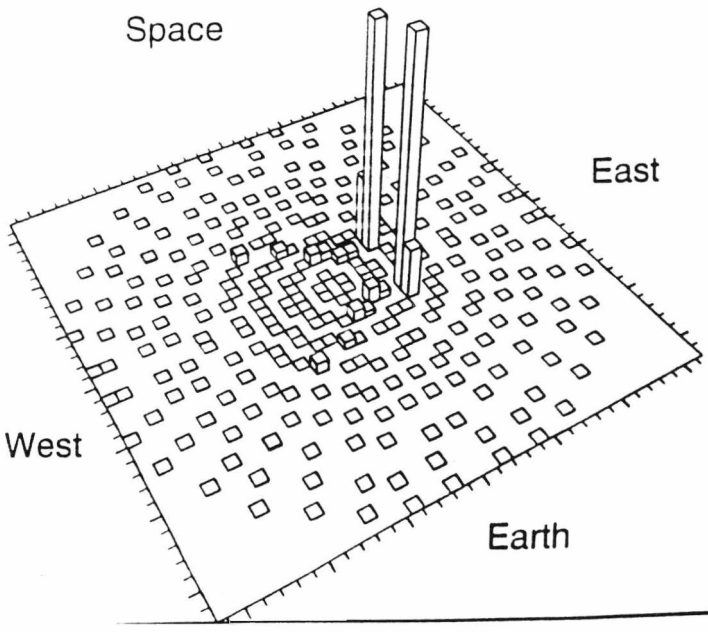

Apogee = 26400 km
Perigee = 6600 km
Inclination = 60°
Eccentricity = 0.6

South

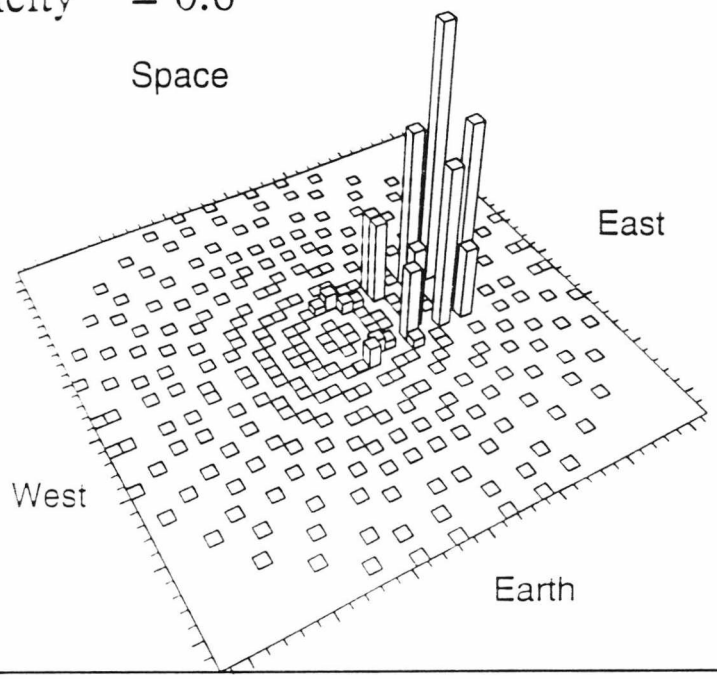

Apogee = 26400 km
Perigee = 6600km
Inclination = 90°
Eccentricity = 0.6

South

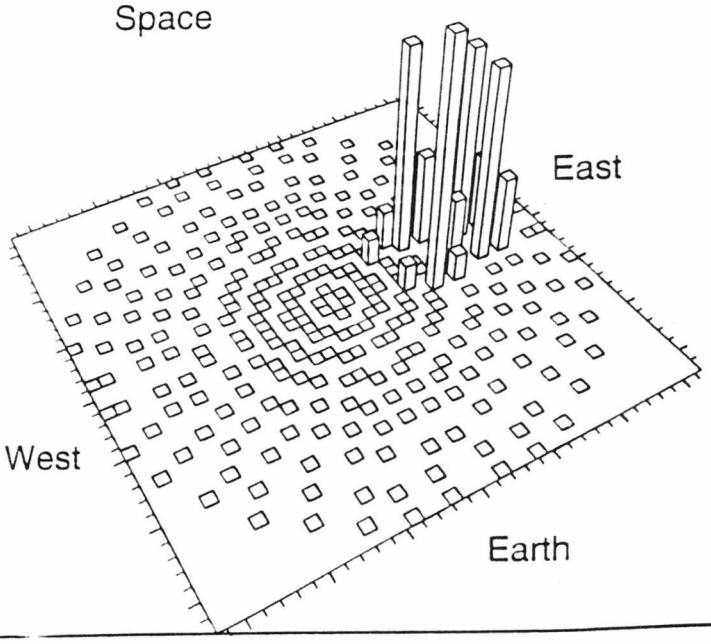

Apogee = 26400 km
Perigee = 6600 km
Inclination = 120°
Eccentricity = 0.6

South

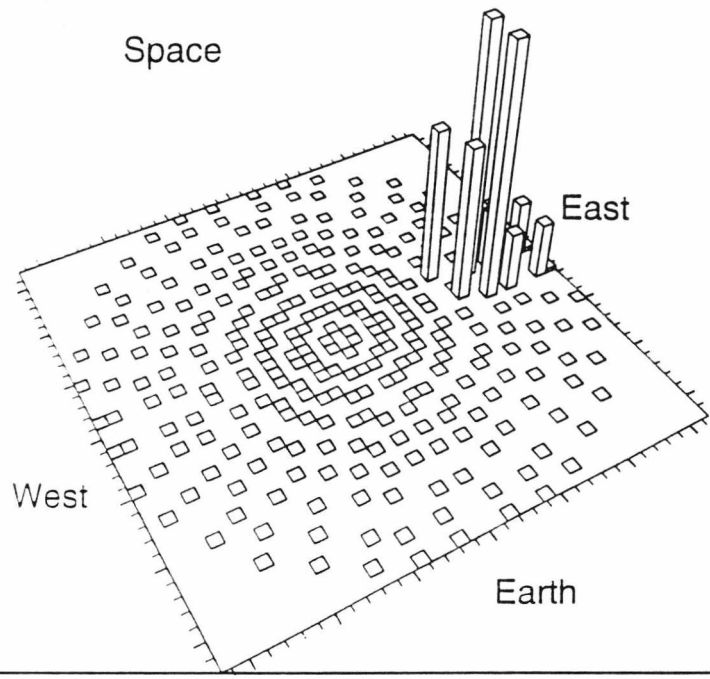

Apogee = 26400 km
Perigee = 6600km
Inclination = 150°
Eccentricity = 0.6

South

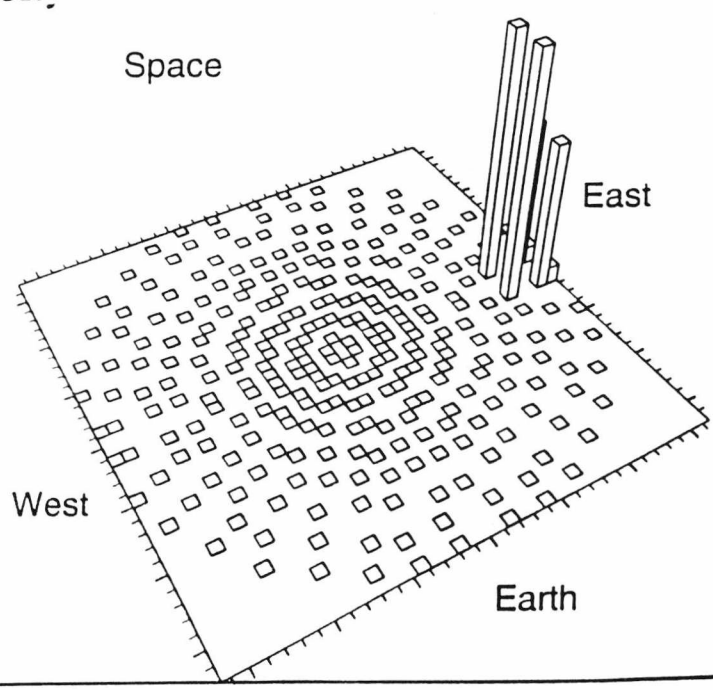

Apogee = 42250 km
Perigee = 6580 km
Inclination = 0°
Eccentricity = 0.73

South

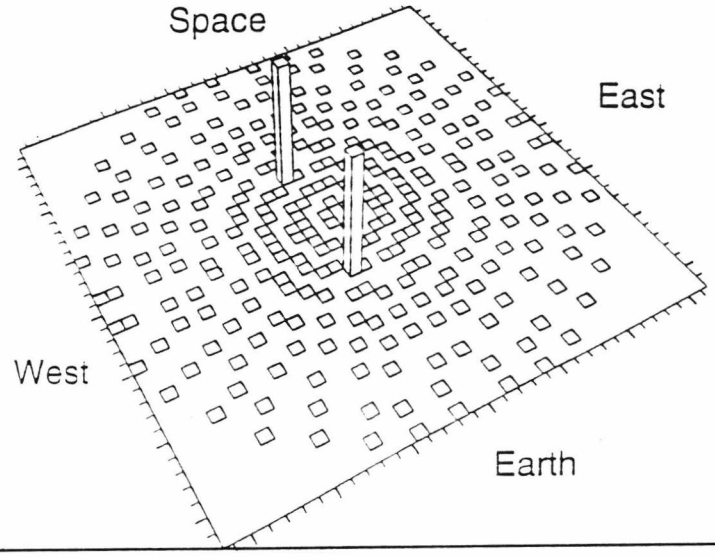

Apogee = 42250 km
Perigee = 6580km
Inclination = 30°
Eccentricity = 0.73

South

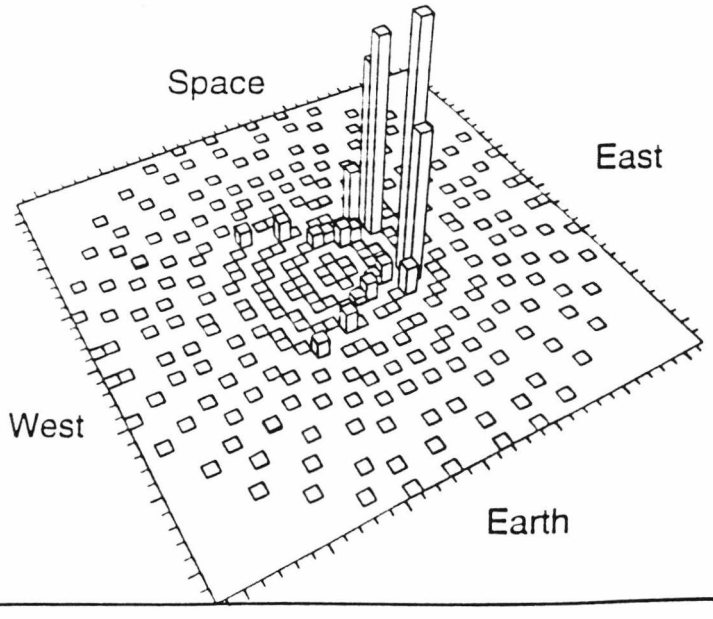

Apogee = 42250 km
Perigee = 6580 km
Inclination = 60°
Eccentricity = 0.73

South

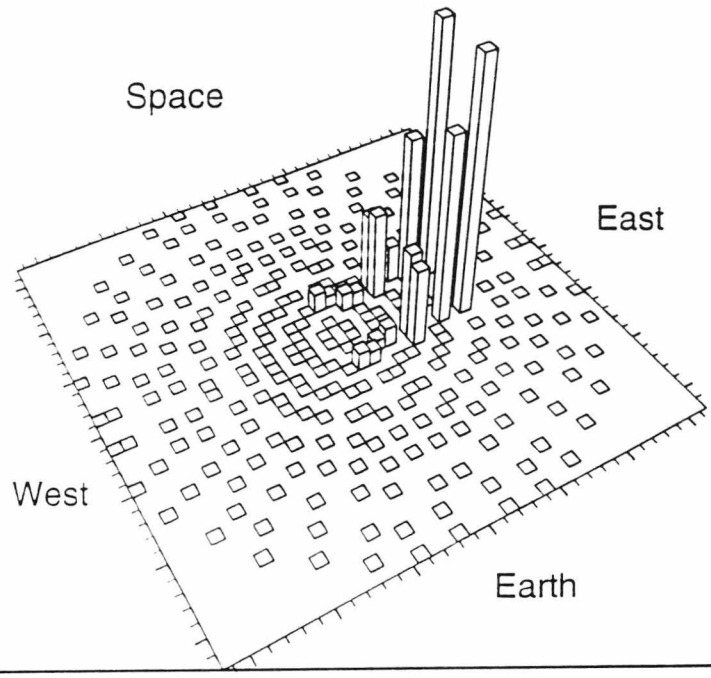

Apogee = 42250 km
Perigee = 6580km
Inclination = 90°
Eccentricity = 0.73

South

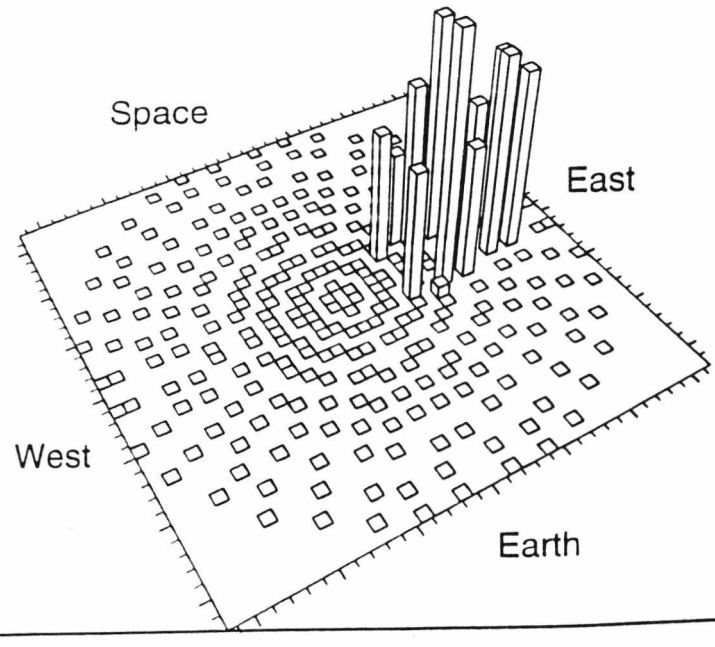

Apogee = 42250 km
Perigee = 6580 km
Inclination = 120°
Eccentricity = 0.73

South

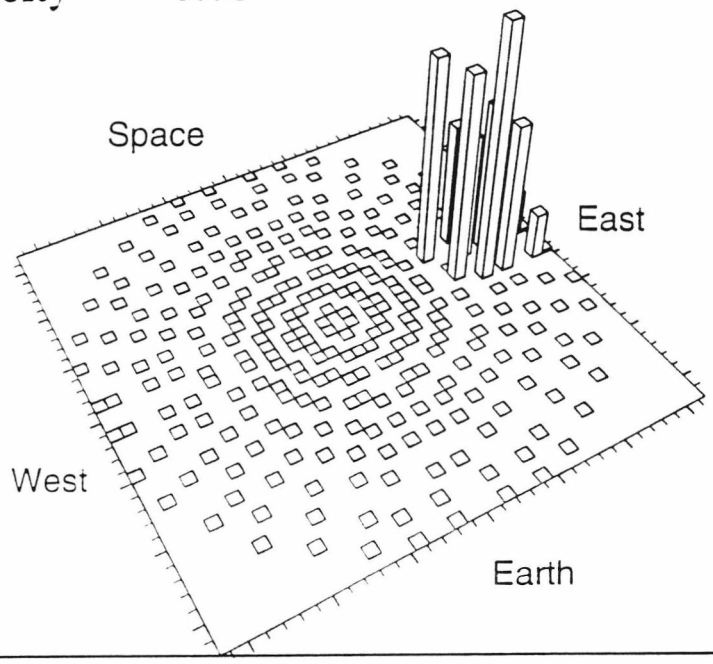

Apogee = 42250 km
Perigee = 6580km
Inclination = 150°
Eccentricity = 0.73

South

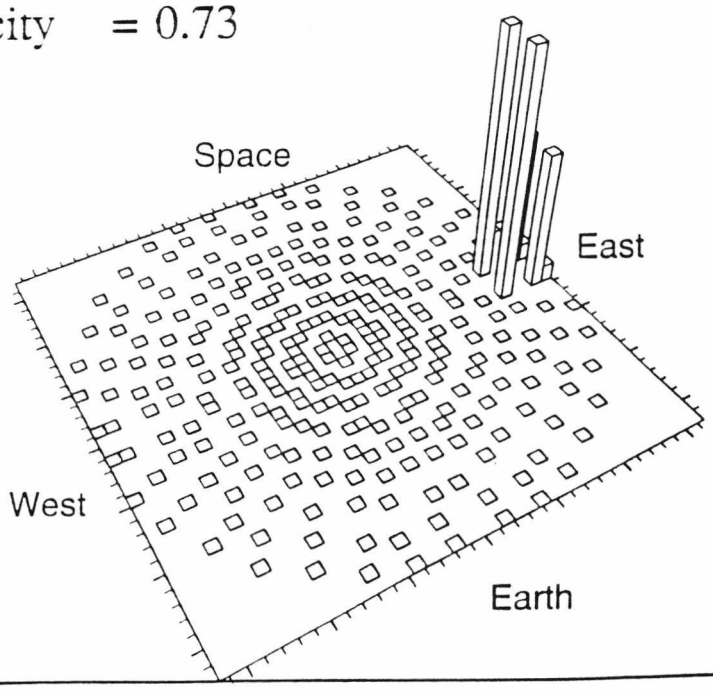

Apogee = 6848 km
Perigee = 6848 km
Inclination = 30°
Eccentricity = 0.0

West

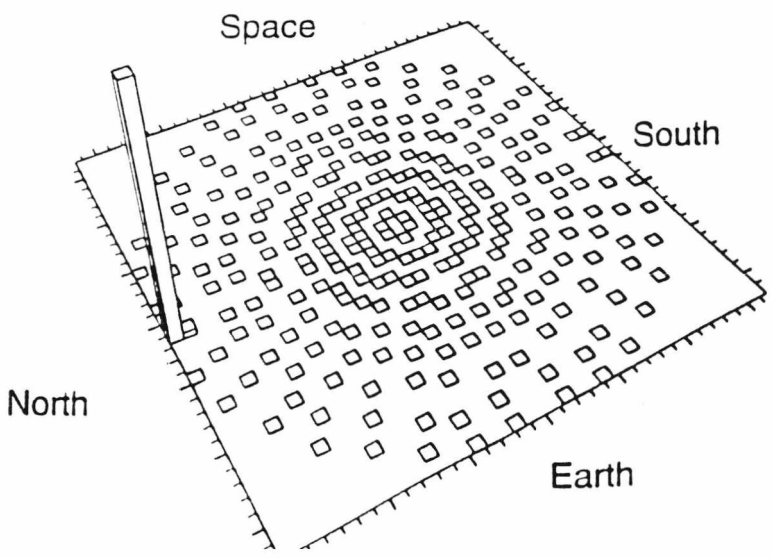

Apogee = 10005 km
Perigee = 6670 km
Inclination = 0°
Eccentricity = 0.2

West

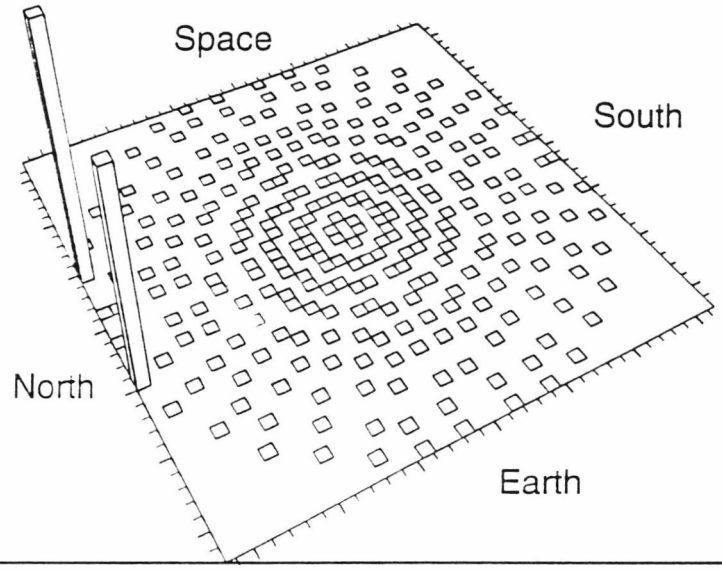

Apogee = 10005 km
Perigee = 6670km
Inclination = 30°
Eccentricity = 0.2

West

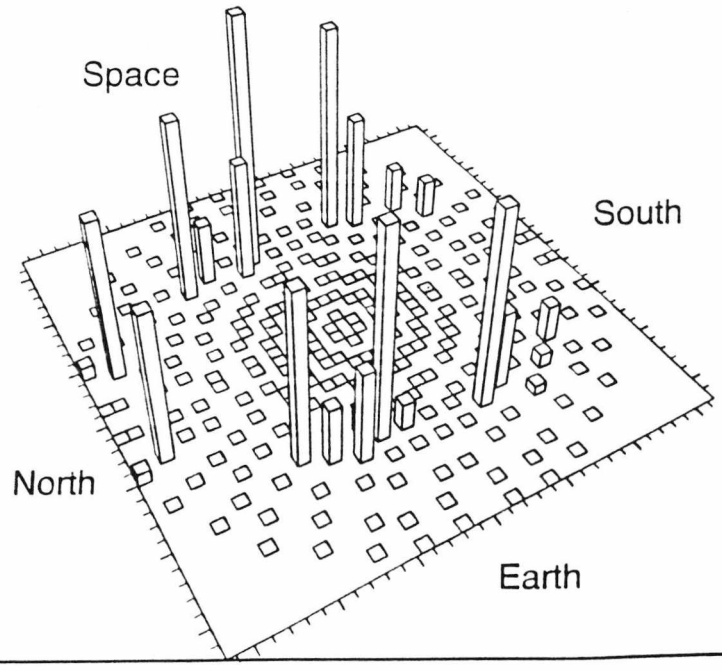

Apogee = 10005 km
Perigee = 6670 km
Inclination = 60°
Eccentricity = 0.2

West

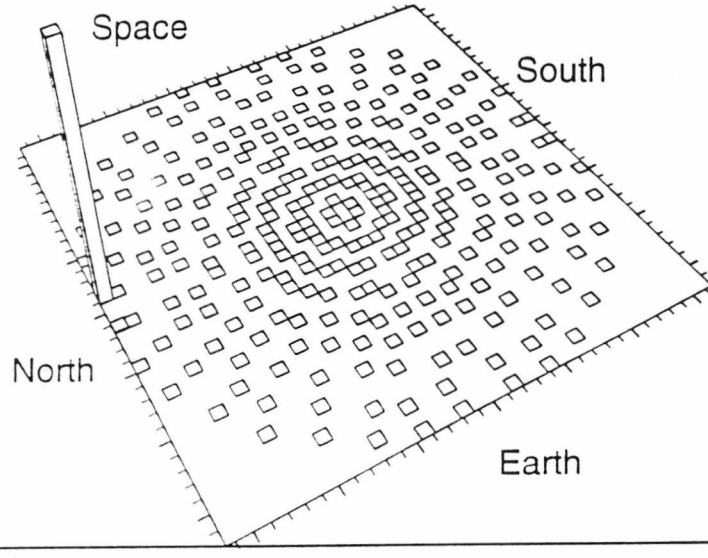

Apogee = 15470 km
Perigee = 6630 km
Inclination = 0°
Eccentricity = 0.4

West

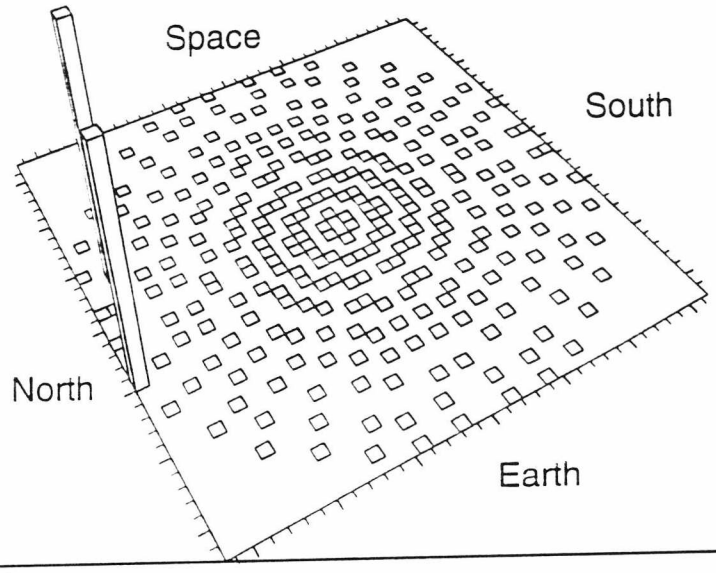

Apogee = 15470 km
Perigee = 6630km
Inclination = 30°
Eccentricity = 0.4

West

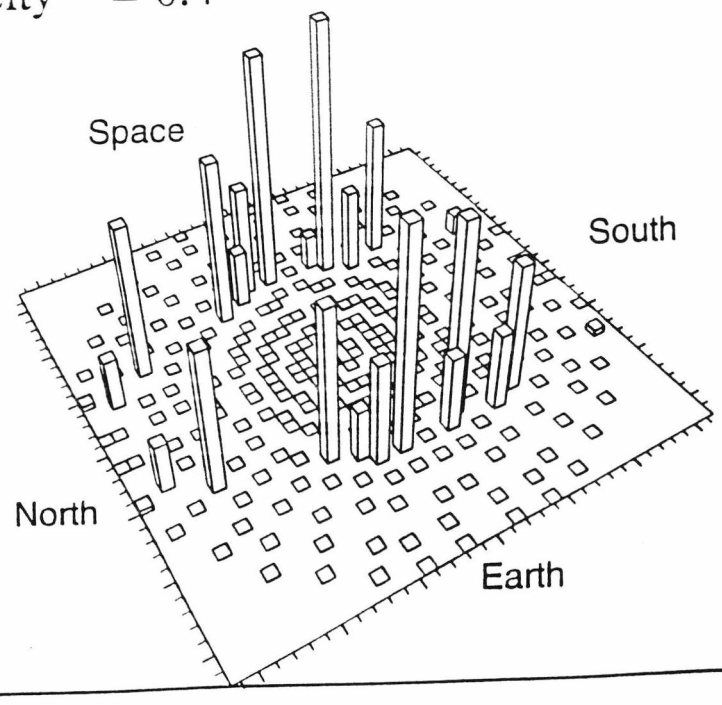

Apogee = 15470 km
Perigee = 6630 km
Inclination = 60°
Eccentricity = 0.4

West

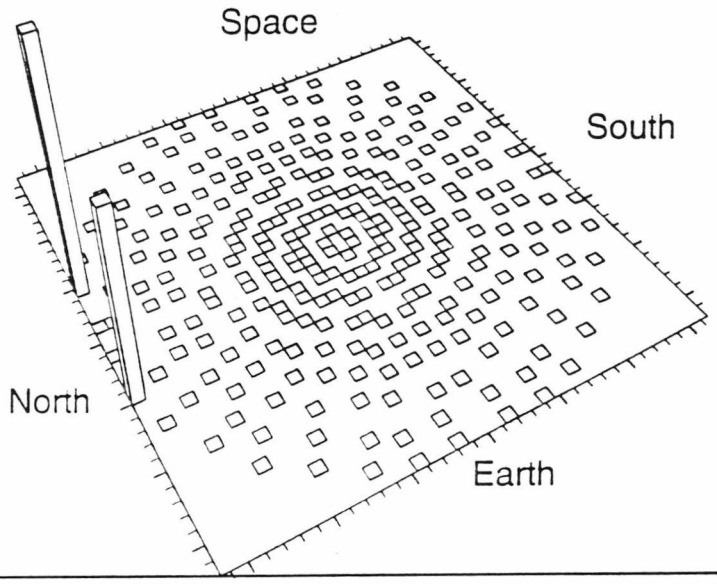

Apogee = 26400 km
Perigee = 6600 km
Inclination = 0°
Eccentricity = 0.6

West

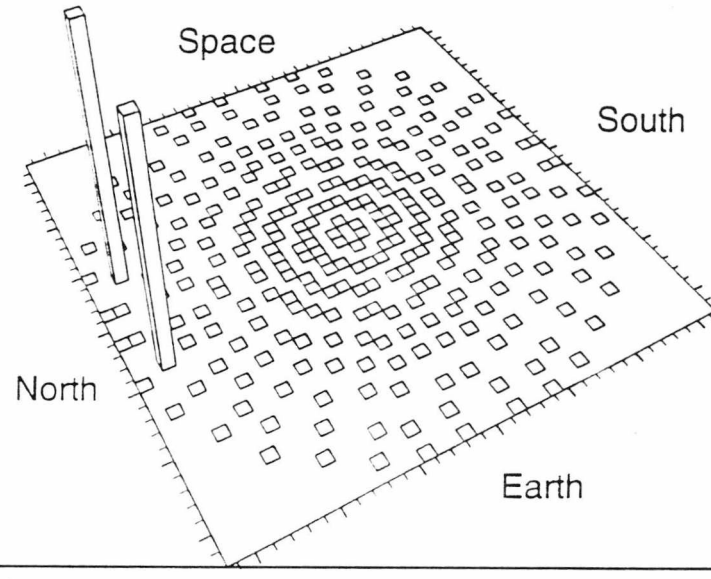

West

Apogee = 26400 km
Perigee = 6600km
Inclination = 30°
Eccentricity = 0.6

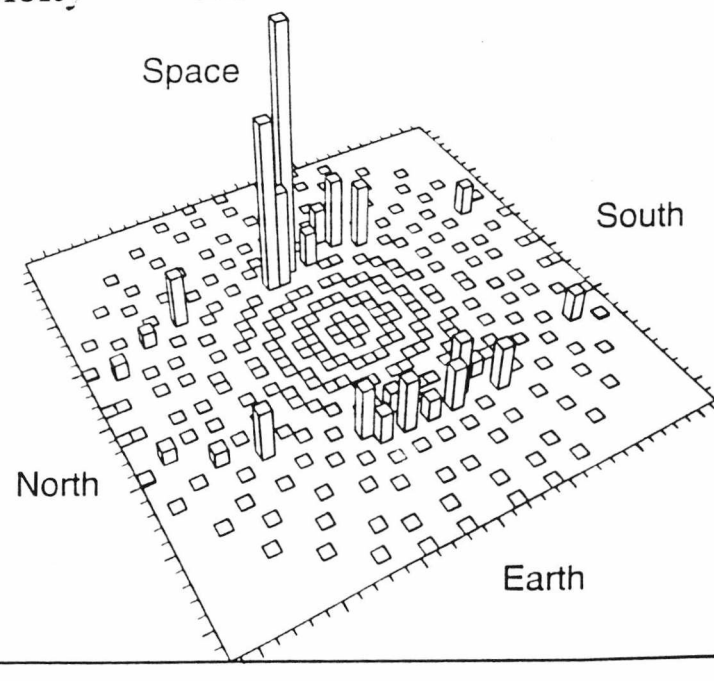

Apogee = 26400 km
Perigee = 6600 km
Inclination = 60°
Eccentricity = 0.6

West

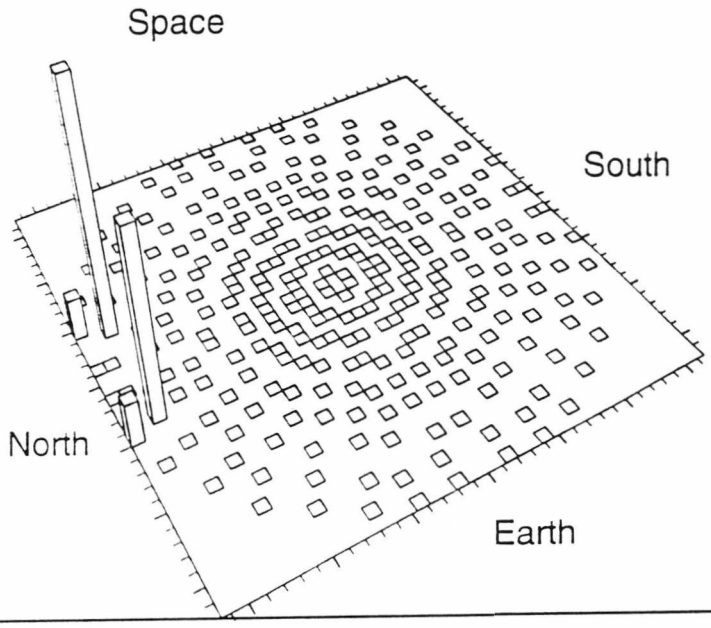

Apogee = 42250 km
Perigee = 6580 km
Inclination = 0°
Eccentricity = 0.73

West

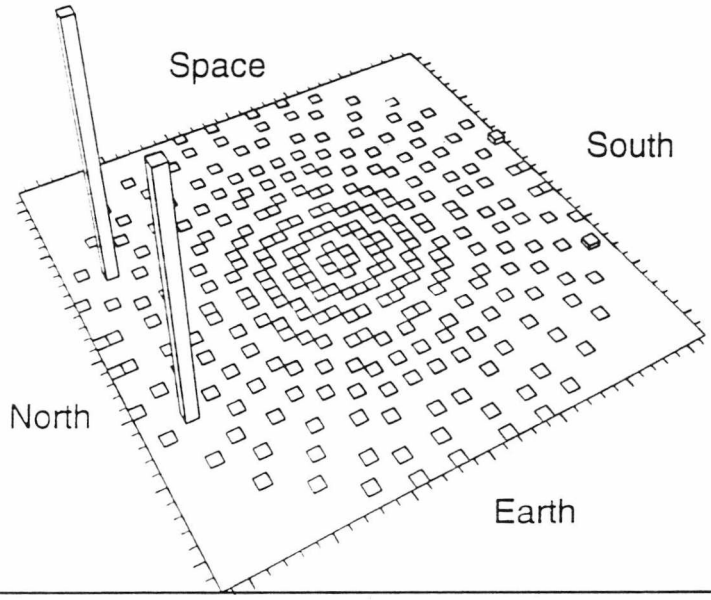

Apogee = 42250 km
Perigee = 6580km
Inclination = 30°
Eccentricity = 0.73

West

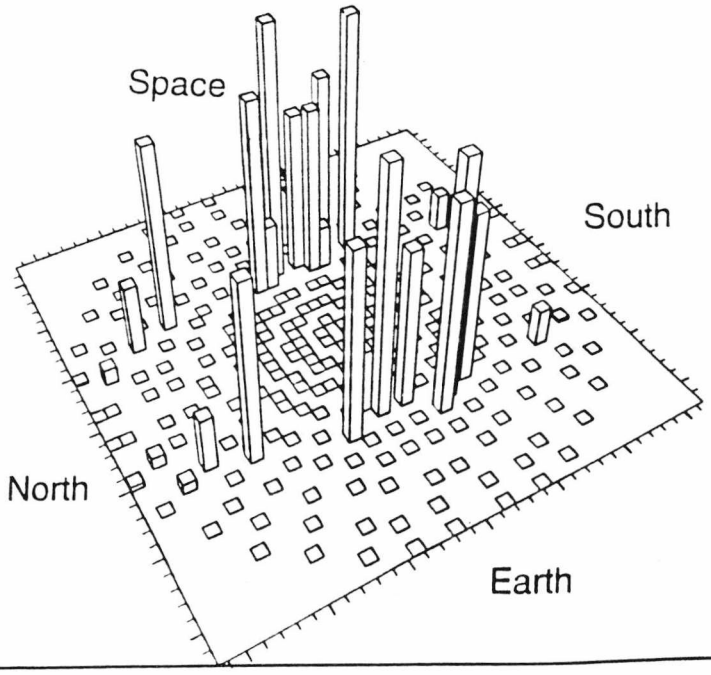

Apogee = 42250 km
Perigee = 6580 km
Inclination = 60°
Eccentricity = 0.73

West

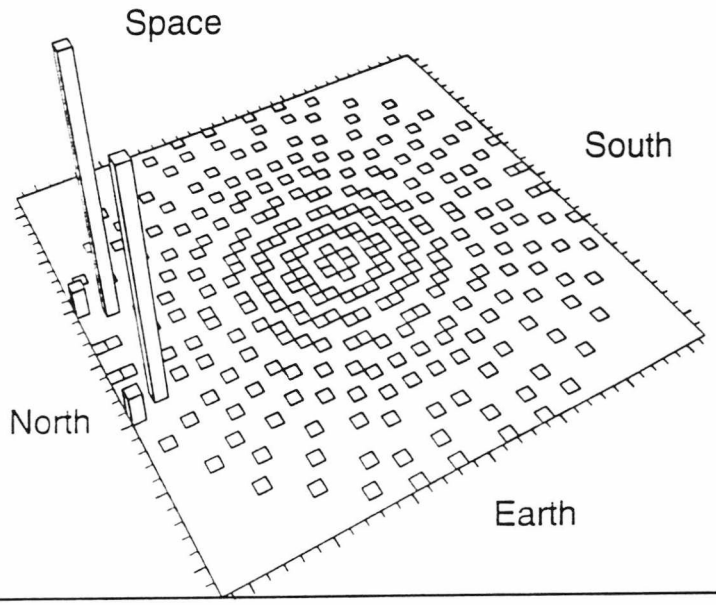

Apogee = 6848 km
Perigee = 6848 km
Inclination = 0°
Eccentricity = 0.0

North

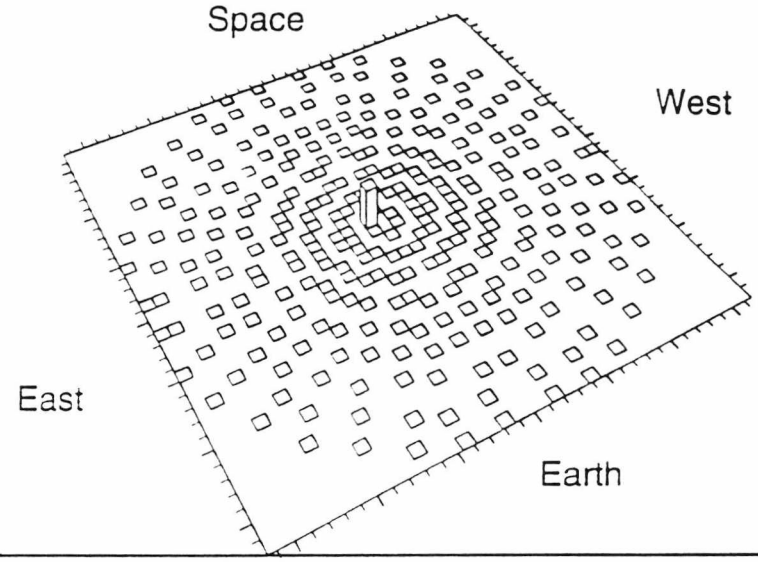

Apogee = 6848 km
Perigee = 6848 km
Inclination = 30°
Eccentricity = 0.0

North

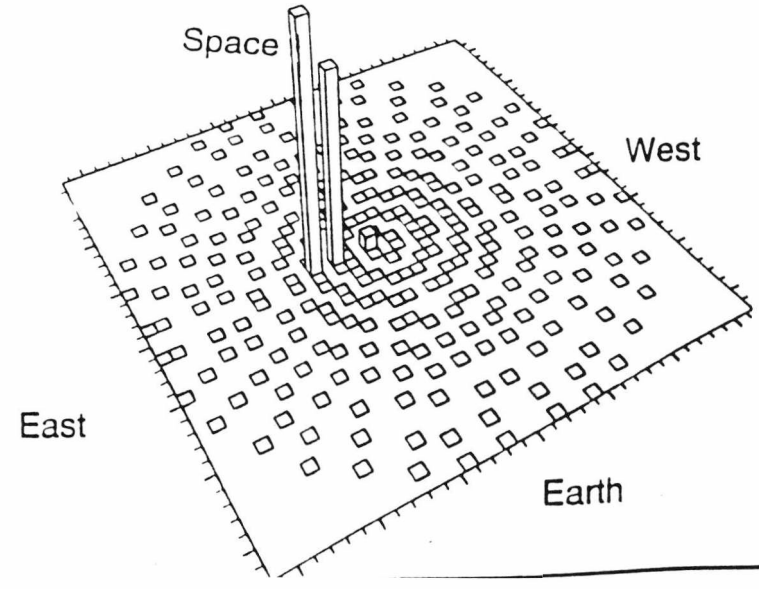

Apogee = 6848 km
Perigee = 6848 km
Inclination = 60°
Eccentricity = 0.0

North

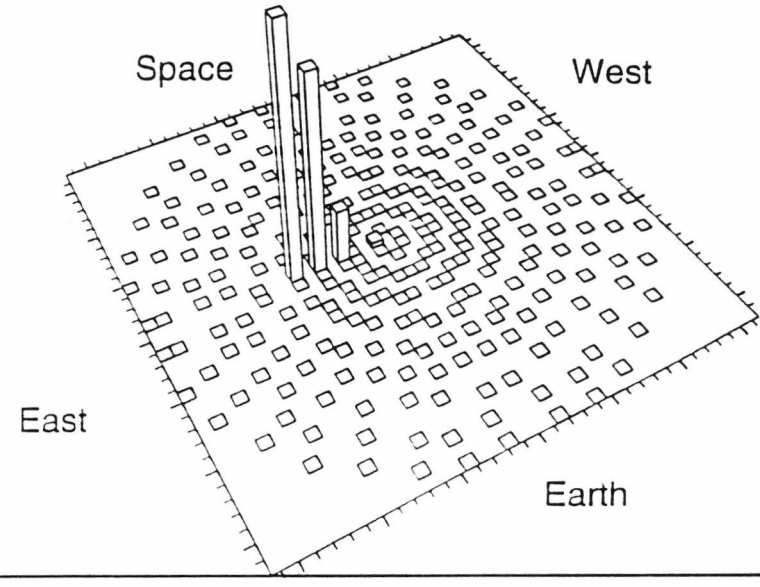

Apogee = 6848 km
Perigee = 6848 km
Inclination = 90°
Eccentricity = 0.0

North

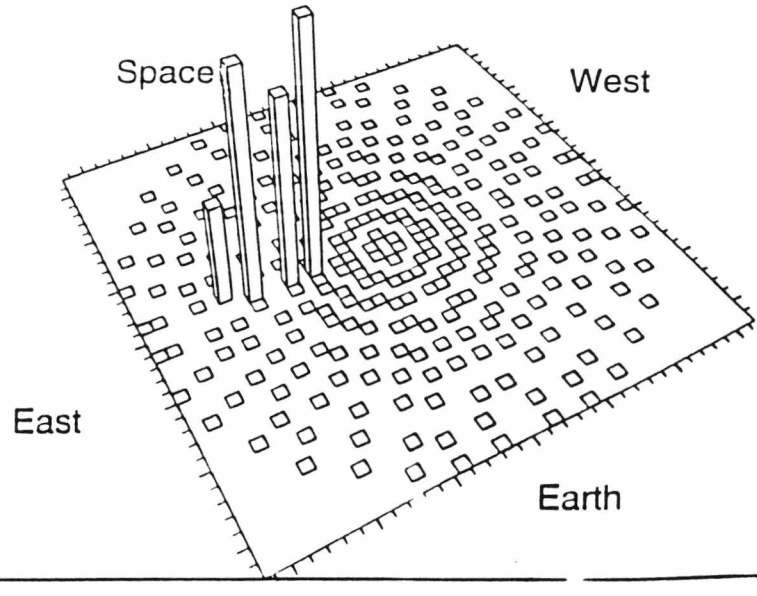

Apogee = 6848 km
Perigee = 6848 km
Inclination = 120°
Eccentricity = 0.0

North

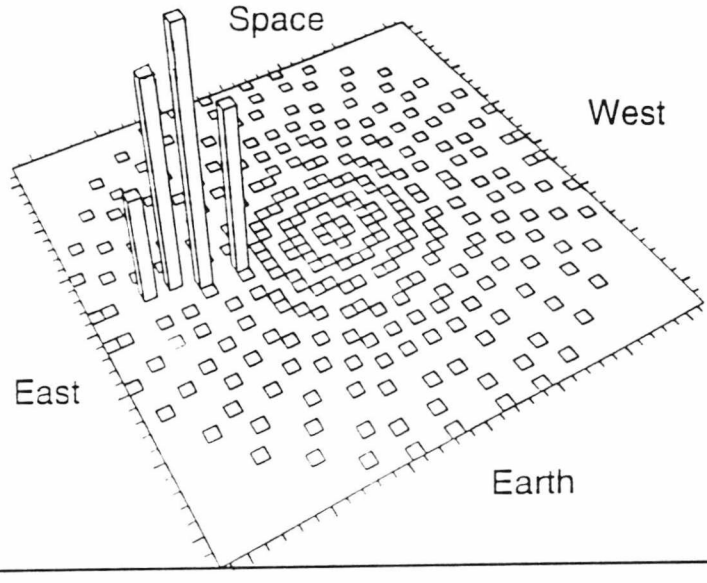

Apogee = 6848 km
Perigee = 6848 km
Inclination = 150°
Eccentricity = 0.0

North

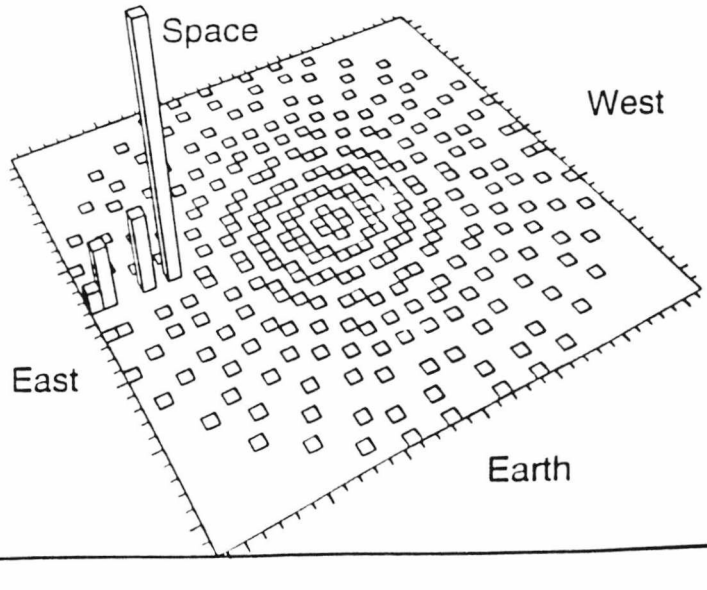

Apogee = 10005 km
Perigee = 6670 km
Inclination = 0°
Eccentricity = 0.2

North

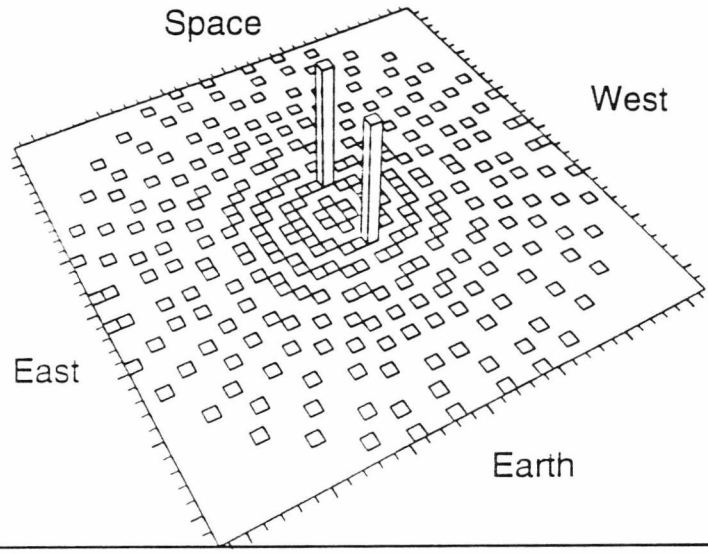

Apogee = 10005 km
Perigee = 6670km
Inclination = 30°
Eccentricity = 0.2

North

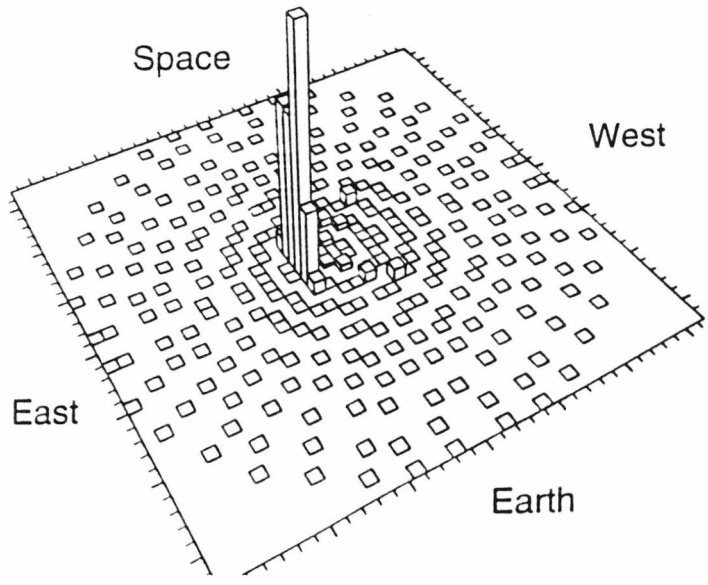

Apogee = 10005 km
Perigee = 6670 km
Inclination = 60°
Eccentricity = 0.2

North

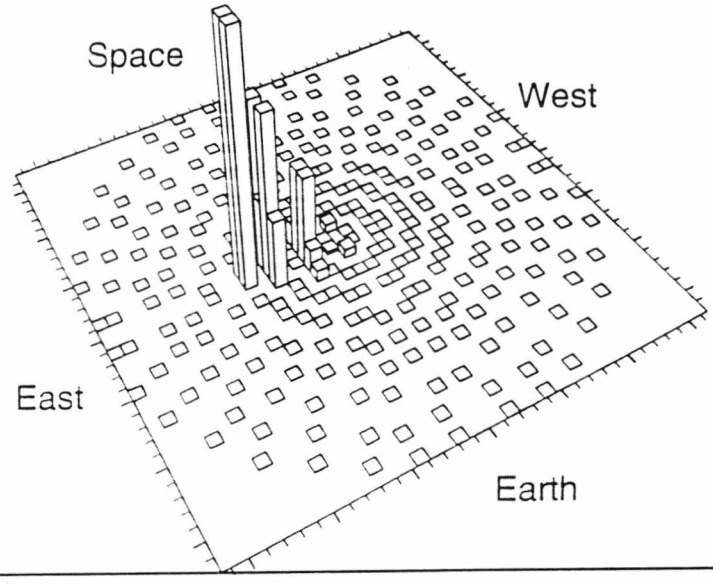

North

Apogee = 10005 km
Perigee = 6670km
Inclination = 90°
Eccentricity = 0.2

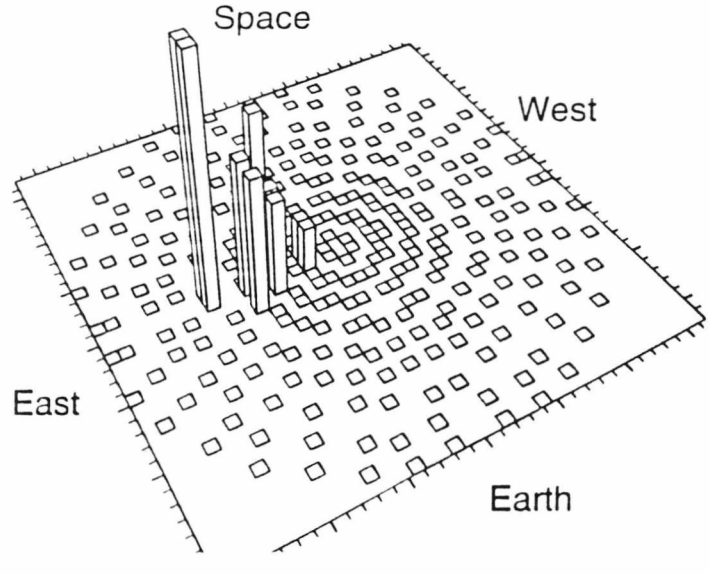

Apogee = 10005 km
Perigee = 6670 km
Inclination = 120°
Eccentricity = 0.2

North

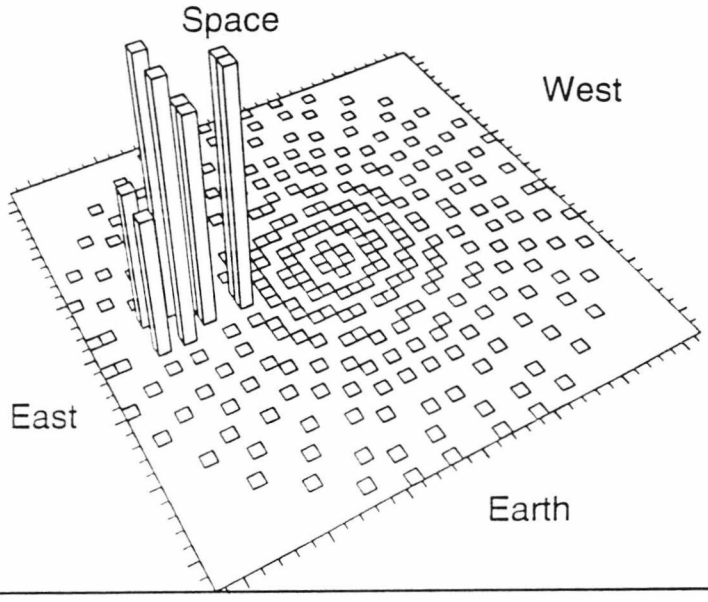

Apogee = 10005 km
Perigee = 6670km
Inclination = 150°
Eccentricity = 0.2

North

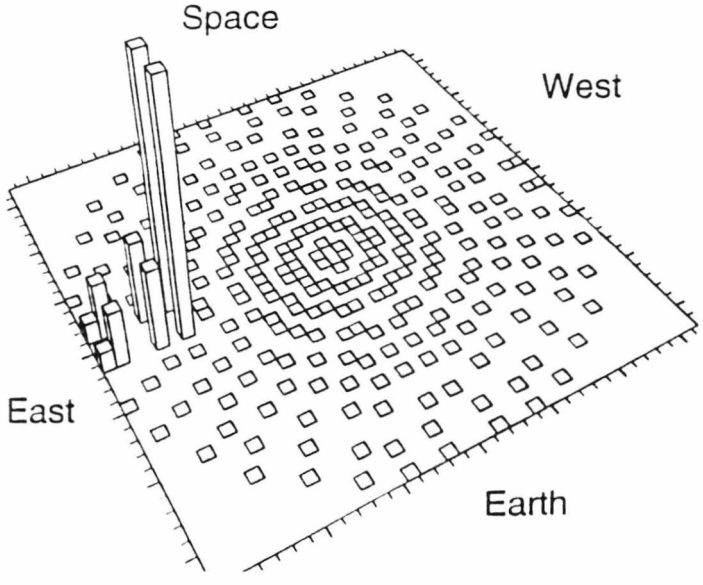

Apogee = 15470 km
Perigee = 6630 km
Inclination = 0°
Eccentricity = 0.4

North

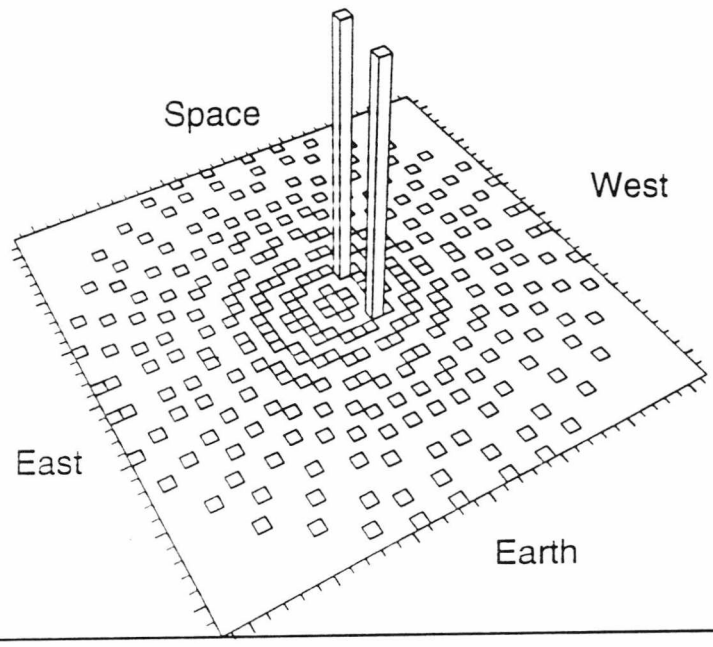

Apogee = 15470 km
Perigee = 6630km
Inclination = 30°
Eccentricity = 0.4

North

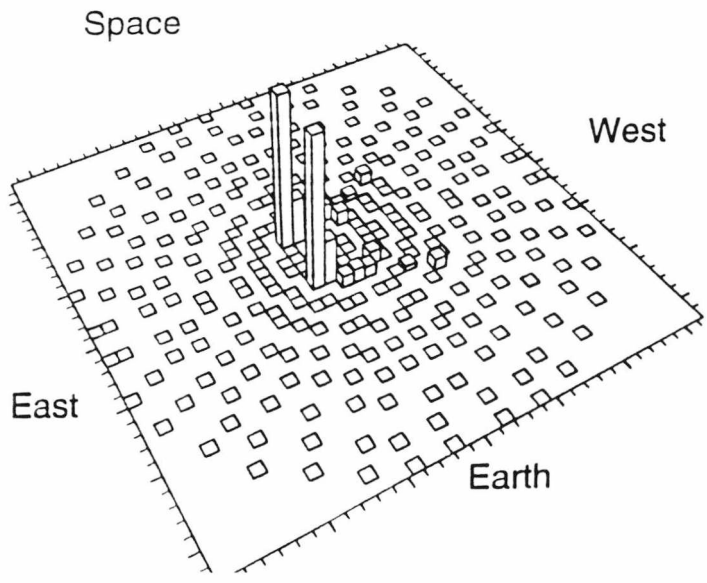

Apogee = 15470 km
Perigee = 6630 km
Inclination = 60°
Eccentricity = 0.4

North

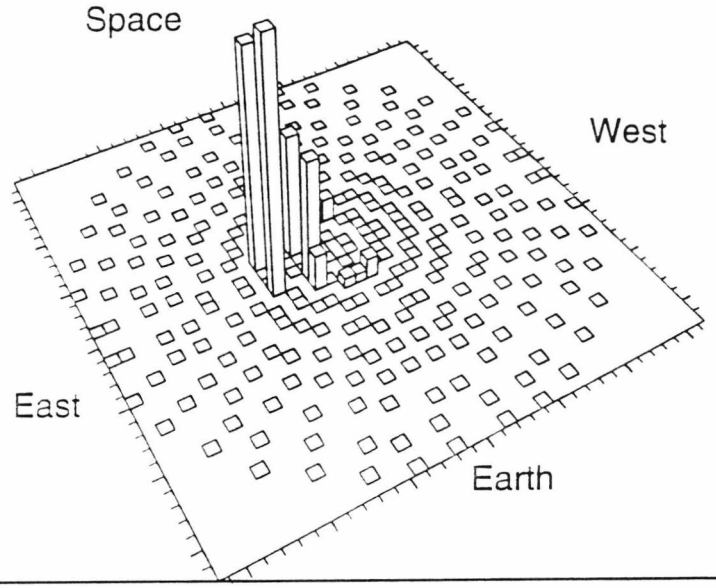

Apogee = 15470 km
Perigee = 6630km
Inclination = 90°
Eccentricity = 0.4

North

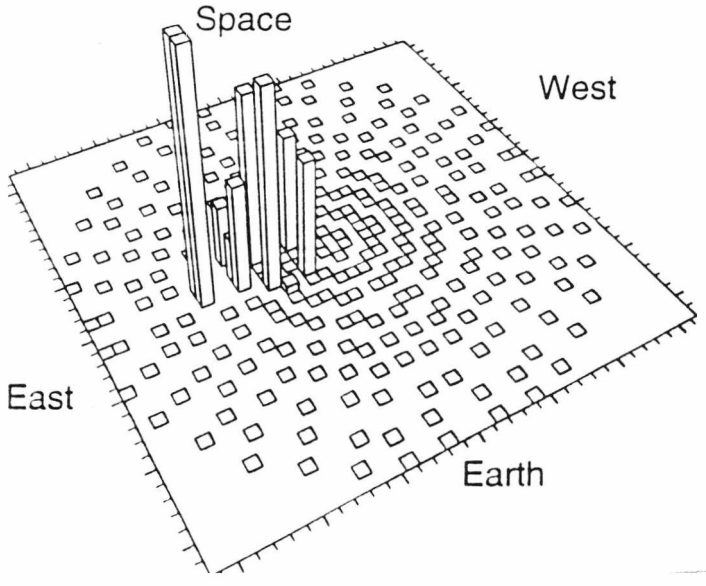

Apogee = 15470 km
Perigee = 6630 km
Inclination = 120°
Eccentricity = 0.4

North

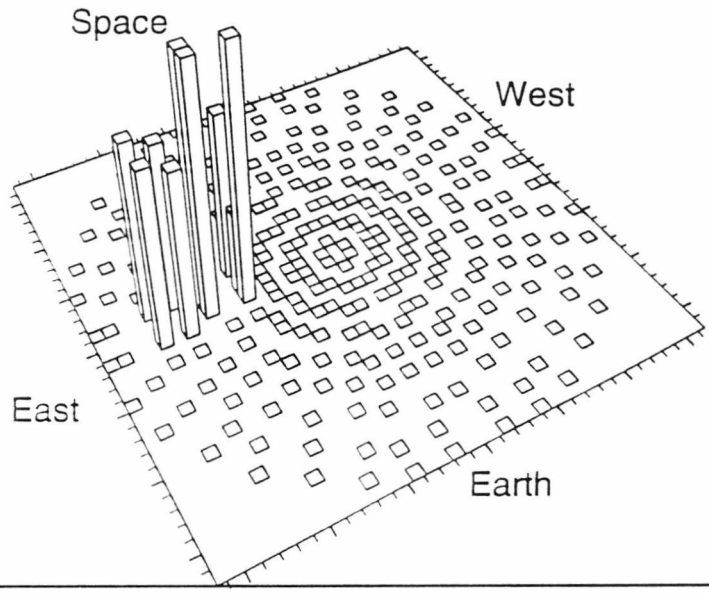

Apogee = 15470 km
Perigee = 6630km
Inclination = 150°
Eccentricity = 0.4

North

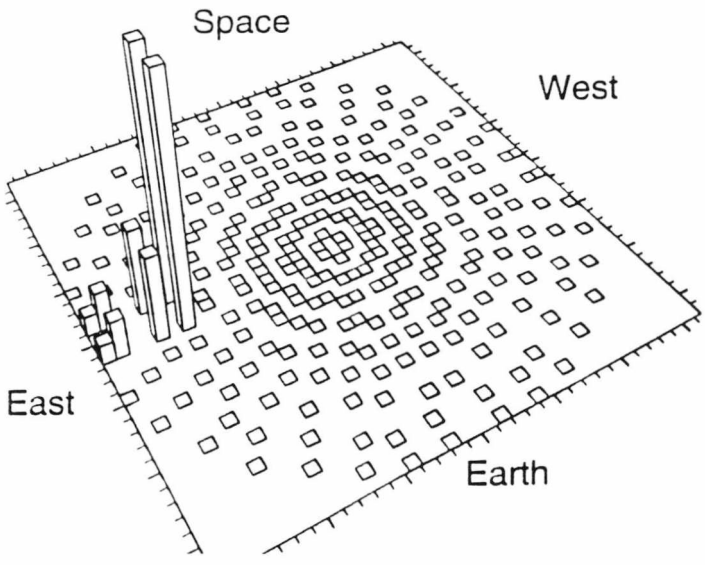

Apogee = 26400 km
Perigee = 6600 km
Inclination = 0°
Eccentricity = 0.6

North

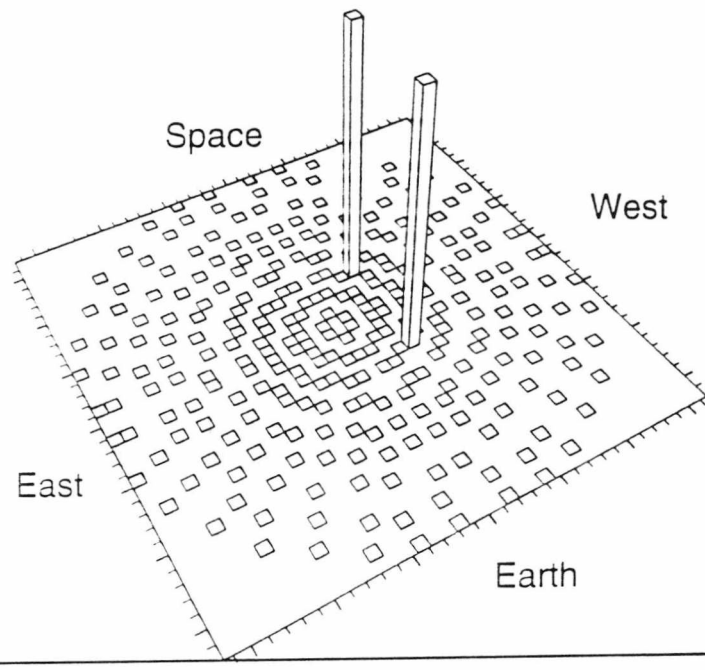

Apogee = 26400 km
Perigee = 6600km
Inclination = 30°
Eccentricity = 0.6

North

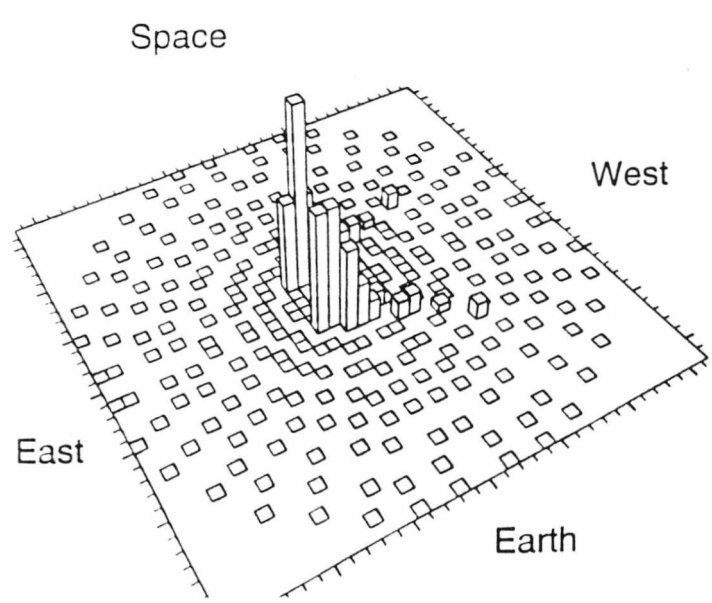

Apogee = 26400 km
Perigee = 6600 km
Inclination = 60°
Eccentricity = 0.6

North

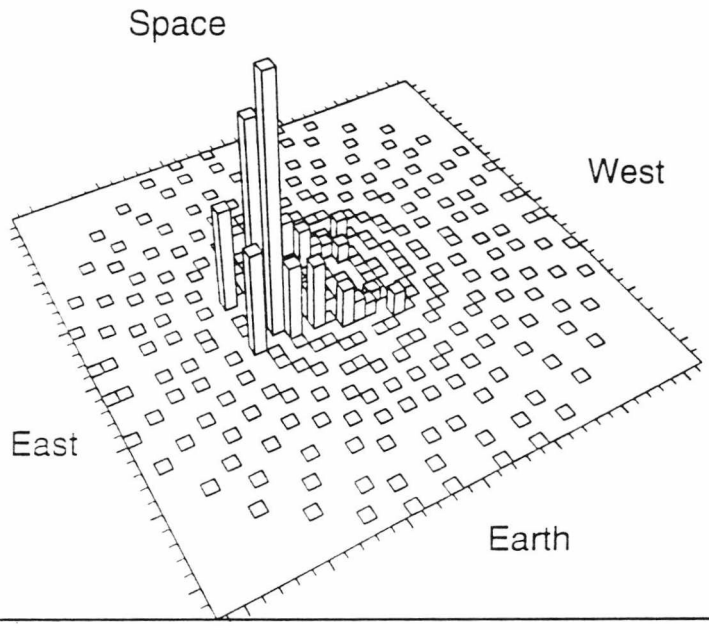

Apogee = 26400 km
Perigee = 6600km
Inclination = 90°
Eccentricity = 0.6

North

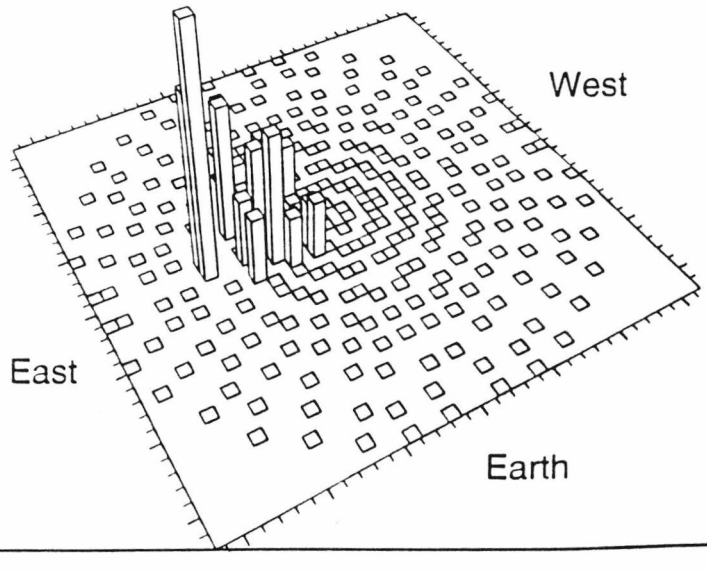

Apogee = 26400 km
Perigee = 6600 km
Inclination = 120°
Eccentricity = 0.6

North

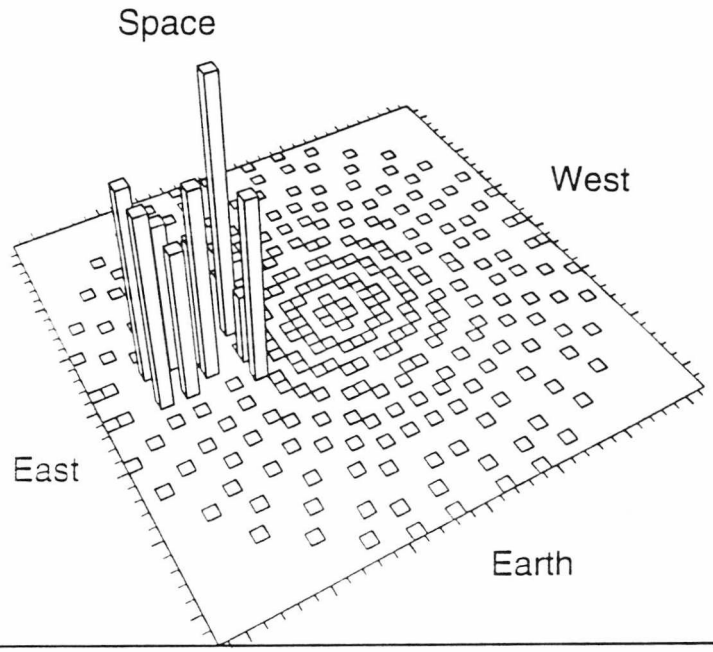

Apogee = 26400 km
Perigee = 6600km
Inclination = 150°
Eccentricity = 0.6

North

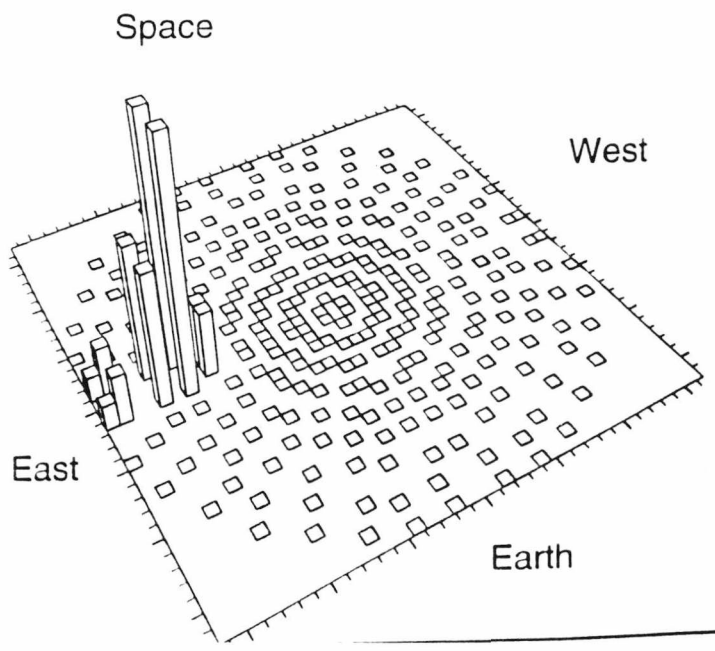

Apogee = 42250 km
Perigee = 6580 km
Inclination = 0°
Eccentricity = 0.73

North

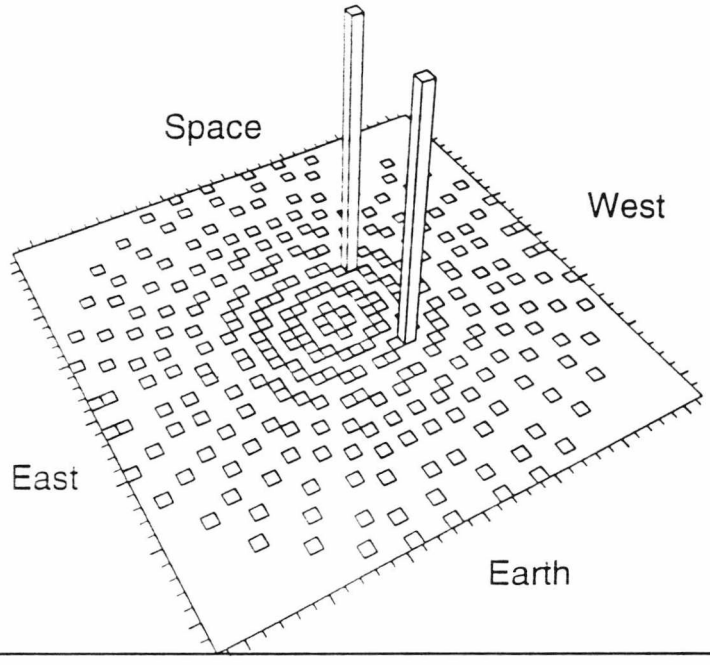

Apogee = 42250 km
Perigee = 6580km
Inclination = 30°
Eccentricity = 0.73

North

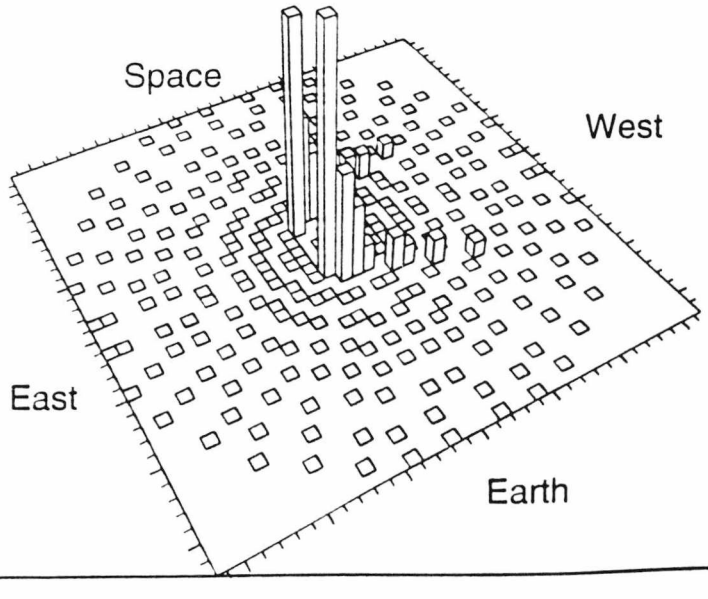

Apogee = 42250 km
Perigee = 6580 km
Inclination = 60°
Eccentricity = 0.73

North

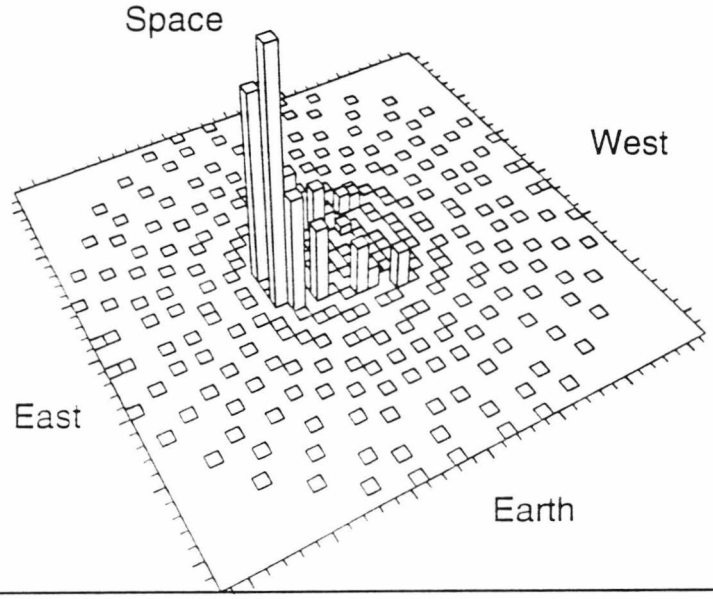

Apogee = 42250 km
Perigee = 6580km
Inclination = 90°
Eccentricity = 0.73

North

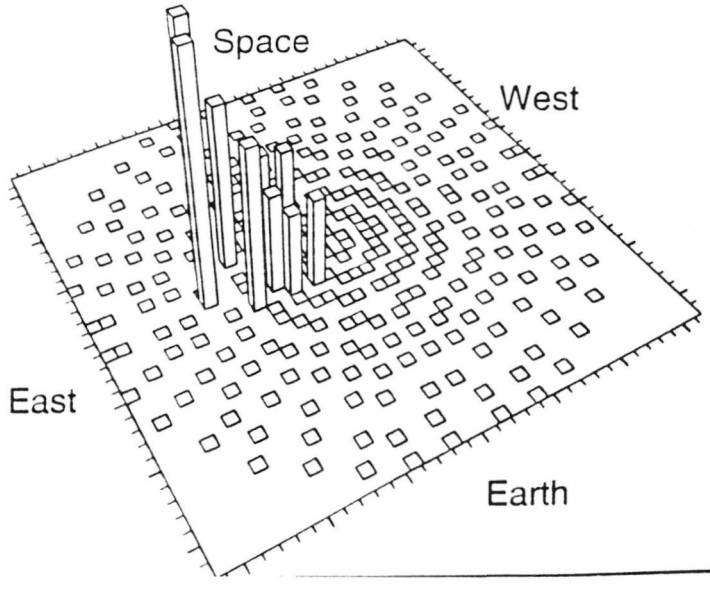

North

Apogee = 42250 km
Perigee = 6580 km
Inclination = 120°
Eccentricity = 0.73

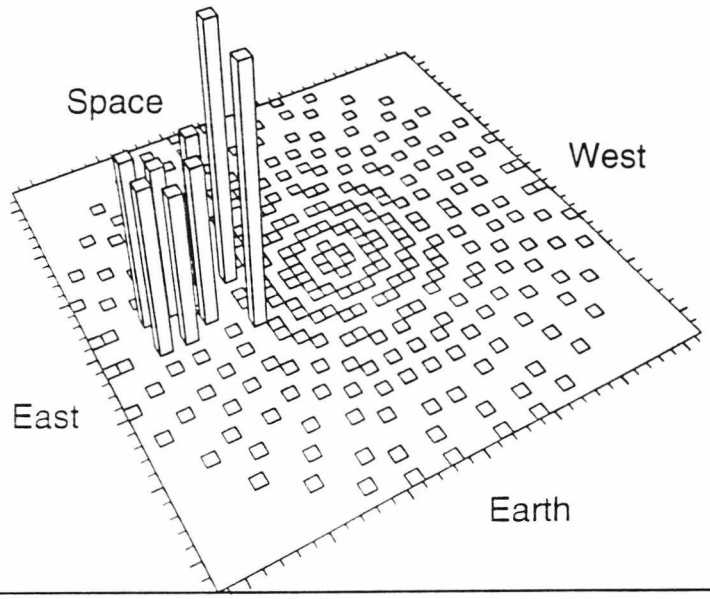

North

Apogee = 42250 km
Perigee = 6580km
Inclination = 150°
Eccentricity = 0.73

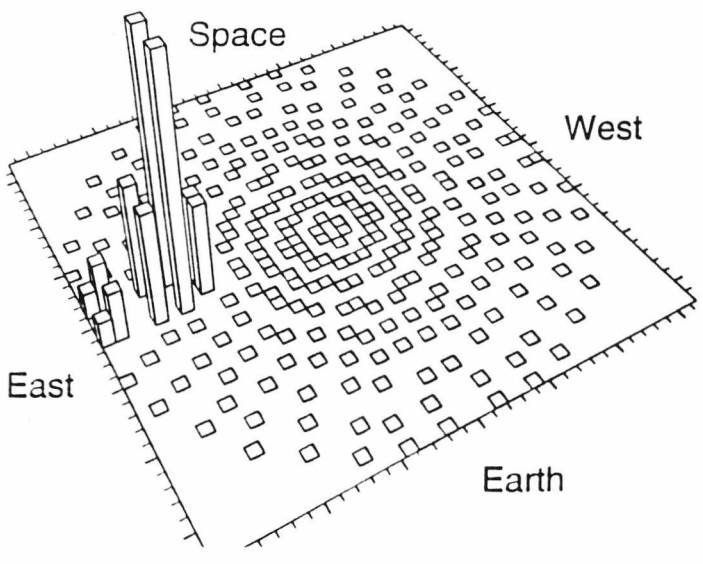

Apogee = 6848 km
Perigee = 6848 km
Inclination = 0°
Eccentricity = 0.0

Space

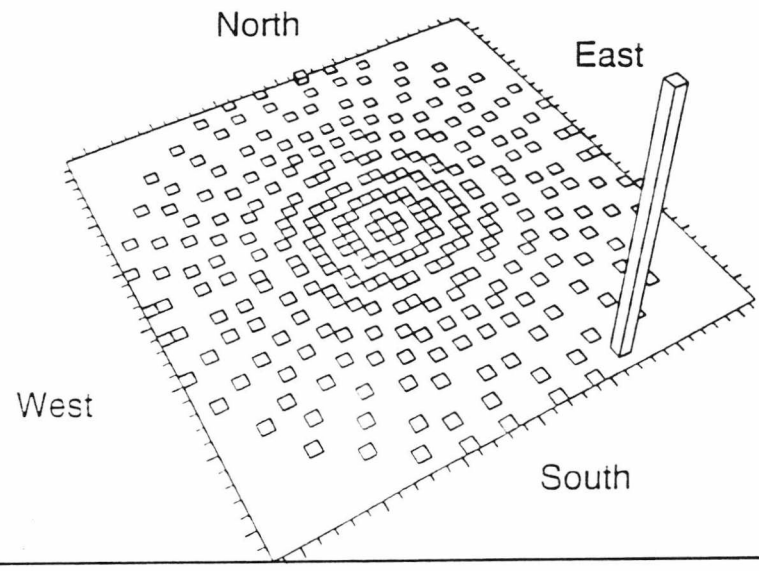

Apogee = 6848 km
Perigee = 6848 km
Inclination = 30°
Eccentricity = 0.0

Space

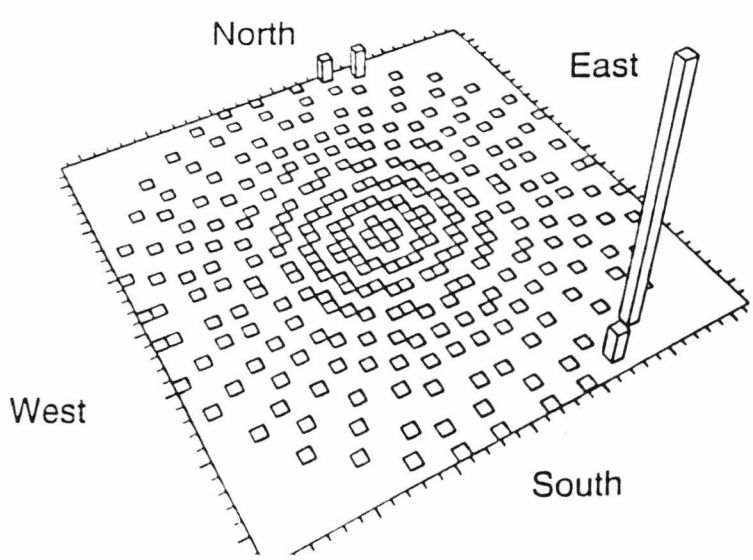

Apogee = 6848 km
Perigee = 6848 km
Inclination = 60°
Eccentricity = 0.0

Space

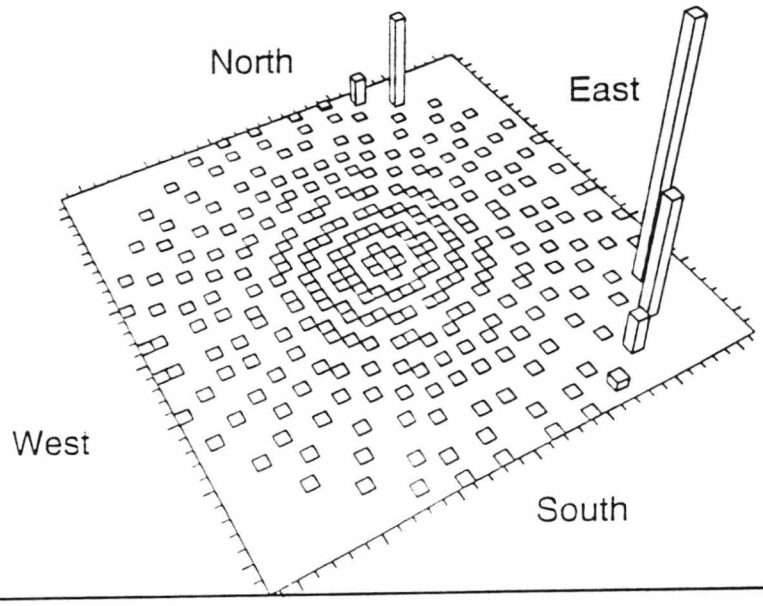

Apogee = 6848 km
Perigee = 6848 km
Inclination = 90°
Eccentricity = 0.0

Space

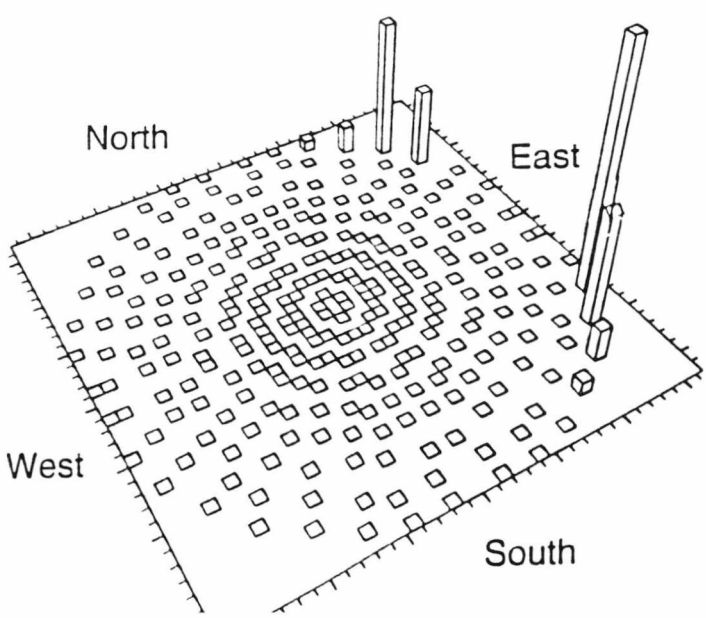

Apogee = 6848 km
Perigee = 6848 km
Inclination = 120°
Eccentricity = 0.0

Space

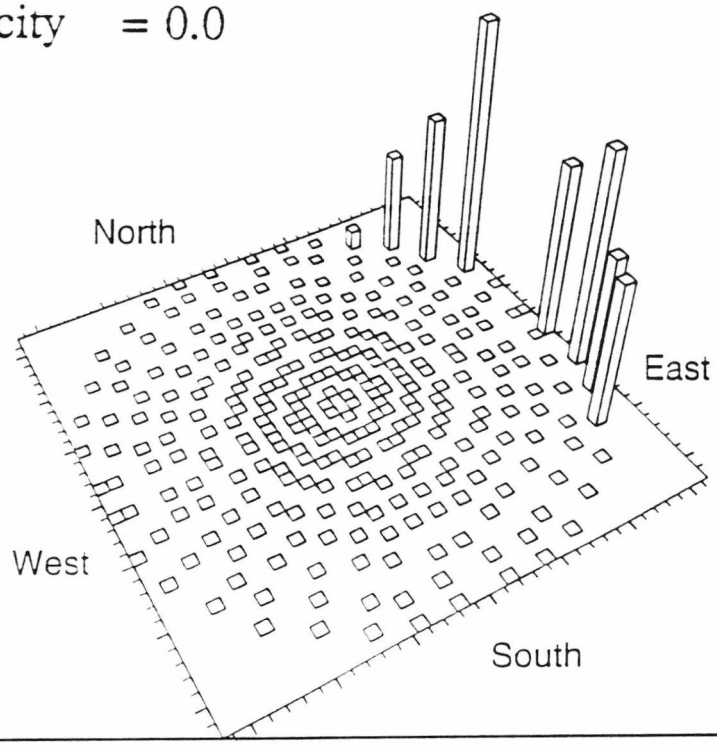

Apogee = 6848 km
Perigee = 6848 km
Inclination = 150°
Eccentricity = 0.0

Space

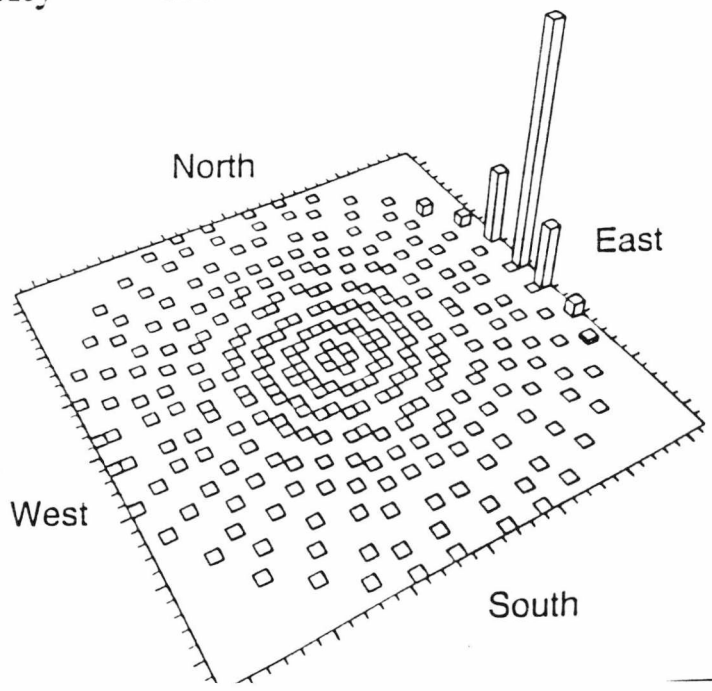

Apogee = 10005 km
Perigee = 6670 km
Inclination = 0°
Eccentricity = 0.2

Space

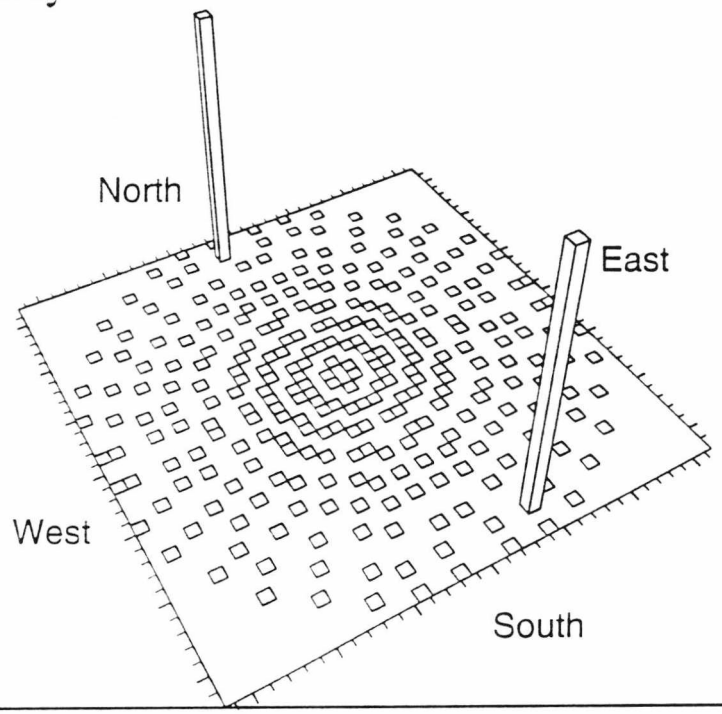

Apogee = 10005 km
Perigee = 6670km
Inclination = 30°
Eccentricity = 0.2

Space

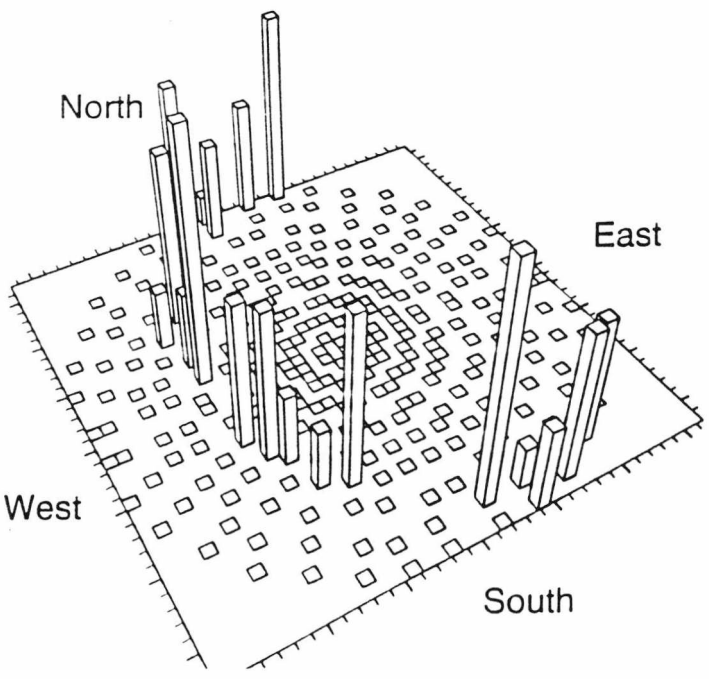

Apogee = 10005 km
Perigee = 6670 km
Inclination = 60°
Eccentricity = 0.2

Space

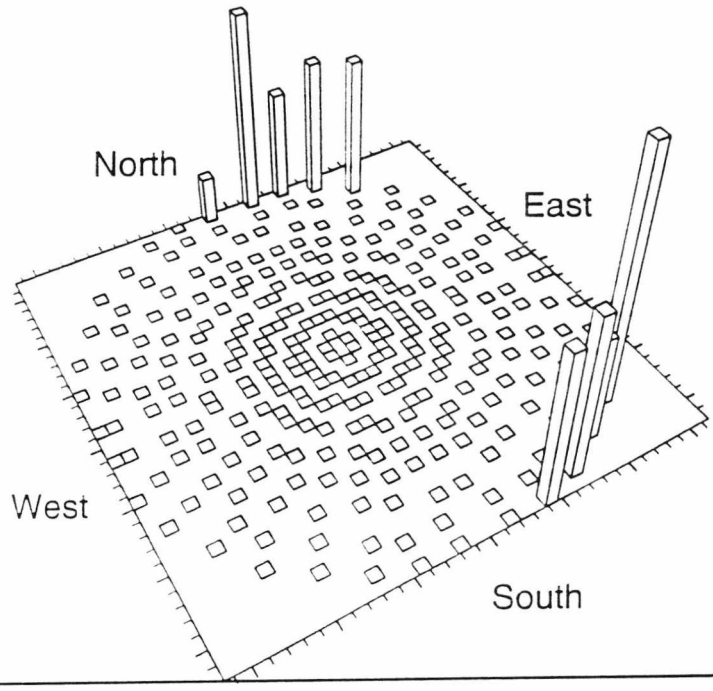

Apogee = 10005 km
Perigee = 6670km
Inclination = 90°
Eccentricity = 0.2

Space

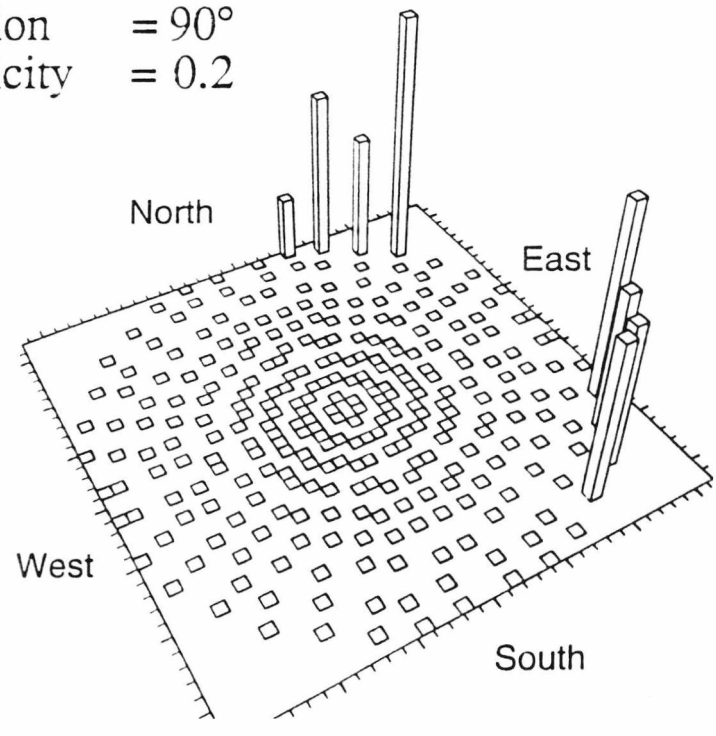

Apogee = 10005 km
Perigee = 6670 km
Inclination = 120°
Eccentricity = 0.2

Space

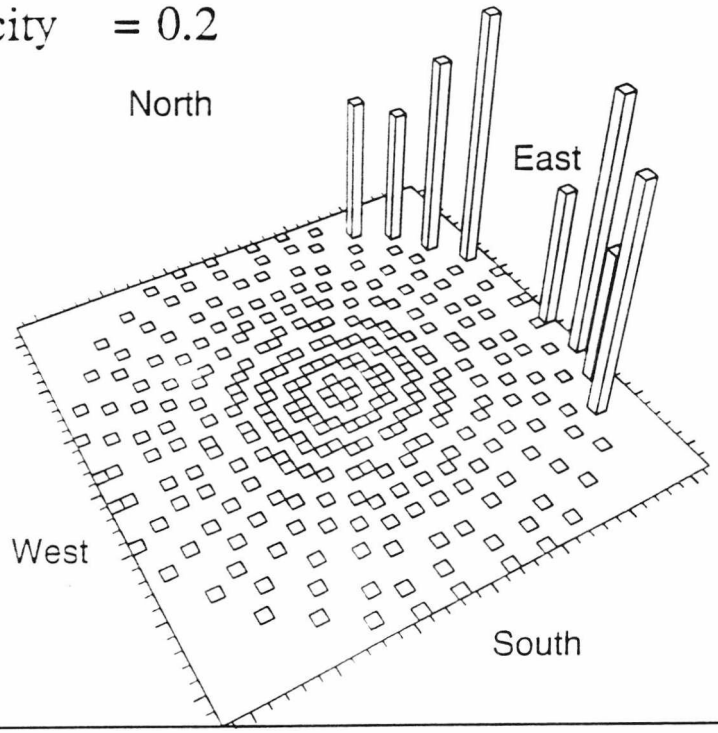

Apogee = 10005 km
Perigee = 6670km
Inclination = 150°
Eccentricity = 0.2

Space

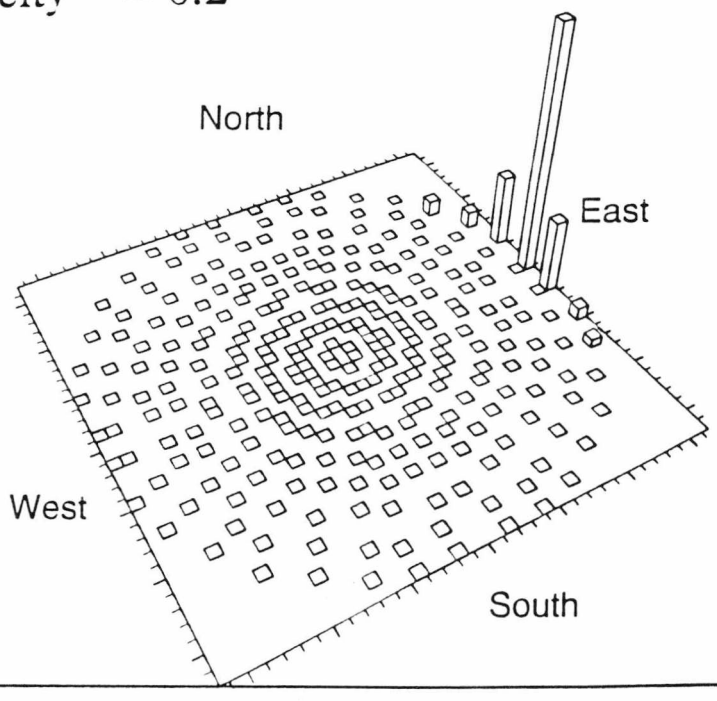

Apogee = 15470 km
Perigee = 6630 km
Inclination = 0°
Eccentricity = 0.4

Space

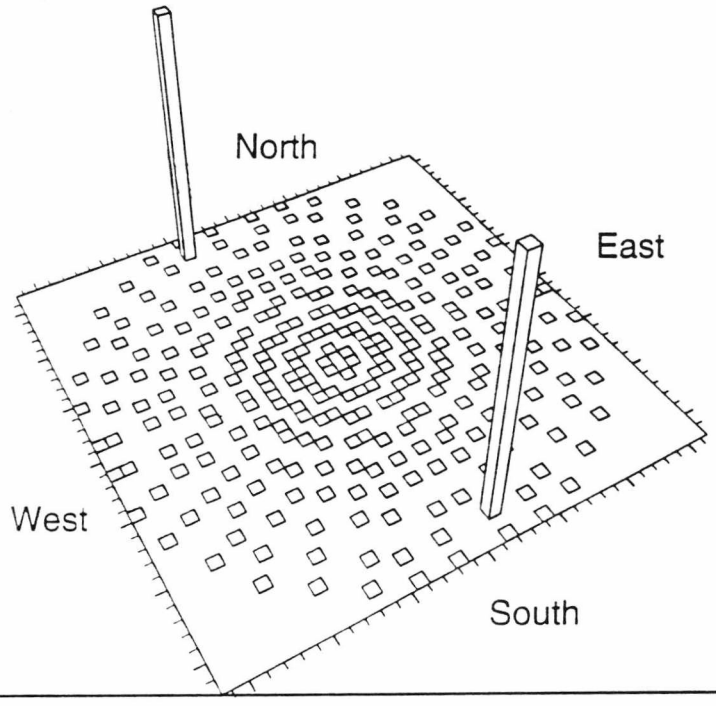

Apogee = 15470 km
Perigee = 6630km
Inclination = 30°
Eccentricity = 0.4

Space

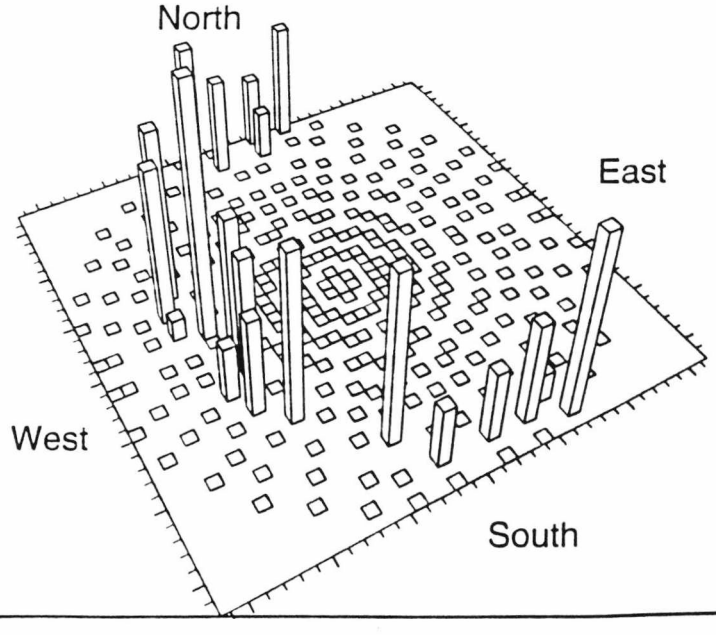

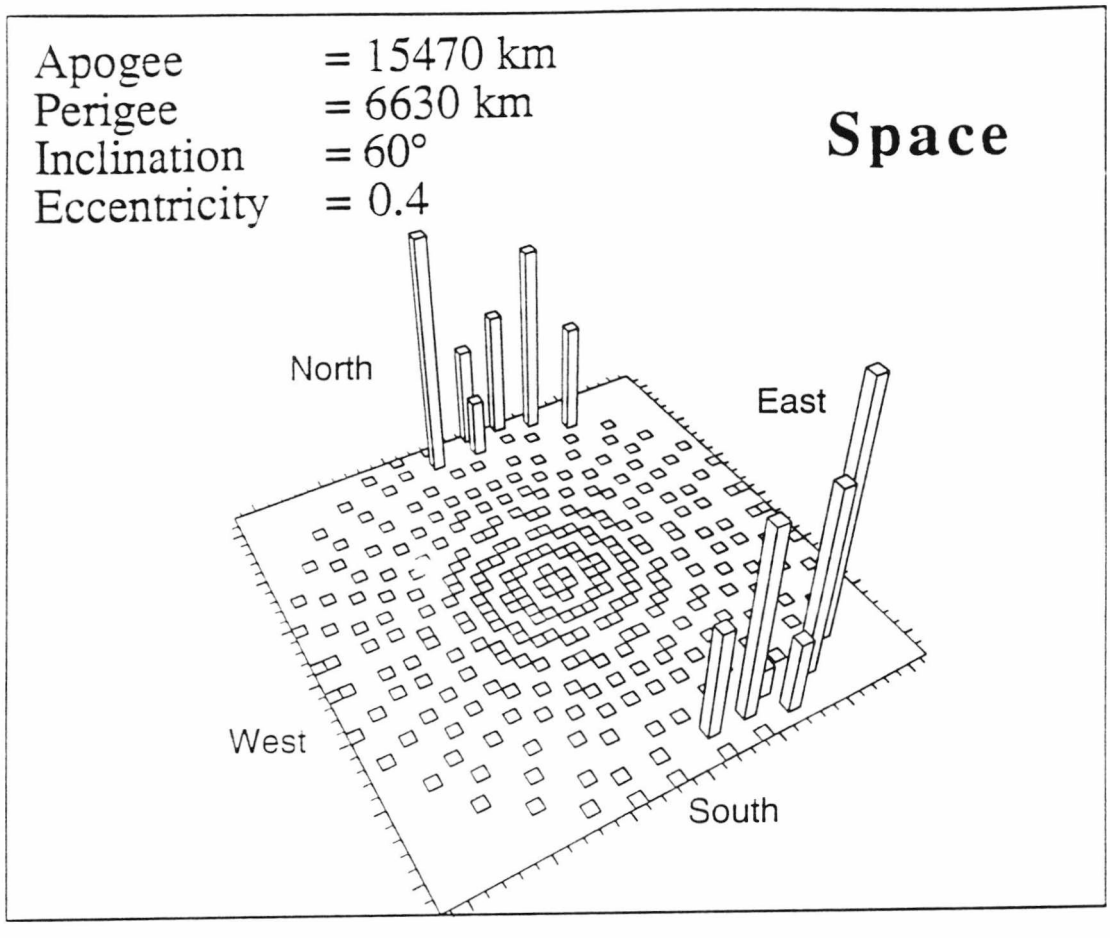
Apogee = 15470 km
Perigee = 6630 km
Inclination = 60°
Eccentricity = 0.4
Space
North
East
West
South

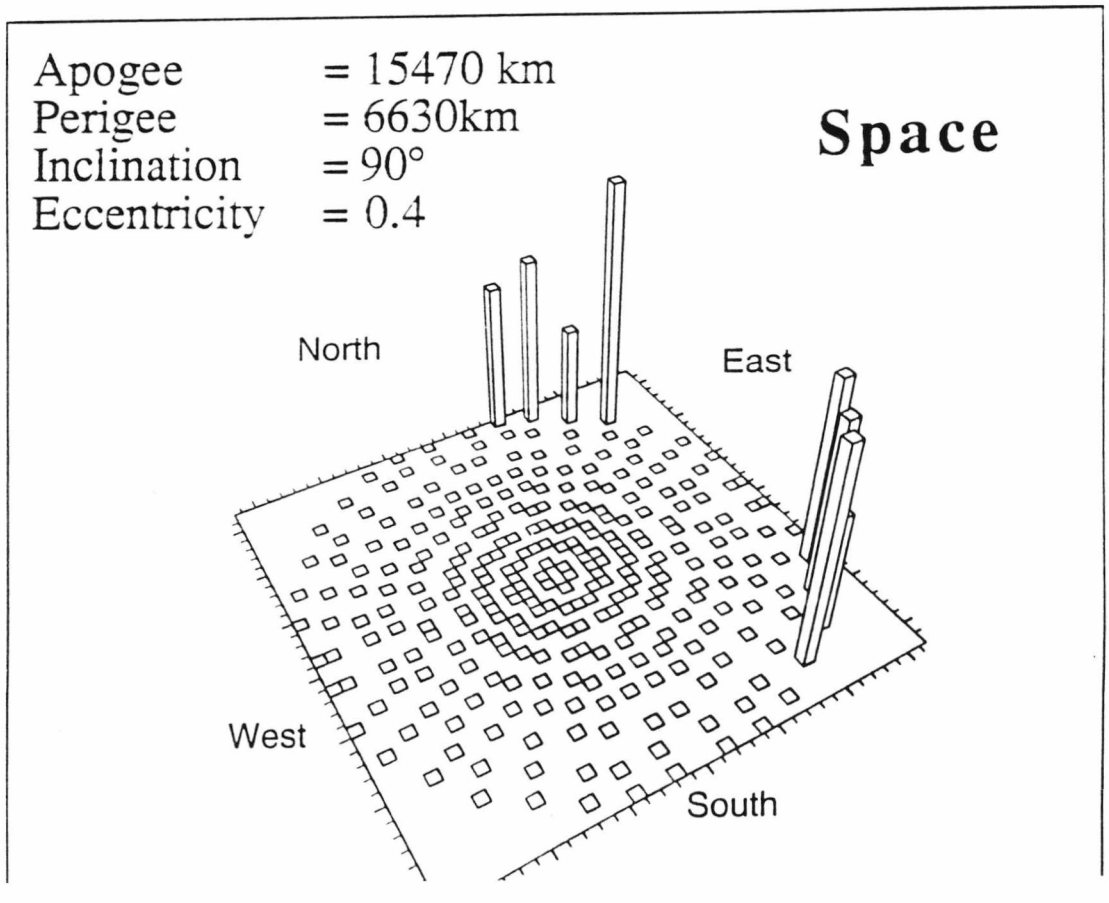
Apogee = 15470 km
Perigee = 6630km
Inclination = 90°
Eccentricity = 0.4
Space
North
East
West
South

Apogee = 15470 km
Perigee = 6630 km
Inclination = 120°
Eccentricity = 0.4

Space

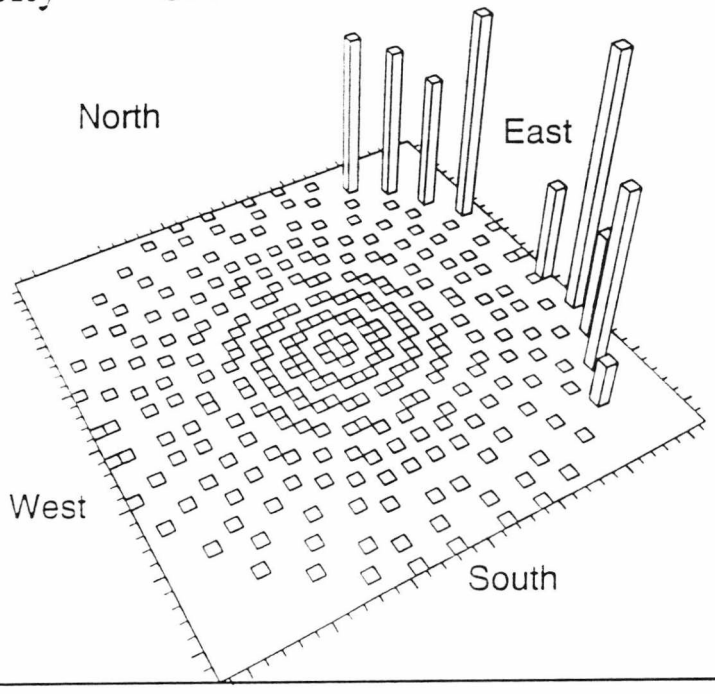

Apogee = 15470 km
Perigee = 6630km
Inclination = 150°
Eccentricity = 0.4

Space

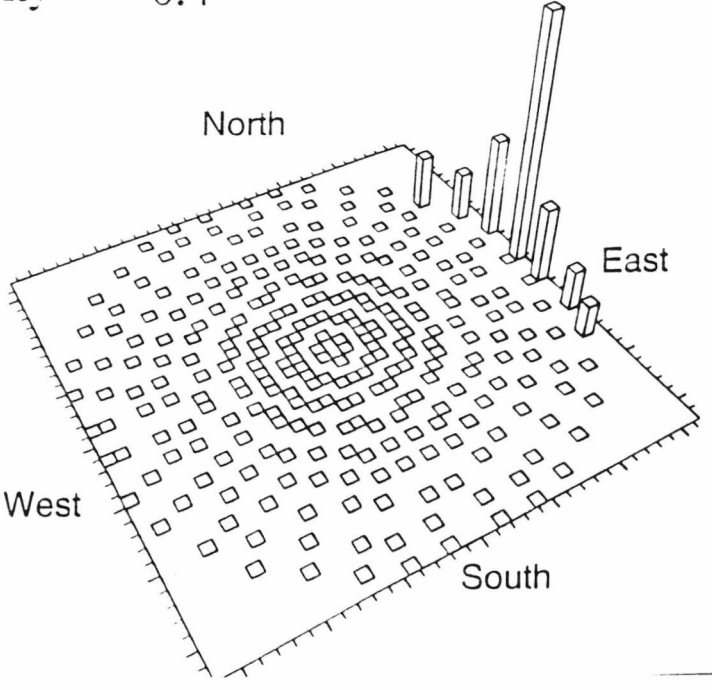

Apogee = 26400 km
Perigee = 6600 km
Inclination = 0°
Eccentricity = 0.6

Space

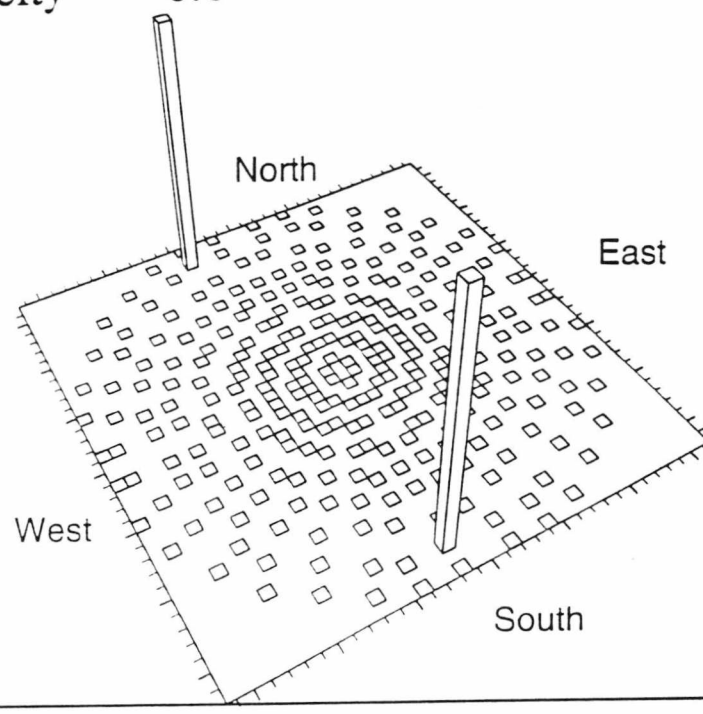

Apogee = 26400 km
Perigee = 6600km
Inclination = 30°
Eccentricity = 0.6

Space

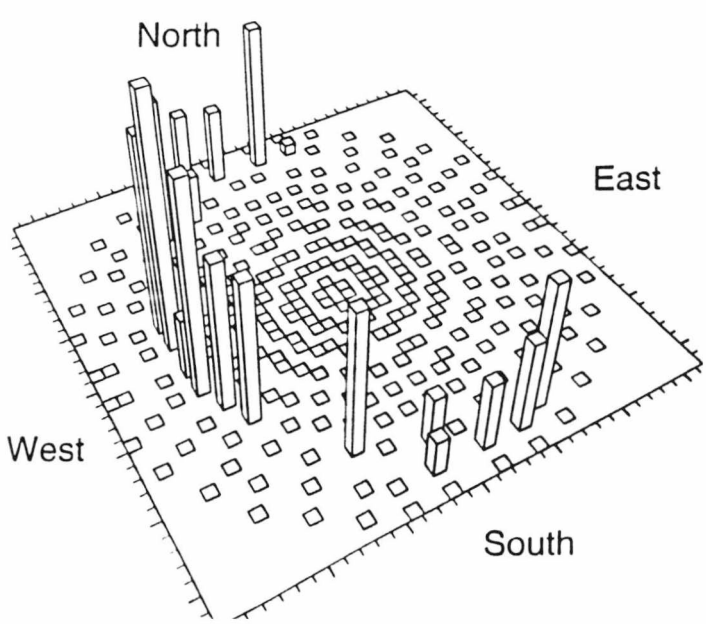

Apogee = 26400 km
Perigee = 6600 km
Inclination = 60°
Eccentricity = 0.6

Space

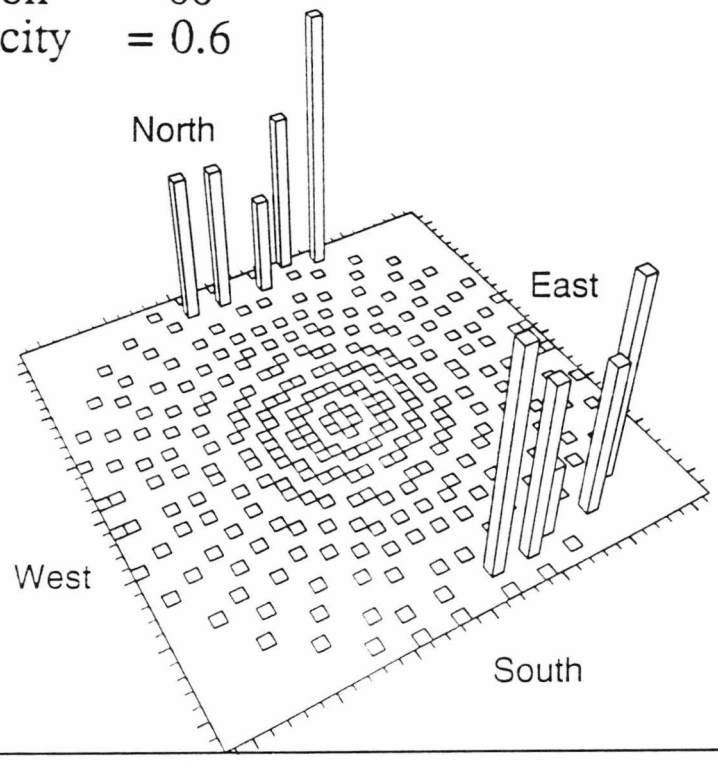

Apogee = 26400 km
Perigee = 6600km
Inclination = 90°
Eccentricity = 0.6

Space

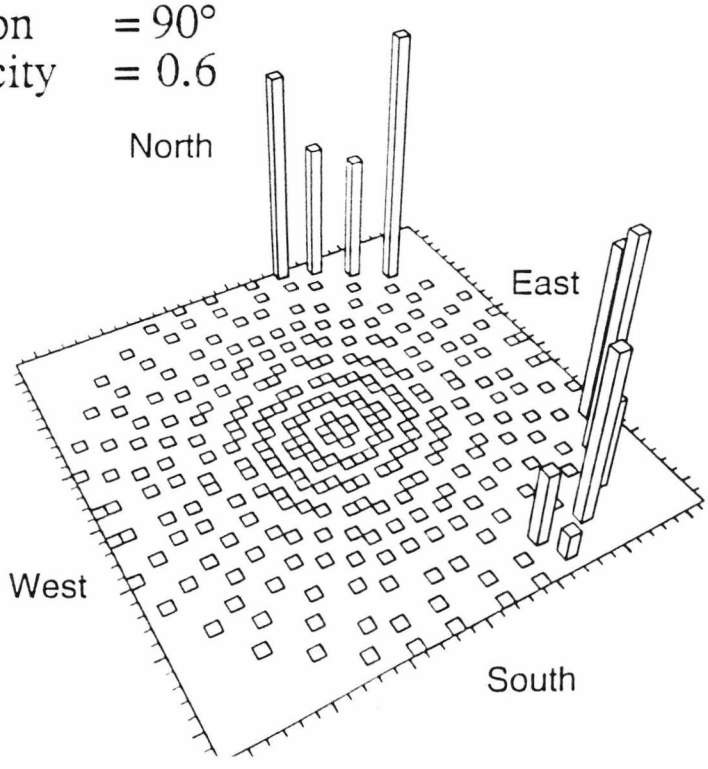

Apogee = 26400 km
Perigee = 6600 km
Inclination = 120°
Eccentricity = 0.6

Space

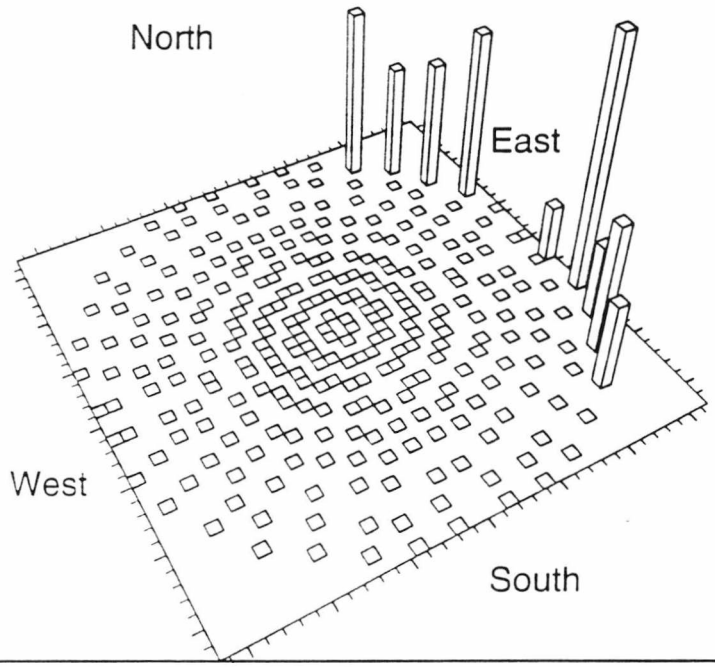

Apogee = 26400 km
Perigee = 6600km
Inclination = 150°
Eccentricity = 0.6

Space

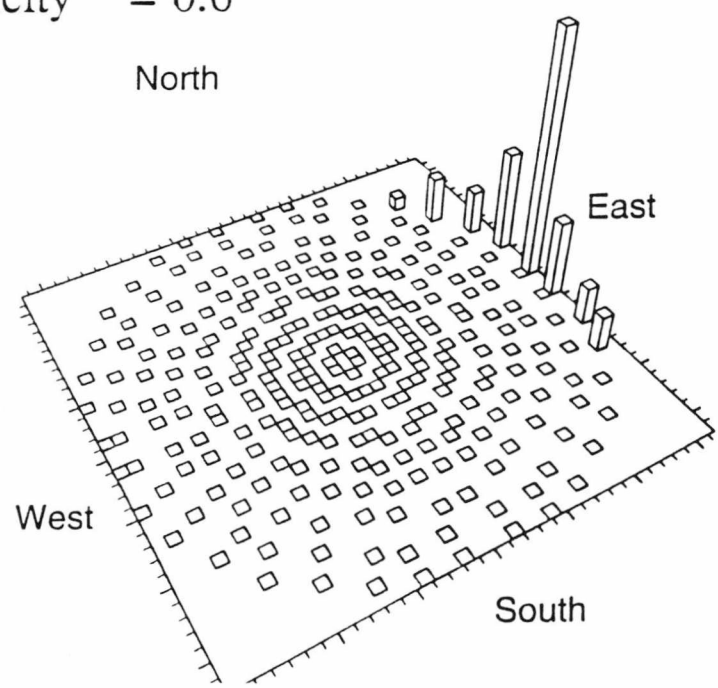

Apogee = 42250 km
Perigee = 6580 km
Inclination = 0°
Eccentricity = 0.73

Space

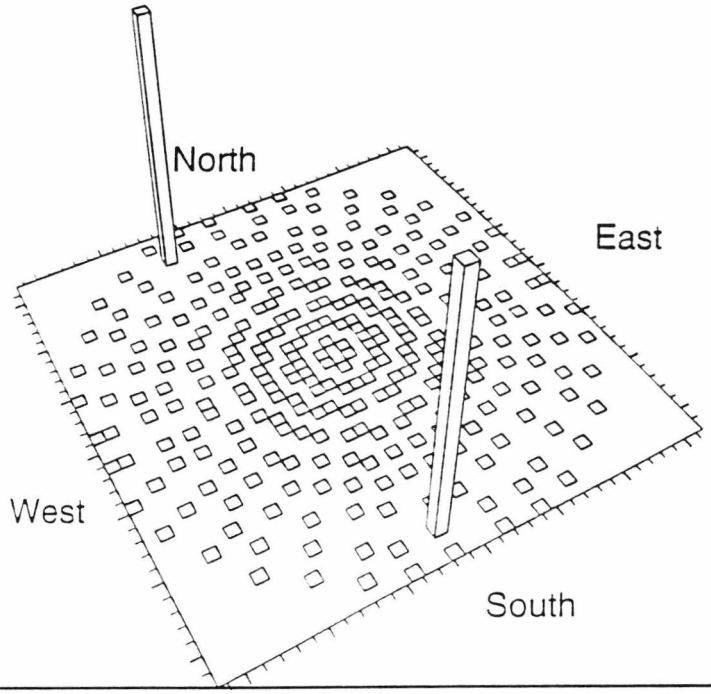

Apogee = 42250 km
Perigee = 6580km
Inclination = 30°
Eccentricity = 0.73

Space

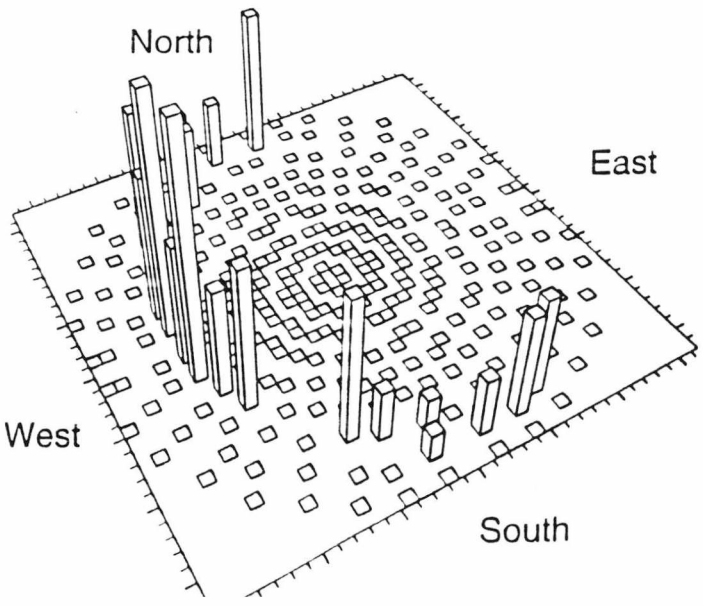

Apogee = 42250 km
Perigee = 6580 km
Inclination = 60°
Eccentricity = 0.73

Space

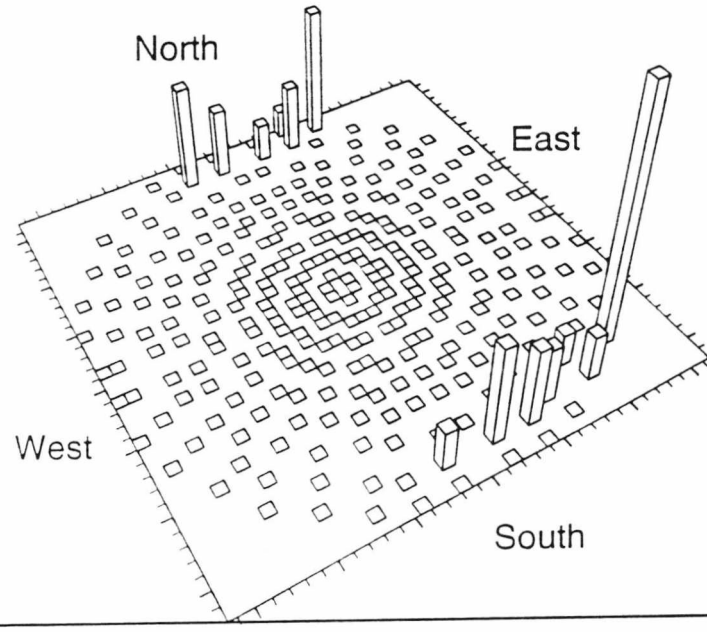

Apogee = 42250 km
Perigee = 6580km
Inclination = 90°
Eccentricity = 0.73

Space

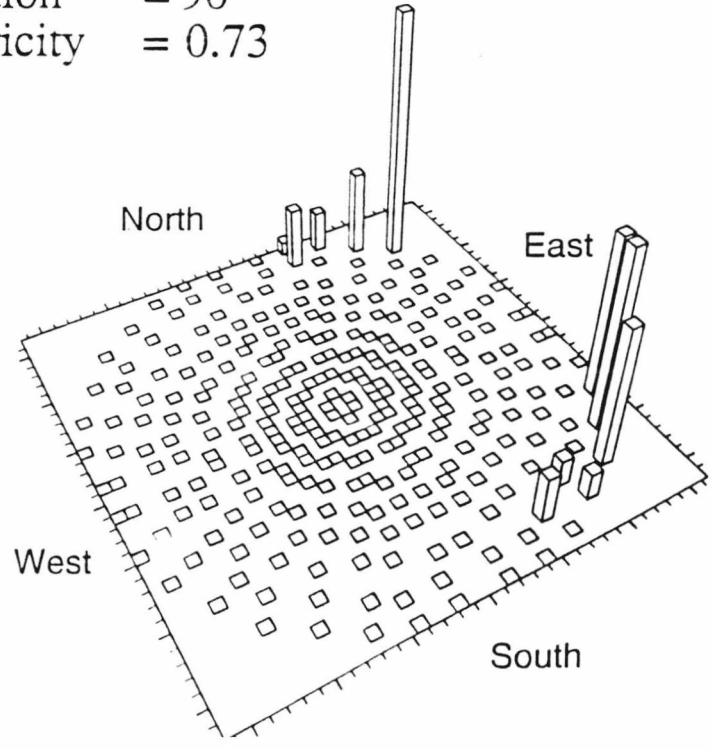

Space

Apogee = 42250 km
Perigee = 6580 km
Inclination = 120°
Eccentricity = 0.73

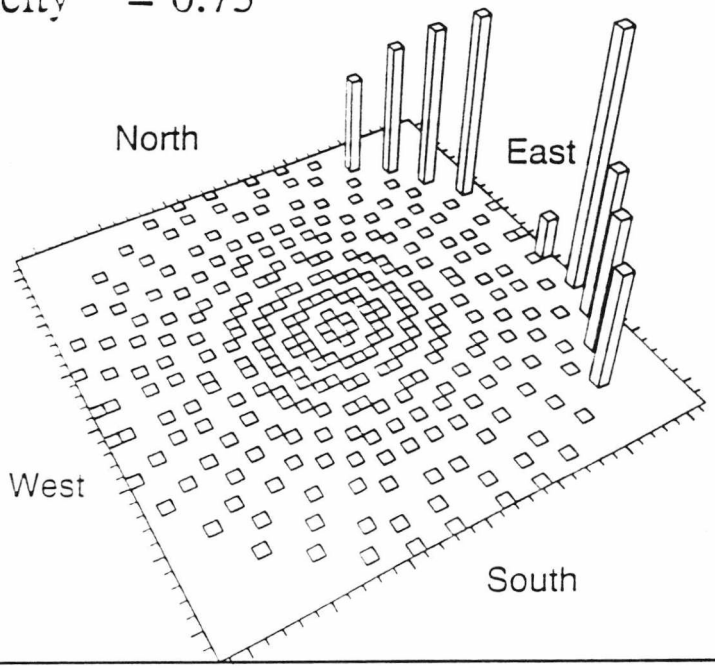

Space

Apogee = 42250 km
Perigee = 6580km
Inclination = 150°
Eccentricity = 0.73

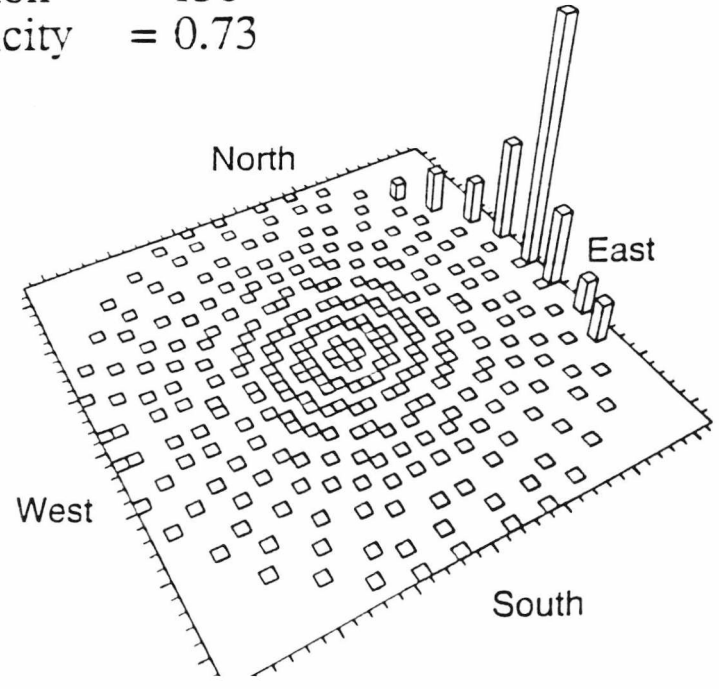

Apogee = 6848 km
Perigee = 6848 km
Inclination = 30°
Eccentricity = 0.0

Earth

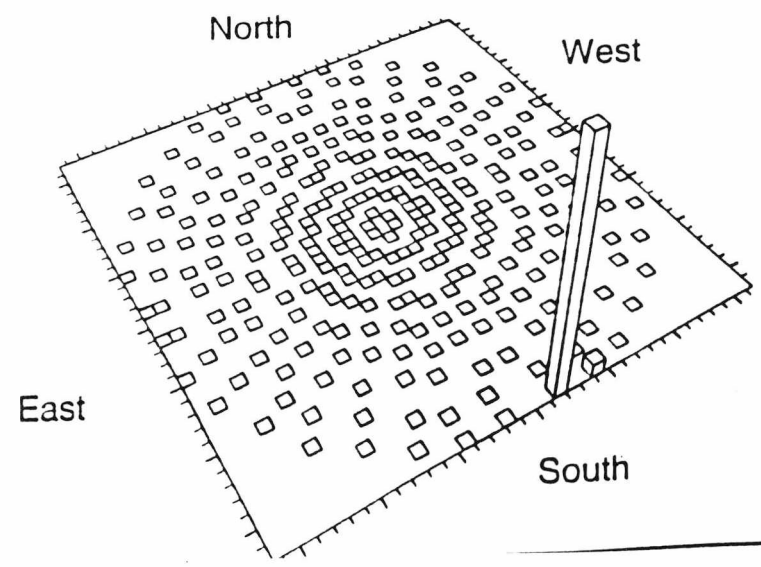

Apogee = 10005 km
Perigee = 6670 km
Inclination = 0°
Eccentricity = 0.2

Earth

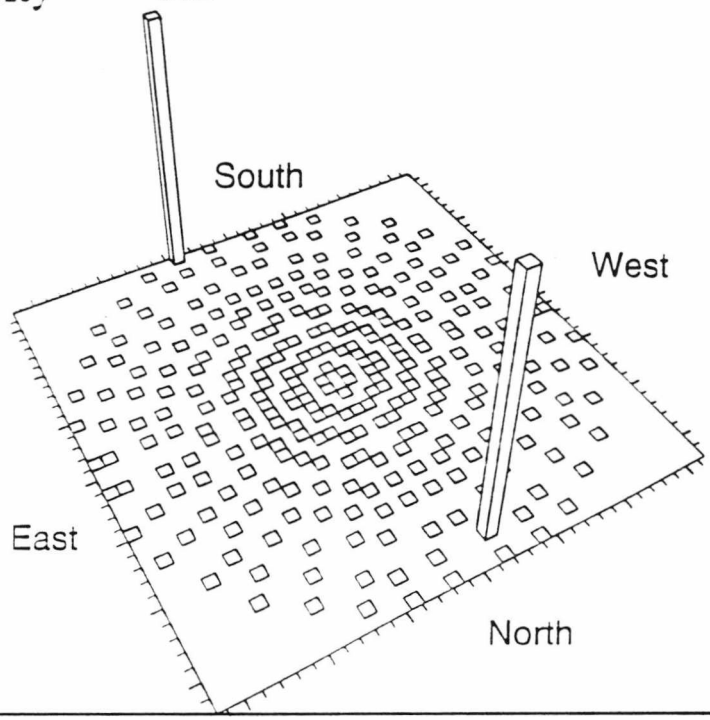

Apogee = 10005 km
Perigee = 6670km
Inclination = 30°
Eccentricity = 0.2

Earth

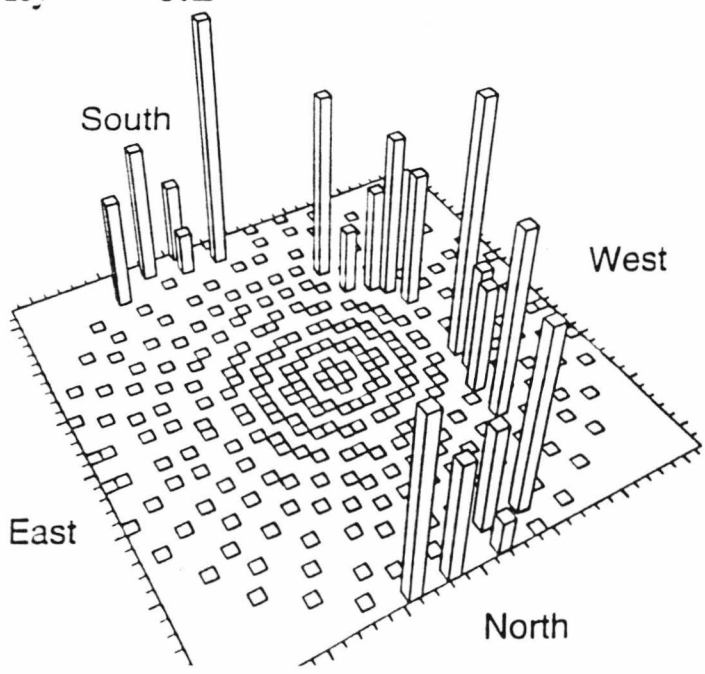

Apogee = 10005 km
Perigee = 6670 km
Inclination = 60°
Eccentricity = 0.2

Earth

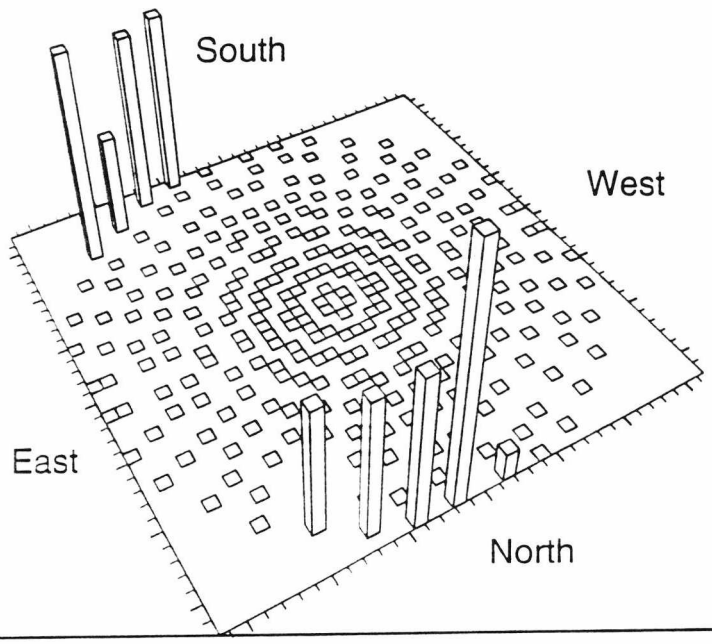

Apogee = 10005 km
Perigee = 6670km
Inclination = 90°
Eccentricity = 0.2

Earth

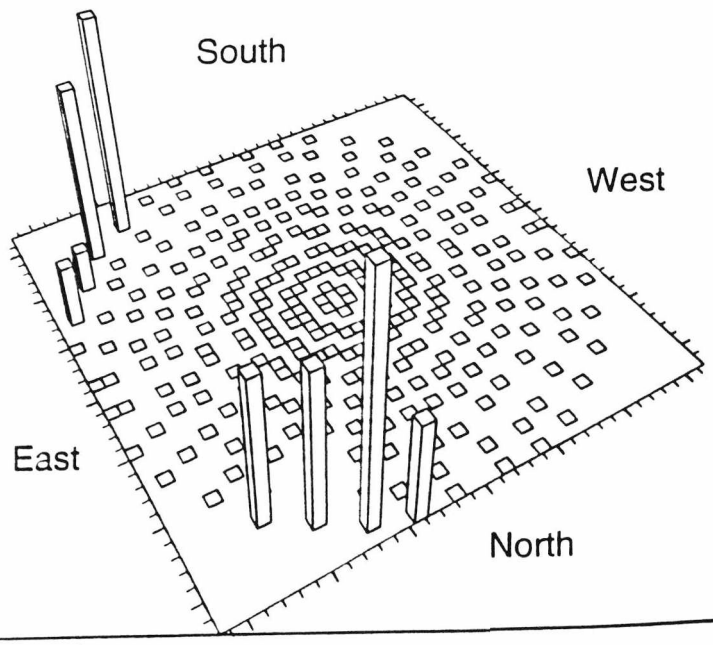

Apogee = 10005 km
Perigee = 6670 km
Inclination = 120°
Eccentricity = 0.2

Earth

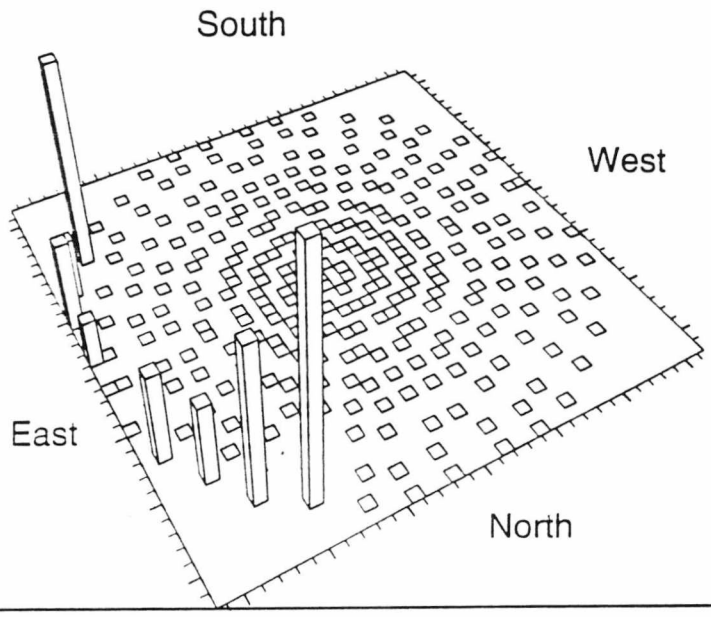

Apogee = 10005 km
Perigee = 6670km
Inclination = 150°
Eccentricity = 0.2

Earth

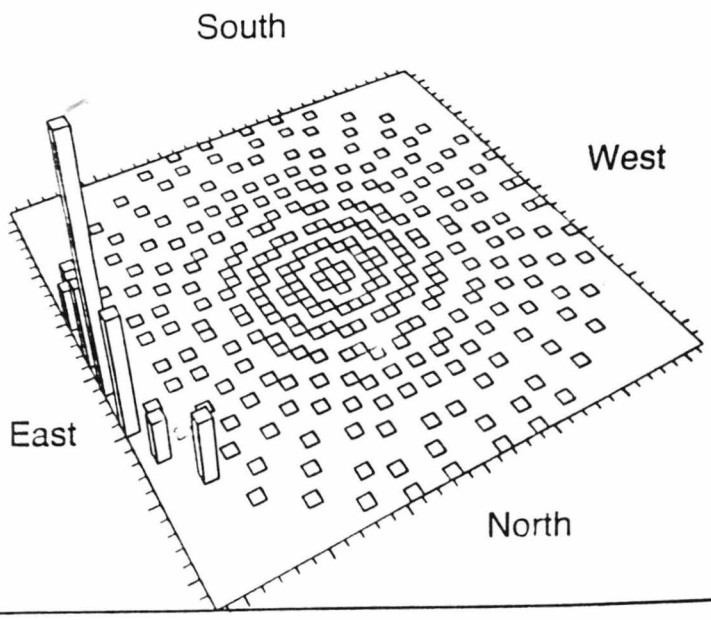

Apogee = 15470 km
Perigee = 6630 km
Inclination = 0°
Eccentricity = 0.4

Earth

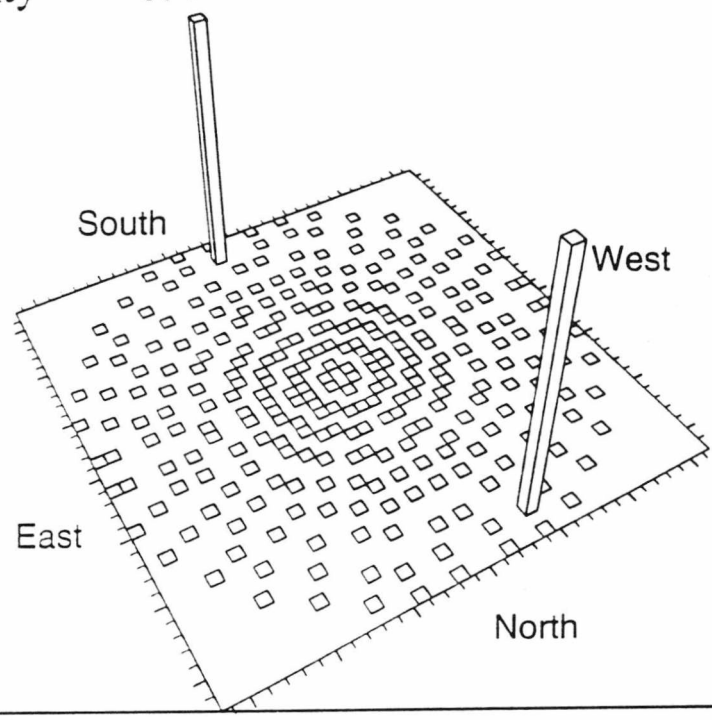

Apogee = 15470 km
Perigee = 6630km
Inclination = 30°
Eccentricity = 0.4

Earth

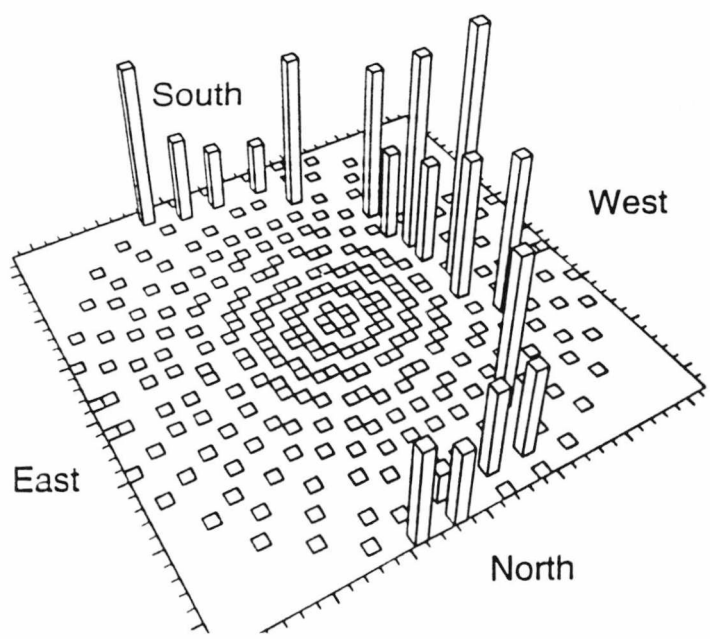

Apogee = 15470 km
Perigee = 6630 km
Inclination = 60°
Eccentricity = 0.4

Earth

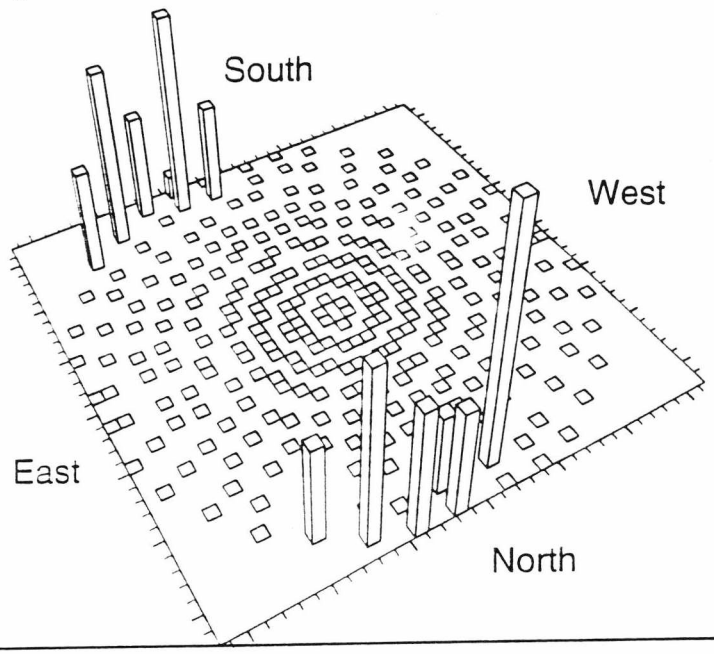

Apogee = 15470 km
Perigee = 6630km
Inclination = 90°
Eccentricity = 0.4

Earth

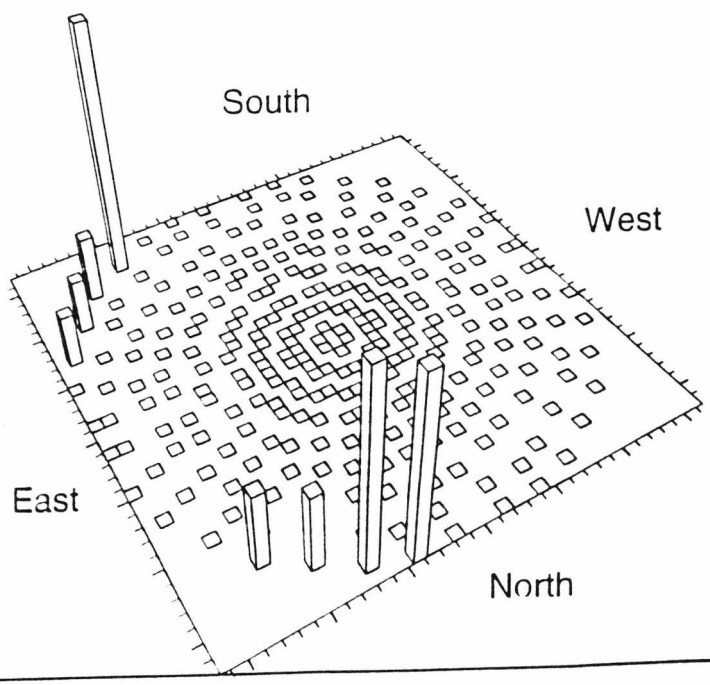

Apogee = 15470 km
Perigee = 6630 km
Inclination = 120°
Eccentricity = 0.4

Earth

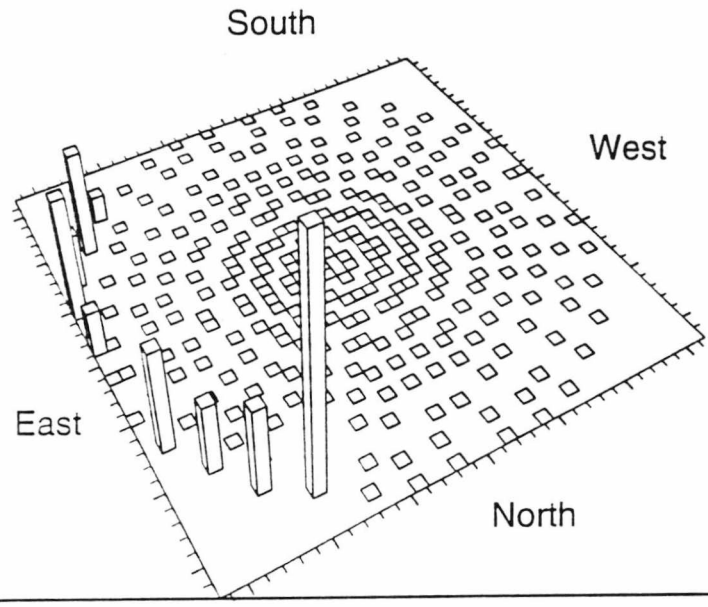

Apogee = 15470 km
Perigee = 6630km
Inclination = 150°
Eccentricity = 0.4

Earth

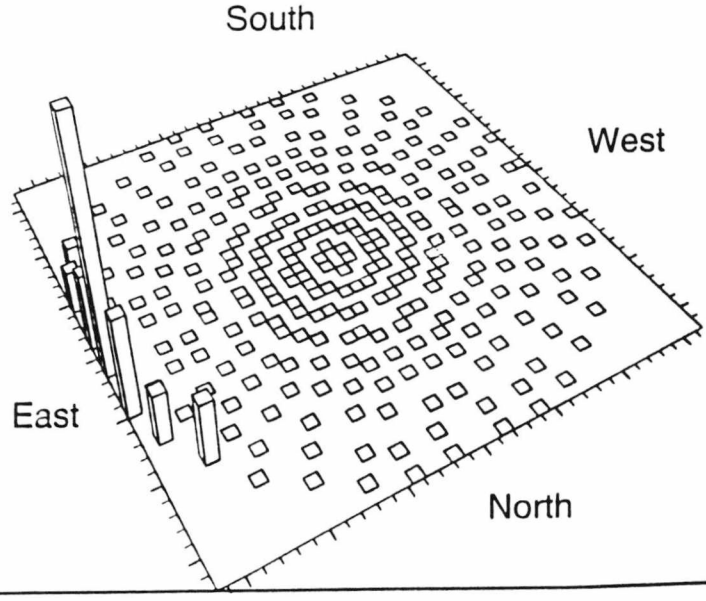

Apogee = 26400 km
Perigee = 6600 km
Inclination = 0°
Eccentricity = 0.6

Earth

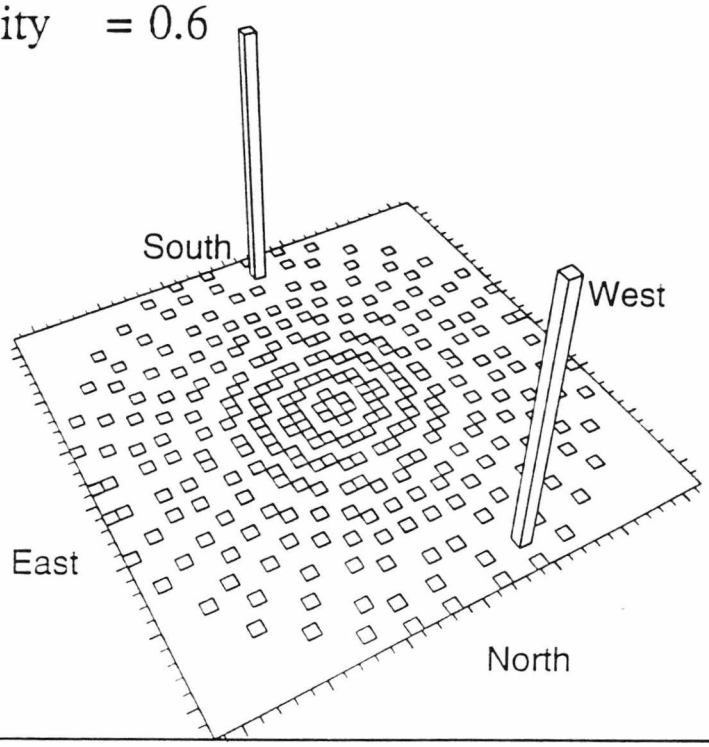

Apogee = 26400 km
Perigee = 6600km
Inclination = 30°
Eccentricity = 0.6

Earth

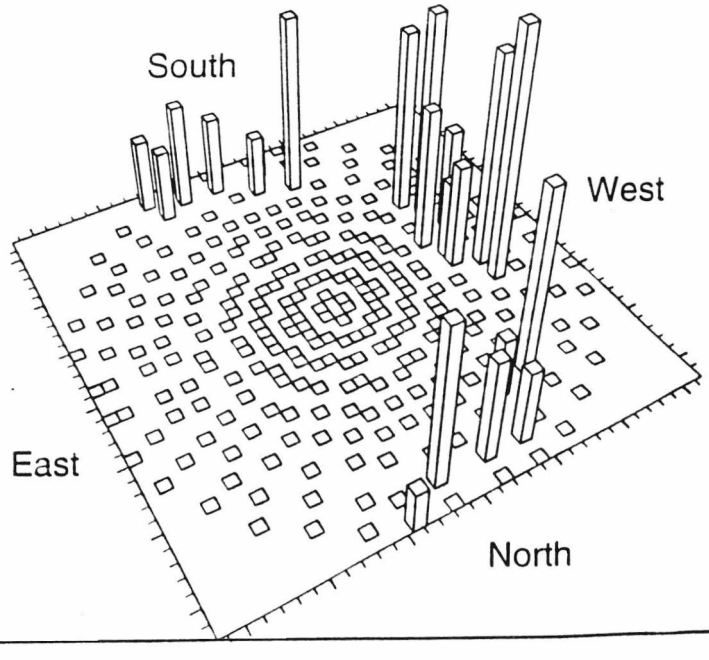

Apogee = 26400 km
Perigee = 6600 km
Inclination = 60°
Eccentricity = 0.6

Earth

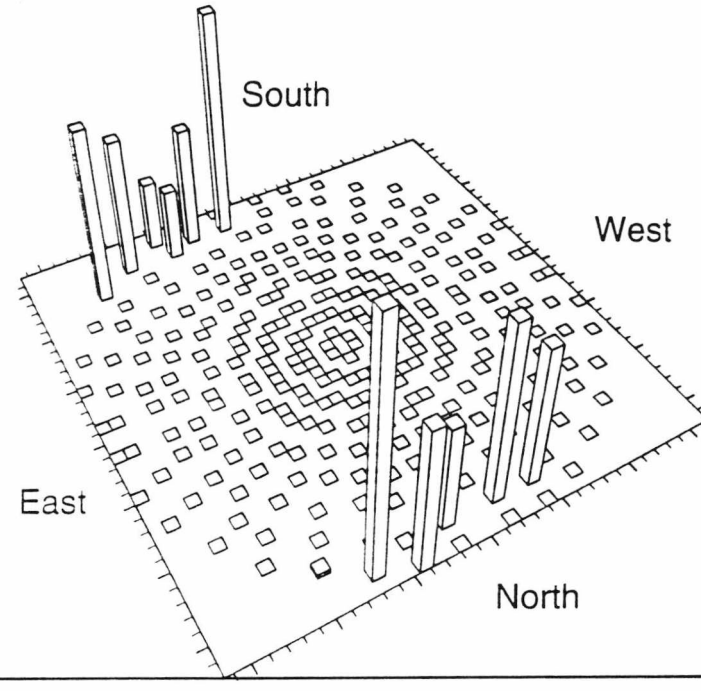

Apogee = 26400 km
Perigee = 6600km
Inclination = 90°
Eccentricity = 0.6

Earth

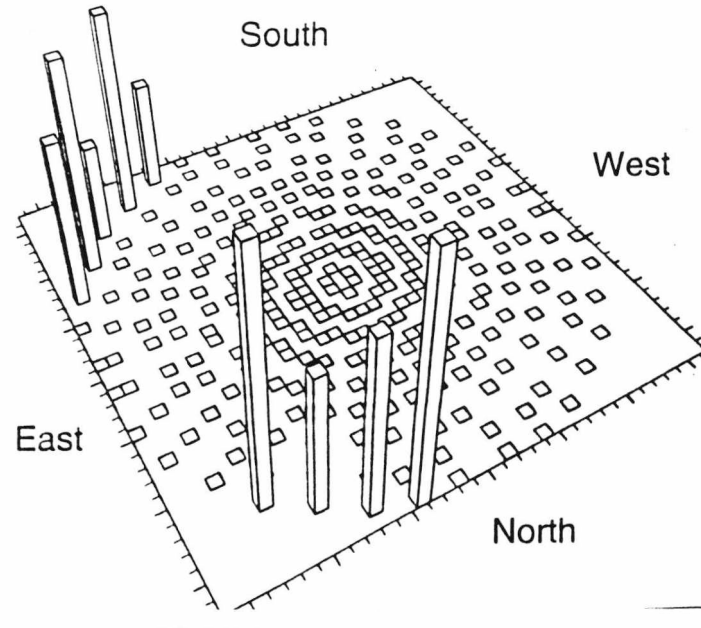

Apogee = 26400 km
Perigee = 6600 km
Inclination = 120°
Eccentricity = 0.6

Earth

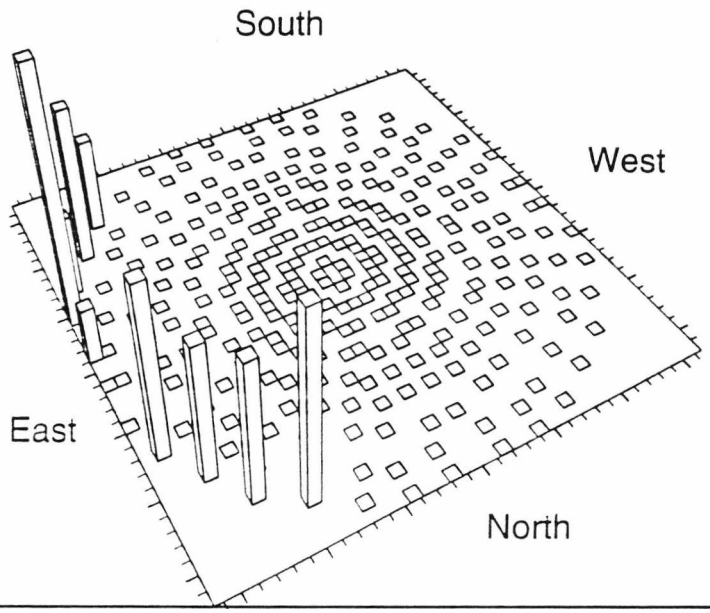

Apogee = 26400 km
Perigee = 6600km
Inclination = 150°
Eccentricity = 0.6

Earth

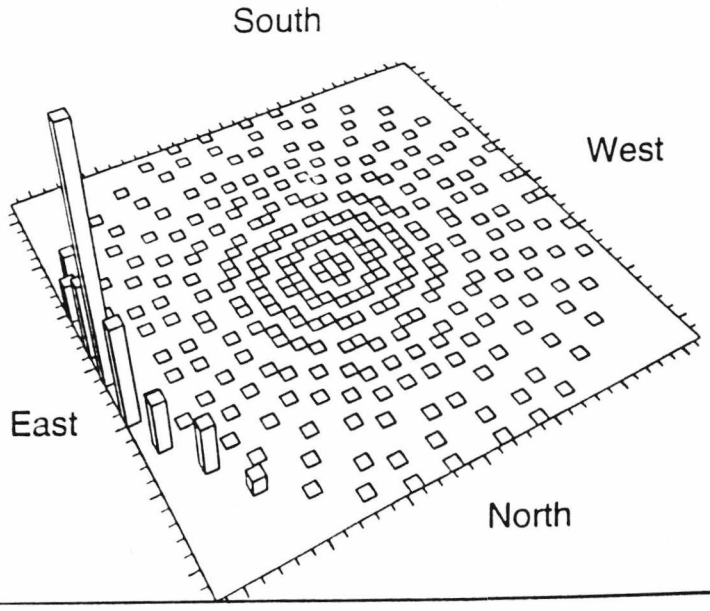

Apogee = 42250 km
Perigee = 6580 km
Inclination = 0°
Eccentricity = 0.73

Earth

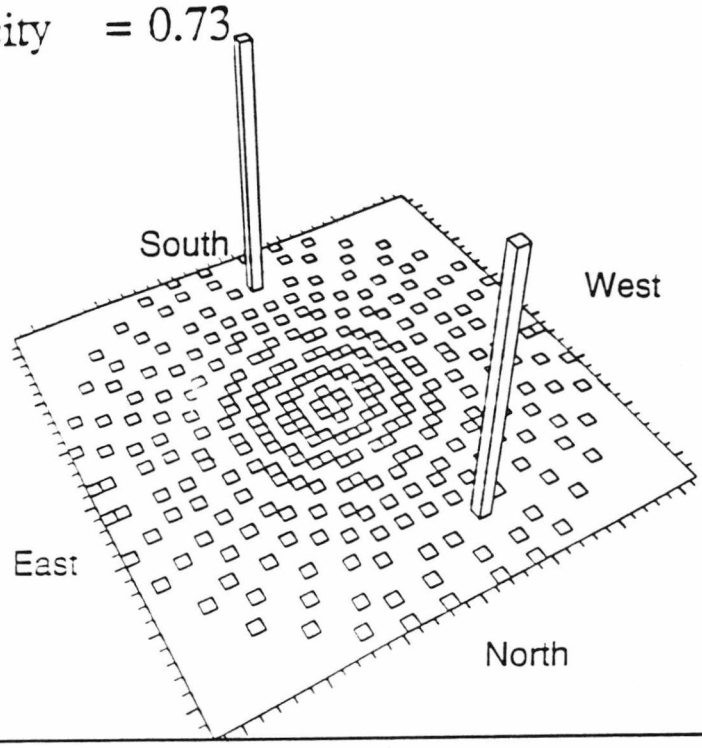

Apogee = 42250 km
Perigee = 6580km
Inclination = 30°
Eccentricity = 0.73

Earth

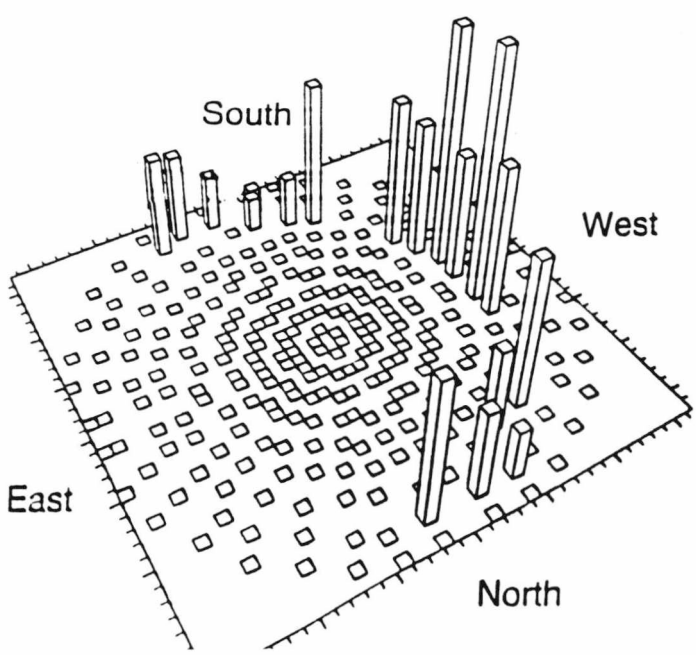

Apogee = 42250 km
Perigee = 6580 km
Inclination = 60°
Eccentricity = 0.73

Earth

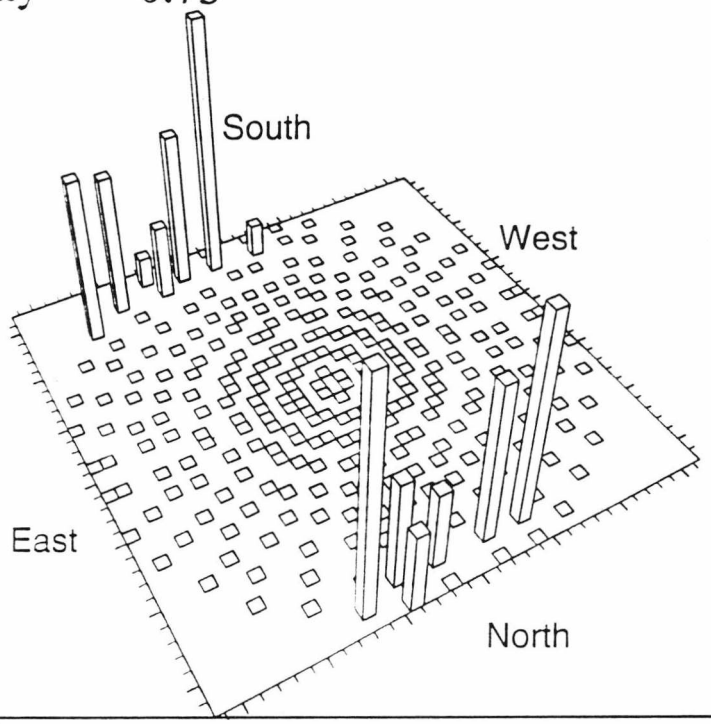

Apogee = 42250 km
Perigee = 6580km
Inclination = 90°
Eccentricity = 0.73

Earth

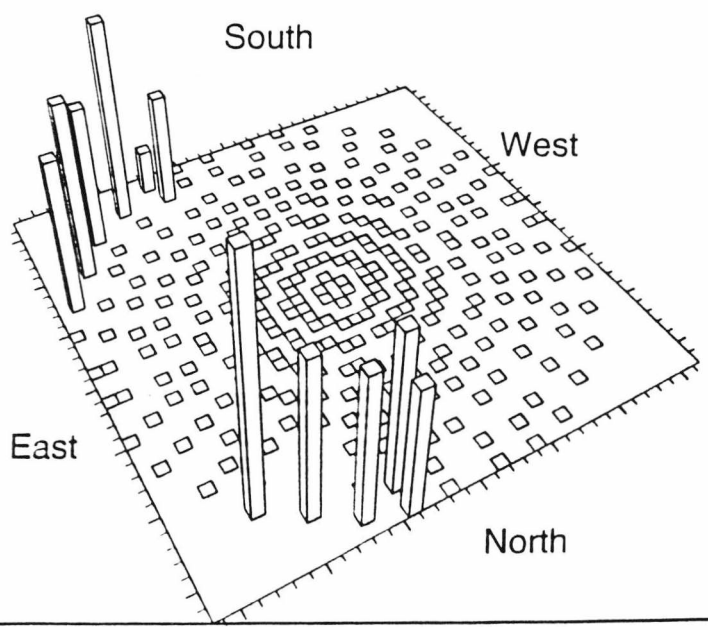

Apogee = 42250 km
Perigee = 6580 km
Inclination = 120°
Eccentricity = 0.73

Earth

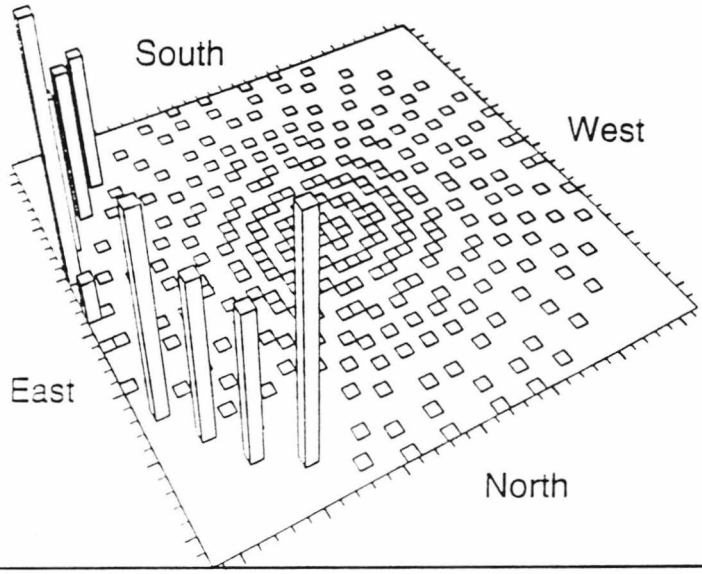

Apogee = 42250 km
Perigee = 6580km
Inclination = 150°
Eccentricity = 0.73

Earth

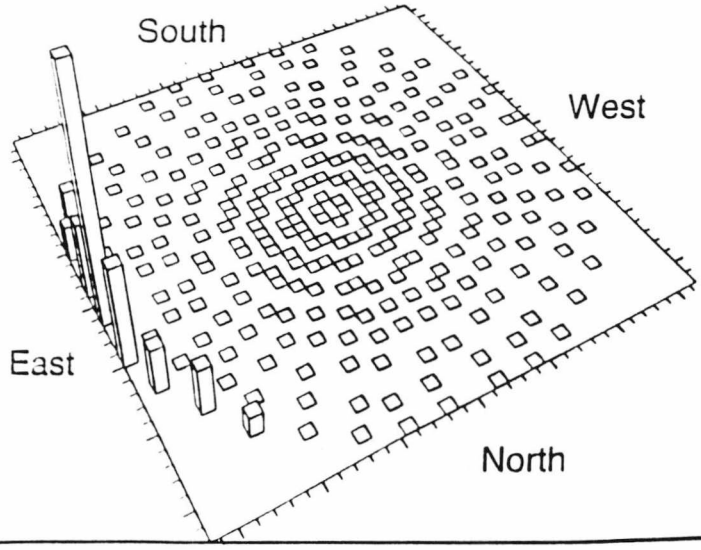

Appendix 4

The experimental Data.

Accelerator Raw Data

long (microns)	short (microns)	short*long	Average Diameter (microns)	angle (degrees)	short/long
3.50E-01	3.00E-01	1.05E-01	3.24E-01	4.55E+01	8.57E-01
4.10E-01	3.00E-01	1.23E-01	3.51E-01	4.94E+01	7.31E-01
5.70E-01	4.10E-01	2.34E-01	4.83E-01	4.66E+01	7.19E-01
5.20E-01	5.30E-01	2.76E-01	5.25E-01	4.86E+01	1.02E+00
5.50E-01	5.50E-01	3.03E-01	5.50E-01	4.78E+01	1.00E+00
7.30E-01	4.40E-01	3.21E-01	5.67E-01	4.58E+01	6.02E-01
7.90E-01	4.40E-01	3.48E-01	5.90E-01	4.99E+01	5.56E-01
9.30E-01	6.80E-01	6.32E-01	7.95E-01	4.48E+01	7.31E-01
1.00E+00	6.70E-01	6.70E-01	8.19E-01	4.88E+01	6.70E-01
1.55E+00	6.40E-01	9.92E-01	9.96E-01	7.60E+01	4.12E-01
1.73E+00	7.00E-01	1.21E+00	1.10E+00	6.54E+01	4.04E-01
1.27E+00	1.04E+00	1.32E+00	1.15E+00	4.53E+01	8.18E-01
1.63E+00	1.36E+00	2.22E+00	1.49E+00	5.32E+01	8.34E-01
2.61E+00	1.01E+00	2.64E+00	1.62E+00	7.60E+01	3.86E-01
2.59E+00	1.14E+00	2.95E+00	1.72E+00	6.52E+01	4.40E-01
2.22E+00	1.45E+00	3.22E+00	1.79E+00	6.10E+01	6.53E-01
2.99E+00	1.23E+00	3.68E+00	1.92E+00	7.58E+01	4.11E-01
3.39E+00	1.13E+00	3.83E+00	1.96E+00	7.59E+01	3.33E-01
2.65E+00	1.80E+00	4.77E+00	2.18E+00	5.39E+01	6.79E-01
2.99E+00	1.86E+00	5.56E+00	2.36E+00	5.87E+01	6.22E-01
3.05E+00	1.85E+00	5.64E+00	2.38E+00	6.11E+01	6.06E-01
2.79E+00	2.11E+00	5.89E+00	2.43E+00	5.09E+01	7.56E-01
3.13E+00	1.99E+00	6.23E+00	2.50E+00	5.92E+01	6.35E-01
4.05E+00	1.54E+00	6.24E+00	2.50E+00	7.61E+01	3.80E-01
3.99E+00	1.58E+00	6.30E+00	2.51E+00	7.58E+01	3.95E-01
4.07E+00	1.66E+00	6.76E+00	2.60E+00	7.58E+01	4.07E-01
3.74E+00	1.84E+00	6.88E+00	2.62E+00	7.60E+01	4.91E-01
3.22E+00	2.14E+00	6.89E+00	2.63E+00	5.62E+01	6.64E-01
4.74E+00	1.64E+00	7.77E+00	2.79E+00	7.43E+01	3.45E-01
4.57E+00	1.72E+00	7.86E+00	2.80E+00	7.59E+01	3.76E-01
4.00E+00	2.18E+00	8.72E+00	2.95E+00	5.71E+01	5.45E-01
3.66E+00	2.42E+00	8.86E+00	2.98E+00	5.83E+01	6.61E-01
5.46E+00	1.76E+00	9.61E+00	3.10E+00	7.60E+01	3.22E-01
4.53E+00	2.27E+00	1.03E+01	3.21E+00	6.20E+01	5.01E-01
6.32E+00	1.67E+00	1.06E+01	3.25E+00	6.97E+01	2.64E-01
4.94E+00	2.28E+00	1.13E+01	3.36E+00	6.66E+01	4.61E-01
5.91E+00	1.95E+00	1.15E+01	3.39E+00	6.51E+01	3.29E-01
4.42E+00	3.05E+00	1.35E+01	3.67E+00	5.91E+01	6.90E-01
5.94E+00	2.40E+00	1.43E+01	3.78E+00	7.93E+01	4.04E-01
5.79E+00	3.84E+00	2.22E+01	4.72E+00	4.68E+01	6.63E-01
5.98E+00	3.93E+00	2.35E+01	4.85E+00	5.81E+01	6.57E-01
6.42E+00	4.11E+00	2.64E+01	5.14E+00	6.33E+01	6.40E-01
1.40E+01	2.85E+00	3.98E+01	6.31E+00	7.62E+01	2.03E-01
7.89E+00	5.24E+00	4.13E+01	6.43E+00	4.68E+01	6.64E-01
1.14E+01	3.78E+00	4.32E+01	6.58E+00	7.60E+01	3.30E-01
1.08E+01	5.29E+00	5.72E+01	7.57E+00	6.12E+01	4.88E-01
1.60E+01	3.59E+00	5.75E+01	7.58E+00	7.59E+01	2.24E-01

Light Gas Gun Oblique Angle Raw Data

Target	Projectile	Velocity (km s^{-1})	Angle (degrees)	Short axis(cm)	abs error(cm)	Long axis (cm)	abs error(cm)	Short/Long
St.St.	AISI52100	5.90E+00	5.50E+01	4.76E-01	5.00E-03	3.88E-01	5.00E-03	8.15E-01
		5.85E+00	6.00E+01	4.28E-01	5.00E-03	3.33E-01	5.00E-03	7.78E-01
		5.42E+00	6.00E+01	3.73E-01	5.00E-03	3.21E-01	5.00E-03	8.61E-01
		5.30E+00	7.00E+01	4.02E-01	5.00E-03	2.87E-01	5.00E-04	7.14E-01
		5.50E+00	7.50E+01	3.53E-01	5.00E-03	2.42E-01	5.00E-03	6.86E-01
		5.50E+00	8.00E+01	2.94E-01	5.00E-03	1.85E-01	5.00E-03	6.29E-01
		5.69E+00	8.50E+01	6.10E-01	5.00E-03	5.10E-02	5.00E-03	8.36E-02
					5.00E-03		5.00E-03	
					5.00E-03		5.00E-03	
	AISI420C	5.90E+00	5.50E+01	1.51E-01	5.00E-03	1.49E-01	5.00E-03	9.87E-01
			5.50E+01	1.62E-01	5.00E-03	1.33E-01	5.00E-03	8.21E-01
			5.50E+01	1.49E-01	5.00E-03	1.39E-01	5.00E-03	9.33E-01
			5.50E+01	1.54E-01	5.00E-03	1.25E-01	5.00E-03	8.12E-01
			5.50E+01	1.48E-01	5.00E-03	1.20E-01	5.00E-03	8.11E-01
			5.50E+01	1.51E-01	5.00E-03	1.20E-01	5.00E-04	7.95E-01
			5.50E+01	1.39E-01	5.00E-03	1.29E-01	5.00E-03	9.28E-01
			5.50E+01	1.52E-01	5.00E-03	1.30E-01	5.00E-03	8.55E-01
		5.90E+00	5.50E+01	1.45E-01	5.00E-03	1.28E-01	5.00E-03	8.83E-01
			5.50E+01	1.43E-01	5.00E-03	1.15E-01	5.00E-03	8.04E-01
			5.50E+01	1.55E-01	5.00E-03	1.27E-01	5.00E-03	8.19E-01
			5.50E+01	1.41E-01	5.00E-03	1.37E-01	5.00E-03	9.72E-01
			5.50E+01	1.51E-01	5.00E-03	1.38E-01	5.00E-03	9.14E-01
			5.50E+01	1.43E-01	5.00E-03	1.35E-01	5.00E-03	9.44E-01
			5.50E+01	1.50E-01	5.00E-03	1.33E-01	5.00E-03	8.87E-01
			5.50E+01	1.43E-01	5.00E-03	1.35E-01	5.00E-03	9.44E-01
			5.50E+01	1.44E-01	5.00E-03	1.30E-01	5.00E-04	9.03E-01
			5.50E+01	1.45E-01	5.00E-03	1.29E-01	5.00E-03	8.90E-01
		5.83E+00	6.00E+01	1.35E-01	5.00E-03	1.01E-01	5.00E-03	7.48E-01

Target	Projectile	Velocity (km s^{-1})	Angle (degrees)	Short axis(cm)	abs error(cm)	Long axis (cm)	abs error(cm)	Short/Long
St. St.	AISI420C	5.83E+00	6.00E+01	1.33E-01	5.00E-03	1.14E-01	5.00E-03	8.57E-01
			6.00E+01	1.30E-01	5.00E-03	1.01E-01	5.00E-03	7.77E-01
			6.00E+01	1.35E-01	5.00E-03	1.17E-01	5.00E-03	8.67E-01
			6.00E+01	1.49E-01	5.00E-03	1.15E-01	5.00E-03	7.72E-01
		5.42E+00	6.00E+01	1.19E-01	5.00E-03	1.06E-01	5.00E-03	8.91E-01
		5.30E+00	7.00E+01	1.45E-01	5.00E-03	1.02E-01	5.00E-03	7.03E-01
			7.00E+01	1.19E-01	5.00E-03	8.40E-02	5.00E-03	7.06E-01
			7.00E+01	1.30E-01	5.00E-03	9.70E-02	5.00E-03	7.46E-01
			7.00E+01	1.40E-01	5.00E-03	9.20E-02	5.00E-04	6.57E-01
			7.00E+01	9.90E-02	5.00E-03	8.00E-02	5.00E-03	8.08E-01
		5.30E+00	7.50E+01	1.30E-01	5.00E-03	9.10E-02	5.00E-03	7.00E-01
			7.50E+01	1.41E-01	5.00E-03	7.80E-02	5.00E-03	5.53E-01
		5.50E+00	7.50E+01	1.37E-01	5.00E-03	7.80E-02	5.00E-03	5.69E-01
			7.50E+01	1.27E-01	5.00E-03	7.70E-02	5.00E-03	6.06E-01
			7.50E+01	9.60E-02	5.00E-03	7.40E-02	5.00E-03	7.71E-01
			7.50E+01	1.30E-01	5.00E-03	8.30E-02	5.00E-03	6.38E-01
			7.50E+01	1.32E-01	5.00E-03	7.40E-02	5.00E-03	5.61E-01
			7.50E+01	1.08E-01	5.00E-03	8.50E-02	5.00E-03	7.87E-01
			7.50E+01	1.34E-01	5.00E-03	7.70E-02	5.00E-03	5.75E-01
			7.50E+01	1.18E-01	5.00E-03	8.20E-02	5.00E-04	6.95E-01
			7.50E+01	1.07E-01	5.00E-03	8.00E-02	5.00E-03	7.48E-01
		5.50E+00	8.00E+01	6.22E-01	5.00E-03	6.60E-02	5.00E-03	1.06E-01
			8.00E+01	2.62E-01	5.00E-03	5.60E-02	5.00E-03	2.14E-01
		5.69E+00	8.50E+01	2.86E-01	5.00E-03	6.30E-02	5.00E-03	2.20E-01
					5.00E-03		5.00E-03	
Lead	AISI52100	4.40E+00	6.00E+01	6.89E-01	5.00E-03	6.35E-01	5.00E-03	9.22E-01
		5.69E+00	8.50E+01	3.53E-01	5.00E-03	2.04E-01	5.00E-03	5.78E-01
					5.00E-03		5.00E-03	
	AISI420C	4.40E+00	6.00E+01	2.17E-01	5.00E-03	2.07E-01	5.00E-03	9.54E-01
			6.00E+01	2.13E-01	5.00E-03	2.04E-01	5.00E-03	9.58E-01
			6.00E+01	2.19E-01	5.00E-03	1.98E-01	5.00E-04	9.04E-01

Target	Projectile	Velocity (km s^{-1})	Angle (degrees)	Short axis(cm)	abs error(cm)	Long axis (cm)	abs error(cm)	Short/Long
Lead	AISI420C	4.40E+00	6.00E+01	2.26E-01	5.00E-03	2.14E-01	5.00E-03	9.47E-01
			6.00E+01	2.18E-01	5.00E-03	2.02E-01	5.00E-03	9.27E-01
			6.00E+01	2.07E-01	5.00E-03	1.91E-01	5.00E-03	9.23E-01
			6.00E+01	2.10E-01	5.00E-03	2.07E-01	5.00E-03	9.86E-01
			6.00E+01	2.13E-01	5.00E-03	2.05E-01	5.00E-03	9.62E-01
			6.00E+01	2.12E-01	5.00E-03	1.93E-01	5.00E-03	9.10E-01
			6.00E+01	2.19E-01	5.00E-03	2.18E-01	5.00E-03	9.95E-01
		4.70E+00	7.00E+01	1.69E-01	5.00E-03	1.65E-01	5.00E-03	9.76E-01
			7.00E+01	1.38E-01	5.00E-03	1.38E-01	5.00E-03	1.00E+00
			7.00E+01	1.59E-01	5.00E-03	1.39E-01	5.00E-03	8.74E-01
			7.00E+01	1.51E-01	5.00E-03	1.40E-01	5.00E-04	9.27E-01
			7.00E+01	1.35E-01	5.00E-03	1.26E-01	5.00E-03	9.33E-01
		5.27E+00	8.00E+01	3.57E-01	5.00E-03	1.10E-01	5.00E-03	3.08E-01
			8.00E+01	2.60E-01	5.00E-03	9.60E-02	5.00E-03	3.69E-01
		4.50E+00	8.50E+01	2.14E-01	5.00E-03	6.80E-02	5.00E-03	3.18E-01
			8.50E+01	2.22E-01	5.00E-03	6.60E-02	5.00E-03	2.97E-01
			8.50E+01	2.15E-01	5.00E-03	6.90E-02	5.00E-03	3.21E-01
			8.50E+01	2.38E-01	5.00E-03	6.80E-02	5.00E-03	2.86E-01
			8.50E+01	1.49E-01	5.00E-03	6.10E-02	5.00E-03	4.09E-01
			8.50E+01	2.59E-01	5.00E-03	7.50E-02	5.00E-03	2.90E-01
			8.50E+01	1.52E-01	5.00E-03	5.90E-02	5.00E-03	3.88E-01
			8.50E+01	4.18E-01	5.00E-03	9.80E-02	5.00E-04	2.34E-01
					5.00E-03		5.00E-03	
					5.00E-03		5.00E-03	
HE30 Al	AISI52100		5.50E+01	6.00E+00	5.00E-03	5.40E+00	5.00E-03	9.00E-01
			5.50E+01	6.00E+00	5.00E-03	5.10E+00	5.00E-03	8.50E-01
			6.50E+01	6.40E+00	5.00E-03	4.00E+00	5.00E-03	6.25E-01
			7.00E+01	5.90E+00	5.00E-03	4.60E+00	5.00E-03	7.80E-01
			7.50E+01	5.20E+00	5.00E-03	3.10E+00	5.00E-03	5.96E-01
		5.90E+00	8.00E+01	1.42E+00	5.00E-03	2.42E-01	5.00E-03	1.71E-01
			8.00E+01	4.49E-01	5.00E-03	2.76E-01	5.00E-03	6.15E-01

Target	Projectile	Velocity (km s^{-1})	Angle (degrees)	Short axis(cm)	abs error(cm)	Long axis (cm)	abs error(cm)	Short/Long
HE30 Al	AISI52100	5.90E+00	8.50E+01	9.00E-01	5.00E-03	1.09E-01	5.00E-03	1.21E-01
					5.00E-03		5.00E-04	
					5.00E-03		5.00E-03	
					5.00E-03		5.00E-03	
	AISI420C		5.50E+01	2.40E+00	5.00E-03	2.00E+00	5.00E-03	8.33E-01
			5.50E+01	2.60E+00	5.00E-03	2.00E+00	5.00E-03	7.69E-01
			5.50E+01	2.20E+00	5.00E-03	2.00E+00	5.00E-03	9.09E-01
			5.50E+01	2.20E+00	5.00E-03	2.00E+00	5.00E-03	9.09E-01
			5.50E+01	2.50E+00	5.00E-03	2.00E+00	5.00E-03	8.00E-01
			5.50E+01	2.30E+00	5.00E-03	2.00E+00	5.00E-03	8.70E-01
			6.50E+01	2.30E+00	5.00E-03	1.50E+00	5.00E-03	6.52E-01
			6.50E+01	2.50E+00	5.00E-03	1.60E+00	5.00E-03	6.40E-01
			6.50E+01	2.10E+00	5.00E-03	1.50E+00	5.00E-04	7.14E-01
			7.00E+01	2.10E+00	5.00E-03	1.30E+00	5.00E-03	6.19E-01
			7.00E+01	2.10E+00	5.00E-03	1.30E+00	5.00E-03	6.19E-01
			7.00E+01	2.10E+00	5.00E-03	1.40E+00	5.00E-03	6.67E-01
			7.00E+01	2.10E+00	5.00E-03	1.50E+00	5.00E-03	7.14E-01
			7.00E+01	2.10E+00	5.00E-03	1.60E+00	5.00E-03	7.62E-01
			7.50E+01	2.10E+00	5.00E-03	1.40E+00	5.00E-03	6.67E-01
			7.50E+01	1.90E+00	5.00E-03	9.00E-01	5.00E-03	4.74E-01
			7.50E+01	1.90E+00	5.00E-03	1.40E+00	5.00E-03	7.37E-01
			7.50E+01	2.30E+00	5.00E-03	1.30E+00	5.00E-03	5.65E-01
			7.50E+01	1.80E+00	5.00E-03	1.20E+00	5.00E-03	6.67E-01
			7.50E+01	2.00E+00	5.00E-03	1.20E+00	5.00E-04	6.00E-01
			7.50E+01	1.90E+00	5.00E-03	1.20E+00	5.00E-03	6.32E-01
			7.50E+01	1.90E+00	5.00E-03	1.20E+00	5.00E-03	6.32E-01
			8.50E+01	2.06E-01	5.00E-03	5.50E-02	5.00E-03	2.67E-01
			8.50E+01	2.49E-01	5.00E-03	6.50E-02	5.00E-03	2.61E-01
			8.50E+01	2.76E-01	5.00E-03	4.90E-02	5.00E-03	1.78E-01
			8.50E+01	2.80E-01	5.00E-03	6.70E-02	5.00E-03	2.39E-01
			8.50E+01	2.95E-01	5.00E-03	6.90E-02	5.00E-03	2.34E-01

Target	Projectile	Velocity (km s^{-1})	Angle (degrees)	Short axis(cm)	abs error(cm)	Long axis (cm)	abs error(cm)	Short/Long
HE30	AISI420C		8.50E+01	5.79E-01	5.00E-03	5.00E-02	5.00E-03	8.64E-02
			8.50E+01	2.42E-01	5.00E-03	1.62E-01	5.00E-03	6.69E-01
			8.50E+01	5.52E-01	5.00E-03	5.90E-02	5.00E-03	1.07E-01
			8.50E+01	3.22E-01	5.00E-03	3.10E-02	5.00E-04	9.63E-02
			8.50E+01	2.68E-01	5.00E-03	5.90E-02	5.00E-03	2.20E-01

Light Gas Gun Normal Incidence Raw Data

Target	Projectile	Velocity (km s^{-1})	short axis (cm)	abs error (cm)	long axis (cm)	abs error (cm)	short/long
Mild Steel	Cu Wire, aspect ratio~4	4.77E+00	9.40E-02	5.00E-03	8.50E-02	5.00E-03	9.04E-01
			1.30E-01	5.00E-03	1.05E-01	5.00E-03	8.08E-01
			1.41E-01	5.00E-03	1.17E-01	5.00E-03	8.30E-01
			1.53E-01	5.00E-03	1.10E-01	5.00E-03	7.19E-01
			1.51E-01	5.00E-03	1.12E-01	5.00E-03	7.42E-01
			1.57E-01	5.00E-03	1.15E-01	5.00E-03	7.32E-01
			1.33E-01	5.00E-03	1.22E-01	5.00E-03	9.17E-01
			1.70E-01	5.00E-03	1.12E-01	5.00E-03	6.59E-01
Pb 8mm	as above	4.77E+00	2.67E-01	5.00E-03	2.63E-01	5.00E-03	9.85E-01
			1.80E-01	5.00E-03	1.70E-01	5.00E-03	9.44E-01
			2.50E-01	5.00E-03	2.25E-01	5.00E-03	9.00E-01
Pb 8mm	hexagonal polyester projectiles	5.00E+00	5.70E-02	5.00E-03	4.70E-02	5.00E-03	8.25E-01
			5.00E-02	5.00E-03	3.40E-02	5.00E-03	6.80E-01
			4.50E-02	5.00E-03	4.30E-02	5.00E-03	9.56E-01
			3.40E-02	5.00E-03	2.90E-02	5.00E-03	8.53E-01
			2.80E-02	5.00E-03	2.40E-02	5.00E-03	8.57E-01
			4.60E-02	5.00E-03	4.10E-02	5.00E-03	8.91E-01
			3.90E-02	5.00E-03	3.90E-02	5.00E-03	1.00E+00
			4.90E-02	5.00E-03	3.60E-02	5.00E-03	7.35E-01
			2.10E-02	5.00E-03	2.10E-02	5.00E-03	1.00E+00
			5.70E-02	5.00E-03	2.20E-02	5.00E-03	3.86E-01